

University of Strathclyde

Department of Electronic and Electrical Engineering

**Techniques for analysis and interpretation of
UHF partial discharge signals**

by

Tanya Pinpart

A thesis presented in fulfilment of the requirements for the degree
of Doctor of Philosophy

2010

This thesis is the result of the author's original research. It has been composed by the author and has not been previously submitted for examination which has led to the award of a degree.

The copyright of this thesis belongs to the author under the terms of the United Kingdom Copyright Acts as qualified by University of Strathclyde Regulation 3.50. Due acknowledgement must always be made of the use of any material contained in, or derived from, this thesis.

Signed:

Date:

Abstract

Detecting partial discharge (PD) is an effective approach to warn of insulation degradation. Ultra high frequency (UHF) detection has been applied for monitoring of gas insulated substations and power transformers with successful results. The technique involves detecting the sub-nanosecond PD current pulses by the signals which they radiate in the 300 – 3000 MHz band. In this research, an envelope comparison was successfully developed for distinguishing between different PD sources based on signals sampled at rates of 5 or 10 GHz. A key benefit of envelope comparison is for reducing measurement bandwidth while retaining a good ability to differentiate between different PD sources. A 2-channel UHF envelope detector was constructed and its outputs intentionally sampled at a lower sampling rate. Results obtained from a model transformer validated the hypothesis that reduced sampling rate envelopes can be used for this purpose, thereby decreasing the hardware specification required for PD analysis. A critical factor for locating PD accurately is arrival time measurements for UHF signals. In this research, various approaches for improving arrival time measurements were evaluated. An alternative technique, the relative increase in energy, was proposed and assessed using pulse injection tests on a power transformer. This new method was shown to be capable of giving more accurate arrival times than existing methods. The use of wavelet de-noising on UHF PD signals was investigated experimentally. Results suggest that care is required when UHF signals are processed in this way because the waveform may be altered in a way that changes its apparent arrival time. The use of wavelet decomposition to identify arrival times was also investigated but it did not show improvements over existing methods. Laboratory experiments which varied factors that might affect arrival time measurements were carried out. Results showed that variations in PD current direction have no strong effect on the observed arrival times and it is possible to improve the accuracy of arrival times by increasing the sensitivity of measurement at the expense of signal clipping. Furthermore, the accuracy of arrival times at more distant sensors appears to be degraded. A new arrival time consistency index has also been introduced to assess the sensitivity of arrival times to small changes in threshold value used to determine signal onset.

Acknowledgements

First and foremost, I would like to offer my sincerest gratitude to my supervisor, Dr Martin Judd, who has supported me throughout my study with his patience and knowledge. Without Dr Judd, my study would not be completed.

My gratitude must also go to Dr John Fletcher, who helped me through the heaviest period at the beginning of my study in the UK. Without Dr Fletcher, my achievement would not be possible. I would like to thank Jack Barrasford for his invaluable practical assistance. I would also like to thank Peter Kakeeto, who always gave me excellent discussions, and the rest of the High Voltage Technologies research group. Special thanks go to Professor Chengke Zhou and Dr Xiaodi Song of Glasgow Caledonian University for their advice about wavelet analysis. I am grateful for a Thai Government Science and Technology Scholarship that provided financial support during my study.

I would also like to thank my parents and Ruchuchai Kochawat for their love, support and encouragement through my study in the UK.

Preface

This thesis is divided into seven chapters:

Chapter 1 introduces the concept of partial discharge (PD) and its significance in electrical systems. Four types of PD are discussed. Common detection techniques for PD signals and the use of PD monitoring as a diagnostic test for insulation are outlined. Finally, the novel contributions of the research in this thesis are presented.

Chapter 2 proposes a new technique, the *envelope comparison method*, for distinguishing between different PD sources of UHF signals and evaluates its performance using UHF PD signals obtained from both laboratory experiments and industrial tests.

Chapter 3 discusses the importance of arrival time of UHF signals for PD location and the key factors that affect measured UHF waveforms. It also discusses existing techniques for determining arrival times and proposes an alternative technique, namely *relative increase in energy* to assist with automatically determining arrival times.

Chapter 4 reports an investigation into the use of wavelet de-noising and wavelet decomposition to improve arrival time measurements.

Chapter 5 describes evaluations of the accuracy of arrival time measurements by means of laboratory experiments using three approaches, i.e., selection of UHF sensor design and installations, variations of PD sources and increasing the sensitivity of measurement. A new *arrival time consistency index* is also introduced.

Chapter 6 presents a practical implementation of some numerical techniques presented in previous chapters.

Chapter 7 summarises the findings of the research and suggests future work.

2. Envelope comparison method	42
2.1 Introduction.....	42
2.2 Concept and practical advantages.....	42
2.3 Procedures for envelope comparison.....	50
2.4 Experimental arrangement.....	56
2.5 Experimental results.....	60
2.5.1 Effects of varying W for envelope creation.....	60
2.5.2 Potential sampling rate reduction.....	69
2.6 Case studies.....	73
2.6.1 The switched HVDC reactor.....	74
2.6.2 The 252 MVA power transformer.....	75
2.6.3 Analysis and results of case studies.....	77
2.7 Additional recommendations to the envelope comparison method.....	80
2.8 Discussion and conclusions.....	81
3. Study of techniques for determining arrival times of UHF signals	83
3.1 Introduction.....	83
3.2 Importance of arrival times.....	83
3.3 Factors that affect measured UHF waveforms.....	87
3.3.1 Shape of a PD current pulse.....	87
3.3.2 Internal propagation path.....	90
3.3.3 Response of UHF sensor and its installation method.....	90
3.3.4 Measurement bandwidth.....	91
3.4 Existing techniques for determining arrival times.....	91
3.4.1 Expanding time scale and identifying the arrival time manually... ..	92
3.4.2 Threshold crossing method.....	93
3.4.3 Knee point of cumulative energy curve.....	95
3.4.4 Energy criterion method.....	97
3.5 A new technique: Relative increase in energy.....	100

3.6	Results and analysis.....	103
3.6.1	Pulse injection tests.....	103
3.6.2	Reference time differences.....	105
3.6.3	Time differences obtained from the 2% threshold.....	106
3.6.4	Time differences obtained from the relative increase in energy..	107
3.6.5	Evaluation of relative increase in energy.....	109
3.7	Discussion and conclusions.....	110
4.	Investigating the use of Wavelet techniques for improving UHF time of flight measurements	111
4.1	Introduction.....	111
4.2	Overview of wavelet techniques.....	111
4.2.1	Introduction.....	111
4.2.2	Wavelet transform.....	114
4.2.3	Wavelet decomposition.....	118
4.2.4	Wavelet de-noising.....	121
4.2.5	Applications of wavelets in the field of PD diagnosis.....	123
4.3	Effect of wavelet de-noising on arrival times.....	123
4.3.1	UHF partial discharge signals to be analysed.....	124
4.3.2	De-noising partial discharge signals.....	129
4.3.3	Results and discussion.....	133
4.4	Wavelet decomposition for determining arrival times.....	137
4.4.1	Experimental arrangement.....	137
4.4.2	Time differences obtained from geometric calculations.....	143
4.4.3	Results and analysis.....	143
4.4.4	Comparison of time differences obtained between wavelet decomposition and original UHF signal.....	148
4.5	Discussion and conclusions.....	150

5. Experimental investigations into the accuracy of signal arrival time measurements	152
5.1 Introduction.....	152
5.2 Selection of UHF sensor for arrival time measurements.....	152
5.2.1 Test arrangement and methodology.....	152
5.2.2 Test procedures.....	155
5.2.3 Analysis.....	158
5.2.4 Results.....	161
5.3 Experimental arrangement.....	163
5.3.1 Study 1: The PD moved around the shielded room.....	163
5.3.2 Study 2: Variation of spark plug tip orientation.....	164
5.2.3 Study 3: Increasing the sensitivity of the measurement.....	166
5.4 Methodology.....	168
5.5 Results and analysis.....	170
5.5.1 Study 1: The PD moved around the shielded room.....	170
5.5.2 Study 2: Variation of spark plug tip orientation.....	173
5.5.3 Study 3: Increasing the sensitivity of the measurement.....	175
5.5.4 Evaluation of results.....	176
5.6 Arrival time consistency index for evaluating the signal onset.....	179
5.6.1 Concept.....	179
5.6.2 Results and analysis.....	184
5.7 Discussion and conclusions.....	187
6. Practical implementations	189
6.1 Introduction.....	189
6.2 Practical implementation of the envelope comparison method.....	189
6.2.1 Hardware concept of the envelope detector circuit.....	189
6.2.2 Investigating use of reduced sampling rate envelopes for distinguishing between different PD sources using computer modelling.....	191

6.2.3	The envelope detector circuit.....	196
6.2.4	Laboratory experiments.....	199
6.3	Applications of the relative increase in energy.....	210
6.3.1	Determining arrival times by an automated process.....	210
6.3.2	Contribution to time offset compensation.....	215
6.4	Applications to other types of monitoring system.....	218
6.5	Discussion and conclusions.....	220
7.	Conclusions and Future Work	223
7.1	Envelope comparison.....	223
7.2	Relative increase in energy.....	224
7.3	The use of wavelet analysis.....	226
7.4	Experimental investigation into the accuracy of signal arrival time measurements.....	227
7.5	Future work.....	228
8.	References	230
	Appendix A	244
	Appendix B	245

List of Figures

1.1	Dust figures in a mixture of 1% SF ₆ and 99% N ₂ at atmospheric pressure, applied voltage: 1×40 μs lightning impulse [4]: (a) Electrode arrangement, (b) -25 kV applied, (c) +20 kV applied.....	3
1.2	Current – voltage relationship in the pre-spark region [16].....	5
1.3	Space charge field [E_r] around avalanche head [16].....	7
1.4	Cloud chamber photographs showing the transformation from avalanche at an anode to completely connect a cathode by a plasma channel [16]: (a) avalanche near anode, (b) and (c) cathode directed streamer starts, (d) and (e) time period for a plasma channel to connect cathode and anode.....	8
1.5	Mechanism of failure and variation of breakdown strength in solids with time of stressing [16].....	10
1.6	Internal discharges [2]: (a) Flat cavity that is perpendicular to the electric field, (b) Spherical cavity,(c) Long and parallel to the electric field cavity.....	13
1.7	Paschen’s curve shows the breakdown voltage of air as a function of pressure×electrode spacing [2]. The dotted line indicates the breakdown voltage at 1 atm.....	15
1.8	A plane-plane configuration to show surface discharge and to indicate breakdown of an airgap in series with a solid dielectric.....	17
1.9	Corona discharges at the sharp edge [2].....	18
1.10	Electrical trees [27]: (a) Branch-type tree, (b) Bush-type tree.....	19
1.11	Basic PD test circuit when coupling device CD in series with the test object C_r	22
1.12	Key gases obtained from two types of developing faults in oil insulated power transformers used for DGA [28]: (a) PD, (b) Electrical arcing.....	24
1.13	Coordinates and fault zones of Duval’s triangle.....	26
1.14	Acoustic PD detection.....	27
1.15	Various mounting positions for UHF PD sensors on GIS [42].....	29
1.16	Three UHF sensors for power transformers [42].....	30
1.17	Mapping the training samples from input space to feature space [69].....	38

2.1	Frequency response of the UHF sensor. The region between 500 MHz and 1500 MHz is normally used to specify UHF PD sensors for GIS. [73]	44
2.2	Sensor positions (S1 –S4) inside the reactor housing [73]	44
2.3	Typical UHF signals generated from two different PD sources, which were captured by four UHF sensors simultaneously: (a) Signals of type A, (b) Signals of type B. This is to show that two groups of UHF signals can be distinguished ‘by eye’	45
2.4	Diagram to illustrate the principle of the envelope comparison method	47
2.5	Typical UHF PD waveform recorded during site testing. This is to show the presence of DC offset	50
2.6	UHF waveform after removal of DC offset	51
2.7	Normalised squared voltage of the signal shown in Figure 2.6	52
2.8	Several PD waveforms and their envelopes (recorded during 252 MVA power transformer test): (a) PD signals captured by the same sensor (variable triggering positions are evident), (b) Voltage squaring, smoothing and normalisation of the envelope belonging to PD event 1, both shown on a normalised scale, (c) Normalised envelopes of the three original PD signals, (d) Normalised envelopes after time offset compensation.	54
2.9	Contact discharge test cell positioned inside the tank	57
2.10	Structure of the contact discharge test cell [79]	57
2.11	Schematic diagram of the experimental arrangement: (a) Tank dimension and S1, S2 and S3 UHF sensors coordinates, (b) Test cell positions (P1 – P5) tested on plane $z = 0.63$ m	58
2.12	UHF PD waveforms captured by 3 UHF sensors simultaneously at P1	59
2.13	Typical frequency spectrum of PD signal (this example belonging to S3 of Figure 2.12)	60
2.14	Normalised envelopes obtained using different window widths and its normalised UHF voltages squared, observed by S1 with the test cell at P1	61
2.15	Normalised envelopes of the same PD using $W = 20$ ns for smoothing, observed by three sensors with the test cell at P1	61

2.16	Difference coefficient values for investigating margins between same and different PD positions: (a) Overlapping data for $W = 60$ ns, (b) Very narrow margin for $W = 40$ ns, (c) Clear margin with 1 value match from 285 values for $W = 20$ ns.....	63
2.17	Difference coefficient values and margin for $W = 20$ ns, sorted into ascending order (Note that for D from different sensor comparisons only the lowest 95 values are deemed).....	64
2.18	Comparison among the three envelopes obtained from sensor S2 that produce 1 value mismatch. Values of D_{SA} for the similarity assessment between (1) reference and 6 th envelope and (2) reference and 10 th are 3.38 and 1.04, respectively.....	65
2.19	Values of average multi-sensor D compared between same and different PD locations, sorted into ascending order: (a) $W = 4$ ns, (b) $W = 20$ ns.....	67
2.20	Frequency spectrum of ‘S3’ in Figure 2.12 plotted in log-log scale.....	69
2.21	Frequency spectra of the smoothed envelopes for P1: (a) $W = 4$ ns, (b) $W = 20$ ns. This is to illustrate the reduction of frequency spectrum using larger W	70
2.22	The 512-sample with a sampling rate of 5×10^9 samples/sec and its smoothed curve using Gaussian kernel smoothing $W = 4$ ns, for example.....	71
2.23	The normalised spectral density of the smoothed envelope of the 512-sample impulse.....	71
2.24	The selection of -3dB cut-off frequency.....	72
2.25	Bandwidth of filtering by Gaussian kernel smoothing as a function of window width W	72
2.26	The switched HVDC reactor: (a) Typical UHF waveforms captured using three sensors simultaneously, (b) Their normalised envelopes created from $W = 4$ ns.....	74
2.27	Diagram of the 252 MVA power transformer showing four UHF sensors positions (S1 – S4) and their coordinates in the (x, y, z) directions. The 3 large and 3 small circles on top of the tank mark the approximate locations of the HV and LV bushings respectively.....	75

2.28	The 252 MVA power transformer: (a) Typical UHF waveforms captured using three sensors simultaneously, (b) Their normalised envelopes created from $W = 4$ ns.....	76
2.29	Ascending difference coefficient values between the signals from the same sensors and different sensors comparisons of the switched HVDC reactor. This is to illustrate the clear separation between them.....	78
2.30	Ascending difference coefficient values between the signals from the same sensors and different sensors comparisons of the 252 MVA power transformer. This is to illustrate the overlap region presenting in this case.....	78
2.31	Average multi-sensor D values (sorted into ascending order) of the switched HVDC reactor. This is to illustrate the improved margin obtained using average multi-sensor D	79
2.32	Average multi-sensor D values (sorted into ascending order) of the 252 MVA power transformer. This is to illustrate the margin instead of overlap obtained using average multi-sensor D	79
3.1	A section of 400 kV GIS containing a PD source. S1 and S2 are UHF sensors.....	84
3.2	UHF PD signals measured at S1 and S2 with their measured arrival times.....	84
3.3	Schematic diagram of Figure 3.1, where L is the total length of GIS section and x is the distance of the PD from S1.....	85
3.4	UHF signals captured from pulse injected: (a) UHF signals, (b) Expanded view of (a) to illustrate approximate arrival times. This is to show the difference of apparent and ambiguous arrival times.....	86
3.5	Positive PD current pulses at 0.1 MPa for four gasses [86].....	88
3.6	Idealised PD current pulse represented using a Gaussian function with $\sigma = 1.0$ and its rise time (10% - 90%) = 1.6 ns.....	89
3.7	Plot of the idealised PD pulse ($\sigma = 1.0$) and its time-derivative proportional to radiated electric field of the PD current pulse.....	89

3.8	Time-derivative waveforms obtained for two Gaussian PD current pulses ($\sigma=0.5$ and 1.0). This is to illustrate the potential difference of arrival times for fast (A) and slow (B) rise times.....	90
3.9	UHF voltage signal illustrating an unclear arrival time.....	92
3.10	Expanded view of the signal shown in Figure 3.9 to illustrate the arrival time obtained from manually expanding sub-nanosecond time scale.....	93
3.11	Normalised squared UHF voltage of the signal in Figure 3.9. This is to exhibit improved visibility of the arrival time using the squared waveform.....	94
3.12	Illustration of two thresholds used for determining arrival times for the UHF signal of Figure 3.9. This is to show the squared sample points every 0.2 ns (5×10^9 samples/sec) in order to demonstrate how the arrival time is determined.....	94
3.13	Cumulative energy curve analysis for the signal shown in Figure 3.9: (a) Cumulative energy curve, (b) Expanded view that shows knee area containing the arrival time.....	96
3.14	UHF waveform and its partial energy S'_i curve: (a) S'_i obtained using $\alpha = 250$, (b) Expanded view of (a) to determine the arrival time using the global minimum of S'_i curve.....	98
3.15	UHF waveform and its partial energy S'_i curve generated using $\alpha = 100$. This is to illustrate that the S'_i curve cannot provide the global minimum for determining the arrival time. This is to show that the value of α influences the shape of S'_i	99
3.16	The UHF waveform and its R_{iEj} curve: (a) The UHF signal obtained from the laboratory, (b) R_{iEj} curve for this signal.....	101
3.17	Combined plot of R_{iEj} (solid line) and e_i (dotted line) to identify the arrival time.....	102

3.18	Flowchart to determine the arrival time automatically using the relative increase in energy. Note that two parameters indicated by * (the window time and the threshold with respect to the highest peak of R_{iEj}) need to be adjusted to suit PD signals characteristics. The values shown here are only representative for the purpose of understanding the process. Further analysis will be presented in Section 6.3	103
3.19	Model of the 252 MVA power transformer shows coordinates (x, y, z) of the UHF sensors (S1 – S4) in metres	104
3.20	UHF signals obtained when a 100 V impulse was injected at S4	105
3.21	Internal propagation paths when the pulse was injected at S4	106
3.22	Arrival times obtained from R_{iEj} for the UHF signals of Figure 3.20 (solid lines are R_{iEj} and dotted lines are cumulative energy curves): (a) Arrival time of S1, (b) Arrival time of S2, (c) Arrival time of S3	108
3.23	Error comparisons between $ \Delta T_{ref} - \Delta T_{2\%TH} $ and $ \Delta T_{ref} - \Delta T_{RiEj} $	109
4.1	The UHF waveform obtained from the HVDC reactor PD testing	112
4.2	Spectrograms generated from the signal depicted in Figure 4.1: (a) With a 64-point time window, (b) With an 80-point time window. This is to illustrate the difference between time and frequency of spectrograms created from different sizes of the time window	113
4.3	Discrete wavelet transform operation consisting of filtering and down sampling processes (F_s = sampling rate)	116
4.4	The UHF PD signal and its decomposed signals obtained from the discrete wavelet transform: (a) The UHF signal, (b) Approximations, (c) Details	117
4.5	Wavelet decomposition tree for three levels	118
4.6	A UHF PD signal and its decomposed signals resulting from wavelet decomposition to three levels using db11	119
4.7	Relationship between maximum decomposition level and the length of the signal using db4 and db11	121
4.8	Three UHF sensors installed at the top of the 18 MVA single phase power transformer [46]	124

4.9	Typical UHF PD signals recorded simultaneously at 3 sensors S1-S3	125
4.10	Reference arrival times derived from the instantaneous UHF voltages squared of the signal depicted in Figure 4.9. The symbols on each trace correspond to the sample points. Note that the time axis is limited between 7 ns and 12 ns for illustrating the initial wavefronts of signals	126
4.11	Waveforms of wavelet functions: (a) db4, (b) db7, (c) db10, (d) db11 (db12 is not shown here because its shape is very similar to db11)	127
4.12	UHF signal combined with white Gaussian noise: (a) Original UHF signal – clean signal, (b) With SNR = 10 dB, (c) With SNR = 0 dB	128
4.13	Clean signal and de-noised waveforms using db4-1 setting for Figure 4.12: (a) Clean signal (original signal), (b) SNR = 10 dB, (c) SNR = 0 dB	129
4.14	Comparison between clean and de-noised PD signals based on SNR = 0 dB (db4-1 setting). This is to illustrate that the shape of de-noised signals is altered in a way that changes its arrival time	130
4.15	‘Block 1’ outlining the approach for calculating differential arrival time between clean and de-noised signals	132
4.16	‘Block 2’ outlining the approach for calculating the differential time of flight error	132
4.17	Differential arrival times as a function of SNR obtained from: (a) S1, (b) S2, (c) S3	134
4.18	Examples of differential time of flight errors: (a) Signals processed by db4-1, (b) Signals processed by db4-2	136
4.19	Schematic diagram of the test arrangement and coordinates of two sensors (sensor REF and sensor S) in the shielded room	138
4.20	Spark unit functioning as a movable PD source	139
4.21	Disc-type UHF sensor installed in the shield room	140
4.22	Diagram illustrating flow of UHF signals to be analysed	140
4.23	Outputs obtained by connecting both measurement cables to REF. This is to validate equality of electrical length of the measurement cables between each sensor and the oscilloscope	141
4.24	Typical UHF signals obtained from two sensors when the spark unit is about halfway between two sensors (P11)	142

4.25	Diagram illustrating the analysis procedures	145
4.26	Typical approximation waveform for decomposition level 1 (cA_I): (a) cA_I , (c) Normalised amplitude of cA_I^2 , (c) Expanded view of (b) to determine the arrival time using the 2% threshold crossing method	146
4.27	Relationship between ΔT_{MEA} and Δd derived from: (a) Decomposition level = 1, (b) Decomposition level = 2	147
4.28	Relationship between ΔT_{MEA} and Δd obtained from the 2% threshold crossing method of UHF voltages squared	149
4.29	Comparison of mean values of absolute errors obtained from wavelet decomposition at 5 levels and from the UHF signal itself	149
5.1	Three types of UHF sensors used in the experiments together with a mask showing the shape of the logarithm spiral antenna	153
5.2	The avalanche pulser functioning as a movable PD source inside the tank	154
5.3	The test tank with 2 sensors (S1 and S2) installed showing 15 positions of the PD source (circles) on the plane at $z = 0.71$ m	154
5.4	GTEM system used to measure the sensor step response	155
5.5	Step responses of the sensors measured on the GTEM system	156
5.6	Step responses when only the step response of the spiral type was multiplied by a factor of 10 to show initial wavefront more clearly	157
5.7	Measured UHF waveforms for each type of sensor for the pulser at P15	158
5.8	Relationship between absolute errors of 3 types of UHF sensors plotted against distances	162
5.9	Top view of the shielded room to illustrate five PD positions (D1 – D5)	165
5.10	UHF signals at position D1 of study 3. This is to indicate the different noise levels may arise when different sensitivity settings are used	166
5.11	Top view of the shielded room to illustrate PD positions (R1 – R9)	167
5.12	Diagram to illustrate the process for evaluating the accuracy of the UHF PD location	169

5.13	Diagram to illustrate the entire procedure used in the analysis.....	170
5.14	Relationship between ΔT and Δd for ΔT_{MEA} and ΔT_{GEO} , tested in the shielded room.....	171
5.15	x - y plane plots for each z -plane to illustrate the means of absolute errors (e) of each PD position, tested in the shielded room: (a) At plane $z = 0.23$ m, (b) At plane $z = 0.92$ m, (c) At plane $z = 1.34$ m.....	172
5.16	Relationship between ΔT and Δd for ΔT_{MEA} and ΔT_{GEO} when variation of the spark plug tip orientation was investigated.....	173
5.17	x - y plane plots for each variation of the spark plug tip orientation to illustrate the means of absolute errors (e) for each PD position in the shielded room:(a) Upright, (b) Pointing-to-REF, (c) Pointing-to-S, (d) Pointing-to-Back.....	174
5.18	Relationship between ΔT and Δd for ΔT_{MEA} and ΔT_{GEO} when the sensitivity of 2 mV/div was utilised.....	175
5.19	x - y plane plots to illustrate the means of absolute errors (e) for each PD position of the shielded room when the sensitivity of 2mV/div was utilised.....	176
5.20	Experimental (ΔT_{MEA}) and theoretical (ΔT_{GEO}) relationships for study 1 showing the error e relative to differential propagation distances (Δd)....	178
5.21	An impulse to show the ideal scenario for determining the signal arrival time.....	180
5.22	UHF signal obtained from sensor S at R3: (a) Initial wavefront, (b) Its constant arrival times resulted from 1% to 5% threshold crossing. This is to demonstrate consistent arrival times.....	181
5.23	UHF signal obtained from sensor REF at R2: (a) Initial wavefront, (b) Its variable arrival times resulted from 1% to 5% threshold crossing. This is to illustrate the challenge of selecting a specific threshold that gives a consistent arrival time when there is high sensitivity of arrival times to small changes of threshold value.....	182
5.24	$1/CI$ evaluated in the range of threshold values between 2% and 5% for each PD positions (R1 – R9) producing from the signals captured at: (a) Sensor REF, (b) Sensor S.....	187

6.1	Comparison of UHF signal and its envelope obtained from one type of defect [126]: (a) UHF signal, (b) Envelope	190
6.2	Hardware diagram for capturing the envelope of UHF signals	190
6.3	Diagram to illustrate procedures for obtaining envelopes at original sampling rate	192
6.4	Typical UHF signal obtained from the experiment in Section 2.4	192
6.5	Normalised UHF voltage squared of the signal shown in Figure 6.4	193
6.6	The envelope of the signal shown Figure 6.4 generated using 4-ns Gaussian kernel smoothing. This envelope still comprises 8,192 samples over 1,600 ns	193
6.7	Diagram to illustrate procedures for obtaining reduced signal sampling rate envelopes	194
6.8	Half-wave rectified version of the signal shown in Figure 6.4	194
6.9	Reduced sampling rate envelope created from the third-order Butterworth 10 MHz low-pass filter. This envelope consists of 81 samples over 1,600 ns	195
6.10	Margin between the same and different PD positions derived from the envelopes sampled with the sampling rate of 5×10^9 samples/sec	195
6.11	Margin between the same and different PD positions derived from the envelopes sampled with the sampling rate of 50×10^6 samples/sec, a sampling rate reduction by a factor of 100	196
6.12	Simple circuit diagram of the envelope detector	197
6.13	Diagram to illustrate the input and output of the envelope detector circuit	197
6.14	Pair of identical envelope detector circuits used in the experiments	197
6.15	Output of the envelope detector circuit obtained from the contact discharge test cell: (a) Normalised voltage envelope, (b) Its frequency spectrum	198
6.16	Test arrangement, REF and S are disc-type UHF sensors	199
6.17	Diagram to illustrate how the envelopes to be analysed were acquired	200

6.18 Comparison between the output of the envelope detector and its ‘eres’ filtered envelope created from UHF signals excited by the contact discharge test cell: (a) Normalised voltage envelopes, (b) Frequency spectra.....	201
6.19 Comparison between the envelopes generated from two different types of PD sources recorded at sensor S: (a) Their direct sampled envelopes from the envelope detector, (b) Their filtered envelopes to be analysed	202
6.20 Comparison between the envelopes generated from two different types of PD sources recorded at sensor REF: (a) Output envelopes from the envelope detector, (b) Their filtered envelopes to be analysed	203
6.21 Margin between the same and different PD positions.....	205
6.22 Test arrangement: (a) Transformer model consisting of a steel core structure and three windings in a steel tank. Note that the winding assembly was moved to the centre of the transformer tank and the end panel was replaced during the experiments (b) The spark unit used as a movable PD source.....	206
6.23 Reduced sampling rate envelopes (five envelopes per sub-figure) obtained from: (a) S1 at SPK1, (b) S2 at SPK1, (c) S1 at SPK2, (d) S2 at SPK2, (e) S1 at SPK3, (f) S2 at SPK3.....	208
6.24 Values of average multi-sensor D calculated from three comparisons of SPK1, SPK2 and SPK3, sorted into ascending order: (a) SPK1 and SPK2, (b) SPK1 and SPK3, (c) SPK2 and SPK3. Note that upper bands are for different PD position comparisons and lower bands are for same PD position comparisons.....	209
6.25 UHF signal obtained from UHF PD monitoring of an HVDC reactor..._	210
6.26 Normalised R_{iEj} waveform of the signal shown in Figure 6.25. This is to show that T_p can be indentified immediately.....	211
6.27 Expanded view of Figure 6.26 to illustrate the boundaries and search region for the expected arrival time.....	211
6.28 UHF signals obtained from four sensors, recorded simultaneously.....	212

6.29 Average values of absolute errors for 4 sensors plotted against threshold levels. This is to illustrate that the 15% threshold level is the most effective option in this study.....	214
6.30 Original UHF signals captured by sensor 1.....	216
6.31 Waveforms after time offset compensation, which is done by aligning peaks of R_{iEj}	216
6.32 Normalised envelopes of: (a) Original UHF signals shown Figure 6.30, to show that original envelopes appear dissimilar when considering in the same period of time, (b) Shifted version.....	217
6.33 Acoustic signal created from the PD source in power transformer [95]..	218
6.34 Envelope signal taken from the signal shown in Figure 6.33 [95].....	219
6.35 Demodulated output of the sensor, switch voltage (U_s) and current (I_s). Contact separation is seen at $t_0 = 3.4$ ms and the arc is extinguished at $t_1 = 6.8$ ms, so that its arcing time is 3.4 ms [130]......	220

List of Tables

1.1	Lists of typical oil composition gases.....	23
1.2	Five gas ratios.....	25
2.1	Values of difference coefficient (D) and average multi-sensor D for all possible comparisons for P1.....	66
2.2	Mean and standard deviation (STD) values of difference coefficient (D) and average multi-sensor D values for the same PD positions with $W = 20$ ns.....	68
2.3	Mean and standard deviation (STD) values of difference coefficient (D) and average multi-sensor D values for the different PD positions with $W = 20$ ns.....	68
2.4	Data set and sensors being used to capture UHF signals for each set.....	77
2.5	Number of Difference coefficient values for possible comparisons.....	77
3.1	Reference time differences when the pulse is injected at each of the four sensors.....	105
3.2	Time differences obtained from 2%TH when the pulse is injected at each of the four sensors.....	107
3.3	Time differences obtained from R_{iEj} when the pulse is injected at each of the four sensors.....	107
4.1	Properties of the data obtained during wavelet decomposition to 3 levels.....	120
4.2	Mother wavelets and threshold selection methods used in this study.....	126
4.3	Coordinates of PD positions in the shield rooms.....	142
4.4	Summary of sample points, times between successive samples and equivalent sampling rate of each decomposed level.....	144
4.5	Mean values of absolute errors and their propagation distance in air and transformer oil for each decomposition level.....	148

5.1	Distances (m) between S2 and the PD positions.....	158
5.2	Differential distances (m) for each pair of PD positions.....	159
5.3	Theoretical propagating times (ns) resulted from Table 5.2.....	160
5.4	Arrival times (ns) of measured signals.....	160
5.5	Observed propagating times (ns) between pairs of PD positions obtained from the disc type sensor.....	161
5.6	Absolute errors (ns) for the disc type sensor.....	162
5.7	Coordinates of PD positions for study 1.....	164
5.8	Coordinates of PD positions for study 2.....	165
5.9	Coordinates of PD positions for study 3.....	167
5.10	Summary of test arrangements.....	177
5.11	Results obtained from test arrangements shown in Table 5.10.....	177
5.12	Arrival times obtained from PD at R1 measured using sensor REF.....	184
5.13	Values of squared terms for evaluating using 2% threshold.....	185
5.14	Values of $1/CI_{x\%}$ for all PD positions.....	186
6.1	Coordinates of two different PD sources.....	200
6.2	Values of difference coefficient (D) and average multi-sensor D calculated from the <i>spark unit</i>	204
6.3	Values of difference coefficient (D) and average multi-sensor D calculated from the <i>contact discharge test cell</i>	204
6.4	Values of difference coefficient (D) and average multi-sensor D compared between the spark unit (set 1) and contact discharge test cell (set 1 – set 11)	205
6.5	Coordinates of UHF sensors and PD sources.....	207
6.6	Time of highest peak, T_p (ns).....	213
6.7	Examples of arrival times (ns) obtained from PD set 2.....	213
6.8	Time differences (ns) calculated from Table 6.7.....	213
6.9	Absolute errors (ns) and their average values for each threshold level calculated from Table 6.8.....	214
6.10	Time shifts and their averages.....	215

List of Publications

Much of the work contained in this thesis is based on the following papers, which the author has published during the course of the research:

Published conference papers

- [77] T. Pinpart, G. West, S. Galloway, and M. D. Judd. A method for distinguishing between complex transient signals in condition monitoring applications, In *Proceedings of International Conference on 5th Condition Monitoring and Machinery Failure Prevention Technologies*, pp. 1163 – 1171, Edinburgh, 2008.
- [82] T. Pinpart, J. E. Fletcher, and M. D. Judd. Methods for distinguishing between partial discharges based on the UHF detection technique, In *Proceedings of International Conference on Condition Monitoring and Diagnosis*, pp. 1060 – 1064, Beijing, 2008.
- [100] T. Pinpart, and M. D. Judd. Improving UHF partial discharge location in high voltage equipment, In *Proceedings of the 44th International Universities' Power Engineering Conference*, Glasgow, 2009.
- [101] T. Pinpart, and M. D. Judd. Improved technique for locating insulation defects in high voltage equipment, In *Proceeding of 2nd UHVnet Colloquium*, pp. 69 – 72, Glasgow, 2009.
- [120] T. Pinpart, A. M. bin Ishak, and M. D. Judd. Effect of wavelet de-noising on signal timing accuracy for UHF partial discharge location, In *Proceedings of 11th International Electrical Insulation Conference*, pp 128 – 133, Birmingham, 2009.

- [123] T. Pinpart, and M. D. Judd. Experimental comparison of UHF sensor types for PD location applications, In *Proceedings of IEEE Electrical Insulation Conference*, pp 26 – 30, Montreal, 2009.
- [127] T. Pinpart, and M. D. Judd. Differentiating between partial discharges by comparing UHF signal envelopes with reduced signal sampling rate, In *Proceeding of 3rd UHVnet Colloquium*, Manchester, 2010.

Journal papers

1. T. Pinpart and M. D. Judd. Differentiating between partial discharge sources using envelope comparison of UHF signals, accepted in *Proceedings of IET Science, Measurement and Technology*.

1. Introduction

1.1 Significance of Partial Discharge in electrical systems

Electrical insulation is as important for electrical systems as electrical conductors because good insulation allows high voltage equipment to be made compact, reducing cost and saving space. In this role, insulating materials may be subjected to high levels of electrical stress for many decades of the equipment's operational life. Compact structures necessitate higher electric fields, which exert a greater physical force on any electrical charges present within the insulation. Acceleration of these charges by the electric field can lead to collisional avalanche phenomena in which parts of the insulation become conducting. Electrical breakdown (in which the insulation fails completely and provides a conducting path between conductors) can have severe consequences for the equipment itself, the power network as a whole, the environment and personnel. However, before the situation becomes this severe, many types of insulation defect exhibit partial discharge activity over long periods of time. Detection of partial discharges by various means provides a way of assessing the condition of electrical insulation and monitoring the health of high voltage equipment in service.

The term 'Partial Discharge' (PD) is defined as a localised electrical discharge that only partially bridges the insulation between conductors and which may or may not occur adjacent to a conductor. Techniques for measuring PD are defined by the International Standard IEC 60270 [1]. PD pulses occur as a consequence of local electrical stress concentrations that exceed the dielectric strength of the insulation. The pulses normally have a duration of much less than $1 \mu\text{s}$ [1]. Moreover, the emission of sound, light, heat and associated chemical reactions often accompanies the PD pulses. Electrical equipment can often operate normally even with the occurring of PD pulses, because the PD pulses do not link the conductors completely. In a short circuit condition, those conductors are completely linked which can cause severe damage to the whole insulation system. However, the insulation system of the equipment is gradually damaged when PD pulses occur and they contribute to

insulation degradation that may lead to ultimate breakdown [2]. Therefore, the goal of understanding PD phenomena has become an important research topic in electrical systems because PD can be an indication of the degradation of insulation system. In fact, even before high voltage (HV) technology was introduced for electrical power generation and transmission systems, a particular form of PD was recognised in the form of corona discharges [3].

In the eighteenth century, examples of PD phenomena which are now called Lichtenberg's figures were discovered [4]. Lichtenberg created the figures which result from surface discharges by using a huge electrophorus of about 2 metres and very fine rosin powder. However, his discoveries were not recognised as being created from electrical discharges propagating along the dielectric surface until 100 years later. Some examples of Lichtenberg's dust figures are shown in Figure 1.1. They have subsequently been used for discharge physics studies, such as creepage discharges measurements [4].

In the 1960s and early 1970s, a lot of research relative to PD pulses concentrated on PD physics, such as understanding phenomena of discharges in voids [5]. Since then, focus has shifted to studies of internal discharges, their effects and to insulation aging [6, 7, 8], including numerical modelling of PD [5]. However, in the last twenty years, the level of research has increased in certain areas, especially relating to automatic analysis and classification procedures for PD, such as the work done by Gulski [9], Krivda [10] and Cavallini [11]. These automated procedures can be implemented successfully because of the development of computer technologies, transducer technologies, signal processing algorithms and artificial intelligent techniques.

Since many electrical apparatus such as power transformers are approaching or have already exceeded their design life [12], PD could be the indication of an early stage of insulation degradation. The combination of PD condition monitoring and diagnosis techniques to detect, measure, locate and evaluate the level of insulation degradation [2], has been investigated and implemented, mainly via automated

systems [13, 14, 15]. The systems prevent the failures of electrical equipment and maintain them in good operation. Automated systems have become powerful tools for condition monitoring and they require high levels of sensitivity, reliability and intelligence as well as low cost [15].

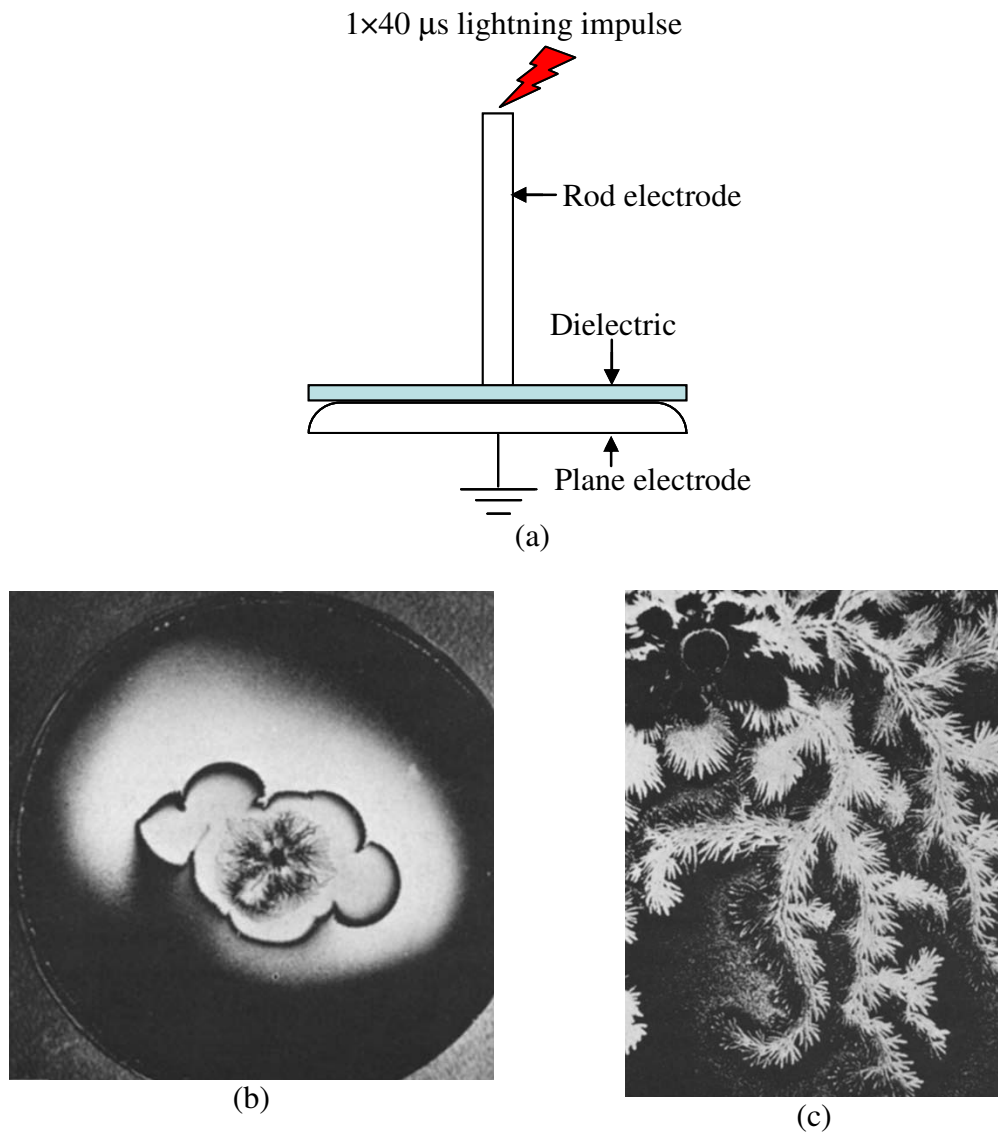


Figure 1.1 Dust figures in a mixture of 1% SF₆ and 99% N₂ at atmospheric pressure, applied voltage: 1x40 μs lightning impulse [4]: (a) Electrode arrangement, (b) -25 kV applied, (c) +20 kV applied.

Power transformers are among the most critical components in power system networks. Their health and safe operation is so important because unexpected faults and plant shutdown may have severe consequences [15]. The health and safety of people and environment are also important considerations. Most of the insulation in transformers is potentially flammable and sometimes toxic, which could cause very intense fire and air pollution. In terms of the revenue of power companies, high penalty may be incurred because of lost power generation and supply. In the context of ever-increasing competitive markets for power companies and high cost for repair and maintenance of the equipment, the application of condition monitoring has become one of the most important tasks. This could make the systems more reliable, avoid sudden breakdown, reduce downtime and maintenance cost, and extend the lifetime of equipment.

PD can be a sign of insulation degradation which is adopted in condition monitoring of power transformers and other electrical apparatus. Therefore, it is necessary to understand PD phenomena, which will be discussed in the following section.

1.2 Partial discharges

1.2.1 Partial discharge mechanisms

Insulating materials commonly used for electrical systems can be categorised into three different phases, i.e. gas, solid and liquid. The best way of presenting an overview of these mechanisms is to begin with gases, where the phenomena involved are better understood than in solids and liquids. The basic electrical breakdown mechanism in a gas will be introduced for the uniform field situation [16].

1.2.1.1 Breakdowns in gases

Under normal temperature and pressure as well as low electric field, air is a good insulator but it still has the conducting current density in the region of 10^{-16} to 10^{-17} A/cm² [16]. To cause breakdown or ionization in gas, three main factors are required. The first factor is the availability of free electrons. The second factor is sufficient mean free path λ of free electrons between collisions with molecules (e.g. λ is 6.79×10^{-8} m in oxygen at 15°C and 1 atm (100 kPa)). The last factor is that kinetic energies of these electrons must exceed the threshold required to cause ionization of gas molecules.

The first breakdown mechanism, Townsend breakdown, will be discussed as follows. The relationship between current and voltage discovered by Townsend (in the so-called ‘pre-spark region’) is illustrated schematically in Figure 1.2. The quantities on x -axis and y -axis on this figure are the applied voltage between two parallel plate electrodes and the variation of gas current measured between them, respectively.

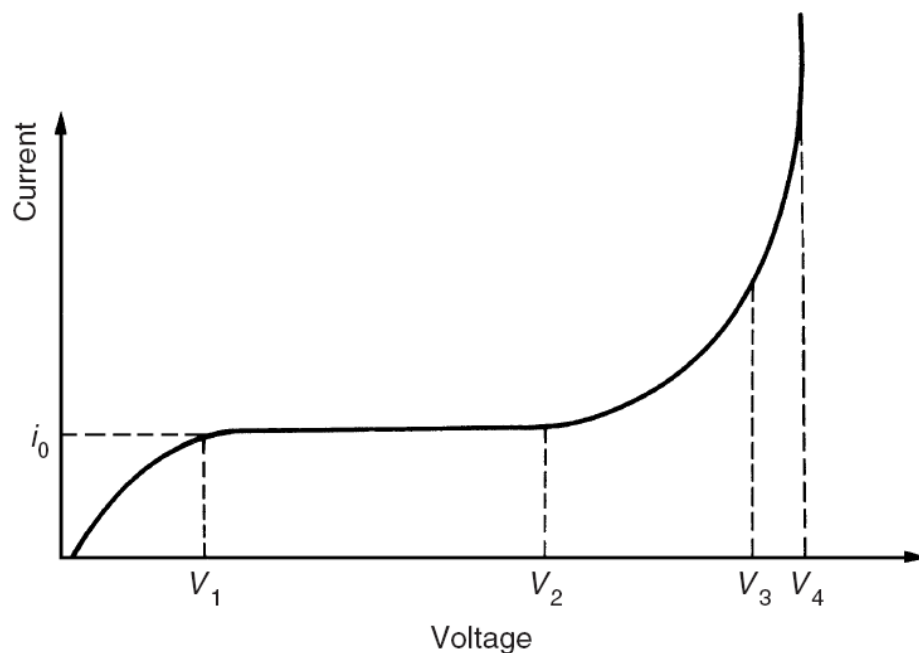


Figure 1.2 Current– voltage relationship of gaseous insulation in the pre-spark region [16].

Figure 1.2 shows that the current at first increases with the applied voltage until it becomes constant at i_0 with applied voltage V_1 . This constant current i_0 corresponds to the background current (saturation current). It remains constant with increasing applied voltage to V_2 . The current beyond V_2 then increases at an exponential rate. With increasing applied voltages V_3 and V_4 the current increases more rapidly than that in the range between V_2 and V_3 .

Townsend's first ionization coefficient (α), defined as the number of electrons produced by an electron per unit length of path in the direction of the field, was introduced to represent this current increase in the range of V_2 to V_3 in Figure 1.2 as $I = I_0 e^{\alpha d}$ where I_0 is the current leaving the cathode and d is the distance between two parallel plate electrodes. The term $e^{\alpha d}$ is called the electron avalanche. It corresponds to the number of electrons produced by one electron in travelling from cathode to anode (electron multiplication within the avalanche) for the first time. However, with further increases of the applied voltage at V_3 to V_4 in Figure 1.2, current increases at a more rapid rate than that defined by α . Thus, the Townsend second ionization coefficient (γ) was introduced to explain this phenomenon. The more rapid current increase is produced by photon impact and photoionization in the gas itself (self-sustained discharge). The transition from the so-called 'dark current' to the very large current (the current above V_4 in Figure 1.2, or the onset of spark), which is called Townsend breakdown criterion, is satisfied when the product of $\bar{\alpha} d$ reaches a value of 8 – 10. $\bar{\alpha}$ is the effective ionization coefficient calculated from $\alpha - \eta$, where α is Townsend's first ionization coefficient and η is the electron attachment coefficient for the particular gaseous insulation.

Another breakdown mechanism of gas discharges is a streamer breakdown. Space charge developed in an avalanche can transform the avalanche into channels of ionization known as streamers that lead to rapid developing of breakdown when the charge within the avalanche head reaches a critical value. This critical value is reached when the product $\bar{\alpha} x_c$ reaches about 18 – 20, where x_c is the length of the avalanche path in field direction when it reaches the critical size and is still less than or equal to d . This is illustrated in Figure 1.3, where E_r is the space charge field

strength directed radially at the head of avalanche and E is the externally applied field strength.

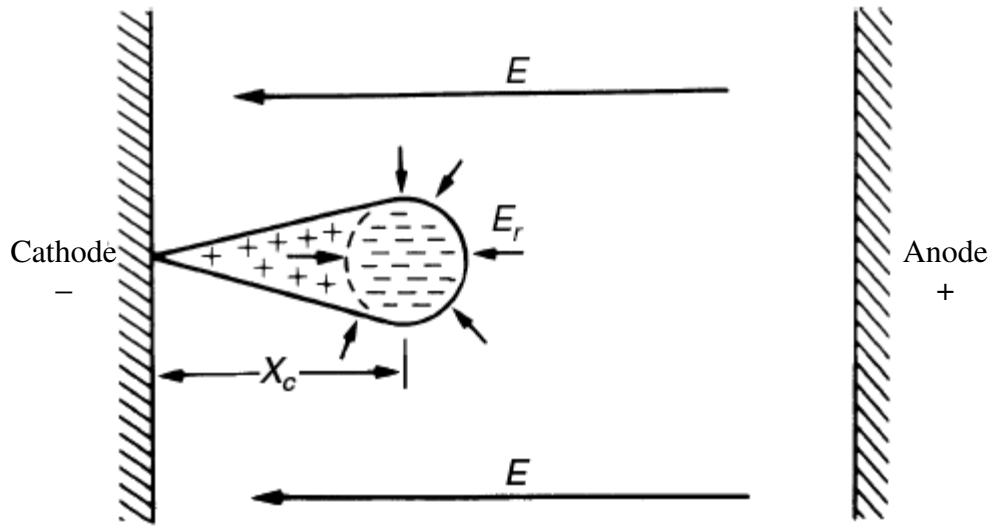


Figure 1.3 Space charge field (E_r) around avalanche head [16].

From Figure 1.3, within the head of the avalanche (assumed to be a spherical volume), the space charge is concentrated with negative charges at its head because of the higher electron mobility. The resultant field magnitude in front of the avalanche is approximately $(E + E_r)$ whereas that of the positive ion region just behind the negative ion is decreased to a value of $(E - E_r)$. The transition from avalanche to streamer can take place when E_r approaches the externally applied field E .

To investigate the transition from an avalanche to a streamer, cloud chamber photographs have been used [16]. Typical images showing development of electron avalanche to streamer are illustrated in Figure 1.4. In Figure 1.4(a) the discharge has been arrested before reaching the critical size. It has then grown beyond this critical size and a cathode directed streamer starts, which is shown in Figure 1.4(b). When the avalanche reaches the critical size, the combined space charge and externally applied field lead to intense ionization and the gas molecules in front of the avalanche head are excited. This phenomenon continues until a plasma channel, which is caused by rapid recombination between positive ions and electrons, forms a

conduction channel between the anode and the cathode (complete breakdown). This development is illustrated in Figure 1.4(c), (d) to (e).

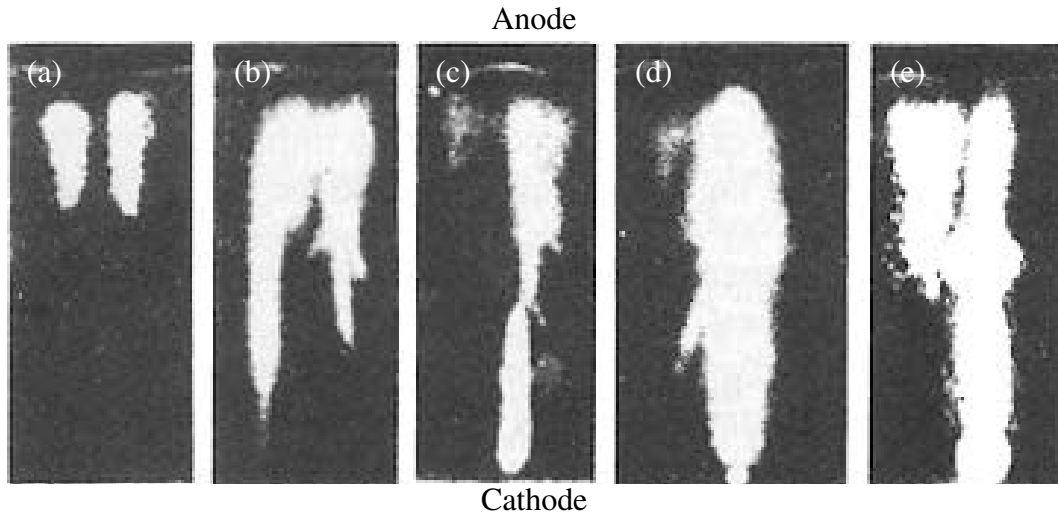


Figure 1.4 Cloud chamber photographs showing the transformation from avalanche at an anode to completely connect a cathode by a plasma channel [16]: (a) avalanche near anode, (b) and (c) cathode directed streamer starts, (d) and (e) time period for plasma channel to connect cathode and anode.

There is an avalanche mechanism at lower voltages and a spark discharge at higher voltages. For breakdowns in gases, there are two different mechanisms, i.e. Townsend breakdown and streamer breakdown mechanisms. The Townsend mechanism involves an electron leaving the cathode to an anode at a distance d such that an electron avalanche $e^{\alpha d}$ occurs with an increased applied voltage. To cause spark or breakdown, the condition of $\bar{\alpha} d$ reaching a value of 8 – 10 must be satisfied. The streamer breakdown mechanism involves an electron avalanche reaching the critical value (the product $\bar{\alpha} x_c$ reaching about 18 – 20) for the local field to be distorted sufficiently to cause self-sustaining streamers, where the negative and positive charges in the avalanche recombine rapidly.

The most commonly used insulating gas is sulphur-hexafluoride (SF_6) because it is relatively inert, has good arc-quenching properties and its electrical breakdown strength is very high. It is a highly electronegative gas, which means that it readily attaches electrons to form negative ions [17], thereby removing these electrons as potential initiators of avalanches. SF_6 possesses this property because fluorine belongs to the seventh group of the periodic table and the outer shell of the molecule consists of the inherently electronegative fluorine atoms. SF_6 is widely used in pressurised high voltage systems as insulation. Discharges in SF_6 based on the streamer mechanism are most applicable according to the studies reported in [17].

1.2.1.2 Breakdowns in solid and liquid

Solid insulation is used not only for its electrical insulation properties, but also for providing mechanical support for conducting components. Under normal operations, solid insulating materials have a wide range of dielectric strength properties, depending on environmental conditions and test methods, so a measured breakdown voltage is influenced by temperature, types of applied voltage excitation (DC, AC or impulse), test duration, and many other factors [18]. As a result, a single theory does not sufficiently explain a process of breakdown in solid insulating materials. In general terms, the process of breakdown in solids develops over time [16] as shown in Figure 1.5.

At the beginning of the curve showing in Figure 1.5, there are three mechanisms. The first one is intrinsic breakdown, which is initiated in times of the order of 10^{-8} s and considered to be electronic in nature. It requires an electrical stress in excess of 10^6 V/cm, which can enable a valence electron to cross the forbidden energy gap to the conducting band using energy from the externally applied voltage source. The second one is an avalanche breakdown similar to breakdown in gases. Under strictly uniform fields with the electrodes embedded in the specimen, the avalanche breakdown may be accomplished in solids. Avalanche breakdown in a solid insulator can be caused by an electron entering its conduction band under the influence of the externally applied voltage. The electron gains kinetic energy from the electric field

and loses it during molecular collisions in which additional electrons may be produced. This process is repeated and may lead to an electron avalanche, which is finally transformed to a streamer breakdown. The last one in this region is an electromechanical breakdown, which normally takes place in solid dielectrics which have low Young's modulus value of elasticity (Y). When voltage is applied, compression forces arise from the electrostatic attraction between surface charges. A solid insulator is broken down if this electrostatic force exceeds its mechanical strength. The highest apparent strength E_a before breakdown can be calculated approximately using $E_a = 0.6 \left[\frac{Y}{\epsilon_0 \epsilon_r} \right]^{1/2}$ [16], where ϵ_0 , and ϵ_r are the permittivity of free space and the relative permittivity of the dielectric. Note that this equation ignores plastic flow and that the value of Y itself may be dependent on both time and stress [16].

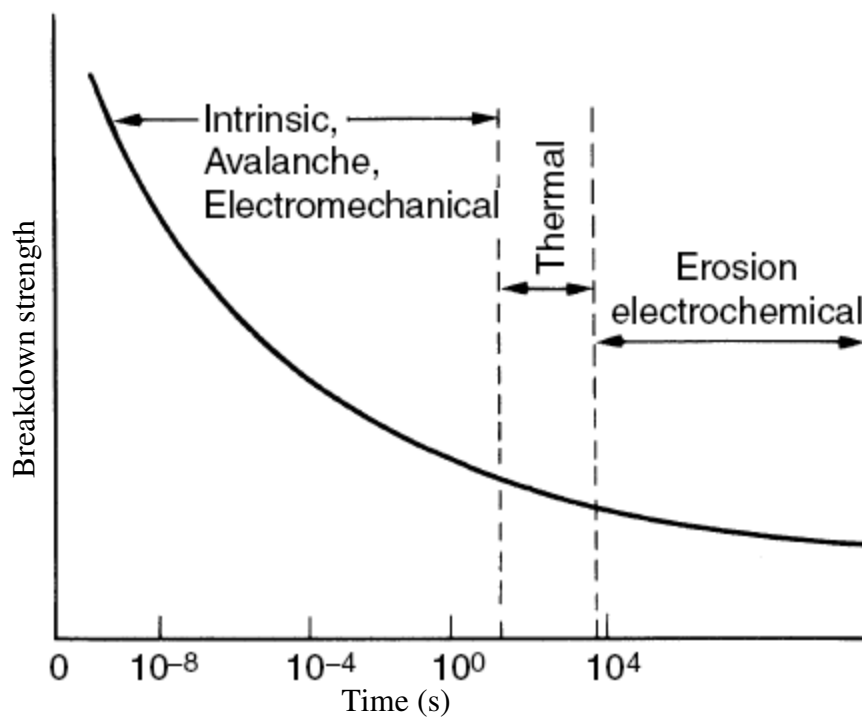


Figure 1.5 Mechanism of failure and variation of breakdown strength in solids with time of stressing [16].

Towards the upper end of the curve in Figure 1.5, thermal breakdown may take place when heat is continuously generated within solid dielectric when insulation is stressed because of conduction currents and dielectric losses. Conductivity generally tends to increase with temperature and when the rate of heating exceeds that of cooling, thermal failure and breakdown of solid dielectrics will occur. Moreover, all breakdowns in solid insulating materials are finally thermal since these solid materials melt and sometimes vaporise whether or not the original breakdown cause of discharge was thermal [19].

The final part of the curve in Figure 1.5 relates to erosion breakdown, which may occur in cavities or voids within the solid insulation or at boundaries between the solid and the electrodes. These voids usually contain gas or liquid of lower breakdown strength than the solid and the permittivities of these filling media are usually lower than that of the solid insulation. As a result, the electric field within the cavity will be accentuated and is likely to exceed the breakdown value and initiate breakdown in the void. During breakdown in the cavity, its surfaces act instantaneously as cathode and anode. Bombardment of the cathode by positive ions may damage the insulation by increasing the surface temperature, producing local thermal instability, as well as chemical degradation. When discharges occur on the surface, the erosion destroys the interface region and gradually penetrates the solid insulation. This type of deterioration mechanism reduces the breakdown strength of the solid insulation over time.

In terms of breakdown in liquids, the general state of research is less advanced than even that of solids [16]. This is because findings and conclusions obtained from many researchers cannot be reconciled and lack of comprehensive theory concerning the physical basis of the liquid phase.

Breakdowns in liquids can be divided into two approaches [16]. The first attempts to consider the breakdown of liquids based on the avalanche ionization of atoms caused by electron collision (an extension of gaseous breakdown) within homogeneous liquids of extreme purity. However, this type of liquid is not used for commercial

insulation purposed in the field. A second approach is to investigate the breakdown of liquids containing foreign particles (e.g. water suspended, solid particles, and gaseous bubbles of lower breakdown than liquid). These impurities can accumulate and form a bridge (partially or fully) across the gap that can lead to breakdown. However, field conditions (e.g. AC and impulse excitation, presence of insulating solids covering electrodes, or creating a 'barrier' for discharge propagation, industrial liquids contaminated by foreign particles) all play a major role. For example, the study in [20] investigated the mean breakdown fields (kV/mm) of the mineral oil containing a needle tip embedded at the HV side of the two parallel plates. This was tested under impulse excitation. This study shows that mean breakdown fields drop with increasing lengths of metallic particles and at the same length of a needle the larger tip radius provides higher mean breakdown fields. In addition, experiments using a rod-plane electrode arrangement under AC excitation showed that the number of streamers per minute occurring in the mineral oil increased steeply with the addition of cellulose particles obtained from destructed pressboards.

1.2.2 Internal discharges

Internal discharges can occur in low dielectric strength materials of solid insulation, for examples gas filled cavities, inclusions within insulating material and oil-filled cavities [2]. Some examples of internal discharges are illustrated in Figure 1.6. These can include cavities in extruded plastics, cast resins, lapped resin-impregnated paper, etc. Since internal discharges are not visible, it is necessary to detect them as early as possible to avoid permanent failures of the insulating materials.

Gas filled cavities are prone to internal PD due to the electrical stress in the cavity and the critical breakdown strength of that cavity [2]. However, it is not simply the case that a discharge will occur whenever the electrical stress of the cavity exceeds the critical breakdown strength. It is also dependent on the number of the initiating free electrons that must be sufficiently far from the cavity wall. These free electrons

must be capable of acquiring sufficient energy to cause an ionisation avalanche for initiating the discharge inside the void [21].

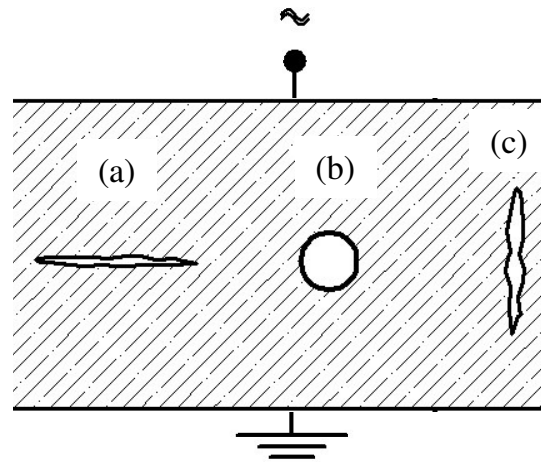


Figure 1.6 Internal discharges [2]: (a) Flat cavity that is perpendicular to the electric field, (b) Spherical cavity, (c) Long and parallel to the electric field cavity.

Gas filled cavities in solid or liquid dielectrics can be present due to many causes. For instance, in the case of epoxy resin casting, cavities can be caused by air leaking into the mold during the curing. This may be due to insufficient pressure on the liquid resin [21]. Therefore, process control errors during manufacturing are important to avoid gas filled cavities in any type of solid, liquid-impregnated solid or liquid-impregnated dielectrics.

For internal discharges caused by inclusions which contain dirt, fibres and other foreign particles, the dielectric strength is reduced by these inclusions. When the breakdown of the inclusion develops, a gas filled void is formed, followed by gas discharge in that void [2]. In terms of oil-filled equipment, gas bubbles might occur between layers of oil-impregnated papers, such as in transformer windings and power cables [2].

The electrical stress within a cavity can be estimated dependent on the shape of the cavities [2]. For example, the electrical stress within the flat cavity shown in Figure 1.6(a) can be calculated using Eqn. 1.1, which is defined as follows:

$$E_c = \epsilon E_d \quad (1.1)$$

where E_c is the electrical stress in the cavity
 ϵ is the dielectric constant of the insulating material
 E_d is the electrical stress in the surrounding dielectric

For a spherical cavity shown in Figure 1.6(b), the electrical stress can be calculated using Eqn. 1.2, tending to 1.5 times the stress in the surrounding dielectric if ϵ is much larger than 1.

$$E_c = \left(\frac{3\epsilon}{1+2\epsilon} \right) E_d \quad (1.2)$$

For the cavity which is long and parallel to the electric field, as in Figure 1.6(c), the electrical stress can be computed using Eqn. 1.3, which is defined as follows:

$$E_c = E_d \quad (1.3)$$

The actual breakdown strength of the cavity also depends on the type of gas and the gas pressure in the cavity [2]. For example, Paschen's curve in Figure 1.7 shows the breakdown voltage of air as a function of pressure \times electrode spacing. A significant line at 1 atm shows the 3 kV/mm critical breakdown voltage of air.

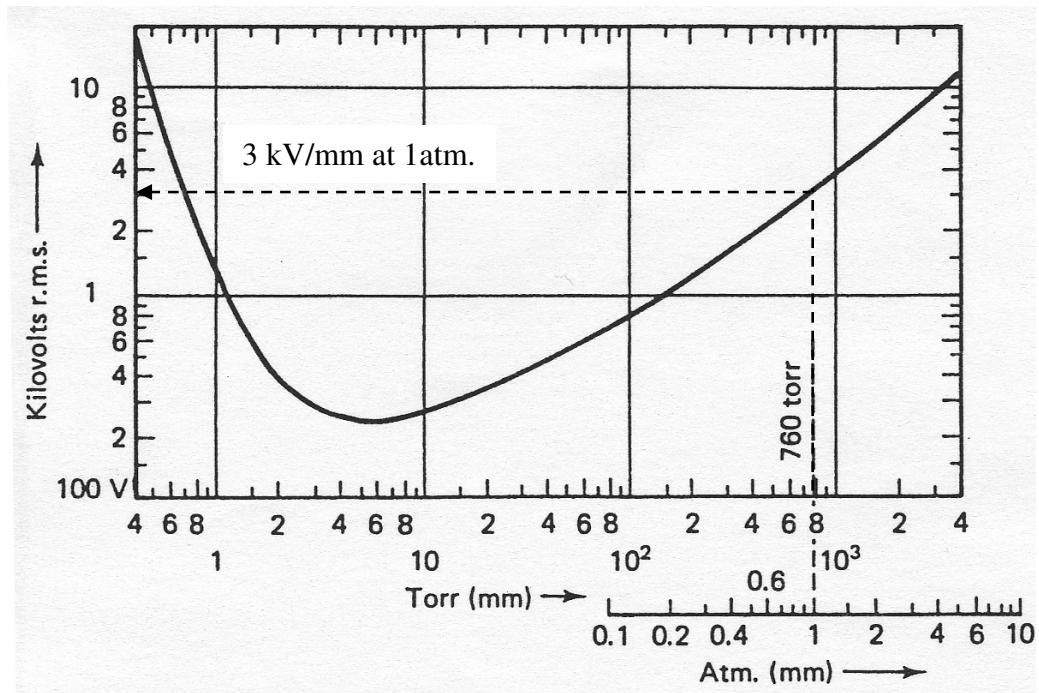


Figure 1.7 Paschen's curve shows the breakdown voltage of air as a function of pressure \times electrode spacing [2]. The dotted line indicates breakdown voltage at 1 atm.

In terms of charge accumulated in a cavity, it is possible to quantify the level of PD magnitude in picocoulomb (pC) in some cases, such as charge accumulated in the gas-filled spherical cavity [22] that can be computed using Eqn. 1.4.

$$Q = 1.64 \times 10^{-8} a^{5/2} \epsilon p^{1/2} \nabla \lambda \quad (1.4)$$

where

- Q is charge accumulated in the cavity (pC)
- a is the cavity radius (m)
- ϵ is the dielectric constant of the insulating material
- p is the pressure inside the cavity (Pa)
- $\nabla \lambda$ is the function, which gives the ratio of the electric field at the position of the void, in absence of the void, to the voltage between the electrodes or conductors

Moreover, charges can be trapped on the insulating surfaces of materials and this can affect breakdown depending on whether the local electric field they produce enhances or diminishes the external electric field.

1.2.3 Surface discharge

Surface discharges may take place if the electrical stress is parallel to the dielectric surface [2], as shown in Figure 1.8. They may occur in bushings and cable spacers, for example. Surface discharges have been investigated since the beginning of 20th century, driven by increasing practical problems arising within engineering applications [23]. For example, the developing length of a corona streamer on the surface of insulators is a function of the applied voltage. Another example is that a new technique to record the surface discharge patterns on a complicated insulation surface was discovered.

In a few specific cases, PD inception voltage at the edge of the configuration shown in Figure 1.8 when the inhomogeneity of the electric field is neglected for simplicity can be calculated using Eqn. 1.5 [2].

$$V_i = d_{airgap} E_i + d_{dielectric} \frac{E_i}{\epsilon} \quad (1.5)$$

where V_i is the inception voltage
 $d_{airgap}, d_{dielectric}$ are the distances of an airgap and dielectric, respectively
 E_i is breakdown stress of an airgap
 ϵ is dielectric constant of solid dielectric

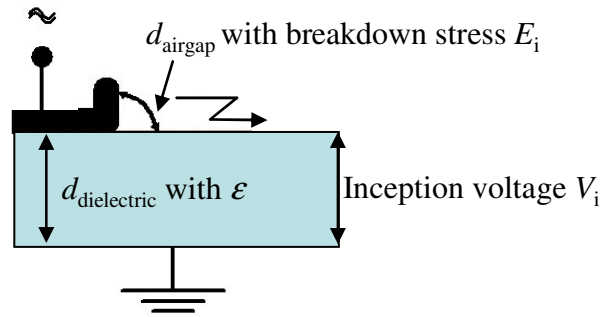


Figure 1.8 A plane-plane configuration to show surface discharge and to indicate breakdown of an airgap in series with a solid dielectric.

In terms of the surface discharge in oil, a similar formula might be applied but the breakdown voltage of an oil-gap cannot be calculated accurately as in air. Moreover, oil which is used in engineering applications often contains contamination, such as moisture, solid particulates and multifarious gases. The effects of these impurities would not be taken into account for calculating the breakdown using this manner. The impurities can influence the characteristics of the surface discharges significantly [24].

1.2.3 Corona discharges

Corona discharge takes its name from its appearance like a ‘crown’ at the mast. The term ‘corona’ is a Latin word for crown. Corona discharges can occur in gases at sharp points in an electric field [2], as shown in Figure 1.9. Corona discharges usually take place at the HV side; however, they may occur at the sharp edges of the ground plane or even mid-gap. Corona discharges produce light, audible noise, ozone, heat, and other effects which can be detected [2]. Corona discharges are readily detected by acoustic or optical sensors.

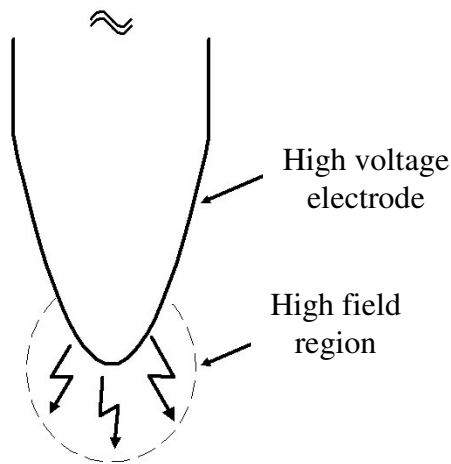


Figure 1.9 Corona discharges at the sharp edge [2].

1.2.4 Treeing

Treeing phenomena [25] can be categorised into two groups, electrical and water treeing.

Electrical treeing in a solid dielectric is a phenomenon which starts from defects in the insulation and results in the growth of a dendritic pattern (treeing) caused by PD activities in the tree channel [2, 26]. No water or any other polar liquid is involved in electrical treeing [25]. Electrical treeing in solid insulation, especially polymeric type (e.g. XLPE), can originate from many kinds of defect within the insulation, for example, sharp edges from a semiconducting layer protruding into the dielectric, voids, contaminations, etc, [26]. Electrical treeing can exhibit various tree-like structures [27], such as the branch and bush types shown in Figure 1.10. After electrical treeing has developed for some time, its branches will be hollow [2]. Discharges that take place in the hollow spaces are known as internal partial discharges. These discharges are highly unstable and can sometimes grow rapidly which could cause breakdown in a very short period, within seconds or minutes. Additionally, electrical treeing is hard to detect at an early stage. Therefore, PD activities associated with electrical treeing can be one of the main reasons of long-term insulation degradation with the high ultimate breakdown possibility.

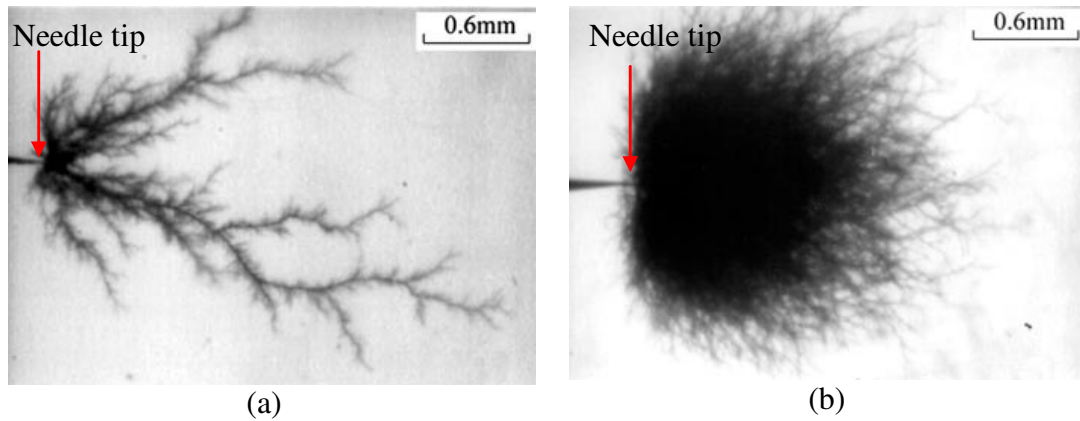


Figure 1.10 Electrical trees [27]: (a) Branch-type tree, (b) Bush-type tree.

In terms of water treeing, water or any other polar liquid must be involved in the process. The electrical stress to generate water treeing is usually much lower than that of electrical treeing [25]. In addition, water treeing could transform to electrical treeing. Both electrical and water treeing are always studied separately but they have a lot in common [25], such as having a basic mechanism of solid insulation degradation that involves cleaving of molecular bonds.

1.3 Partial discharge detection

This section outlines common detection techniques used for PD signals, covering electrical detection, chemical detection, acoustic detection and electromagnetic wave detection. Electrical detection will be explained according to the IEC 60270 standard. This standard is accepted world-wide. Chemical detection will focus on dissolved gas analysis, which is widely used for power transformers. Several common methods of dissolved gas analysis will be outlined. Acoustic detection will be discussed in terms of advantages for locating PD. Those three techniques have some practical deficiencies; therefore, electromagnetic wave detection has been developed and applied in major HV apparatus, such as gas insulated substations (GIS) and power transformers. Electromagnetic wave detection will be explained in the context of successful applications both in GIS and power transformers. Recent work on correlation between IEC 60270 and UHF detection will also be presented.

A PD source is effectively a current pulse and the most vital characteristic of a PD pulse is the time of the pulse, which normally has a duration of nanosecond scale. This time duration and the pulse shape vary statistically because they depend on many factors, such as pressure of gas, type of defect, magnitude of applied voltage, etc. However, these PD current pulses cannot normally be directly measured since they are inaccessible. Therefore, what is obtained from PD measurements and detection is a quantity (e.g. voltage signals) dependent on PD current pulses measured at the terminals of the test object. When a UHF sensor is used to detect radiated electric fields its output does not correspond to directly measured quantities of PD current pulses.

In addition, PD pulses are often accompanied by emission of sound, light, heat and products of chemical reactions. These emissions can also be an indicator of the presence of PD activity. For example, using acoustic sensors in conjunction with amplifiers may be useful for detecting PD. Another example is visual observations of light emitted from PD pulses when tests are carried out in a darkened room.

The more common PD detection techniques will now be outlined:

1.3.1 Electrical detection

The standardised electrical detection of PD pulses according to IEC 60270 [1, 3] will be explained in this section. This international standard is applicable to PD measurements taking place in electrical apparatus that operate under AC excitation at frequencies of up to 400 Hz. This standard:

- ❑ defines terms used, and the quantities to be measured;
- ❑ describes test and measuring circuits which may be used;
- ❑ describes analogue and digital measurement methods;
- ❑ specifies methods for calibration including requirements of calibration instruments;
- ❑ provides test procedures;

- gives some guidelines for discriminating PD from external interference.

The important quantity to be measured is the apparent charge q usually expressed in picocoulombs (pC). Since origins of PD pulses are usually inaccessible, this apparent charge q is not equal to the actual amount of charge locally involved at the site of the discharge. However, if a unipolar charge of this quantity was rapidly injected between the terminals of the test object in a specific test circuit, it would give the same reading on the measurement system as the PD pulse itself. Measurement of the apparent charge is widely accepted and there are other quantities to be measured as well, such as pulse repetition rate, phase angle of the pulses, average discharge current, and so on. There are many commercially available IEC60270 instruments and this standard is internationally accepted with many years of field experience gained in its applications.

One of the standard circuits to measure PD defined in IEC 60270 is illustrated in Figure 1.11, where the coupling device is connected in series with a test object. In Figure 1.11, the test object can be anything from a simple dielectric specimen to large HV equipment. The AC voltage supply (U_{\sim}) should possess sufficiently low level background noise and the filter Z is inserted to further reject high interference or disturbances coming from the HV side or PD from the supply. The coupling capacitor C_k should be a low inductance design and it must have sufficiently low PD levels up to the highest test voltage. The measurement circuit consists of a coupling device (CD) that presents a measuring impedance (Z_{mi}) which converts the input PD current pulses into equivalent voltage PD pulses that are fed to the measuring instrument via a coupling cable. A proper calibration procedure is required in order to correctly measure the PD magnitude because this measured PD magnitude is dependent on both the test object and the test circuit. This can be performed by injecting a short duration pulse of known charge magnitude generated from a calibrator into the terminals of the test object.

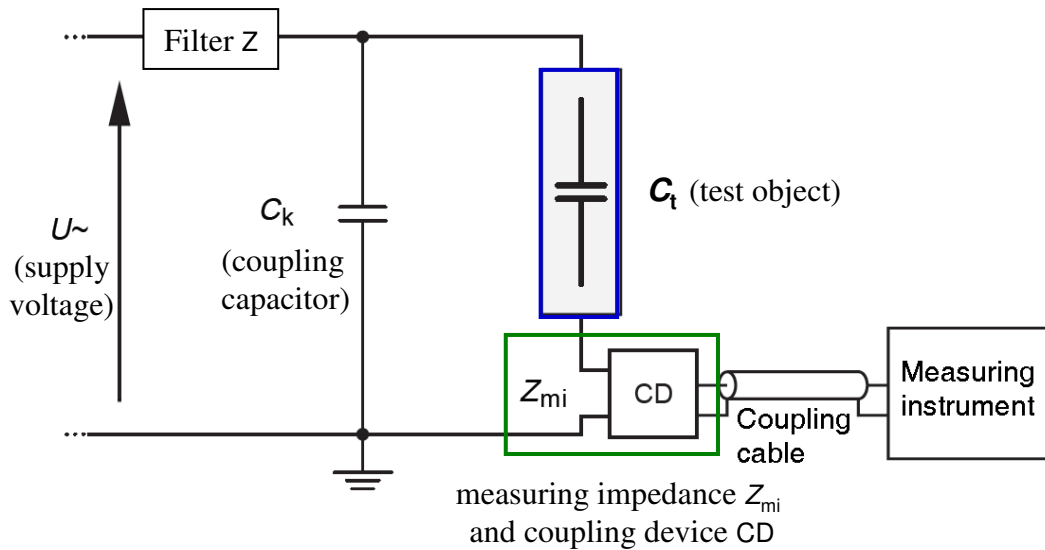


Figure 1.11 Basic PD test circuit when coupling device CD in series with the test object C_t .

External interferences or disturbances mentioned in IEC 60270 can be categorised into two groups. The first group is disturbances which occur if the test circuit is not energized (e.g. switching operations in other circuits, HV tests in the vicinity, radio transmissions, etc). The second group is disturbances which only occur when the test circuit is energised, but not within the test object. This group can vary from PD in HV conductors to improperly earthed components and it usually increases in magnitude with increasing voltage. However, methods to reduce disturbances are suggested, for example, screening and filtering properly, using balanced circuits, and so on.

Although the IEC 60270 PD measurement is widely used, it has several limitations. For example, true shapes of PD pulses are not recorded, and it is not possible to locate PD positions. The IEC 60270 PD measurement is not applicable in some applications, such as GIS because of the size of external coupling capacitance required.

1.3.2 Chemical detection

PD pulses usually involve ionisation of insulating materials, so that one consequence is chemical reactions, which produce breakdown products (e.g. hydrocarbons in oil) mixing in the insulators of HV apparatus. These mixtures may decrease the dielectric strength of insulation of those apparatus. A technique called *dissolved gas analysis* (DGA) has long been developed and widely applied in oil-filled HV equipment, such as power transformers. Periodic DGA can be used for routine monitoring of power transformers in-service (e.g. annual basis) and can provide information related to transformer problems [12]. Additionally, DGA may be used for monitoring of factory acceptance tests. To apply DGA, small samples of insulating oil must be taken.

In power transformers, when PD pulses take place in insulating oils, typical oil decomposition gases are produced. These include hydrogen gases (H_2), hydrocarbons, carbon oxides and non-fault gases, which are listed in Table 1.1. Based on types of faults, production rates and concentration of those different gases, it is possible to distinguish between different types of incipient faults, as the example in Figure 1.12 indicates [28]. From this figure, if hydrogen gases are appearing, this means electrical faults (either PD or arcing) may be occurring in a system being monitored. However, it is more effective to rely on all diagnosis gases to indicate one type of developing fault, or combination of PD, arcing and thermal developing faults.

Table 1.1 Lists of typical oil composition gases.

Typical oil decomposition gases	Lists
Hydrocarbons	Methane (CH_4) Ethane (C_2H_6) Ethylene (C_2H_4) Acetylene (C_2H_2)
Carbon oxides	Carbon monoxide (CO) Carbon dioxide (CO_2)
Non-fault gases	Nitrogen (N_2) Oxygen (O_2)

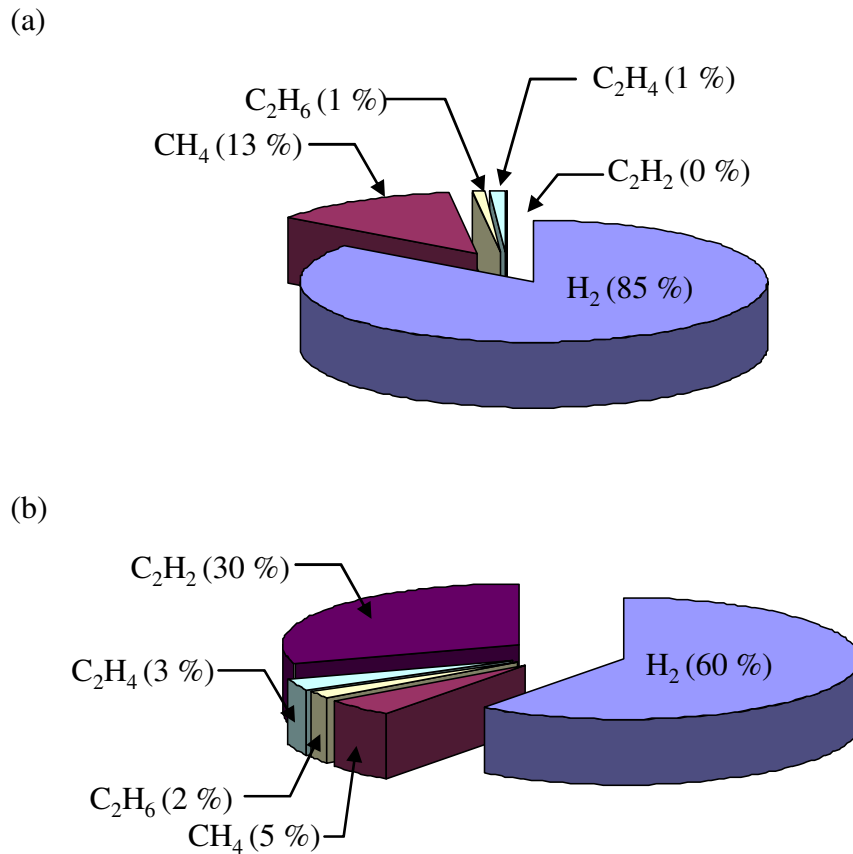


Figure 1.12 Key gases obtained from two types of developing faults in oil insulated power transformers used for DGA [28]: (a) PD, (b) Electrical arcing.

Three DGA methods are commonly used including IEEE C57.104, IEC 60599 and Duval's triangle.

IEEE C57.104 [28] relies on five gas ratios of combustible gases (R1, R2, R3, R4 and R5) to indicate possible fault types, where these five gas ratios are summarised in Table 1.2. In IEEE C57.104, two different methods, Doernenburg and Rogers', are also reported. Doernenburg uses R1, R2, R3 and R4 while Rogers' uses R1, R2 and R5.

Table 1.2 Five gas ratios.

Gas ratios	Calculated from
Ratio 1 (R1)	CH ₄ /H ₂
Ratio 2 (R2)	C ₂ H ₂ /C ₂ H ₄
Ratio 3 (R3)	C ₂ H ₂ /CH ₄
Ratio 4 (R4)	C ₂ H ₆ /C ₂ H ₂
Ratio 5 (R5)	C ₂ H ₄ /C ₂ H ₆

IEC 60599 [29] categorises faults usually found in electrical equipment by visual inspection of the equipment after the fault has occurred in service into five groups as follows:

- PD = partial discharges of corona type and sparking type inducing small carbonized punctures in paper;
- D1 = low energy discharge, evidenced by larger punctures in paper, tracking, or carbon particles in oil;
- D2 = high energy discharge, evidenced by extensive carbonization, metal fusion, possible tripping of equipment;
- T1 = thermal faults of temperature < 300°C if paper has turned brown and T2 = thermal faults of temperature > 300°C if paper has carbonized;
- T3 = thermal faults of temperature > 700°C, evidenced by fusion, metal coloration, oil carbonization.

R1, R2 and R5 are used in IEC 60599 with two additional gas ratios (i.e. the ratio of C₂H₂/H₂ and of O₂/N₂).

Duval's triangle method shown in Figure 1.13 is the graphical interpretation derived from DGA [30]. The triangle coordinates corresponding to DGA results in parts per million (ppm) can be computed as follows:

$$\%C_2H_2 = \frac{100x}{x + y + z} \quad (1.6)$$

$$\%C_2H_4 = \frac{100y}{x + y + z} \quad (1.7)$$

Chemical detection is a relatively simple technique for on-line monitoring. It can indicate the presence of fault conditions (e.g. PD, thermal deterioration and arcing) but chemical detection alone is not sufficient for complete condition monitoring. For instance, DGA relies on levels of gases dissolved in such a large volume of oil so that it is not possible to locate the PD. However, during the last ten years the research relative to DGA has shifted to an area of utilising artificial intelligent techniques to enhance the interpretation of DGA results, such as work reported in [32].

1.3.3 Acoustic detection

PD acts as a point source of acoustic waves, which are excited from a small explosion (expansion of materials) during PD activity [33]. This mechanical energy wave propagates from the discharge site throughout the structure and its waveshape is dependent on the source, the detection apparatus and the sensor. The acoustic wave can be detected using a variety of transducers, such as the handheld ultrasonic device shown in Figure 1.14. Normally, acoustic sound sources are wideband (> 1 MHz), but due to characteristics of insulation and apparatus structures, acoustic emission is usually measured in the 20 kHz to 500 kHz frequency range [34]. The acoustic detection technique is also immune to electromagnetic interferences under field conditions [35].

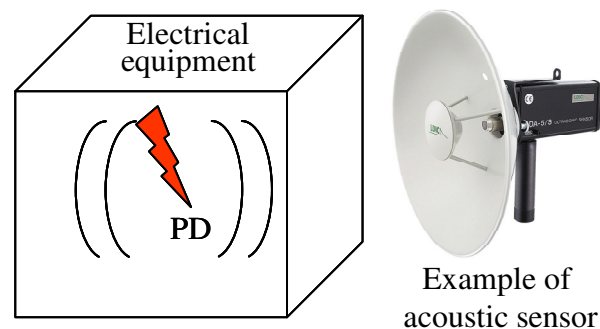


Figure 1.14 Acoustic PD detection.

Electrical and chemical detection can indicate the presence of PD activities but provide only limited information to locate PD sources. Therefore, the main reason to use acoustic detection is to complement PD diagnosis by locating PD sites, especially in GIS and power transformers. To locate a PD, the simplest technique is based on the fact that the level of acoustic signal will be relatively large when an acoustic sensor is close to the PD source [35]. This technique requires only a single movable sensor as in Figure 1.14 but it is time consuming. The other location technique is to use time of flight (time of arrival) measurement by comparing the delay between acoustic signals recorded simultaneously combined with a triangulation method. Using this approach, two or more acoustic sensors are required. Reports of location techniques based on acoustic detection for power transformers and GIS are presented in [34, 35, 36, 37] and [38], respectively. However, the location technique is not as straightforward as might be expected because different media in electrical apparatus provide different acoustic dispersion characteristics and factors, such as proximity of sensors to PD sources, also influence acoustic waves. These require a complicated mathematical model of electrical apparatus being tested and may require a pre-processing algorithm to obtain better acoustic signals (e.g. wavelet de-noising) as demonstrated by an example presented in [37]. Moreover, the main limitation of acoustic detection is that no calibrated charge measurement can be made.

1.3.4 Electromagnetic wave detection

The IEC 60270 method (electrical detection) is not suitable for on-line monitoring as a result of excessive interference from adjacent apparatus, such as corona discharges in air coming from overhead lines, communication interferences, etc. [39]. Moreover, in some HV applications, such as GIS, the IEC 60270 method is not appropriate [40]. For example, the IEC 60270 needs an external coupling capacitor, which is inapplicable to GIS in service. Therefore, a new on-line detection technique applicable to GIS was developed based on a concept of detecting radiated electromagnetic waves produced by PD pulses in a GIS chamber [41]. As a PD current pulse in GIS has a very short rise time (sub-nanosecond) caused by a rapid acceleration of charge, electromagnetic waves with energy spectra extending to

hundreds of MHz can be obtained [39]. Thus, detecting radiated electromagnetic waves in the ultra high frequency range (UHF, defined as 300 MHz – 3 GHz) in GIS can be used if suitable sensors are fitted.

The problem of external interference levels (e.g. corona discharges in air) can be solved because corona discharges do not create energy spectra at the UHF range and inserting additional filters to reject corona discharges (e.g. 500 MHz high-pass filter) is also helpful [39]. Furthermore, the metal cladding of the busbars in GIS also provides good screening to external interference [42]. In addition, UHF output signals potentially offer high signal-to-noise ratio (SNR) because electromagnetic waves radiating from the PD site contain multiple reflections of the same pulse corresponding to the resonant modes of a GIS chamber. However, it can be difficult to interpret these signals because they combine many effects between PD site and UHF sensor. In terms of UHF sensors, it is possible to install them in a number of ways, as shown in Figure 1.15.

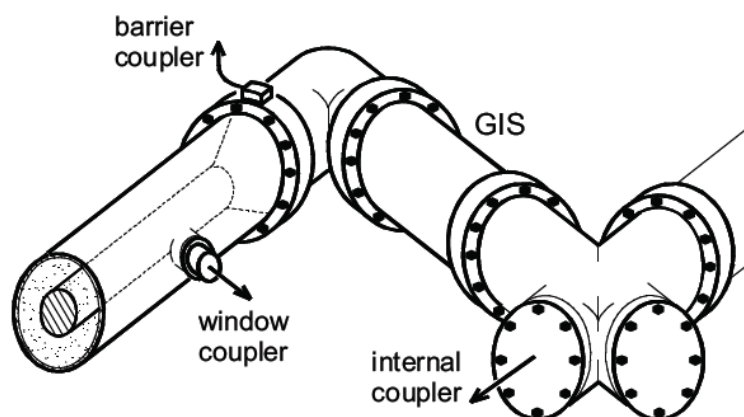


Figure 1.15 Various mounting positions for UHF PD sensors on GIS [42].

UHF detection was pioneered in GIS by Hampton [43]. It has been widely adopted as an effective tool at many GIS for on-line PD monitoring and diagnosis according to examples presented in [41, 44]. After gaining many years of experience of UHF PD monitoring in GIS, UHF detection has been applied in power transformers, as reported in [45, 46]. As with GIS, external interferences can be screened because the

transformer enclosure is steel. In terms of noise entering through bushings, they can be distinguished by means of their lower frequency contents. Many designs of UHF sensor for detecting PD in power transformers have been developed. Three examples are shown in Figure 1.16. Recently, much research on applying UHF detection techniques to monitoring PD in power transformers has focused on aspects, such as designs of UHF sensors [47] and computer simulations of UHF signals in power transformers [48]. However, the most important benefit obtained from the UHF technique is the ability to locate PD sources [42].

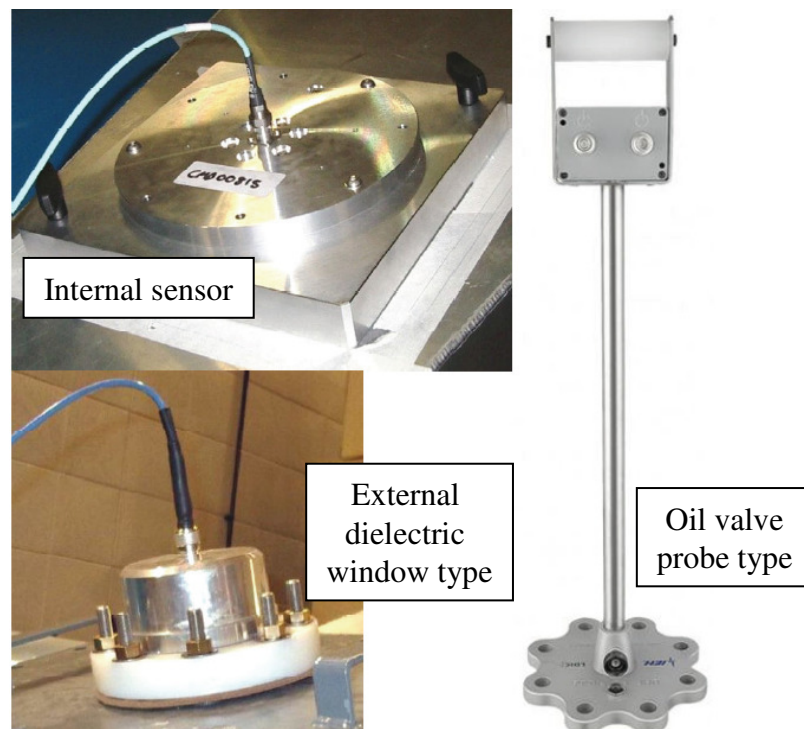


Figure 1.16 Three UHF sensors for power transformers [42].

To locate PD sources in power transformers, at least three UHF sensors must be installed on a transformer tank. Building on the concept of time of flight measurements in conjunction with an advanced mathematical model of a power transformer that includes essential variables (e.g. sensor positions, transformer geometric structure, electromagnetic properties of insulation materials in transformer, etc.), a PD source can be located [49]. To simplify the calculations, it is advantageous to use identical measurement cables from all sensors to an

oscilloscope. As a result, only differential time delays inside the tank are considered. Comprehensive details of locating PD in power transformers and their continuous developments can be found in [49, 50, 51].

To inform the level of PD, the IEC 60270 method quantifies it by means of apparent charge in pC. A similar capability would also be desirable for UHF detection. Since UHF signals contain complex features produced by PD source itself, propagation paths including environmental effects, it will be more convenient to convert those complex features into one parameter. The cumulative energy metric proposed in [49] is suitably representative because the whole UHF signal is taken into account. Recent research has concentrated on seeking correlations between PD measurement according to IEC 60270 and the UHF range. The research presented in [52], for example, developed a combined system between the two methods with the ability to relate the UHF signal (mV) to the apparent charge (pC) in certain circumstances. The work reported in [53] came to similar conclusions.

Among four PD detection techniques (electrical, chemical, acoustic and UHF), to obtain both the severity and location of defects, the combination of outputs among them must be employed. Using electrical detection provides the amount of apparent charge q in pC to evaluate the severity of the defect while using chemical detection indicates types of defect (discharges, thermal faults, etc.). For location of defect purposes, using acoustic or UHF detection is applicable. These two detection techniques can be performed on-line, which are beneficial to insulation monitoring.

1.4 Partial discharge monitoring as a diagnostic test for insulation

1.4.1 Introduction

Partial discharges can cause physical degradation of electrical insulation. They can also be indicators of other forms of aging in HV equipment, such as thermal, mechanical and environmental effects. Therefore, PD measurements have long been under development to monitor the presence of PD in electrical equipment. Their applications can be categorised into three stages, which are design test, quality assurance and diagnostic test [54]. By passing the three assessments, it is expected that the insulation of electrical equipment being investigated has the required life time of reliable operation.

The design test will evaluate a new design of electrical apparatus to ensure that PD is within some specified low levels that are acceptable under normal operation. For example, power transformers must not exhibit PD levels above specific limits set out in the specification. Transformer test procedures are outlined in [55], and a typical requirement would be that PD levels should not exceed 200 pC during a 1 minute overpotential test at 1.6 times the normal operating voltage. However, power transformers are complex structures (both electrical and mechanical) and are basically hand crafted involving a high capital investment. They are also subject to a certain amount of variation, such as skills of manufacturers, natural properties of materials (e.g. wood, paper, etc.). As a result, their final qualities can be variable. Therefore, quality assurance tests have been established to ensure consistent manufacture. The international standard ISO 9000 series provides a frame work for quality assurance testing [56]. For example, BS EN ISO 9001 provides more than 20 essential elements of a quality system covering design, manufacture, installation, and servicing. For diagnostic testing or condition assessment (which is the focus of this section), the aim is to determine whether the electrical insulation has deteriorated due

to electrical, thermal, mechanical or environmental stresses that can be recognised by means of PD activity.

For in-service power transformers, it is reported in [57] by surveying several Dutch utilities that defects which are detectable using PD detection are most commonly found in bushings (50%), followed by tap changers (25%) and elsewhere (25%). Additionally, it is reported in [58] by a South African Utility that during an 11-year period (1996 – 2006) there was approximately 80% of failures found in bushings, tap changers and windings. In terms of PD magnitude, [57] reports that the PD level in bushings and windings were in a range of 5 pC to 100 pC. In addition, the PD level in the tank was often much greater than 100 pC. The PD in the tank refers to discharges caused by improper field grading, broken connections, or damaged contacts in tap changers. Moreover, in any air insulated substation corona discharges always take place, which can produce electromagnetical coupling to power transformers. These external corona discharges can also detect at a power transformer with the magnitude of about 100 – 400 pC. Thus, corona discharges can be a big problem during on-site measurement.

In GIS, a study of on-site tests [59] reviewing a 30-year period (1960s – 1990s) of Electricite de France experience showed that typical defects as a function of their locations were mainly found in switching compartments. Additionally, typical defects as a function of their types were mostly connections and fastenings, as well as contamination by metallic particles and foreign bodies. In terms of PD magnitude, it is reported in [59] that the typical order of PD magnitude is variable dependent on types of defects. For example, the typical range of PD magnitude caused by poor contacts between loose metal parts is between 50 pC and 100 pC. The typical range caused by free particles on enclosures is between 5 pC and 10 pC. These two examples were detected based on the applied voltage of a 420 kV GIS.

1.4.2 Diagnosis techniques

PD diagnostic tests have proliferated in their practical application to determine the condition of the insulation of HV apparatus during the past 20 years. This is because of the advancement of sensing equipment, electronic instrumentation, computer technologies and signal processing [54]. Some well-known researchers who have developed PD diagnostic tests are Gulski, Hampton, Montanari and Okamoto. The main impact of these developments is the reliability improvement of HV equipment based on the levels of insulation degradation which can be detected as early as possible. Then, the equipment can be repaired or replaced before catastrophic in-service breakdown occurs. Note that the PD diagnostic test is just to warn of the possible aging level, not to provide the estimated remaining life of the equipment.

There was large investment in generating capacity in the 1960s and 1970s, so that the major components of the electricity networks (e.g. power transformers, power cables) have reached or passed the end of their design life [60]. As with many other types of equipment, the failure pattern of power transformers follows the well-known 'bathtub' curve. The first part of the curve (infant mortality) represents failures due to manufacturing faults, improper installation, etc. The second region represents a low level of failures during the main active part of the equipment life. The last part is failure due to old age. It is usually preferable to maintain the equipment in order to avoid unexpected breakdown, since repair is extremely costly. In one example [61], the replacement cost and collateral damage in the case of catastrophic failure of a 100 MVA power transformer was calculated as approximately \$5M. Under normal operation, an annual cost of risk without on-line monitoring for this transformer was \$38,325 while that of risk with on-line monitoring was reduced to \$16,590 [61]. Thus, the annual cost benefit for on-line monitoring was considered to be \$21,735. Note that this calculation was based on the principles outlined in CIGRE Technical Brochure 248 'Guide on Economics of Transformer Management' June, 2004 [61]. For larger capacity power transformers, such as a 1,000 MVA power transformer, the replacement cost alone may be approximately \$3M, with an associated delay time for manufacturer and installation of about 2 years. Therefore, it is commercially

advantageous to have diagnostic tests in order to reduce or eliminate unexpected downtime.

(i) PD location

The accuracy of PD location is very important because it is valuable for maintenance and repair purposes, especially for critical HV equipment, such as power transformers, GIS, cables and rotating machines. Acoustic and UHF detection techniques can be used for locating PD. By means of the acoustic technique, the PD sites can be located by placing two or more acoustic sensors on the external surface of the transformer enclosure. Then, the relative arrival times of the acoustic waves which have been generated by each sensor will be measured, and next applied the relative arrival times with a triangulation algorithm [35]. The PD location can be determined based on accumulated data sets, where the resultant locations tend to cluster around the centre on the PD sources. In a similar manner, the PD locations can be determined by using signal waveforms recorded using the UHF technique.

(ii) Continuous monitoring

In the past, PD measurements have been periodically applied to critical HV equipment (e.g. rotating machines, power transformers and switchgear) [54]. These are off-line tests, which can initiate certain problems, such as insufficient qualitative and quantitative data, lack of dynamic parameters that occur during in-service conditions, time consuming procedures and experts required to take and analyse data. Consequently, an on-line continuous monitoring of PD measurement has become a desirable tool for HV apparatus around which a condition-based maintenance can be implemented. By applying an on-line continuous monitoring with condition-based maintenance to the critical HV equipment, the reliability of power networks can be enhanced. Presently, the on-line continuous monitoring of PD [54] has been used in GIS, power transformers and rotating machines.

The benefits from on-line continuous monitoring are as followed:

- Defects are detected quickly in the earlier stages, which will give information on the growth rate and severity of the defects. Additionally, maintenance could be planned at the most convenient time for the operator.
- Capability of providing information on what type of PD exists in the electrical equipment, such as corona discharges, surface discharges and void discharges.
- Higher accuracy of PD data in conjunction with other dynamic parameters (e.g. load current, applied voltages and temperature) can be gathered simultaneously. The correlation among those variables can supply additional insight for diagnostic tests.
- HV equipment health is evaluated based on its history (trending).
- Provide the opportunity for diagnostics to be performed remotely.
- Reduction in related maintenance costs, such as labour, replacement, repair, penalty for lack of energy supply, etc.

The issue of data storage could be a major concern because PD data during the on-line continuous monitoring can accumulate rapidly as the monitoring may be required over long periods of time (months or years). For example, the file size of one event containing a PD signal obtained during an experiment carried out in this thesis is approximately 100 KB, so that in real applications there may be many thousands of events happening. Therefore, several approaches have been developed to solve this concern. Storing envelopes of signals, for example, can reduce the amount of data to be kept, so the reduction in data storage is achievable. The envelope approach will be presented later in Chapter 2.

(iii) Pattern recognition

PD pattern recognition is the ability to recognize and distinguish between different types of PD sources [62]. However, during the PD monitoring period, not only do the PD signals exist, but certain interference may occur as well. Therefore, pattern recognition techniques must have the ability to differentiate the PD signals from any interference. During the last 20 years, one of the most actively researched fields in

insulation diagnostics concentrates on developing new techniques to automate the pattern recognition process. Several techniques will be outlined as follows:

- Statistical analysis

This technique uses the probabilistic quantities, which are mean, standard deviation, skewness and kurtosis, to summarize the shape and location of the positive and negative PD pulse pattern with respect to the AC phase angle. Using this technique, it is presumed that each type of PD and interference has a unique set of statistical values.

- Neural network

A lot of research has been carried out using neural networks for PD pattern recognition [63, 64]. Neural networks need to ‘learn’ by processing PD data from measurement where the source of the PD is known [62]. After the learning period, unknown PD patterns can be fed into the neural network and then are recognised as the most likely cause, such as particular PD types or noise sources. Neural networks can prove to be effective in recognizing different patterns with a low probability of error, but the accuracy of neural networks can sometimes be influenced by the PD mechanism, such as stochastic behaviour, problems of multiple defects and different test voltage levels [63].

- Fuzzy logic

Pattern recognition using fuzzy logic is based on a complicated and variable process that uses vaguer, non-specific rules. As a result, fuzzy logic has been applied for recognising variable sizes of void discharges [65]. PD patterns from voids are variable dependent on many factors, such as void size, free electrons, etc. These factors lead to variation in magnitude, repetition rate and phase position. Examples of work carried out using fuzzy logic are reported in [65, 66, 67]. Nowadays,

combinations between statistical analysis and fuzzy logic have been applied, for example in [68].

□ Support vector machine

Support vector machine (SVM) is another technique that has been used for identification of PD sources [69]. The SVM is a method for finding functions, which can be either a classification or a regression, from a set of labelled training data. The principle of SVM is to map feature vectors (F_1, F_2) in input space into feature vectors in feature space (F_1, F_2, F_3) of higher dimension, in which groups are separated by clear boundary, as illustrated in Figure 1.17.

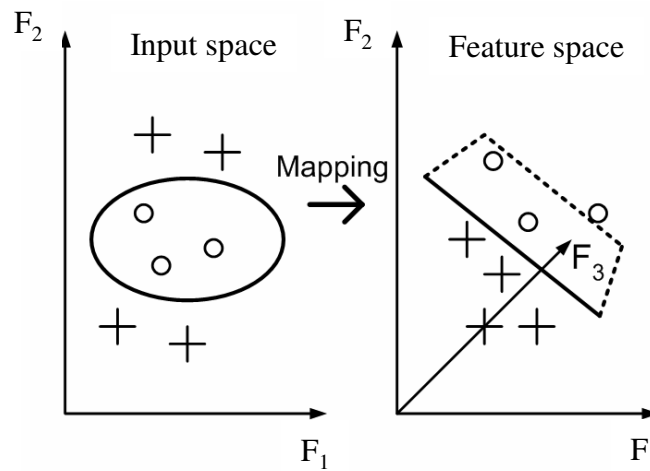


Figure 1.17 Mapping the training samples from input space to feature space [69].

The complete pattern recognition process using SVM consists of feature extraction, training, kernel optimisation and testing. In a real application [69], input feature vectors for SVM identification may contain phase angle (φ) and average apparent charge q (φ -average q) pattern, wavelet decomposition coefficients, and so on.

- Wavelet transformation

Most applications of wavelet transformation to PD are concerned with extracting a train of PD pulses from data that contains noise and other spurious interference signals [70]. After removing the noise, wavelet transformed data can be used as the input to other diagnostic techniques. Wavelet transformation involves varieties of mother wavelet functions that need to be selected appropriately for each specific application. Daubechies' wavelet, for example, is suitable for UHF PD signals [71]. Further investigations of using wavelet analysis will be discussed in Chapter 4.

1.5 Contributions of the present study

1.5.1 Introduction

Previous sections have briefly reviewed fundamental knowledge of PD that commenced with why PD is significant for power system networks, and moved on to cover four major types of PD (internal, surface, corona and treeing), four common detection techniques (electrical, chemical, acoustic and UHF) and diagnostic tests for PD monitoring (PD location, continuous monitoring and PD pattern recognition).

In this thesis only PD signals obtained from the UHF detection technique will be investigated and two main goals are outlined as follows:

- To develop practical and efficient procedures for sorting incoming signals from different sources by means of distinguishing between different signal characteristics.
- To improve both understanding and methodology for determining UHF signal arrival times for time of flight measurements in order to enhance PD location accuracy.

1.5.2 A practical algorithm to distinguish between different PD sources

Most techniques related PD signals deal with primary PD data sets which some/all of these data sets may be generated from different PD sources. It will be beneficial to have a method that can sort mixed data sets into particular groups associated with a single PD source. Each group can be then fed into subsequent PD interpretation techniques, which will perform better with ‘clean’ input data.

In this thesis, a new technique, namely the *envelope comparison method*, is developed. It can sort mixed PD signals by differentiating between PD sources based on comparing only UHF signal envelopes. It requires no complicated procedures, such as data training, iteration, weighting functions, etc. Using the envelope comparison method offers a means to determine the number of PD sources present in a system under test. It is demonstrated that the envelope comparison method will offer significant benefits, such as an efficient algorithm, cost effectiveness for practical measurement systems, the ability to be incorporated into automated system applications and enabling discrimination of multiple PD sources when only one sensor is available. Additionally, the envelope comparison method could be employed more widely in other types of transient-based monitoring systems.

1.5.3 Improvement of the methodology for identifying UHF signal arrival times

A key parameter for locating PD sources accurately is the measured arrival times of signals at different UHF sensors. Several methods have been proposed for identifying accurate arrival times. Some of them require the selection of parameters that can only be chosen by experts’ skill, so the resultant arrival times probably have certain degrees of subjectivity. Additionally, some of them may need sophisticated mathematical calculations. Therefore, it is advantageous to have a method for identifying arrival times that can determine them directly with the minimum of adjustments or selections of particular variables. Once more accurate arrival times are determined, the accuracy of PD source locations can be improved.

In this thesis, a new metric, called the *relative increase in energy*, is introduced. It considers the relative increase in energy between successive samples and its operating parameters can be pre-defined. It is demonstrated that the time of the highest value of relative increase in energy gives an upper boundary on the arrival time. It also possesses the ability to be incorporated into automated system applications.

Additionally, the research highlights possible concerns caused by using wavelet de-noising applied to UHF PD signals for determining arrival times. It is demonstrated that the de-noised signal may be altered in a way that changes apparent arrival times, which could degrade the accuracy of UHF PD location. Therefore, using wavelet de-noising to UHF signals needs to be applied with caution.

Moreover, based on a practical method previously applied in the field to determine arrival times (2% threshold crossing of UHF voltage squared), a new index, called the *arrival time consistency index*, is introduced for evaluating reliability of choices for particular threshold percentage. Using this index, it is demonstrated that a threshold value of 3% and 4% can provide reliable arrival times.

1.5.4 Potential reduction of UHF monitoring costs

Capturing the raw UHF signals requires a very high specification for the acquisition system in terms of bandwidth and sampling rate, as well as massive capacity of data storage devices. It would be advantageous if the capital expenses of measurement systems and data storage devices could be reduced while the quality of measured PD signals are still retained for analysis. Using UHF detector circuits constructed based on the new envelope comparison method it is shown that less costly measurement hardware can be used while the quality and quantity of those signals remain adequate for analysis.

2. Envelope comparison method

2.1 Introduction

This chapter presents a technique, called the *envelope comparison method*, which can be used for differentiating between different PD sources. These different PD sources can be caused by either different PD fault types or different locations based on their distinctive signal envelopes. In this study, only PD signals obtained using UHF detection were considered. However, this method could be implemented for other types of monitoring systems that detect unknown transient signals (e.g. acoustic signals), which will be discussed in Section 6.4. The envelope comparison method is concerned with representing original transient signals as their signal envelopes by applying a smoothing kernel. These envelopes still retain signal variation details that are sufficient for assessing the similarity (or difference) by comparisons between pairs of signal envelopes in order to discriminate between different PD sources. The envelope comparison method has been evaluated by means of experimental tests and by assessing its application to two practical HV tests for PD monitoring: a switched HVDC reactor and a 252 MVA power transformer.

2.2 Concept and practical advantages

Detecting and interpreting transient signals can play a valuable role in condition monitoring systems when the transients are indicative of undesirable effects in the structure or equipment being monitored. An example might be the acoustic signals caused by cracking or structural materials. While the research in this thesis deals specifically with the detection of PD in HV equipment using UHF sensors, the principles described are more generally applicable. Essentially, the aim is to develop a practical, economical means of sorting incoming signals types, using knowledge that the envelope ‘signature’ can be a function of the relative positions of the signal source and sensor, and/or the properties of the transient source itself.

After gaining some experience of measuring UHF PD signals from power transformers (especially when observing signals from several sensors simultaneously), it soon becomes evident that there are commonly occurring sets of signals patterns that must correspond to different PD sources (or other sources of transient electromagnetic signals). One of the most obvious features of these signals is that their individual envelopes tend to exhibit unique shapes that are characteristic of different points of origins. UHF PD signals exhibit these characteristic ‘signatures’ because they are strongly influenced by the propagation path between each PD source and each sensor installed at the periphery of the equipment. Also, signals received from a particular PD pulse by UHF sensors at various positions are different because of the predominant influence on the signal transfer function of the different paths of electromagnetic wave propagation inside the transformer. For other PD detection techniques, such as acoustic, it may also be possible to see different transient signal shapes obtained from different PD sources, such as in the acoustic emission signals illustrated in [72].

This is best illustrated by means of examples taken from a period of continuous UHF monitoring of an HVDC reactor test, as reported in [73]. The test arrangement included four monopole-type UHF sensors spaced around the reactor housing to enable PD location. The frequency response of the UHF sensors used in this test is shown in Figure 2.1. Their average sensitivity values in the frequency range 500 – 1500 MHz was 20 mV/Vm^{-1} . The four monopole sensors were installed at diverse positions inside the reactor housing as illustrated in Figure 2.2.

UHF signals were captured over 100 ns using an oscilloscope with a sampling rate of 5×10^9 samples/sec and an analogue bandwidth of 5×10^9 Hz. Typical UHF waveforms produced by two different PD sources are illustrated in Figure 2.3. Each of those sensors ‘sees’ the PD pulse from a different ‘viewpoint’. In other words, if there is only one UHF sensor, but two or more PD sources in different locations, it may be possible to tell them apart automatically on the basis of the envelope, because an experienced operator can differentiate them by observing the different characteristic traces on an oscilloscope.

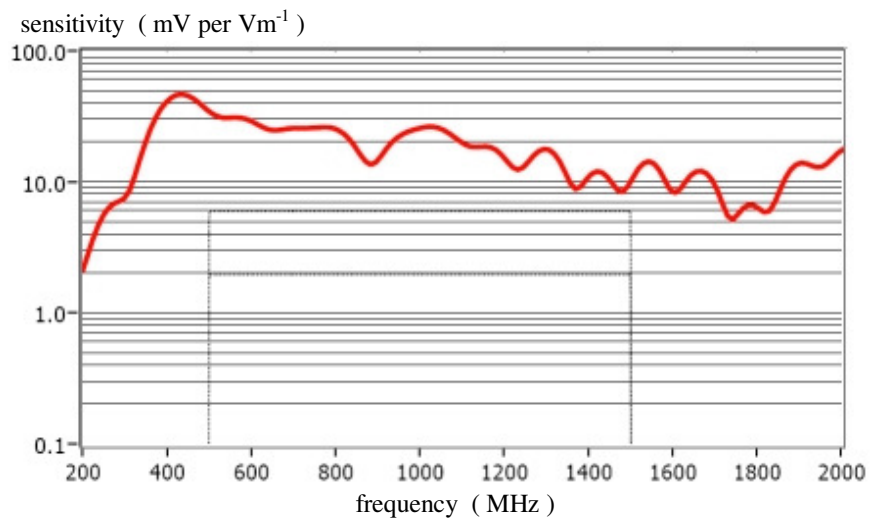


Figure 2.1 Frequency response of the monopole UHF sensor used in the HVDC reactor tests. The region indicated between 500 MHz and 1500 MHz is normally used to specify UHF PD sensors for GIS. [73].

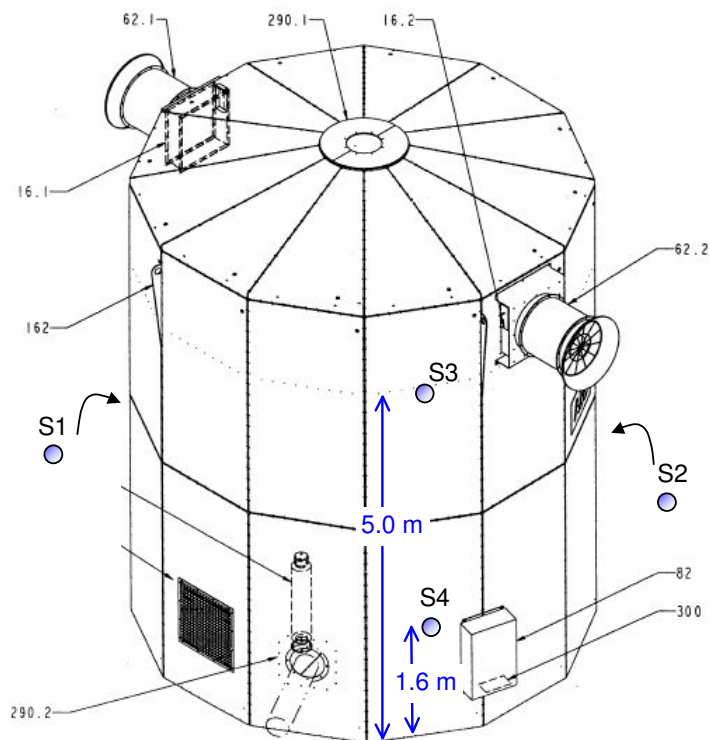


Figure 2.2 Sensor positions (S1 –S4) inside the reactor housing [73].

Figure 2.3(a) shows a set of signals generated from a PD source which will be called ‘type A’ and Figure 2.3(b) shows a set which will be called ‘type B’. In a 48-hour monitoring period, 1,466 sets of type A and 3,190 sets of type B were logged. The data sets could readily be sorted ‘by eye’ into two different groups even without reference to the differences in arrival time because the modulation envelope associated with the signal received at each sensor is an unmistakable feature.

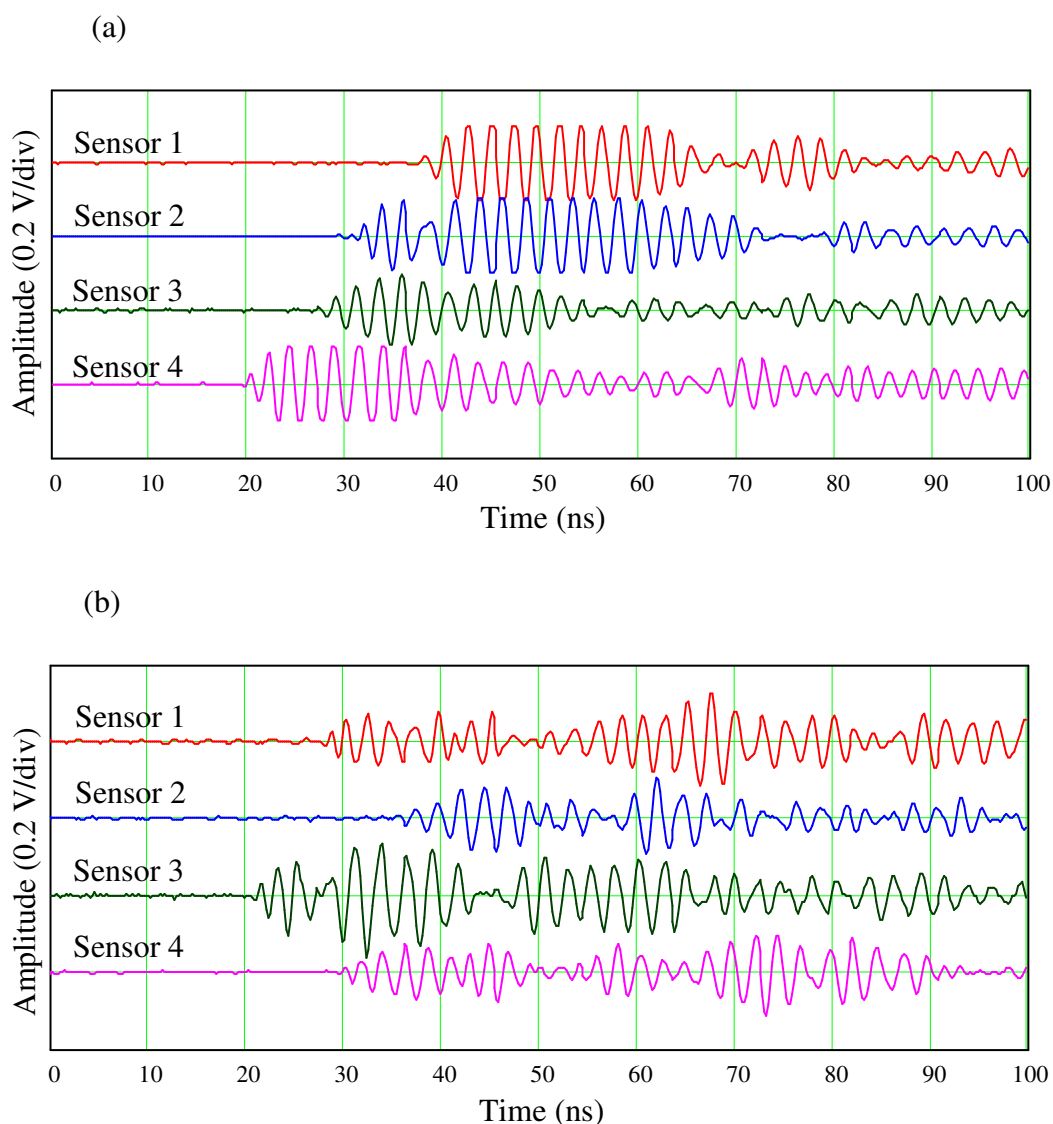


Figure 2.3 Typical UHF signals generated from two different PD sources, which were captured by four UHF sensors simultaneously: (a) Signals of type A, (b) Signals of type B. This is to show that two groups of UHF signals can be distinguished ‘by eye’.

From this evidence, it is shown that UHF signals contain characteristic signatures strongly influenced by propagation paths between each PD source and each sensor attached on the periphery of the plant item. Envelopes of those signals are therefore governed by the same paths. They also contain information about energy variation with time. Since the signal envelopes are representative of the measured waveform detail and they may be used to distinguish between different PD sources effectively. This is the basis of the envelope comparison method that is proposed and evaluated in this study.

The main process of the envelope comparison method is a smoothing algorithm that produces the envelopes of signals. The purpose of the smoothing algorithm of the envelope comparison method is to strike the best compromise between the conflicting aims of reducing bandwidth and yet still retaining a good ability to differentiate between different PD sources.

If it proves effective, using the envelope comparison method can provide the benefits listed below:

- (i) Offer essential knowledge that could predict the number of PD sources that are present in the system being monitored even when only one UHF sensor is available.

In many cases it is likely that UHF monitoring of power transformer for PD would be conducted using a single sensor (at least for routine monitoring) inserted through a spare oil valve [74]. With this arrangement, there are no time differences to measure, but the signal envelope can still be a distinguishing feature. Sorting on the basis of UHF envelopes would allow trending of the temporal progression of multiple PD sources, even with a single sensor, since individual data streams could be kept separately.

Speech recognition is a useful analogy for the envelope comparison method being proposed. Consider a measurement system with a single UHF sensor that is connected to some electrical plant and switched on for the first time. The system has no prior knowledge of what signals it will receive. The envelope of the first signal then becomes a frame of reference for the second signal. The system must then decide whether the second signal is the same ‘word’ that was spoken by the *source* in the first case. Note that the *source* mentioned here can either be PD sources or any interference sources that possess envelope characteristics. If so, it is counted it as a second instance of that *source*. However, if it is sufficiently different, it is considered to be a new ‘word’ (that is, a second *source*) and the third signal would then have to be compared with two known ‘words’ to see which it matched best, and so on. This process is illustrated in Figure 2.4.

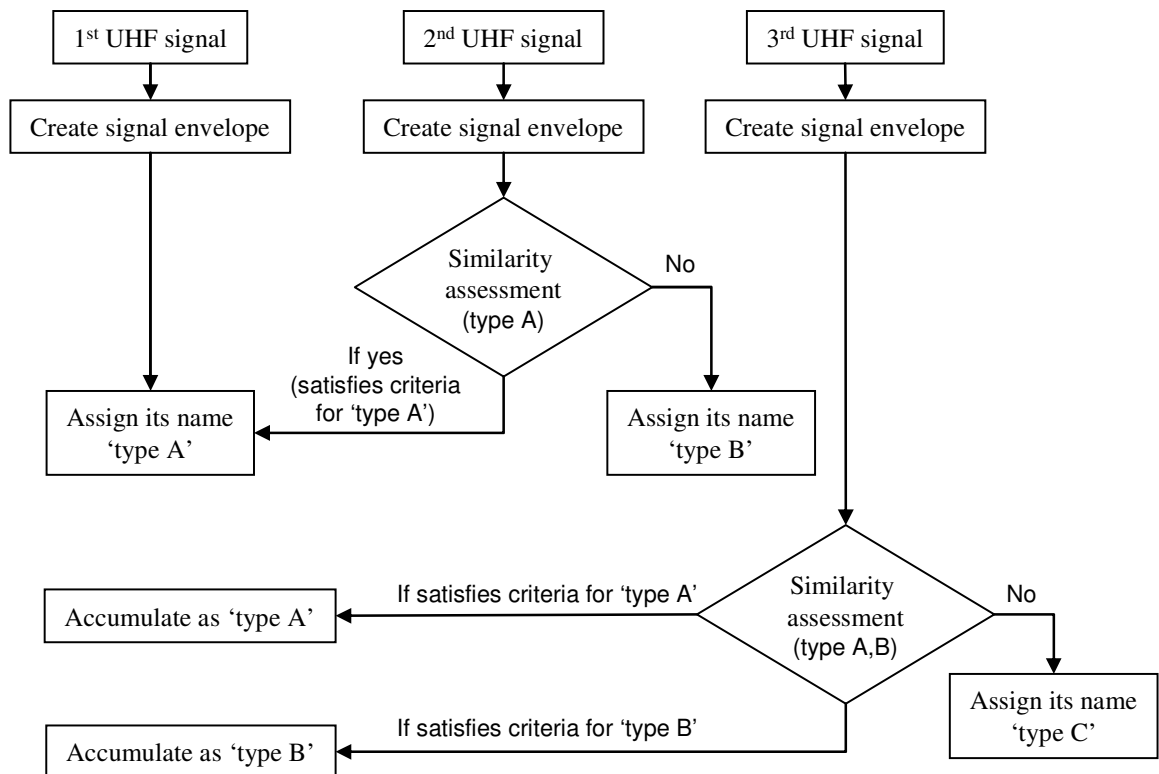


Figure 2.4 Diagram to illustrate the principle of the envelope comparison method.

After a sufficient period of system operation, the number of active *sources* present in the system can be determined. Individual groups of signals can be then fed into subsequent interpretation techniques, which can enhance the accuracy of PD interpretation techniques by means of using separate groups of signals not mixed data stream. In this research, only PD signals were considered.

(ii) The envelope comparison method could be implemented by means of automated systems.

According to the diagram illustrated in Figure 2.4, the envelope comparison method can potentially be implemented using an automated system, which is more desirable approach than the need for repetitive human intervention. Furthermore, mathematical calculations involved in this technique (will be presented in the next section) are relatively simple compared with other automated techniques, such as artificial neural network [64], fuzzy logic [65] and SVM [69]. Calculations and test conditions can also be established following the system behaviours being monitored in a similar manner to other automated systems for differentiating PD sources. In addition, the envelope comparison method could be developed using machine learning technique by combining reinforcement learning [75] and case-based reasoning [76]. The former provides a method of learning without expert intervention and the latter provides a means of representing many events on the basis of relatively few exemplar cases. An introduction to how machine learning can be implemented using the envelope comparison method is given in [77].

(iii) Reduce in bandwidth and sampling rate required.

Acquiring UHF signals with a sufficiently high sampling rate to support the resolution of arrival times on a nanosecond timescale is still a relatively costly process, which means that the technique is more commonly applied to high value assets at transmission voltage levels. A more economical solution is required for distribution level equipment. One way of reaching this goal is to reduce the detection bandwidth and sampling rate required. Hence, if the UHF signals are first ‘detected’

in the analogue sense (using a radio frequency (RF) rectifier diode) to produce a pulse that follows the envelope, this should possess a much smaller bandwidth, allowing it to be captured with sufficient fidelity using a greatly reduced sampling rate. This can essentially be regarded as amplitude modulation (AM) demodulation, but with a 'carrier' frequency that is poorly defined. Since the envelope of the signals varies more slowly with time, it follows that the bandwidth (and hence sampling rate) needed to make the comparison between signals could be significantly reduced. Thus, reduction in bandwidth and sampling rate can be achieved by capturing UHF envelopes rather than sampled UHF signals.

(iv) Improve reliability and reduce in capital expenses of UHF monitoring.

A further concern with UHF PD monitoring is the quantity of signal data that can potentially be generated [13]. Envelope comparison reduces storage requirements because only the signal envelopes would be stored. With the envelope comparison method, a monitoring system could operate for much longer without data overload. In terms of envelope creation, it can be implemented in the field efficiently. The hardware system for envelope creation combined with a low sampling rate device and small size of data storage can all be implemented by means of readily available items, such as RF amplifier, RF detector diode, associated components and a modest sampling rate data acquisition card. The algorithm for comparing pairs of envelopes can be implemented by computer processing. As a result, the envelope comparison method presented here could improve reliability and reduce the capital investment required.

(iv) Perform same method in other transient-based monitoring systems.

The envelope comparison method could also be employed in other types of transient-based monitoring systems because this technique depends on signal envelopes only, while the signals can be any kinds of transients originating from voltage, acoustic emission, vibration signal, pressure, etc.

2.3 Procedures for envelope comparison

The proposed envelope comparison method consists of the following steps:

Step 1) Removal of DC offset

The first step is to remove any DC offset present in the sampled data so that all signals share a common baseline. This is achieved by calculating the mean value of all the data points in a particular PD record (Eqn. 2.1) and subtracting this value from each individual sample within the data (Eqn. 2.2). The transformation is shown in Figure 2.5 to Figure 2.6.

$$V_{mean} = \frac{1}{N} \sum_{i=0}^{N-1} V_i \quad (2.1)$$

$$V_j = V_j - V_{mean} \quad (2.2)$$

where V_i, V_j are the i -th, j -th voltage samples respectively.

N is the total number of sample points and j ranges from 0 to $N-1$.

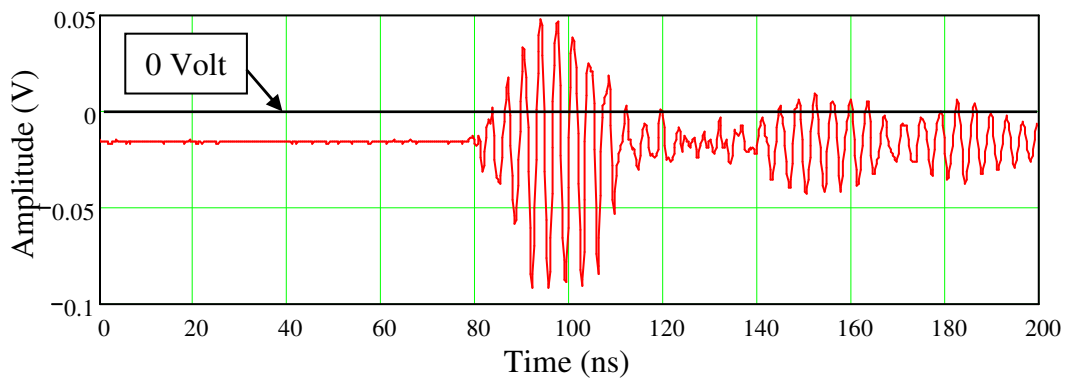


Figure 2.5 Typical UHF PD waveform recorded during site testing. This is to show the presence of DC offset.

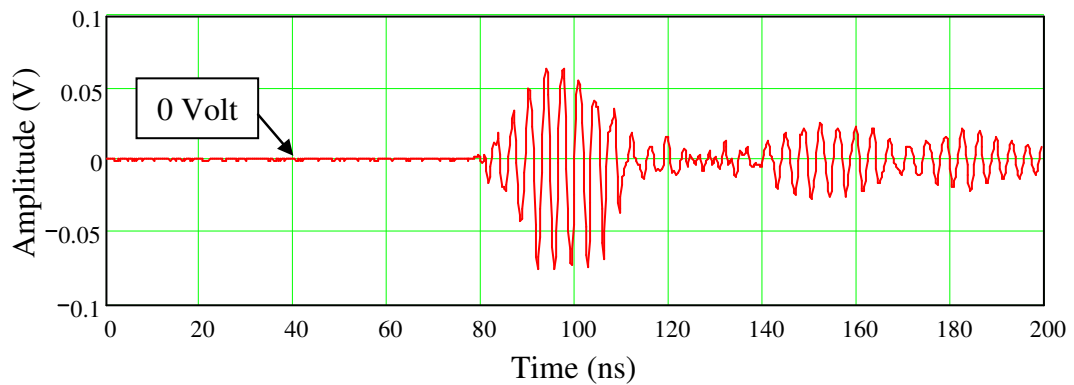


Figure 2.6 UHF waveform after removal of DC offset.

Background noise superimposed on UHF signals within the scope of this research was broadband ('white') noise, so a mean value calculated from the whole signal length (Eqn. 2.1) can be used to determine a DC offset value. However, if there was interference present that could introduce a unipolar spike within the signal record, this method of removing the DC offset would not be valid. Hence it might become necessary to determine the DC offset of the system by averaging samples from a limit period at the start of the data record, which would have the added advantage of reducing computation time

Step 2) Voltage squaring

The second step is to square the sampled voltage data points to produce a unipolar waveform proportional to the instantaneous signal power. The main reason to use the squaring to instantaneous sampled voltage data points is to avoid the possibility of zero values in the smoothed waveform while preserving the waveshape which allows differentiation between PD sources by means of the envelope comparison method. By this step, the signal has been converted in appearance from Figure 2.6 to Figure 2.7.

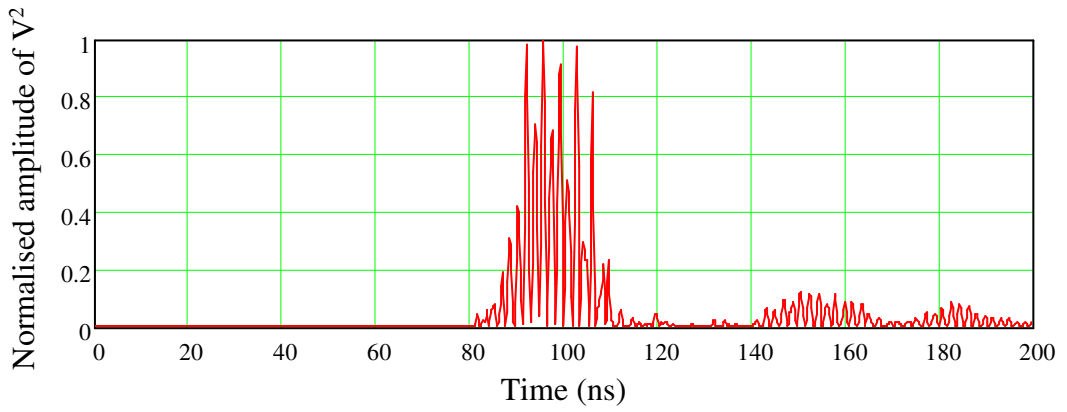


Figure 2.7 Normalised squared voltage of the signal shown in Figure 2.6.

Step 3) Envelope creation

Generating a representative envelope can be an effective way to characterise the signal in fewer data points, provided the parameters are selected appropriately. An algorithm to create envelopes (a smoothing algorithm) is merely a process attempting to smooth signals with their shapes retained but preserving fewer data points. In this research, Gaussian kernel smoothing by the *ksmooth* function of Mathcad is applied to the squared to generate the envelope shape. The *ksmooth* function is defined as follows [78]:

$$EN_i = \frac{\sum_{j=1}^N K\left(\frac{i-j}{W}\right) \cdot VS_j}{\sum_{j=1}^N K\left(\frac{i-j}{W}\right)} \quad (2.3)$$

where EN_i is the smoothed envelope component at i -th sample
 VS_j is the instantaneous voltage squared at j -th sample (volt),
which is being replaced with the EN_i component
 i, j are sampled point i -th and j -th
 W is the width of smoothing window (sample point), which can
be converted to time scale based on the sampling rate

N is the total number of sample points.
 K is the Gaussian kernel smoothing function as defined in Eqn. 2.4

$$K(t) = \frac{1}{\sqrt{2\pi} \cdot (0.37)} \cdot e^{\left(-\frac{t^2}{2 \times 0.37^2}\right)} \quad (2.4)$$

where

t is time
 0.37 is constant value assigned by Mathcad

Consider Eqn. 2.3: the shape of the smoothed envelope is controlled by a parameter W . The larger W , the more detail of the envelope will be suppressed. Small values of W would be expected to provide better separation by retaining more envelope detail, but at the increased bandwidth for the resulting smoothed envelope. To select a trial value of W , since the UHF range begins at 300 MHz, the largest period of this band is 3.33 ns. Therefore, the value of W should be varied from about 3 ns in order to cover at least one cycle of the UHF signal until an upper limit is found that still provides a sufficient margin between similar and dissimilar smoothed envelopes. In practice, the minimum value of W used was 4 ns.

Step 4) Normalisation

After the smoothed envelope shape is generated, it is normalised before comparison with others to remove the effect of varying PD signal amplitude.

Step 5) Time offset compensation

Time offsets can arise between different data sets because of variable oscilloscope triggering positions from pulse to pulse that are caused by stochastic amplitude variations between successive pulses. This can cause apparent differences between smoothed envelopes even when their UHF signals originate from the same source.

Before assessing similarity, it is necessary to time-shift the data sets, so that the envelopes are aligned. This shifting can be carried out manually or automated using cross-correlation techniques. However, envelope shapes are generally simple enough for time shifting by making their peaks coincide. After time offset compensation, it would be expected that little difference between pairs of smoothed envelopes created from the same PD source would be apparent. The transformation covering sampled UHF signals to aligned envelopes is illustrated in Figure 2.8. These pulses were generated from the same PD source.

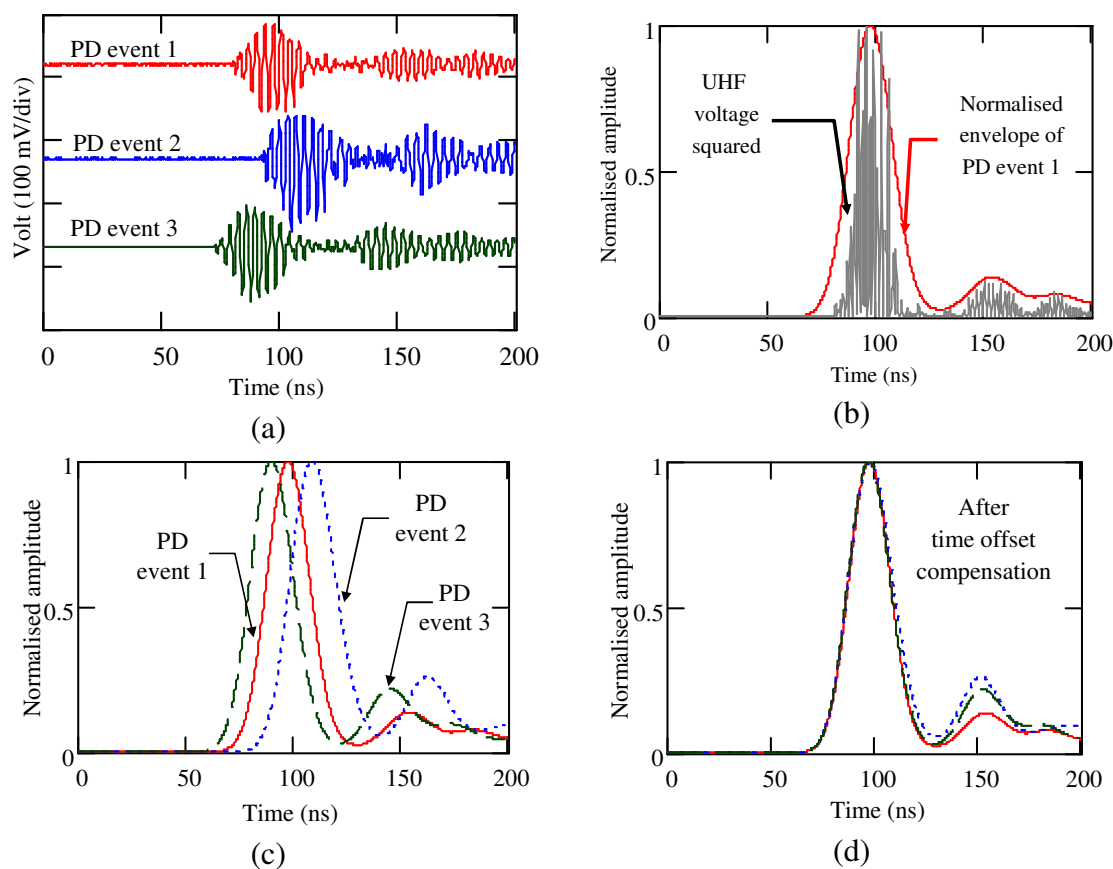


Figure 2.8 Several PD waveforms and their envelopes (recorded during 252 MVA power transformer test): (a) PD signals captured by the same sensor (variable triggering positions are evident), (b) Voltage squaring, smoothing and normalisation of the envelope belonging to PD event 1, both shown on a normalised scale, (c) Normalised envelopes of the three original PD signals, (d) Normalised envelopes after time offset compensation.

Figure 2.8(a) illustrates similar signal profiles but in different triggering positions. It is evident that these signals are potentially generated from the same PD source. Figure 2.8(b) shows the normalised smoothed envelope of PD event 1 with its normalised instantaneous UHF squared voltage. Figure 2.8(c) shows the normalised smoothed envelopes of each signal in which the different triggering positions can be seen as well. Figure 2.8(d) exhibits the normalised smoothed envelopes after time offset compensation, where they were manually shifted by using the differences of the start times of the signals. The start time is defined as the time when the normalised envelope amplitude first crosses 1 % of its peak, so it would be expected that all normalised envelopes have no time offset. Note that using this means to bring those envelopes into alignment, offsets in sub-nanosecond range can still remain, but these will have no significance on the similarity assessment. After time offset compensation, envelopes are ready for similarity assessment.

Step 6) Similarity assessment

To establish whether two envelopes are similar, a difference coefficient was defined as:

$$D = \sum_{i=0}^{N-1} \Delta EN_i^2 \quad (2.5)$$

- where
- D is the Difference coefficient.
 - ΔEN_i is the difference between the two normalised envelopes compared at the i -th sample point.
 - N is the total number of sample points.

Values of D can be calculated for all possible pairs of smoothed envelopes. The lower the value of D , the more two envelopes are considered similar, with $D = 0$ representing identical waveforms. Once a suitable threshold value for D has been established to distinguish between similar and dissimilar envelopes, Eqn. 2.5 can be

applied to all the available envelope data to calculate groups of similar envelopes, which should correspond to different PD sources.

2.4 Experimental arrangement

The experiment presented here was aimed at investigating the ability of the envelope comparison method to differentiate between PD pulses from *different* positions while still recognising the stochastically varying pulses from the *same* position as being similar.

The experiment was carried out in a metal tank ($2.51 \times 1.26 \times 1.26$ m) using the contact discharge test cell [79] shown in Figure 2.9 to generate PD signals. The internal structure of the contact discharge test cell is illustrated in Figure 2.10. The contact discharge test cell generates electrical transients in the UHF range that are fully representative of free-particle type of PD activity in GIS with about 100 pC of charge transferred at each PD pulse [80]. The test cell is operated manually by means of a control unit external to the tank. Activating the controller causes a small charged steel sphere to drop onto an earthed plate, creating a contact discharge pulse

Three monopole UHF sensors (S1 – S3) were used to capture radiated UHF PD waveforms. One of the sensors can be seen in Figure 2.9. A schematic diagram of the test arrangement is illustrated in Figure 2.11. The tank represents in simple form a piece of electrical apparatus, such as a power transformer. Various positions for the test cell are indicated by P1 – P5 in Figure 2.11. These all lie on the centre line of the tank in the x - and y -axes and were spaced at 40 cm and 60 cm intervals in the x - and y - axes on plane $z = 0.63$ m. Monopole sensors S1 – S3 were installed on three different faces of the tank by inserting them through small holes so that they protruded into the enclosure. These correspond to three different ‘viewpoints’ for the UHF signals.

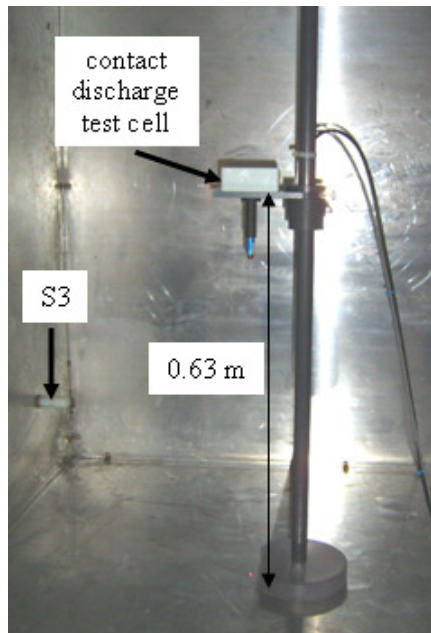


Figure 2.9 Contact discharge test cell positioned inside the tank.

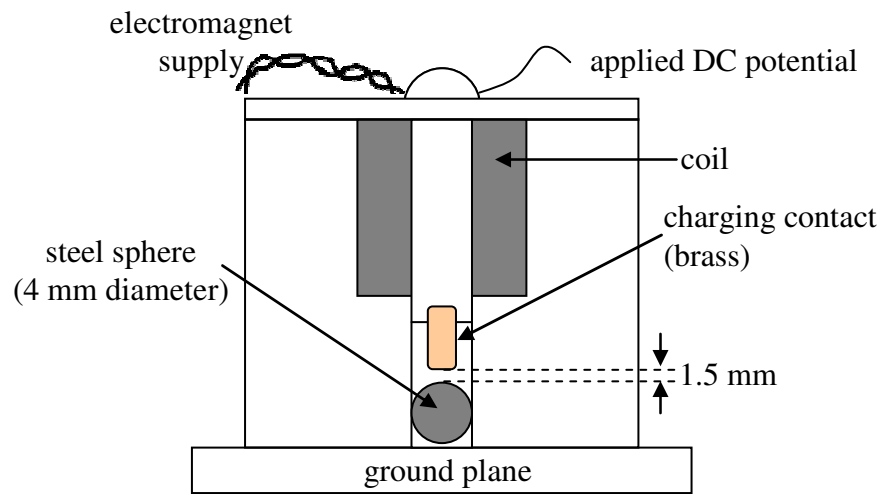
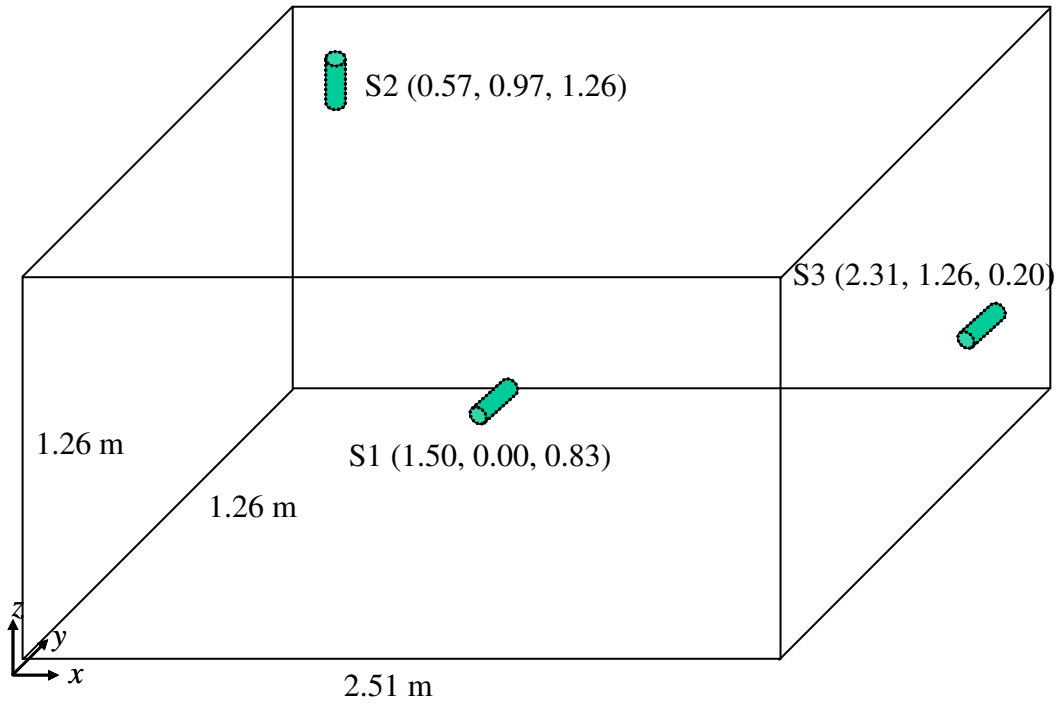


Figure 2.10 Structure of the contact discharge test cell [79].

(a)



(b)

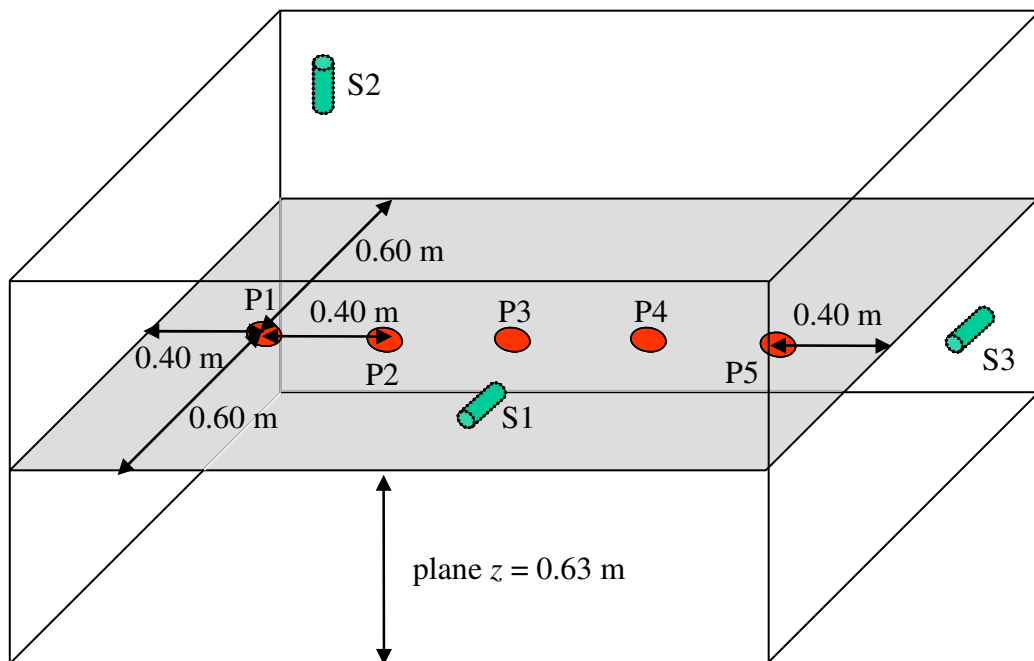


Figure 2.11 Schematic diagram of the experimental arrangement: (a) Tank dimension and S1, S2 and S3 UHF sensors coordinates, (b) Test cell positions (P1 – P5) tested on plane $z = 0.63$ m.

UHF signals were sampled using an oscilloscope at a sampling rate of 5×10^9 samples/sec and an analogue bandwidth of 1×10^9 Hz. The oscilloscope was set to record 10,000 voltage sample points over 2,000 ns. A typical set of UHF PD signals is shown in Figure 2.12. In practice, only the first 8,192 (2^{13}) voltage sample points (1,638 ns) for each PD signal were used for both the similarity assessment and spectral analysis using the Fast Fourier Transform (FFT). The reason for using this number of sample points is that the FFT requires 2^N samples and the required part of the UHF waveform can be fully captured using a value of $N = 13$. Figure 2.13 shows the spectral density of the S3 signal, confirming that frequencies extend into the UHF band (300 – 3,000 MHz), as would be expected for a typical PD source. For each position of the test cell, 20 pulses were recorded. With 3 sensors and 5 test cell positions, a total of 300 UHF signals were captured.

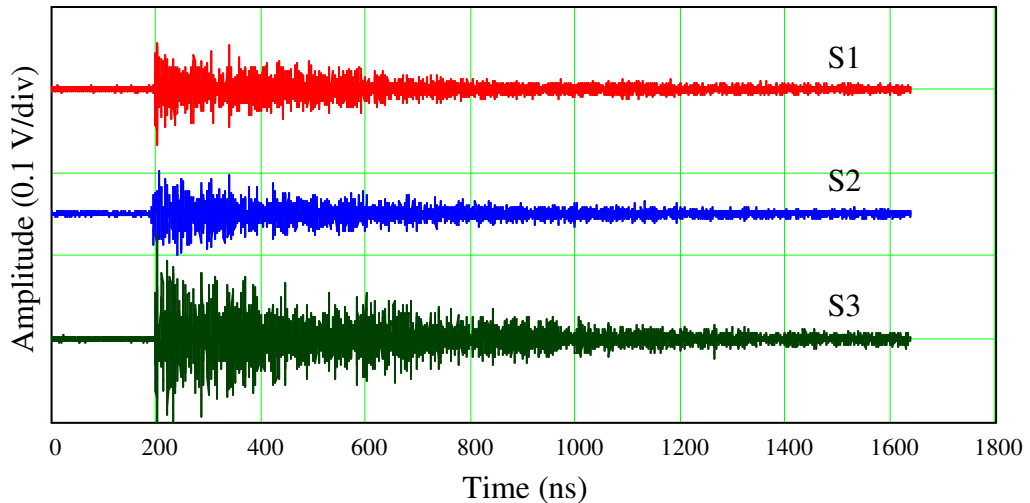


Figure 2.12 UHF PD waveforms captured by 3 UHF sensors simultaneously at P1.

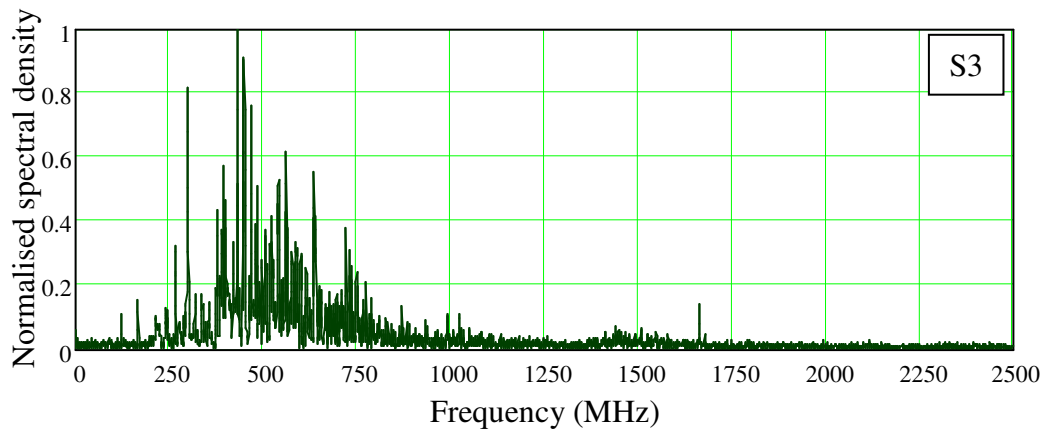


Figure 2.13 Typical frequency spectrum of PD signal (this example belonging to S3 of Figure 2.12).

2.5 Experimental results

Two main factors, (a) effects of varying W for envelope creation and (b) potential sampling rate reduction, were considered with the aim of maximising the width of smoothing window (W) while retaining the ability to discriminate different PD sources.

2.5.1 Effects of varying W for envelope creation

To demonstrate these effects, the signals shown in Figure 2.12 will be used. Figure 2.14 shows the ‘S1’ signal smoothed using values for W of 20, 40 and 60 ns. As W increases, most of the secondary envelope detail is lost. Figure 2.15 shows that, with $W = 20$ ns, the envelopes of signals detected at the three sensors are significantly different for a single PD pulse. It is evident that the effects of the propagation paths between the PD source and each sensor have a clear effect on the shape of the smoothed envelope.

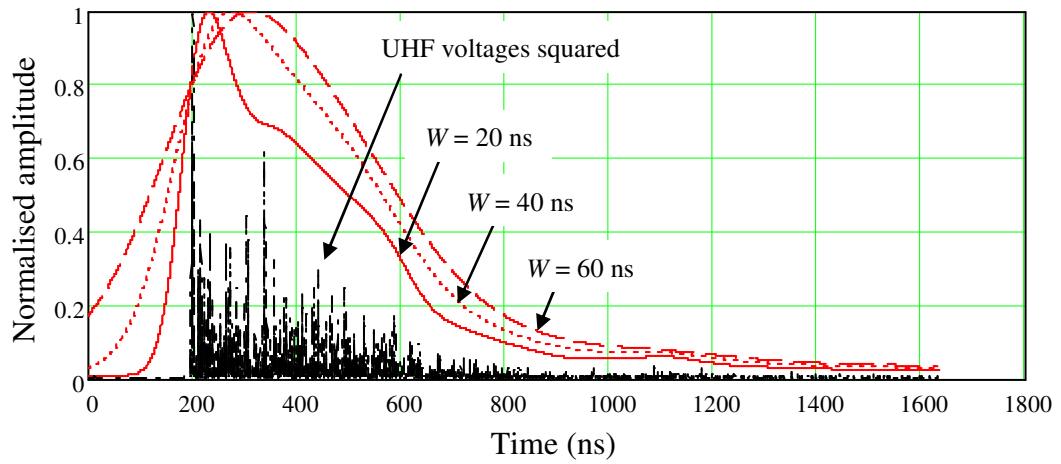


Figure 2.14 Normalised envelopes obtained using different window widths and its normalised UHF voltages squared, observed by S1 with the test cell at P1.

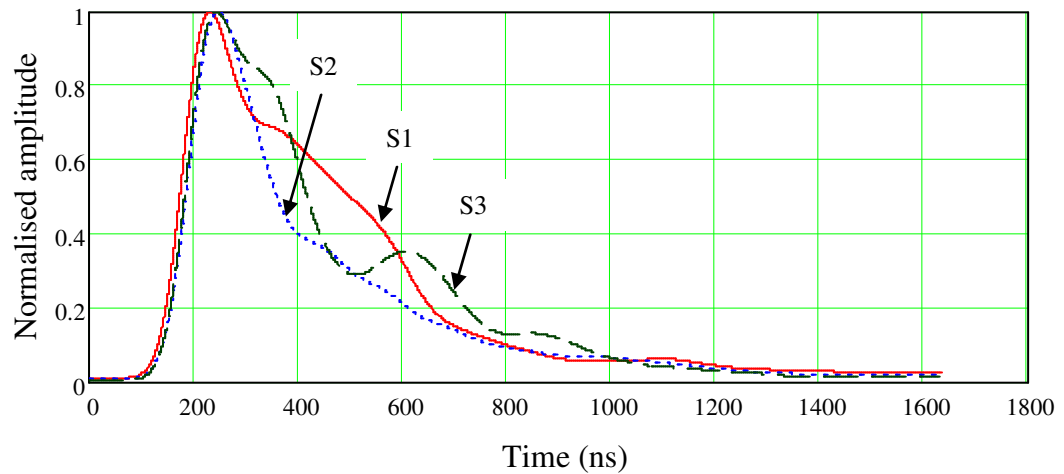


Figure 2.15 Normalised envelopes of the same PD using $W = 20$ ns for smoothing, observed by three sensors with the test cell at P1.

To investigate this further, the envelope comparison method was applied to signals from different sensors for each PD source position to distinguish between the different electromagnetic propagation transfer functions between the PD source and the sensors. This investigation is representative of a test in which a single sensor is available but there are multiple active PD sources taking place in the system being

monitored. Three initial values of W (20, 40, and 60 ns) were selected to create envelopes. To generate a smoothed reference envelope of each sensor for each test cell position, the first signal from each sensor for each test cell position was used, since the system has no prior knowledge what a smoothed envelope looks like (see the diagram of the envelope comparison method in Figure 2.4). After the smoothed envelopes of subsequent UHF signals were created, the similarity assessment was then applied to all smoothed envelopes for all possible comparisons among three sensors and five test cell positions. For each W value, 285 values ($19 \text{ comparisons} \times 3 \text{ sensors} \times 5 \text{ positions}$) of same sensor comparisons (D_{SA}) were calculated for the same sensor outputs (D_{1-1} , D_{2-2} , and D_{3-3}) while 300 values ($20 \text{ comparisons} \times 3 \text{ sensors} \times 5 \text{ positions}$) of different sensor comparisons (D_{DF}) were computed for different sensor outputs (D_{1-2} , D_{1-3} and D_{2-3}). Success will be judged if D_{SA} appears relatively low compared with D_{DF} .

To evaluate the results, values of D obtained from individual D_{SA} were sorted into ascending order while all D_{DF} values were combined and sorted into ascending order afterwards. As the minimum margin between D_{SA} and D_{DF} is most important, the separation between D_{SA} and D_{DF} was considered using the 10 highest values of D_{SA} of each sensor and the 10 lowest values of D_{DF} .

Results are shown in Figure 2.16. This figure shows three possibilities for the margin, which are (i) overlapping data ($W = 60 \text{ ns}$), (ii) very narrow margin ($W = 40 \text{ ns}$) and (iii) clear separation ($W = 20 \text{ ns}$). From trends of these results, it is clear that the larger W provides the smaller margin.

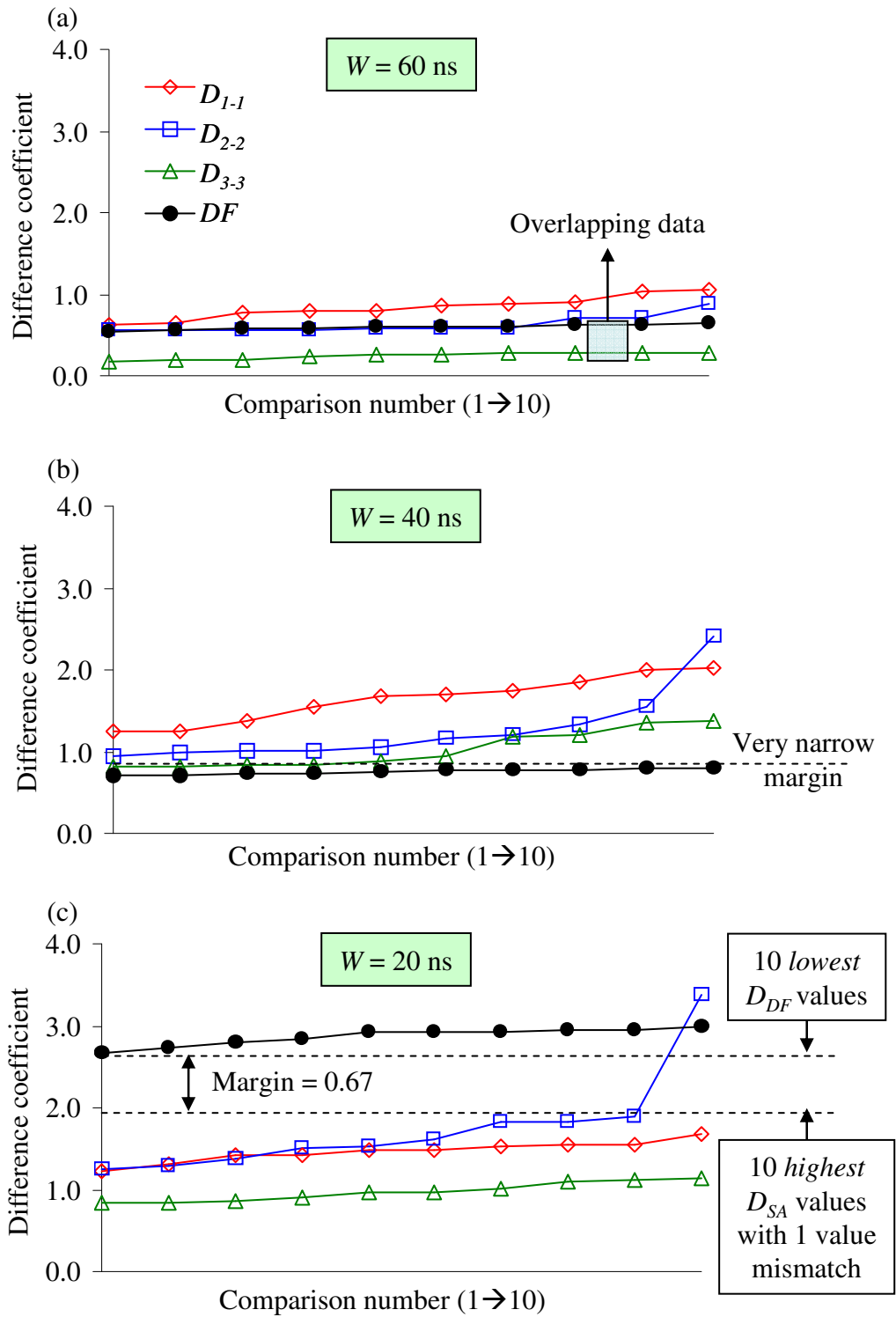


Figure 2.16 Difference coefficient values for investigating margins between the same and different PD positions: (a) Overlapping data for $W = 60 \text{ ns}$, (b) Very narrow margin for $W = 40 \text{ ns}$, (c) Clear margin with 1 value match from 285 values for $W = 20 \text{ ns}$.

Results indicate that $W = 20$ ns is about the maximum value that can be used for smoothing these sets of data because it provides clear separation (apart from a single mismatch where one point for two pulses at S2 appears in the ‘different’ band), as can be seen in Figure 2.17. In contrast, results for $W = 40$ ns and 60 ns contained significant overlap regions and are not shown here. Note that it is possible to use values of W smaller than 20 ns because they can provide larger margins; however, it will be at the cost of increasing bandwidth for the resulting smoothed envelopes.

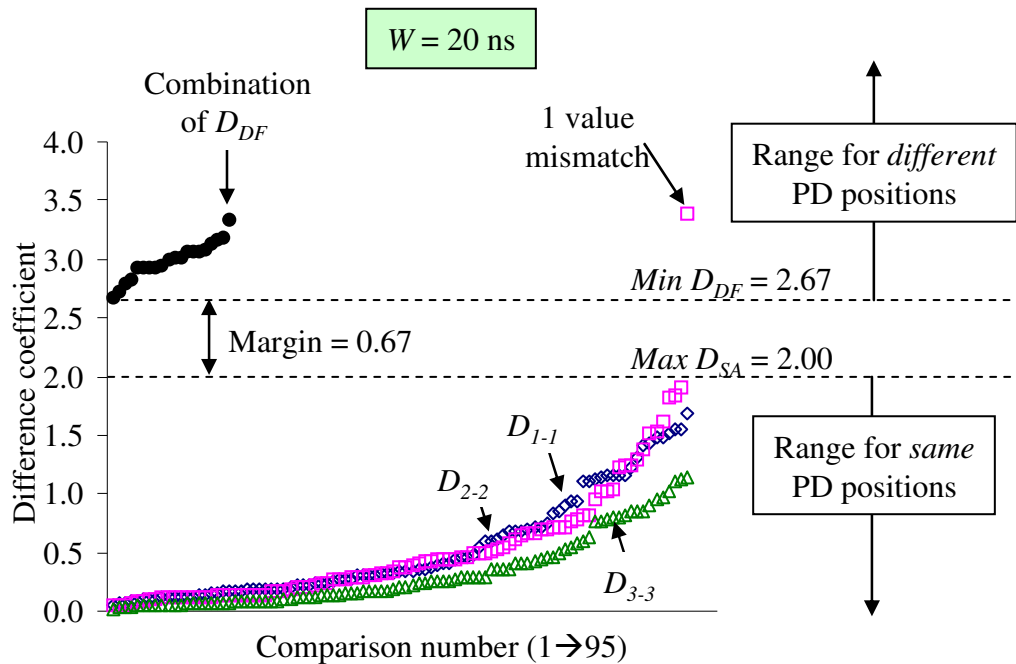


Figure 2.17 Difference coefficient values and margin for $W = 20$ ns, sorted into ascending order (Note that for D from different sensor comparisons only the lowest 95 values are deemed).

In terms of the single value mismatch in Figure 2.17, it is evident from the comparison of three envelopes (i.e. the reference envelope (1st), the problematic envelope (6th), the typical envelope (10th)) illustrated in Figure 2.18 that in the period between 400 ns and 600 ns the problematic envelope is fairly distant from the reference compared with the typical envelope. This region causes the value of D to be relatively higher than the other comparisons.

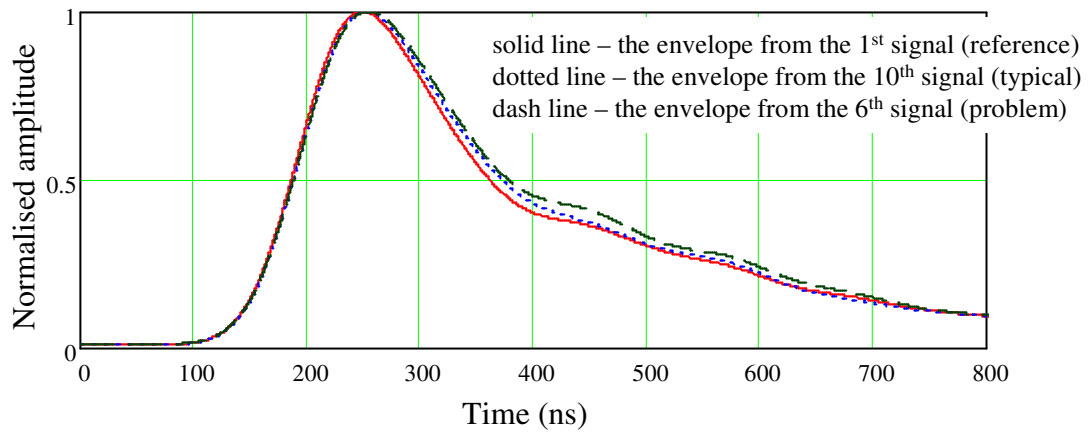


Figure 2.18 Comparison among the three envelopes obtained from sensor S2 that produce 1 value mismatch. Values of D_{SA} for the similarity assessment between (1) reference and 6th envelope and (2) reference and 10th are 3.38 and 1.04, respectively.

After this step, a threshold for distinguishing between PD signals (D_{TH}) can be selected. For example, based on Figure 2.17, D_{TH} might be set at about 2.3 for $W = 20$ ns to separate between similar (<2.3) and dissimilar (>2.3) signals. The particular D_{TH} value will of course be unique to a particular measurement regime, since D_{TH} as defined is dependent on the number of data sample points.

To assess performance as the PD source (test cell) was moved, comparisons were made using two different values of W , 4 ns and 20 ns. This circumstance is similar to practical implementations, where multiple active PD sources take place in a system and multiple UHF sensors (e.g. three UHF sensors for power transformers) are installed in that system. An additional aspect of this analysis was that values of D for signals measured on all three sensors were averaged to give a more robust outcome. To demonstrate the possibility of obtaining a more robust margin, some exploratory calculations were carried out using only the first two of the 20 UHF signals per sensor for each PD position. Values of D were calculated for all possible comparisons of same sensor signals for position P1 to P5 and average among the three sensors in each case. This average value is called ‘Average multi-sensor’ D . A selection of results is presented in Table 2.1. For five PD positions, there are 10 possible comparisons in total. This table only shows values of D calculated by

comparing signals from PD position P1 with themselves and with the other four PD positions (P2 – P5).

Table 2.1 Values of difference coefficient (D) and average multi-sensor D for all possible comparisons for P1.

PD positions compared	$W = 4 \text{ ns}$				$W = 20 \text{ ns}$			
	D_{1-1}	D_{2-2}	D_{3-3}	Average multi-sensor	D_{1-1}	D_{2-2}	D_{3-3}	Average multi-sensor
P1-P1	1.50	1.59	1.07	1.38	0.90	0.95	0.54	0.80
P1-P2	54.09	22.27	100.26	58.87	57.75	8.62	49.24	38.54
P1-P3	61.92	47.75	91.86	67.18	63.96	34.41	64.44	54.27
P1-P4	35.40	37.70	146.36	73.15	23.35	11.56	97.15	44.02
P1-P5	106.61	82.45	74.61	87.89	55.67	31.78	32.67	40.04

From Table 2.1, values of D obtained from the same PD positions are small compared with ones of different PD positions. In some single-sensor D values for different PD positions, there are some lower values compared with others in the same group. For example, D_{2-2} between P1 and P2 for $W = 20 \text{ ns}$ is much smaller than D_{1-1} and D_{3-3} . Therefore, using the average multi-sensor D is more robust when distinguishing between different PD positions. Ten values of multi-sensor D for five position comparisons are presented in Figure 2.19. It displays more robust margins for separating them into two regions. From this figure, it is evident that a substantial margin has been achieved between the PD sources that are at the same and different positions.

To illustrate typical variations of average multi-sensor D between the same and different PD positions, their mean and standard deviation values were calculated. 95 values per sensor for the same sensor comparisons (presented in Figure 2.17) were used in the calculations and the results are summarised in Table 2.2. For comparisons involving different PD positions, the first five UHF signals for each position per each sensor were evaluated. There were 45 signals ($3 \text{ sensors} \times 5 \text{ positions} \times 5 \text{ signals}$) to analyse in total. Results are summarised in Table 2.3.

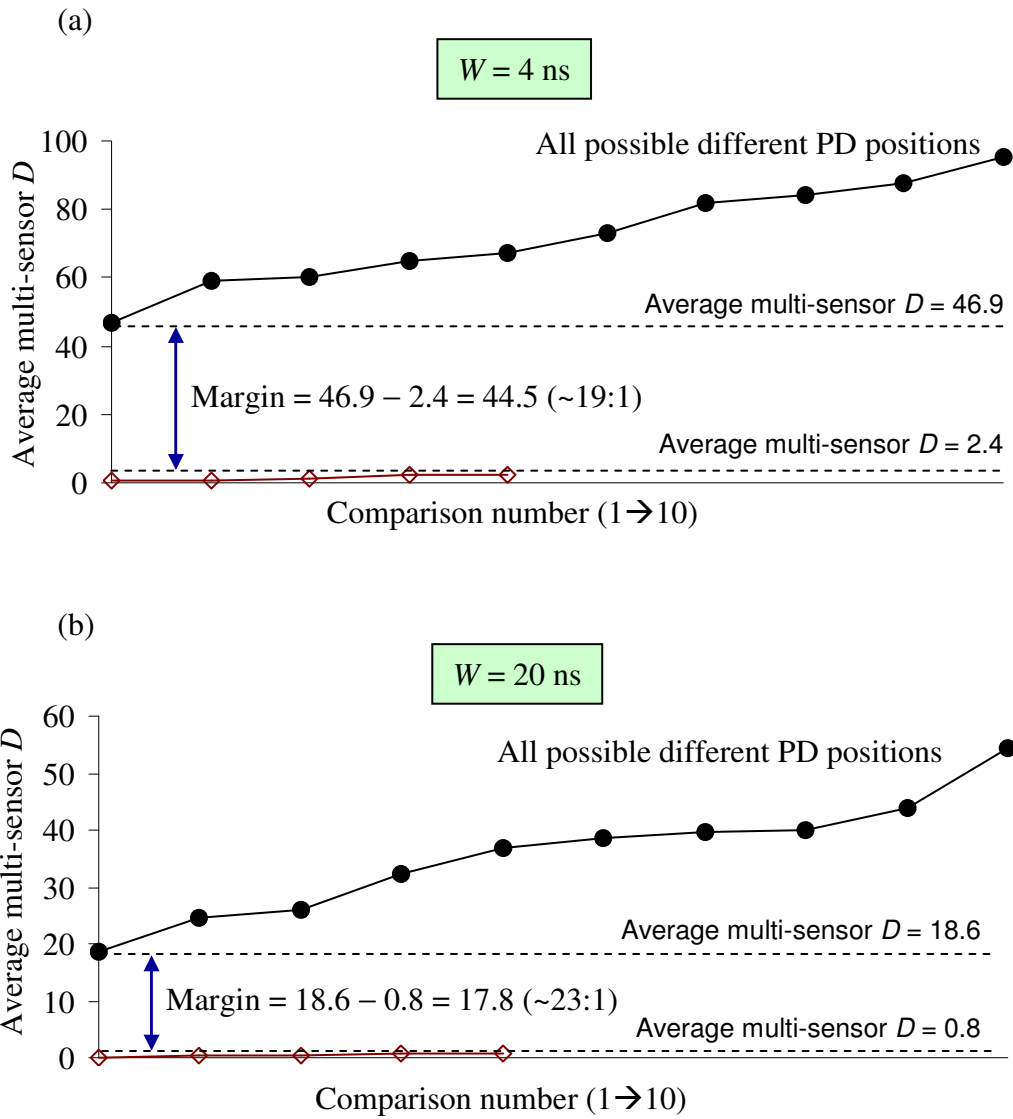


Figure 2.19 Values of average multi-sensor D compared between the same and different PD locations, sorted into ascending order: (a) $W = 4 \text{ ns}$, (b) $W = 20 \text{ ns}$.

Tables 2.2 and 2.3 show that the mean and standard deviation values of average multi-sensor comparisons for all positions obtained from the same PD positions are significantly lower than those obtained from the different PD positions. However, the most significant parameter is the margin between the same and different PD positions. These two tables also reveal that the margin between them is 17.40 ($18.53 - 1.13$), corresponding to the margin of approximately 16:1 for $W = 20 \text{ ns}$. For $W = 4 \text{ ns}$, the margin is higher than 17.40. Using average multi-sensor D values can provide

better results for distinguishing between different PD positions without an overlap region since the margin is very high.

Table 2.2 Mean and standard deviation (STD) values of difference coefficient (D) and average multi-sensor D values for the same PD positions with $W = 20$ ns.

PD positions compared	D_{1-1}		D_{2-2}		D_{3-3}		Average multi-sensor
	Mean	STD	Mean	STD	Mean	STD	
P1-P1	1.18	0.34	1.35	0.63	0.86	0.17	1.13
P2-P2	0.36	0.22	0.44	0.20	0.24	0.09	0.35
P3-P3	0.60	0.43	0.46	0.28	0.33	0.16	0.46
P4-P4	0.29	0.16	0.26	0.16	0.23	0.15	0.26
P5-P5	0.19	0.09	0.13	0.05	0.12	0.06	0.15
Mean of average multi-sensor for all positions							0.47
Standard deviation for all positions							0.39

Table 2.3 Mean and standard deviation (STD) values of difference coefficient (D) and average multi-sensor D values for the different PD positions with $W = 20$ ns.

PD positions compared	D_{1-1}		D_{2-2}		D_{3-3}		Average multi-sensor
	Mean	STD	Mean	STD	Mean	STD	
P1-P2	60.44	2.12	9.99	0.78	47.49	1.24	39.30
P1-P3	64.14	1.66	35.71	1.78	64.25	1.32	54.70
P1-P4	23.86	1.93	11.47	1.82	97.00	0.75	42.20
P1-P5	57.12	1.39	31.26	1.88	33.35	1.91	40.58
P2-P3	56.98	5.13	34.03	2.27	24.98	1.15	38.67
P2-P4	21.72	1.40	15.32	2.70	58.78	0.83	31.94
P2-P5	34.87	2.59	36.73	2.02	6.90	0.47	26.17
P3-P4	39.37	1.95	9.92	0.91	23.57	0.55	24.28
P3-P5	13.73	0.94	14.66	0.52	27.21	1.26	18.53
P4-P5	38.70	2.07	13.19	0.77	67.43	1.79	39.77
Mean of average multi-sensor for all positions							35.61
Standard deviation for all positions							10.52

2.5.2 Potential sampling rate reduction

Since the numerical application of Gaussian smoothing amounts to low-pass filtering of the data, it is instructive to consider the spectral density of the smoothed envelope waveform to assess its bandwidth and the likely sampling rate required to capture it based on the Nyquist criterion [81]. Note that no reduction in data sampling rate was implemented within the analysis in this chapter.

Figure 2.20 shows typical frequency spectrum that uses the signal of S3 from Figure 2.12 as an example, plotted in log-log scale. Figure 2.21 illustrates the FFT spectral density of smoothed envelopes for the test cell at P1 for $W = 4$ ns and 20 ns. Comparing Figure 2.21(b) with Figure 2.13, the original PD signal spectral content in the range of 250 – 1,000 MHz has been reduced to less than 20 MHz using $W = 20$ ns for the smoothing window.

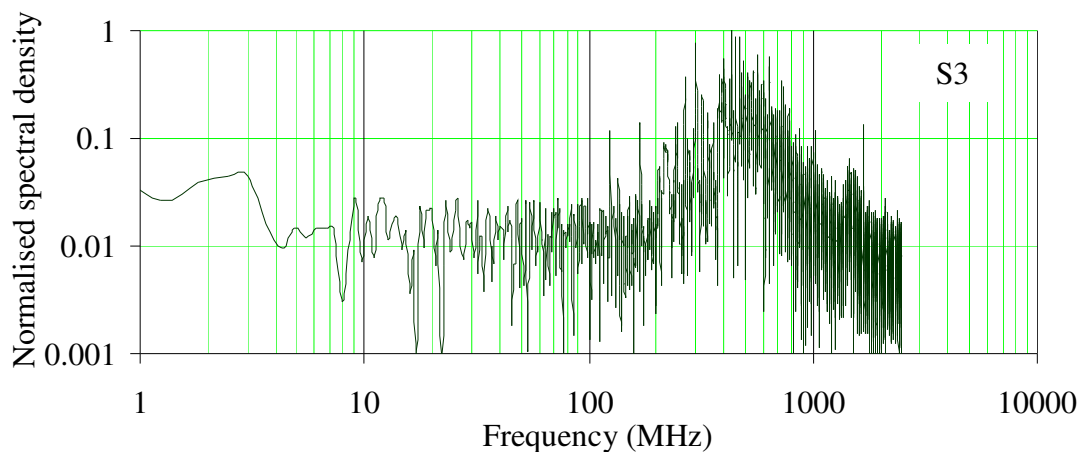


Figure 2.20 Frequency spectrum of 'S3' in Figure 2.12 plotted in log-log scale.

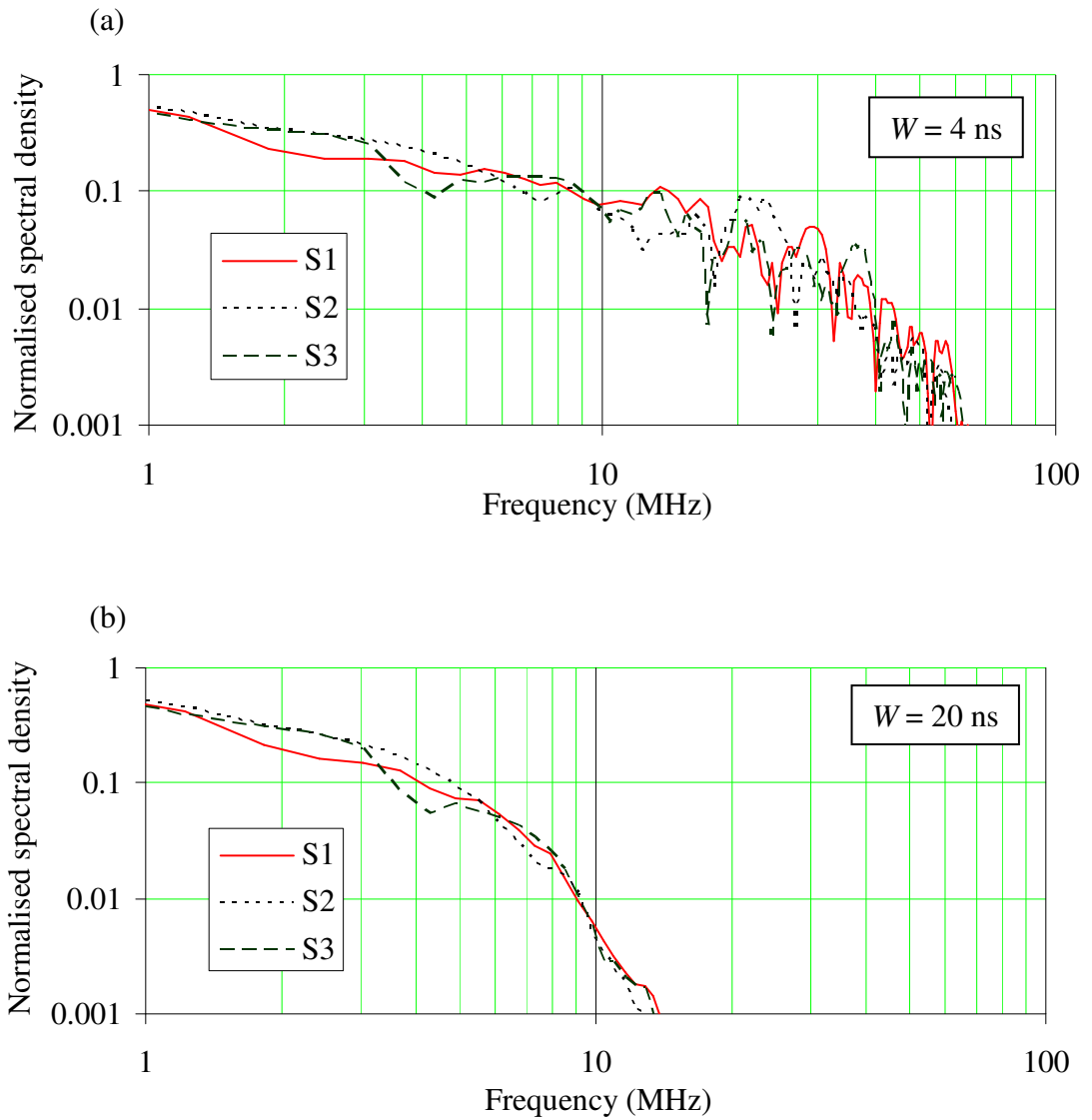


Figure 2.21 Frequency spectra of the smoothed envelopes for P1: (a) $W = 4 \text{ ns}$, (b) $W = 20 \text{ ns}$. This is to illustrate the reduction of frequency spectrum using larger W .

To determine the bandwidth of filtering by Gaussian kernel smoothing in terms of -3dB cut-off frequency, an impulse 512-sample sampling at 5×10^9 samples/sec was smoothed using a Gaussian kernel smoothing for various values of W . The method for determining the bandwidth of filtering by Gaussian kernel smoothing in terms of -3dB cut-off frequency will be demonstrated as follows:

Step 1) Apply Gaussian kernel smoothing to the 512-sample impulse using $W = 4$ ns as an example, which is shown in Figure 2.22.

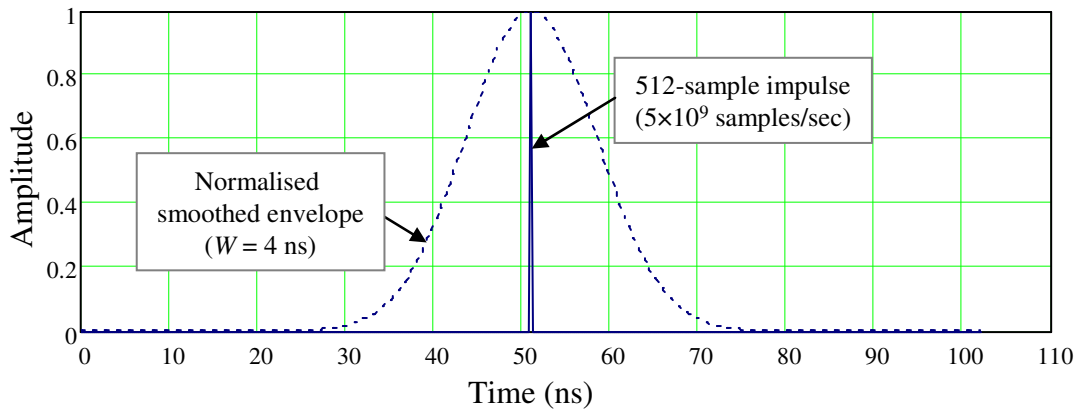


Figure 2.22 The 512-sample with a sampling rate of 5×10^9 samples/sec and its smoothed curve using Gaussian kernel smoothing $W = 4$ ns, for example.

Step 2) Apply the FFT to the smoothed envelope to determine its spectral density, which is illustrated in Figure 2.23.

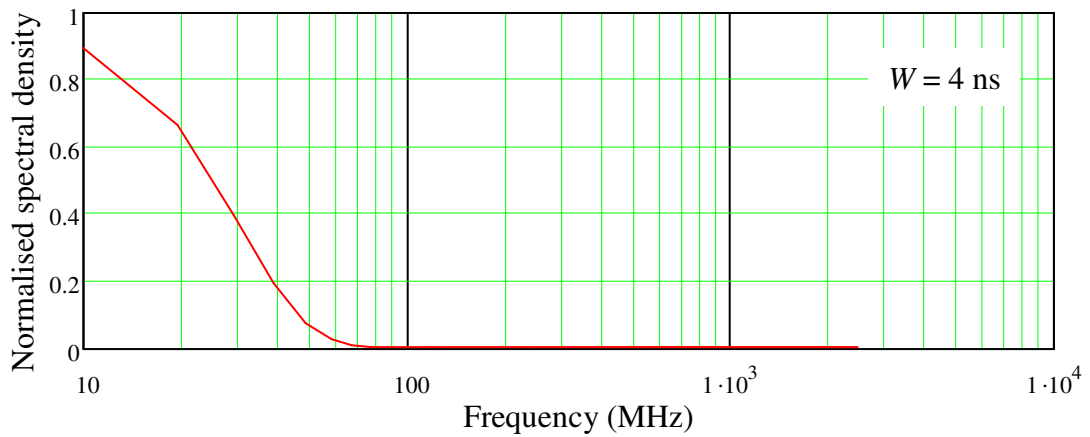


Figure 2.23 The normalised spectral density of the smoothed envelope of the 512-sample impulse.

Step 3) The -3dB cut-off frequency can be determined by means of the normalised spectral density reduction to 0.707 [81] as demonstrated in Figure 2.24.

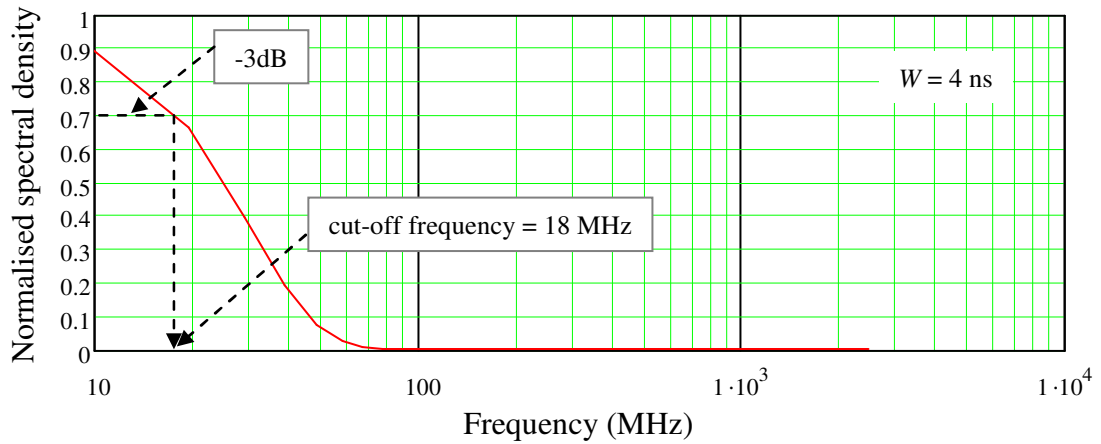


Figure 2.24 The selection of -3dB cut-off frequency.

Step 4) Vary W from 1 ns to 100 ns for the 512-sample impulse. The same procedures (step 1 to step 3) were repeated to determine the -3dB cut-off frequencies, which can be represented by a function of W in the form of a linear approximation in Figure 2.25 and Eqn. 2.6.

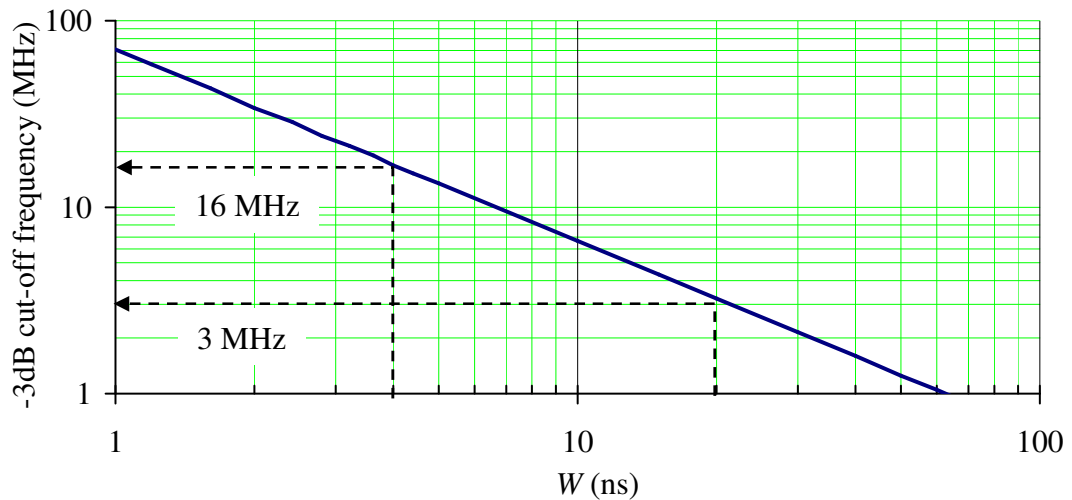


Figure 2.25 Bandwidth of filtering by Gaussian kernel smoothing as a function of window width W .

$$\log f_c = -1.029 \log(W) + 1.847 \quad (2.6)$$

where f_c is -3 dB cut-off frequency in MHz.
 W is window width in ns.

From this relationship, $W = 4$ ns and 20 ns (as used in the experiments) provide the bandwidths of 16 MHz and 3 MHz, respectively. Practically, it will be more effective to use the smaller values of W if that value is still practical to implement in real applications. For example, $W = 4$ ns producing a bandwidth of 16 MHz (available in any laboratories) was used in both laboratory experiments and in the next investigation with UHF signals sampled at 5×10^9 samples/sec. This implies that envelopes of UHF signals sampled at faster than 32×10^6 samples/sec (e.g. 50×10^6 samples/sec, a reduction by a factor of 100) are potentially usable with the envelope comparison method to distinguish between different PD sources. This will be investigated further in Section 6.2.

2.6 Case studies

Results from two practical HV tests were used to assess the performance of the envelope comparison method. The first of these was a set of data from PD monitoring of a switched HVDC testing of a reactor [82], while the second used data from PD monitoring of a 252 MVA power transformer [77]. In both cases, sampled UHF signals from several sensors on the unit being tested had been recorded at a sampling rate of 5×10^9 samples/sec and bandwidth of 1×10^9 Hz. Difference coefficient values were calculated between the various signal envelopes using $W = 4$ ns.

2.6.1 The switched HVDC reactor

For this case study, each set of PD signals consisted of three UHF signals captured from three UHF sensors (S1, S2 and S3) attached in different positions around the reactor housing. Each signal consisted of 500 voltage sample points over 100 ns. One set of PD signals is shown in Figure 2.26(a) and their corresponding envelopes are also shown in Figure 2.26(b). Nine sets (27 signals) were used and D values were calculated between (a) signals from the same sensors (D_{1-1} , D_{2-2} , and D_{3-3}), and (b) signals from different sensors (D_{1-2} , D_{1-3} , and D_{2-3}). The number of comparisons in these categories amounted to 108 and 243 respectively.

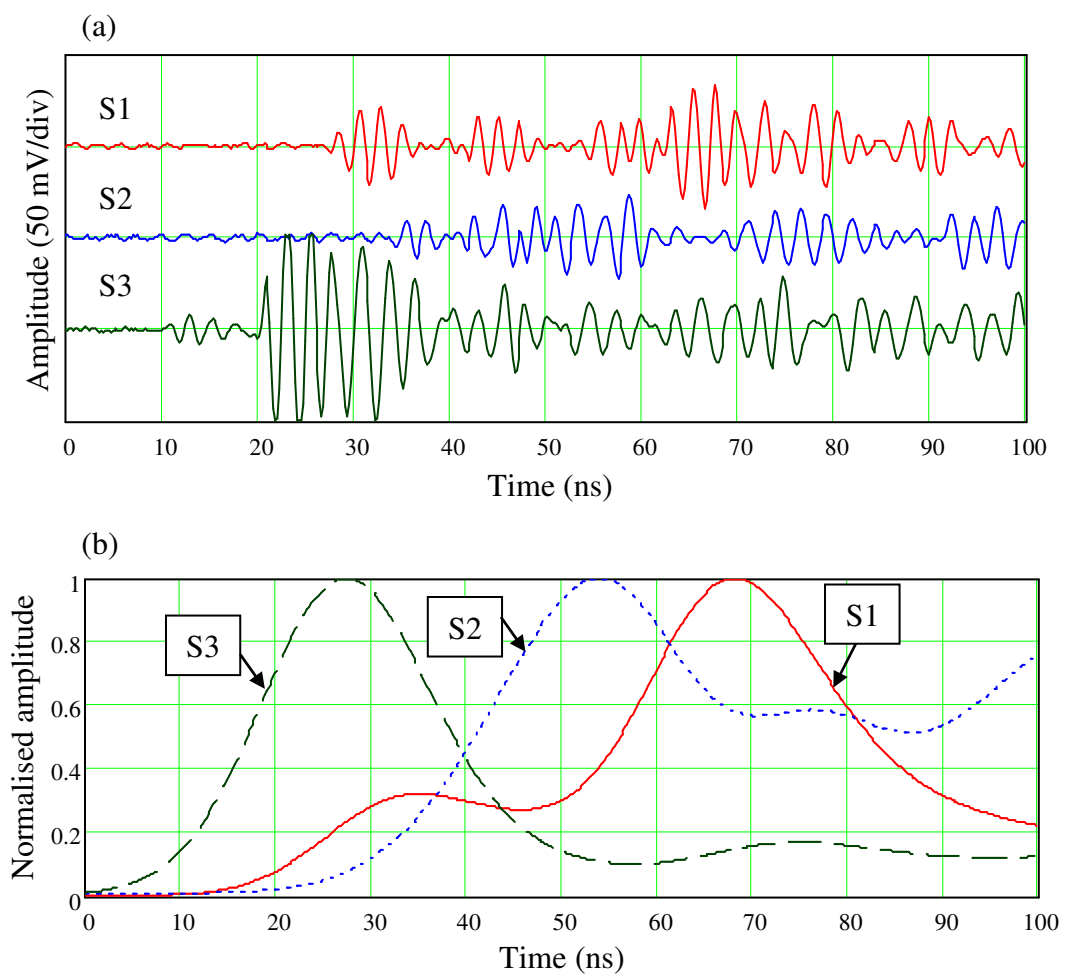


Figure 2.26 The switch HVDC reactor: (a) Typical UHF waveforms captured using three sensors simultaneously, (b) Their normalised envelopes created from $W = 4$ ns.

2.6.2 The 252 MVA power transformer

For this case study, four UHF sensors (S1, S2, S3 and S4) were fitted at different positions on the transformer tank. A simple diagram of the sensor placement is shown in Figure 2.27.

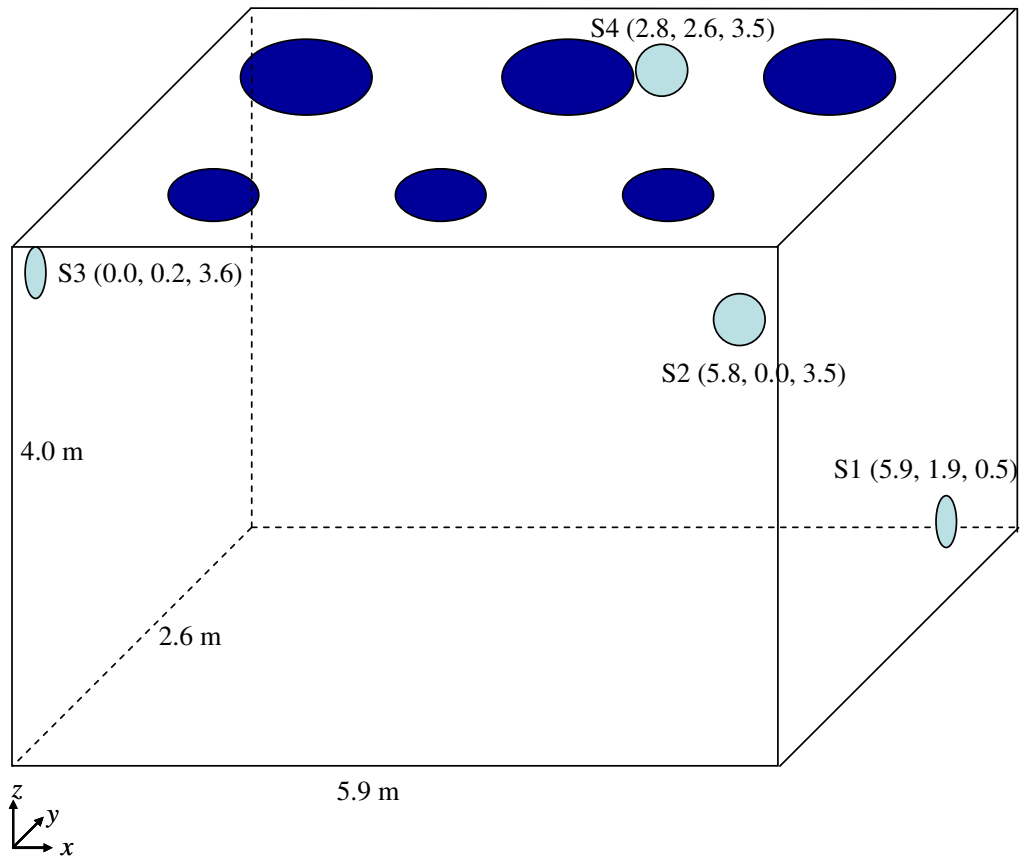


Figure 2.27 Diagram of the 252 MVA power transformer showing four UHF sensor positions (S1 – S4) and their coordinates in the (x, y, z) directions. The 3 large and 3 small circles on top of the tank mark the approximate locations of the HV and LV bushings respectively.

Each set of UHF signals was recorded at a subset of three sensors, as summarised in Table 2.4, which corresponds to various combinations of sensors with three different ‘viewpoints’ for the PD. Each captured UHF signal consisted of 1,000 sample points over 200 ns. Figure 2.28 (a) illustrates the signals of set 1 that was detected at

sensors 1, 2 and 4 and Figure 2.28(b) shows their corresponding envelopes. Eighteen sets of PD signals were used and D values were calculated between (a) signals from the same sensors (D_{1-1} , D_{2-2} , D_{3-3} and D_{4-4}), and (b) signals from different sensors (D_{1-2} , D_{1-3} , D_{1-4} , D_{2-3} , D_{2-4} and D_{3-4}). The number of possible comparisons in these categories amounted to 14 and 120 respectively, as shown in Table 2.5.

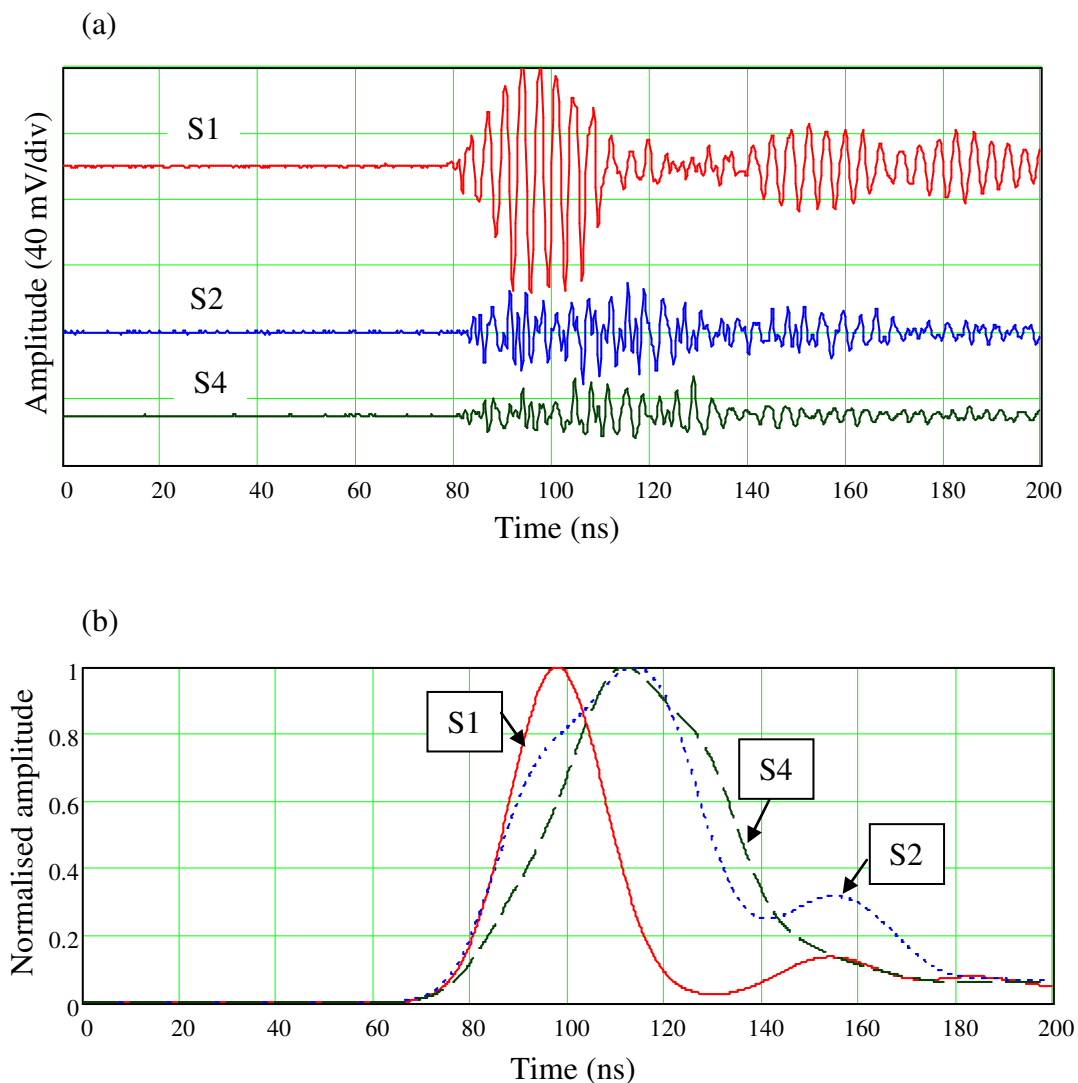


Figure 2.28 The 252 MVA power transformer: (a) Typical UHF waveforms captured using three sensors simultaneously, (b) Their normalised envelopes created from $W = 4$ ns.

Table 2.4 Data set and sensors being used to capture UHF signals for each set.

Data set	Recorded by sensors
1	S1, S2, S4
2	S1, S3, S4
3	S1, S3, S4
4	S1, S2, S4
5	S1, S2, S3
6	S1, S2, S3

Table 2.5 Number of Difference coefficient values for possible comparisons.

Same sensor comparisons	D_{1-1}	D_{2-2}	D_{3-3}	D_{4-4}	-	-	Total
	5	3	3	3	-	-	
Different sensor comparisons	D_{1-2}	D_{1-3}	D_{1-4}	D_{2-3}	D_{2-4}	D_{3-4}	
	24	24	24	16	16	16	120

2.6.3 Analysis and results of case studies

To determine the separation between signals from the same and different sensors comparison, all values of D for the same (D_{1-1} , D_{2-2} , and D_{3-3}) and all for the different (D_{1-2} , D_{1-3} , and D_{2-3}) of the switched HVDC reactor were sorted into ascending order and plotted in Figure 2.29. A clear separation of signals between the same and the different sensor comparisons can be seen. For the results of the 252 MVA power transformer, the same procedure was applied and its plot is shown in Figure 2.30. A small data overlap region is present in this case.

A more robust result can be obtained when more than one sensor is available by using the averaged multi-sensor D values. The results of this approach are shown in Figure 2.31 and Figure 2.32. Discrimination margins for the two HV tests described here are about 30:1 and 9:1, respectively. From these results, it is clear that the envelope comparison method can provide much better separation when more than one sensor is available.

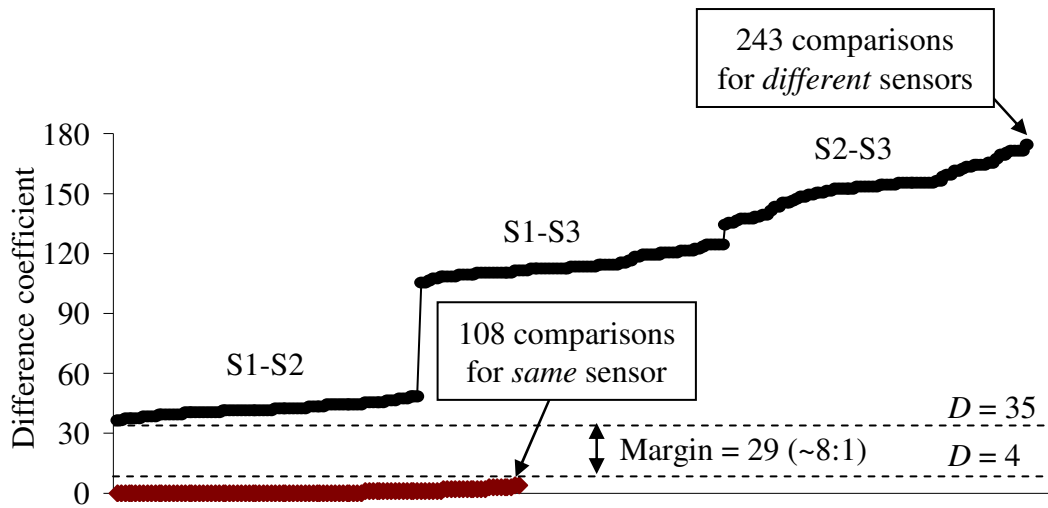


Figure 2.29 Ascending difference coefficient values between the signals from the same sensors and different sensors comparisons of the switched HVDC reactor. This is to illustrate the clear separation between them.

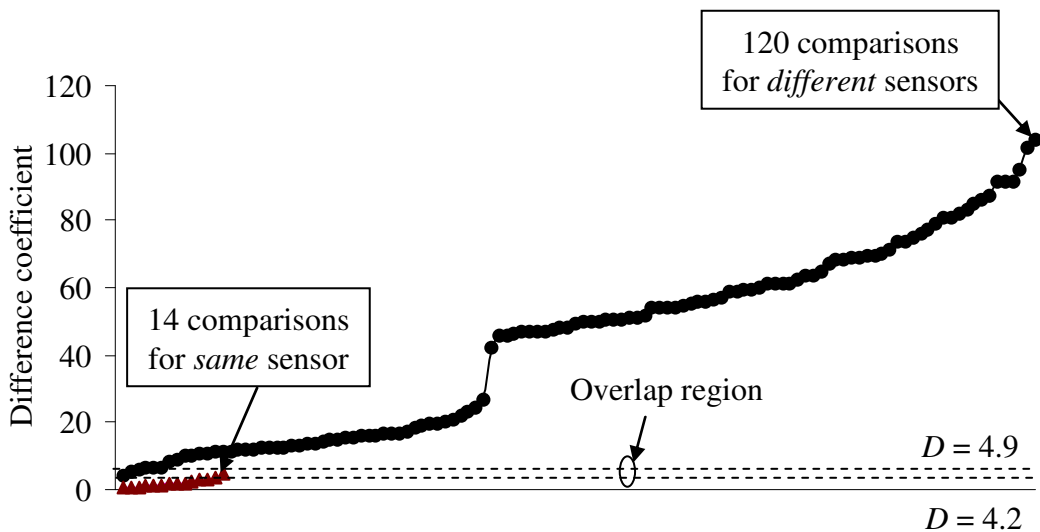


Figure 2.30 Ascending difference coefficient values between the signals from the same sensors and different sensors comparisons of the 252 MVA power transformer. This is to illustrate the overlap region presenting in this case.

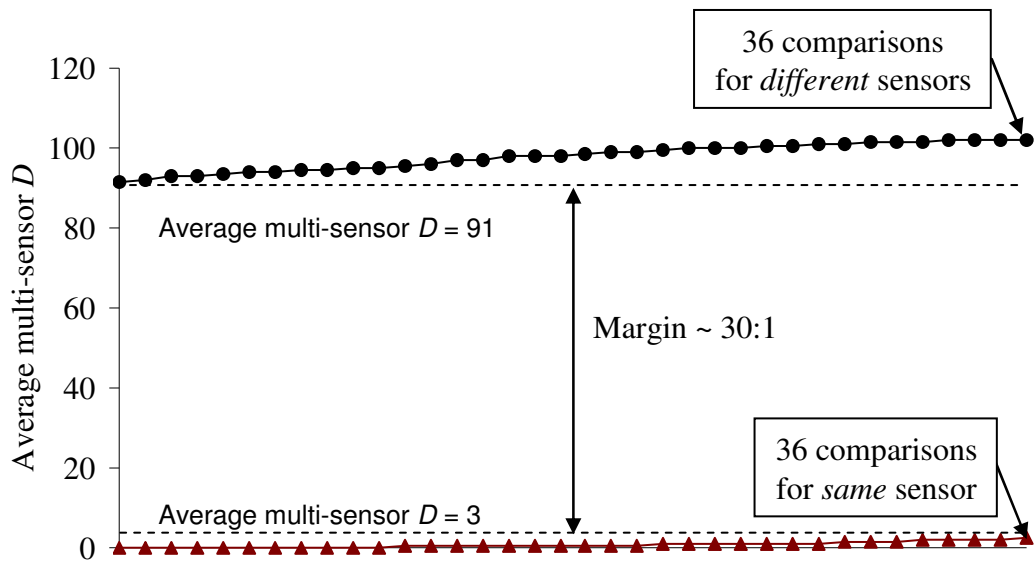


Figure 2.31 Average multi-sensor D values (sorted into ascending order) of the switched HVDC reactor. This is to illustrate the improved margin obtained using average multi-sensor D .

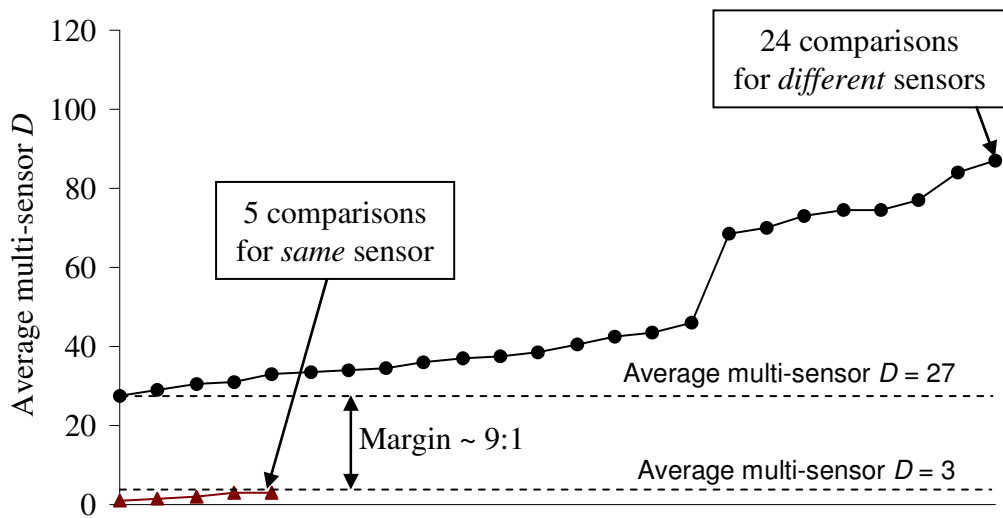


Figure 2.32 Average multi-sensor D values (sorted into ascending order) of the 252 MVA power transformer. This is to illustrate the margin instead of overlap obtained using average multi-sensor D .

2.7 Additional recommendations for the envelope comparison method

As the previous investigations presented, the envelope comparison method is an effective technique for distinguishing between different PD sources. This technique is straightforward to implement using an automated system because of the rigorous mathematical foundations. Additional recommendations when using the envelope comparison method will be discussed as follows:

1) Issue of interference signals

Ideally only the envelopes generated from actual PD signals should be considered while the envelope comparison method itself does not include filtering algorithms to discard any unwanted signals, such as impulsive noise, switching noise and any interference. Based on the basis of envelope comparison, sufficiently similar envelopes (either PD or non PD signals) can be grouped separately. This is an advantage especially if interference signals possess characteristic envelopes. Each group of signals corresponding to each smoothed envelope can be then fed into a PD pattern recognition method, which can identify whether they are PD or non PD signals. As a result, these interference signals could also be separated out. The envelope comparison method would still give ‘clean’ groups of the PD signals, resulting in enhancement in the accuracy of subsequent interpretation techniques. To reject certain interferences (e.g. noise containing frequency spectra below the UHF frequency), inserting a 250 MHz high-pass filter between the UHF sensor and the digitising hardware is probably a practical means.

2) Selection of widths of smoothing windows

Difference coefficient values are dependent on the width W of the smoothing window as illustrated in Eqn. 2.3. In this research, $W = 4$ ns was selected to calculate D values for all case studies because $W = 4$ ns provides an effective discrimination between the same and different PD sources. This particular value of W is specific to

the system under test, including the PD source topology, plant configuration and geometry, sensor configuration, type and position. When the system changes, W needs to be considered again. For example, if signals being analysed are acoustic emission, values of W are expected to be larger because the frequency range of ultrasonic signals are in the microsecond scale.

2.8 Discussion and conclusions

In this chapter, the envelope comparison method has been verified successfully in its capability for discriminating between different PD sources using the UHF signals obtained from both laboratory experiments and two industrial tests of HV equipment.

Firstly, the concept of the envelope comparison method was introduced, recognising several benefits that could be obtained if this method is proven to be effective. The rigorous mathematical calculations for creating signal envelopes were then presented. Smoothed envelopes were generated using a Gaussian kernel smoothing with window width W . The laboratory experiments consisting of one PD source and three UHF sensors were carried out in the metal tank for five different PD locations. UHF signals captured using a sampling rate of 5×10^9 samples/sec were used in the analysis. Experimental results based on individual sensor comparison show that the envelope comparison method can provide clear separation with a small margin = 1.3:1 using $W = 20$ ns while $W = 40$ and 60 ns provide very narrow margin and overlapping region. To acquire more robust separation, values of average multi-sensor D were used and results confirmed that larger margins of 19:1 and 23:1 for $W = 4$ ns and $W = 20$ ns, respectively were possible.

Two industrial sets of HV equipment (switched HVDC reactor testing and a 252 MVA power transformer) were also used to validate this technique with the selected $W = 4$ ns. Results obtained from individual sensor comparison show that the switched HVDC reactor testing offers clear separation (margin = 8:1) while the transformer data provides an overlap. However, using average multi-sensor D values

produced the better results. Margins of the switched HVDC reactor testing and the 252 MVA power transformer obtained from average multi-sensor D were 30:1 and 9:1, respectively.

Additionally, the potential for sampling rate reduction was also discussed. Using $W = 4$ ns (16 MHz -3dB cut-off frequency of a Gaussian kernel smoothing) to create envelopes of UHF signals should allow them to be captured using a sampling rate of 50×10^6 samples/sec (reduction by a factor of 100). An electronic circuit can be built to capture UHF envelopes by means of readily available components and digitised using a low sample rate (e.g. 50×10^6 samples/sec), which will be presented in Section 6.2.

3. Study of techniques for determining arrival times of UHF signals

3.1 Introduction

This chapter starts with a description of the importance of signal onset or arrival times for PD location in HV equipment. Next, key factors that affect characteristics of measured PD waveforms and which influence the accuracy of arrival times are explained. Existing techniques for determining arrival times are discussed and an alternative technique for determining arrival times, called *relative increase in energy*, is presented. This new technique is based on the relative increase in energy between successive samples. By considering this, it is straightforward to identify a time interval containing the exact arrival time. The relative increase in energy method has been investigated by means of experiments and in application to pulse injection tests on a 252 MVA power transformer, with promising results.

3.2 Importance of arrival times

In order to locate PD sources in HV equipment, the key parameter is the arrival time (T), or onset of the UHF signal, which is defined as the time when the initial wavefront of the signal arrives at the sensor. By identifying arrival times, time differences (ΔT) can be calculated and used for PD location by triangulation when four UHF sensors are installed in different positions on the tank. Previous research [49, 83] has indicated that PD sources in HV apparatus can be located using geometric calculations based on signal propagation times when groups of time differences, positions of sensors and the velocities of signal propagation are known.

For example, in GIS a PD source can be located by means of the time of flight measurement when the time difference between two PD signals is determined and speed of UHF signals in SF₆ is known, as described in [83]. The method to locate the

PD can be simply illustrated using a section of 400 kV GIS containing a PD source [84]. A representative section of GIS busbar is shown in Figure 3.1 and a pair of measured UHF signals with arrival times is illustrated in Figure 3.2. Note that equal lengths of cable are used between the sensors and the oscilloscope, so that any difference in arrival time can only be due to different distances travelled inside the GIS.

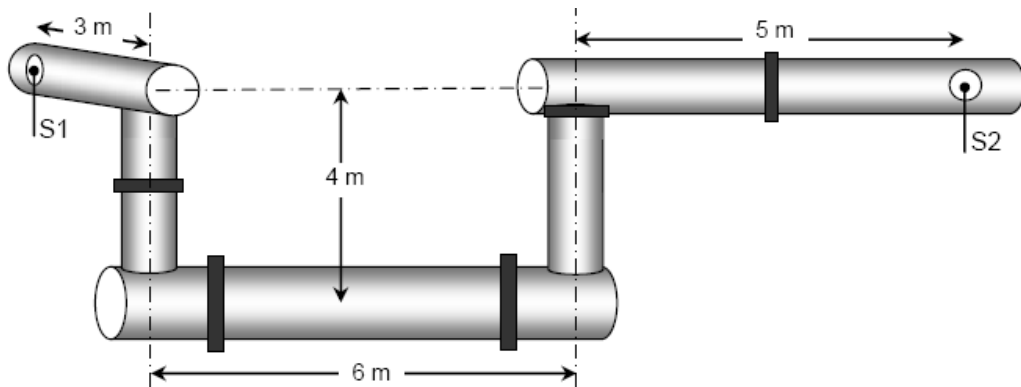


Figure 3.1 A section of 400 kV GIS containing a PD source. S1 and S2 are UHF sensors.

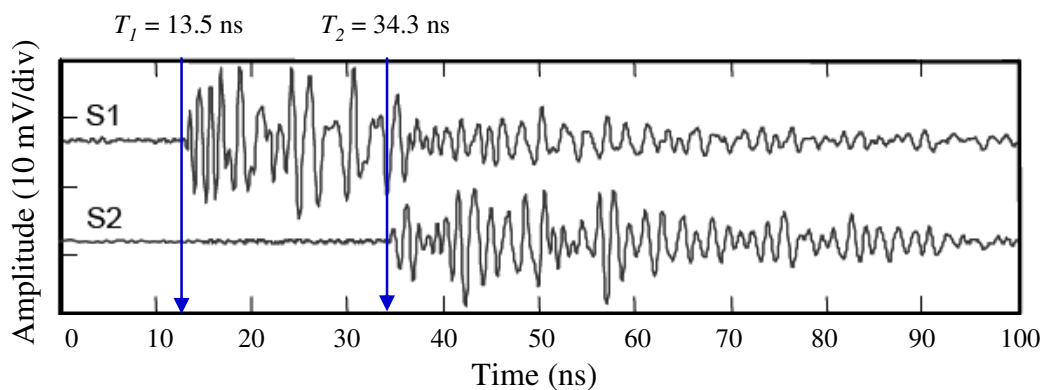


Figure 3.2 UHF PD signals measured at S1 and S2 with their measured arrival times.

To locate the PD, the procedure is as follows:

- 1) Estimate the arrival times of S1 and S2, which are 13.5 and 34.3 ns respectively.
- 2) Calculate the time difference ($\Delta T = |T_1 - T_2|$), which is 20.8 ns.
- 3) Measure the total length of the GIS section between sensors (L), which is 22 m.
- 4) Calculate the distance of the PD from S1 (x), as illustrated in Figure 3.3 using Eqn. 3.1.
- 5) By substituting all variables into Eqn. 3.1, the distance of the PD from S1 can be calculated, which is 7.9 m in this example.



Figure 3.3 Schematic diagram of Figure 3.1, where L is the total length of GIS section and x is the distance of the PD from S1.

$$x = \frac{L - c\Delta T}{2} \quad (3.1)$$

Where

- x = the distance of the PD from S1 (m)
- L = the total length of the GIS section (m)
- ΔT = time difference (s)
- c = velocity of light, 3×10^8 m/sec

Locating the PD position using Eqn. 3.1 assumes a 1-dimensional approximation of the GIS busbar. This is the procedure usually employed and gives an accuracy that is acceptable for practical purposes [83].

Another application is PD location in power transformers. Locating PD sources in three dimensions requires at least three independent time differences. By using a numerical model, which is described in [49], the PD can be located to within a certain tolerance. Therefore, determining arrival times accurately is very important.

Determining arrival times is challenging because it is dependent on signal characteristics that can be influenced by many factors. Consider Figure 3.4, for example. The arrival time T_2 of the signal at S2 is fairly clear while T_1 for S1 lies somewhere in the circled area. Therefore, a method to accurately determine arrival times based on a formal algorithm is needed.

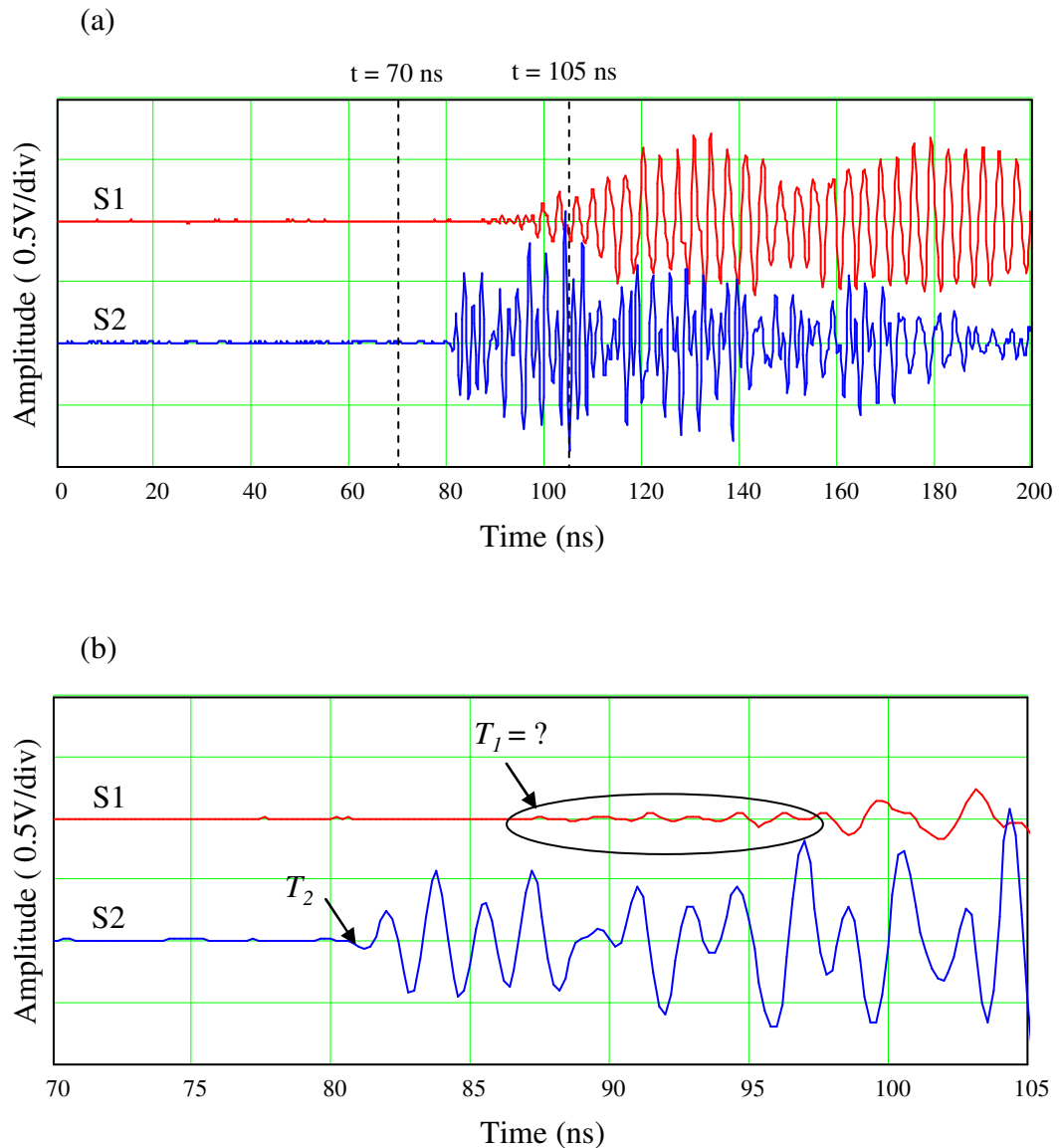


Figure 3.4 UHF signals captured from pulse injected: (a) UHF signals, (b) Expanded view of (a) to illustrate approximate arrival times. This is to show the difference of apparent and ambiguous arrival times.

If the measured waveform presents a high value of signal-to-noise ratio (SNR) and the initial wavefront is clearly visible, it might be straightforward to determine the arrival time of that waveform using a simple threshold. However, measured waveforms vary considerably in amplitude, shape and frequency content and this often makes measured PD waveforms harder to evaluate for accurate arrival times. As a result, it is necessary to consider the factors that influence measured waveforms, which will be discussed in the next section.

3.3 Factors that affect measured UHF waveforms

3.3.1 Shape of a PD current pulse

The rise time (t_r) of the PD current pulse is important because it is responsible for radiating the leading edge of the UHF waveform, which must be timed accurately [85] when it is received some distance away, in order that the PD can be located. PD current rise time is governed by the physical mechanism that ignites the PD. In studies described in [86], it was observed that the rise times of the PD current pulses generated in different gaseous dielectrics are different, as shown in Figure 3.5.

A PD source can be located with high spatial resolution only if time differences between detected UHF signals arriving at various sensors can be measured accurately enough. However, these arrival time measurements are not as straightforward as might at first be expected. In the following consideration of an idealised PD current pulse, specifying a reference point on any of the detected waveforms involved is a challenge that always limits the accuracy which can be obtained. These can be presented using the following explanations.

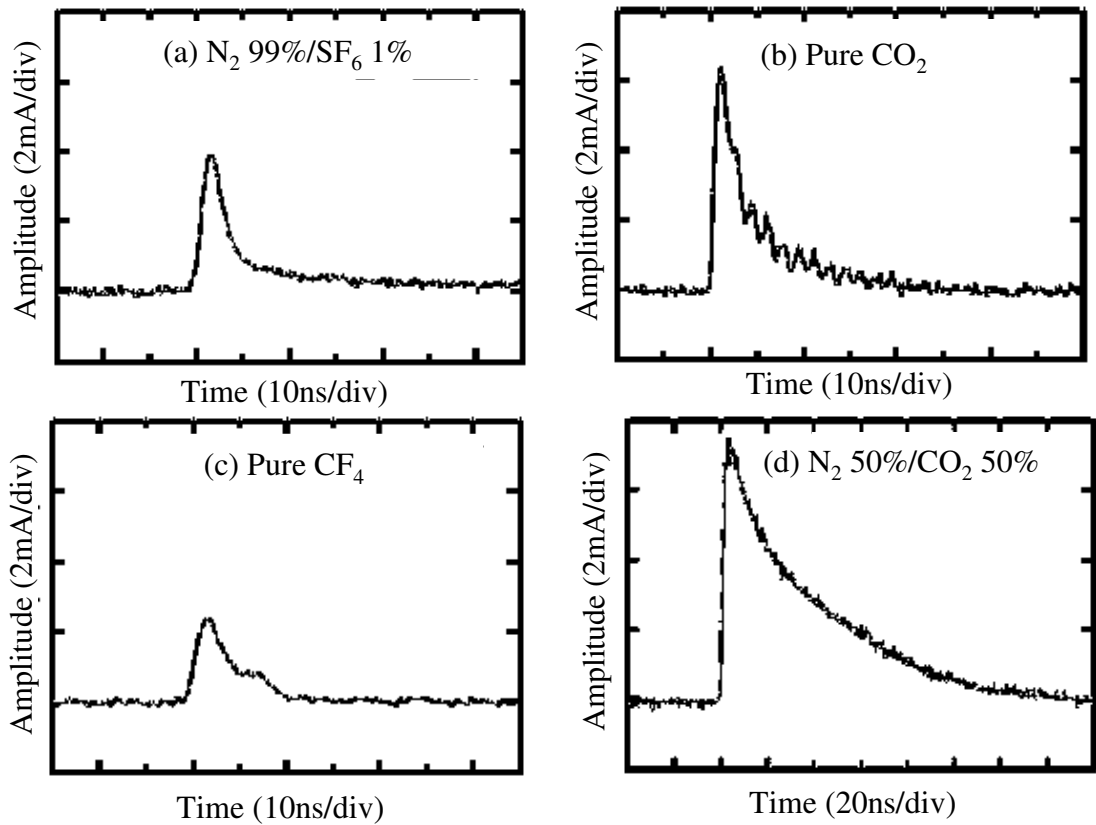


Figure 3.5 Positive PD current pulses at 0.1 MPa for four gasses [86].

An idealised PD current pulse might be represented using a Gaussian function, such as the one with $\sigma = 1.0$ shown in Figure 3.6. The rise time of this waveform is $4.5 - 2.9 = 1.6$ ns. Since the radiated electric field is proportional to the rate of change of current pulse [87] the radiated wavefront will be proportional to time derivative of the current pulse, which is depicted in Figure 3.7.

Essentially, there is no clear point on either waveform that could be said to be the beginning of the pulse. If this is the situation at the PD location, the problem is compounded when the signal has travelled by different paths to different sensors. In any practical measurement, in which noise will be present, the challenge will be to get as close to the true arrival time as possible subject to the limits of the background noise. Furthermore, a PD current pulse itself has a finite, variable pulse width, which can influence its radiated electric field and in turn affects arrival time measurements. Figure 3.8 illustrates the influence of pulse width variation. The longer pulse will

tend to radiate an electric field with a more ambiguous onset time (B) than the shorter pulse (A).

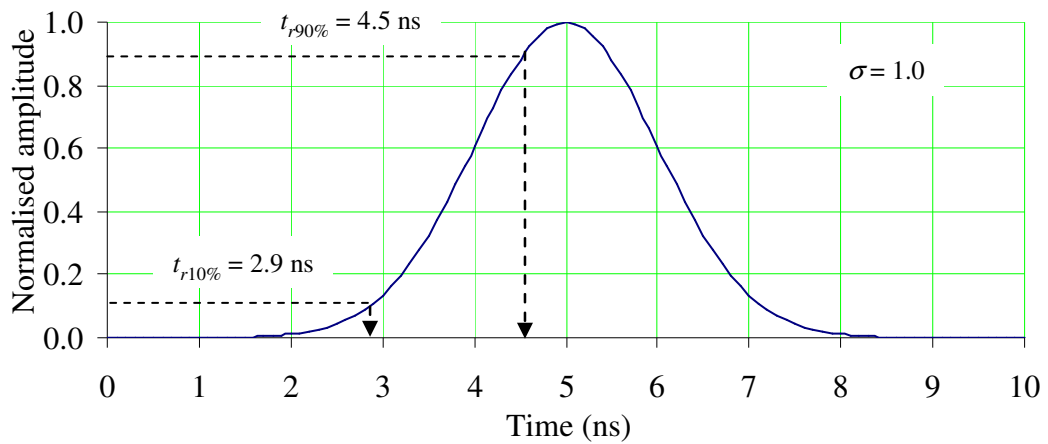


Figure 3.6 Idealised PD current pulse represented using a Gaussian function with $\sigma = 1.0$ and its rise time (10% - 90%) = 1.6 ns.

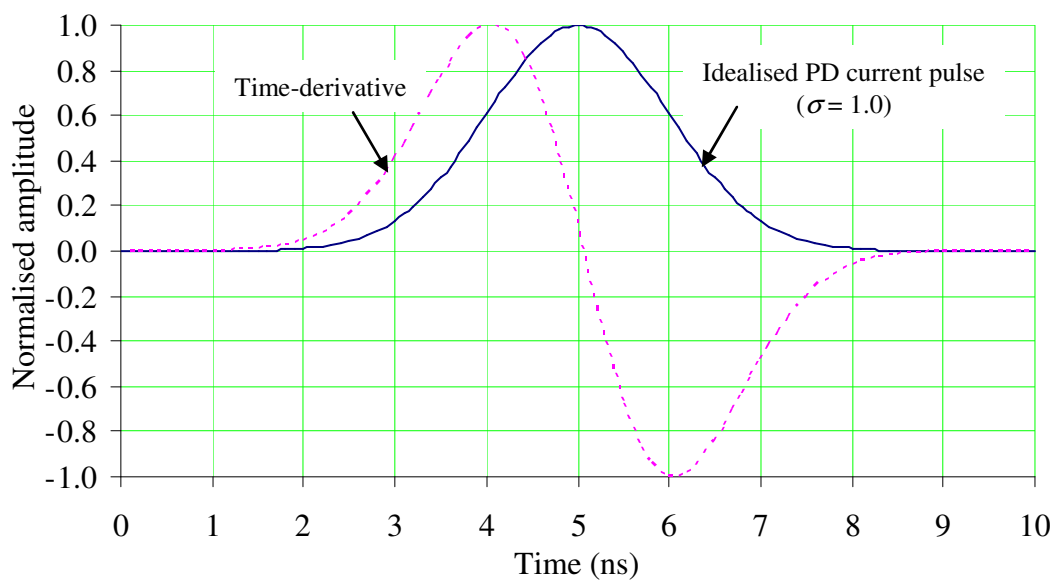


Figure 3.7 Plot of the idealised PD pulse ($\sigma = 1.0$) and its time-derivative proportional to radiated electric field of the PD current pulse.

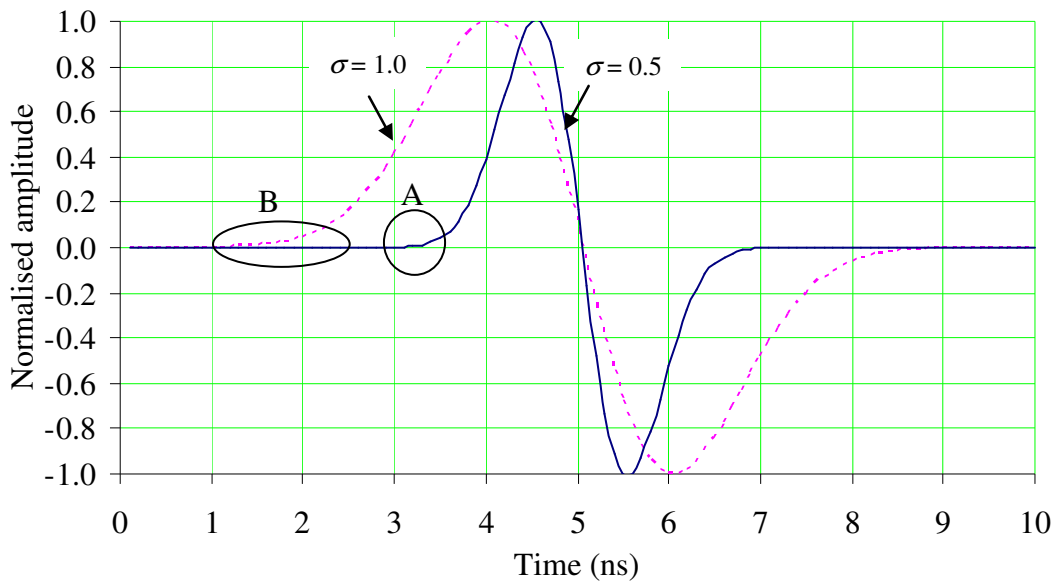


Figure 3.8 Time-derivative waveforms obtained for two Gaussian PD current pulses ($\sigma = 0.5$ and 1.0). This is to illustrate the potential difference of arrival times for fast (A) and slow (B) rise times.

3.3.2 Internal propagation path

A measured UHF waveform is influenced by different properties of materials inside a tank and multiple reflections as it travels around the tank [49], introducing complexity to the waveform. This tends to disperse the initial wavefront of the measured waveform. It is complicated to identify the actual internal propagation path between the PD origin and the sensor using the geometrical calculations. However, to locate the PD source, it is possible to use an indirect means, which considers the minimum time delay paths to each UHF signals, which can be computed using numerical techniques [88].

3.3.3 Response of UHF sensor and its installation method

Different types of UHF sensors provide different output characteristics because of their structures, causing variation in measured PD waveforms even when all other factors remain the same. Prior research has indicated that the sensitivity of the UHF

sensor is an important factor in the transmission of PD energy [89], and different designs of UHF sensors offer different sensitivity. Moreover, other research has shown that designs of UHF sensors and installation methods affect both sensitivity and resultant waveforms [47]. In this research work, further comparisons between three specific UHF sensor designs are given in Section 5.2.

3.3.4 Measurement bandwidth

System bandwidth plays an important role for the rise time (t_r) of measured waveforms, since an approximate relationship for t_r of a measurement system with a first-order bandwidth of B Hz is $t_r = 0.35/B$ [90]. For instance, if the signal was captured by an oscilloscope with a bandwidth of 500 MHz, the minimum observed rise time of the sensor signal output would be 0.7 ns, which corresponds to 14 cm of signal propagation in the bulk oil of a power transformer.

3.4 Existing techniques for determining arrival times

Existing techniques used for determining arrival times of UHF signals compute the arrival times through time domain analysis and can be implemented using automated systems either partially or completely. These techniques are summarised as follows:

3.4.1 Expanding time scale and identifying the arrival time manually

To determine arrival times, an engineer looks at the signals on an oscilloscope and judges where they start. The time scale is usually expanded in the vicinity of the arrival so that sub-nanosecond resolution can be achieved. Previous research has indicated that choosing arrival times in this way can be effective [91, 92]. However, arrival times found by this technique are potentially subjective and are not governed by consistent rules. This technique is also impractical when massive numbers of signals need to be evaluated due to the long period of time (several days or weeks) that a PD monitoring system may be installed at the site. Therefore, this approach is time consuming and human errors may occur.

A UHF signal (sampled at 5×10^9 samples/sec over 100 ns from PD testing of an HVDC reactor [73]) shown in Figure 3.9 is used to demonstrate this technique. Figure 3.10 illustrates the problem of subjective arrival time when judged by eye with sub-nanosecond resolution. The arrival time might be any point in the encircled region.

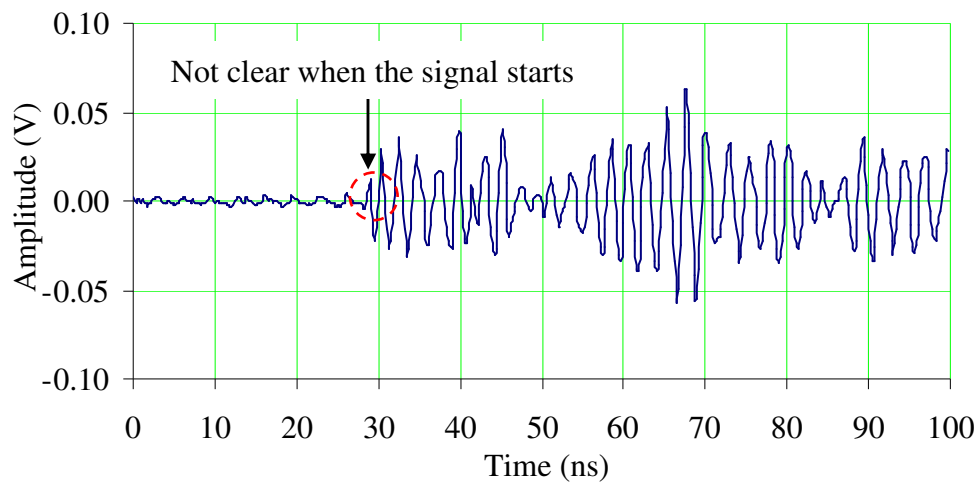


Figure 3.9 UHF voltage signal illustrating an unclear arrival time.

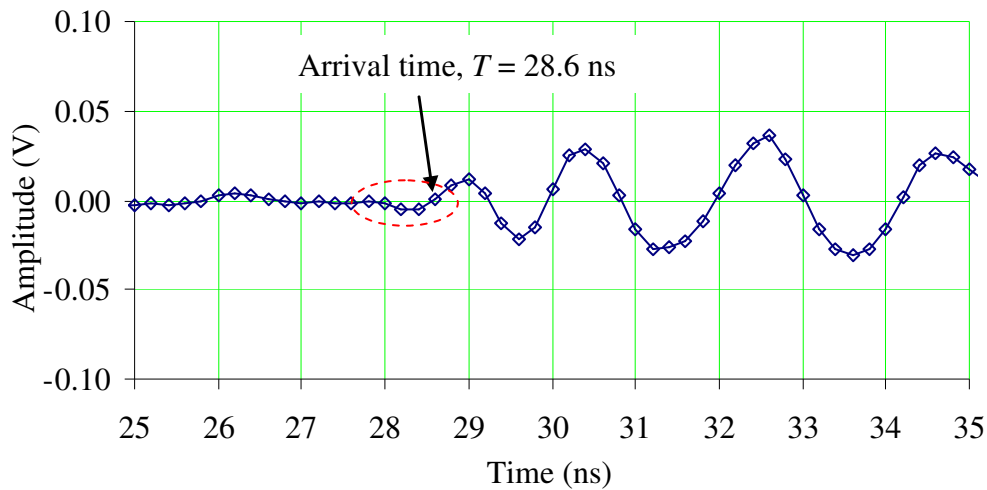


Figure 3.10 Expanded view of the signal shown in Figure 3.9 to illustrate the arrival time obtained from manually expanding sub-nanosecond time scale.

3.4.2 Threshold crossing method

By squaring the UHF signal voltage to obtain a waveform proportional to instantaneous signal power, a clearer difference between the level of the PD signal and of the background noise might be expected. Hence, the initial wavefront or start of that signal may become clearer [93]. After squaring the UHF signal in Figure 3.9, the clarity of the starting point of the squared UHF signal is improved, as illustrated in Figure 3.11.

Therefore, it is possible to apply a certain threshold (TH) relative to the highest peak of the UHF voltage squared to determine the arrival time (e.g. 2% threshold). The arrival time is defined as the time when the squared voltage first crosses the threshold. With discrete sampled data, the arrival time is taken to be the final sample point where the amplitude of the squared voltage is still less than or equal to the threshold. This is illustrated in Figure 3.12, which uses a 2-ns section of Figure 3.11 to determine the arrival time.

Using the squared data also simplifies the process because the threshold is applied to unipolar data. It is also capable of being applied by an automated system to determine arrival times. This technique has been employed in the field using signals both from UHF [94] and acoustic PD detection [95].

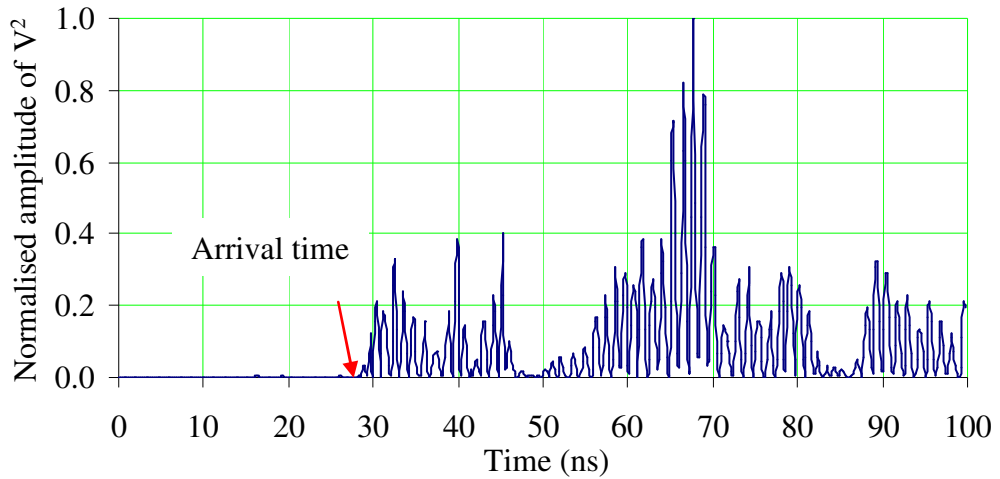


Figure 3.11 Normalised squared UHF voltage of the signal in Figure 3.9. This is to exhibit improved visibility of the arrival time using the squared waveform.

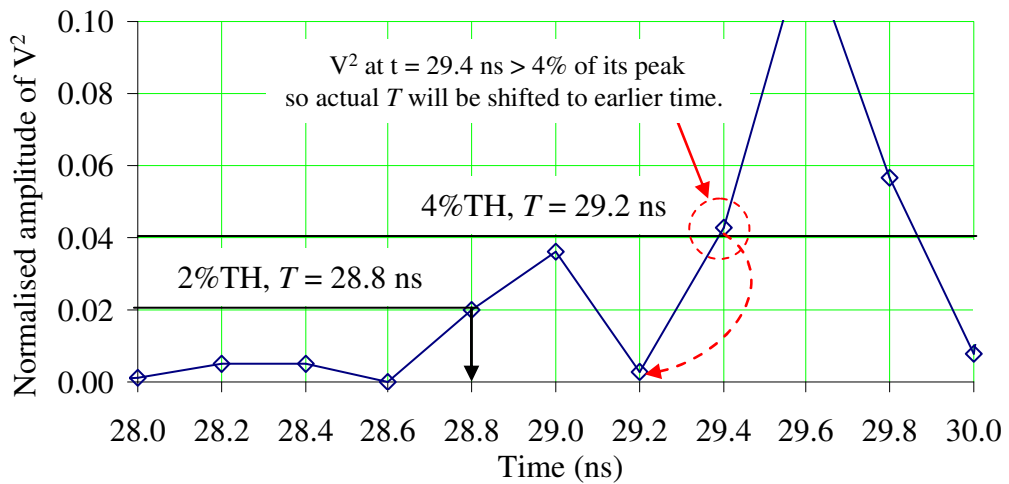


Figure 3.12 Illustration of two thresholds used for determining arrival times for the UHF signal of Figure 3.9. This is to show the squared sample points every 0.2 ns (5×10^9 samples/sec) in order to demonstrate how the arrival time is determined.

A key challenge for this method is the selection of a particular threshold percentage, which is dependent on signal characteristics that vary considerably in their amplitude, shape and background noise levels. As a result, an approach that takes into account both contents of PD signal and noise needs to establish, such as the trigger level method described in [96], which first determines the noise power from a signal sample without a PD pulse. However, this may not always be practical because noise levels can vary dependent on behaviour and environment of the system being monitored.

3.4.3 Knee point of cumulative energy curve

Cumulative energy of a sampled UHF signal can be defined as follows:

$$e_i = e_{i-1} + \frac{\Delta t}{R} \cdot V_i^2 \quad (3.2)$$

- Where
- i = range variable, $1 \dots N - 1$, if there are N samples of the UHF voltage waveform
 - V_i = sampled voltage waveform at i -th sample (volt)
 - Δt = 1/sampling rate (sec)
 - R = input impedance of the measurement system (50Ω)
 - e_i = the energy accumulated up to the i -th sample (Joules)
 - e_0 = 0 Joules (the initial energy level)

It is expected that when a UHF PD signal arrives at the sensor, its cumulative energy at that specific time should rise steeply enough to separate the onset of PD signal from the background noise [71]. The so-called ‘knee point’ indicates the time at which the background noise gives way to the PD signal. This is illustrated in Figure 3.13, again using the signal from Figure 3.9. The arrival time might be any point in the encircled region. Identifying the accurate arrival time from the knee area is not always straightforward and it is dependent on operators’ experiences and skills. Therefore, arrival times obtained from this technique are subjective, similar to the

arrival times obtained from the expanding time scale and identifying the arrival time manually outlined in Section 3.4.1.

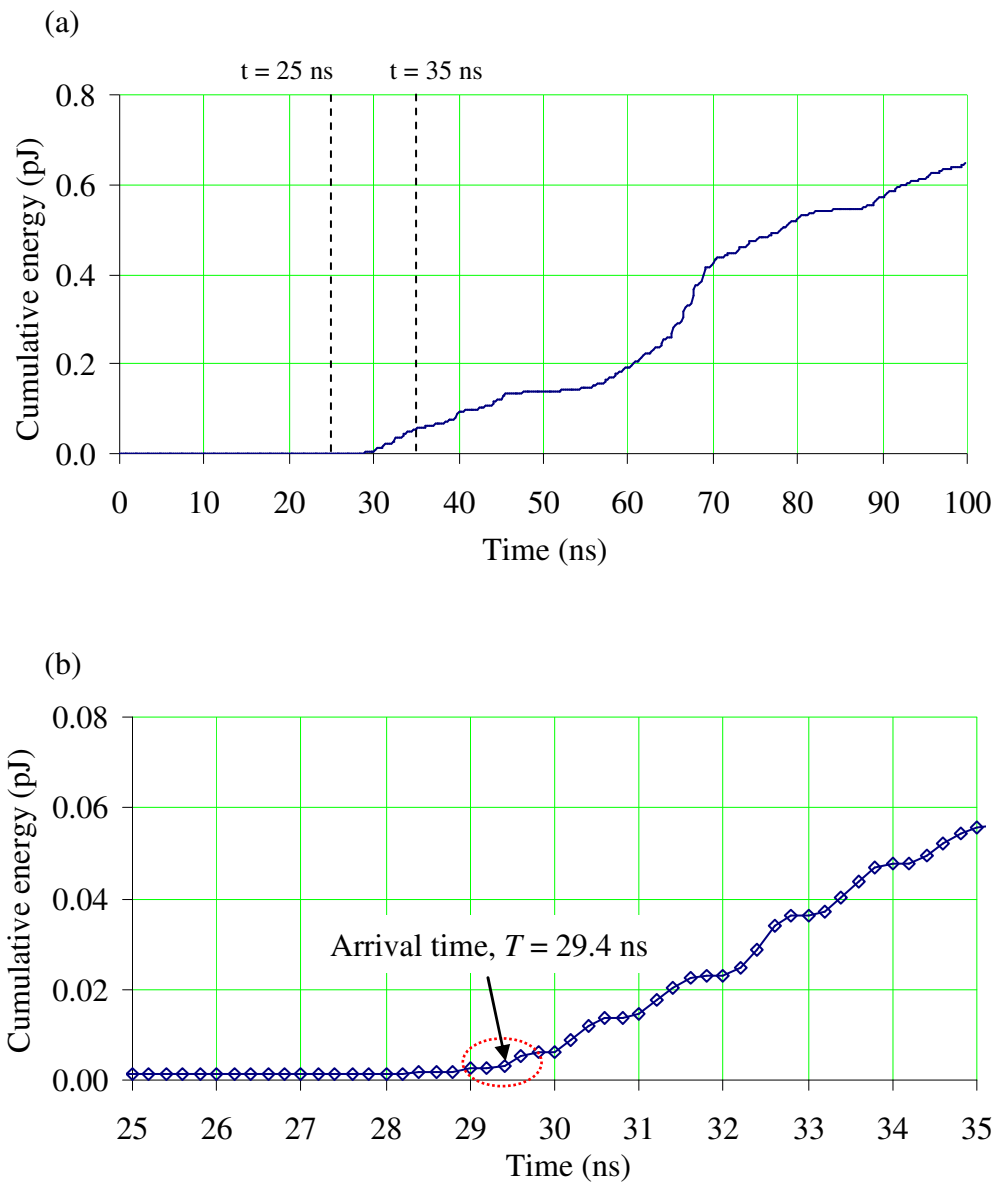


Figure 3.13 Cumulative energy curve analysis for the signal shown in Figure 3.9: (a) Cumulative energy curve, (b) Expanded view that shows knee area containing the arrival time.

The cumulative energy curve for determining arrival times has been used in both UHF [49] and acoustic applications [97]. Moreover, the research in [97] has suggested that time to 2% of maximum cumulative energy is considered as time of arrival. This shows that there is a similarity in principle between the threshold crossing of UHF voltage squared and the knee point of cumulative energy curve.

3.4.4 Energy criterion method

The energy criterion method [98] determines the arrival times by Eqn. 3.3 defined as follows:

$$S'_i = S_i - i \cdot \frac{S_N}{\alpha \cdot N} \quad (3.3)$$

Where i = range variable, $0 \dots N-1$, if there are N samples of the UHF voltage waveform

$$S_i = V_i^2$$

$$S_N = \sum_{i=0}^{N-1} S_i$$

S'_i = partial energy accumulated up to the i -th sample

α = a constant selected to suit the signal characteristics

Arrival times can be calculated from the index i that corresponds to the global minimum S'_i , as illustrated in Figure 3.14 using the signal from Figure 3.9.

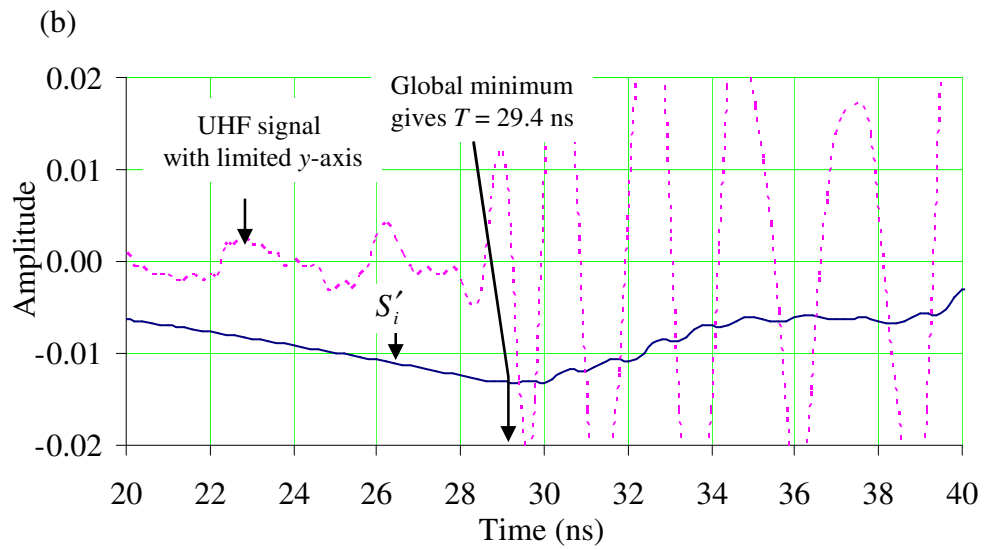
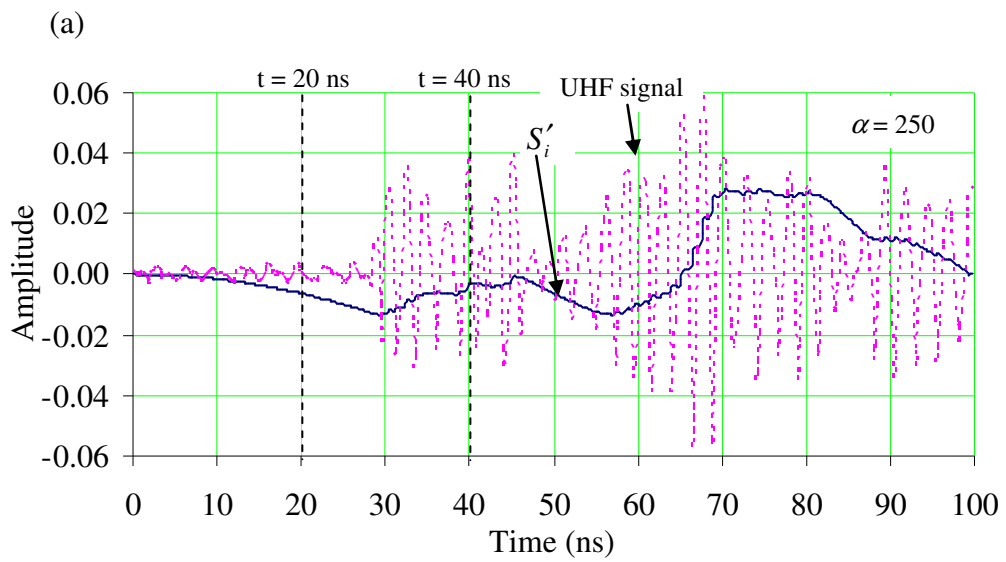


Figure 3.14 UHF waveform and its partial energy S'_i curve: (a) S'_i obtained using $\alpha = 250$, (b) Expanded view of (a) to determine the arrival time using the global minimum of S'_i curve.

However, choosing the factor α influences the shape of the partial energy S'_i curve significantly. Figure 3.15 illustrates the partial energy S'_i curve generated using $\alpha = 100$, again using the signal from Figure 3.9. This shows that the arrival time cannot be determined using the global minimum of S'_i curve when the value of α is changed. Therefore, it is necessary to select α to suit the specific signals being analysed.

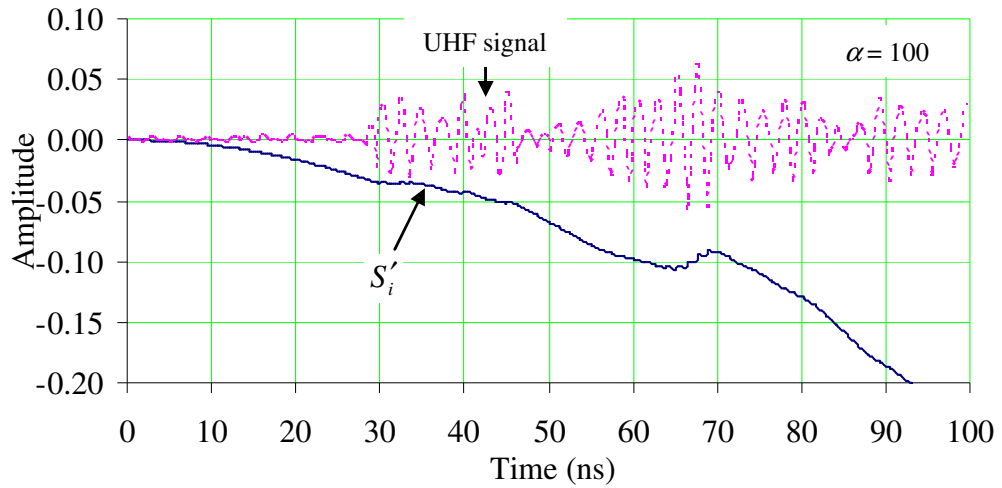


Figure 3.15 UHF waveform and its partial energy S'_i curve generated using $\alpha = 100$. This is to illustrate that the S'_i curve cannot provide the global minimum for determining the arrival time. This is to show that the value of α influences the shape of S'_i .

This technique has been implemented in some PD applications [96, 99]. In fact, the energy criterion is very similar to the knee point of the cumulative energy curve, but with the additional negative term that appears in Eqn. 3.3.

3.5 A new technique: Relative increase in energy

The 2% threshold crossing and cumulative energy methods have been accepted as useful techniques that can provide the location of PD to within a reasonable tolerance. Both of these methods depend on squaring the instantaneous UHF voltage samples. Building on this common concept, relative increase in energy will now be proposed for determining the arrival times of UHF PD signals. This method uses the relative increase in energy between successive points on the sampled waveform and is formulated using two equations. Note that the first equation of this method is Eqn. 3.2 for cumulative energy, which is now extended using Eqn. 3.4:

$$R_{iEj} = \left(\frac{e_j}{e_{j-1}} - 1 \right) \quad (3.4)$$

Where j = integer range variable, $k \dots N-1$, where N is the number of voltage samples
 k = a positive integer index that avoids the initial part of the data where very small values of e_{j-1} can lead to large numerical values that are not of interest. Typically, $k \sim 0.1 \times N$
 R_{iEj} = relative increase in energy at the j -th sample point

The relative increase in energy was first discovered using a signal obtained from the laboratory experiment described in Section 2.4. An illustration of the R_{iEj} curve is remarkable because it has a very distinct peak at the leading edge of the UHF signal, as is apparent in Figure 3.16.

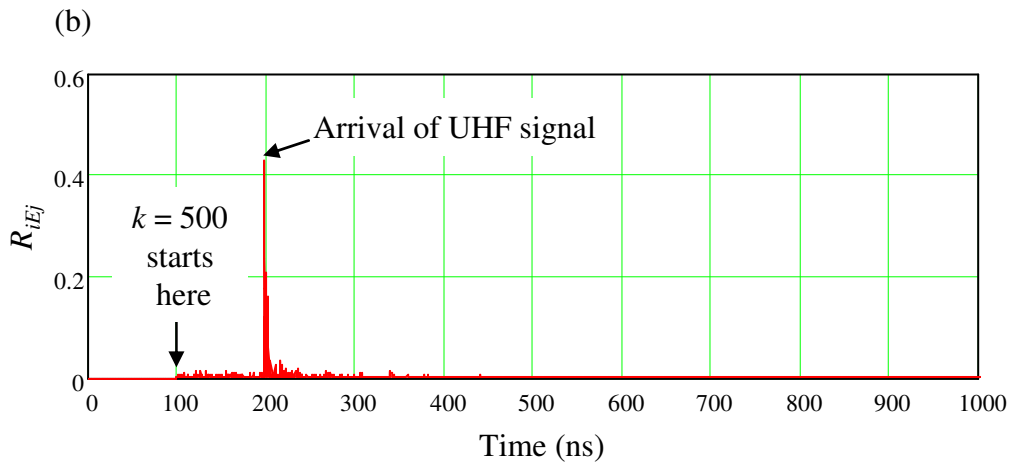
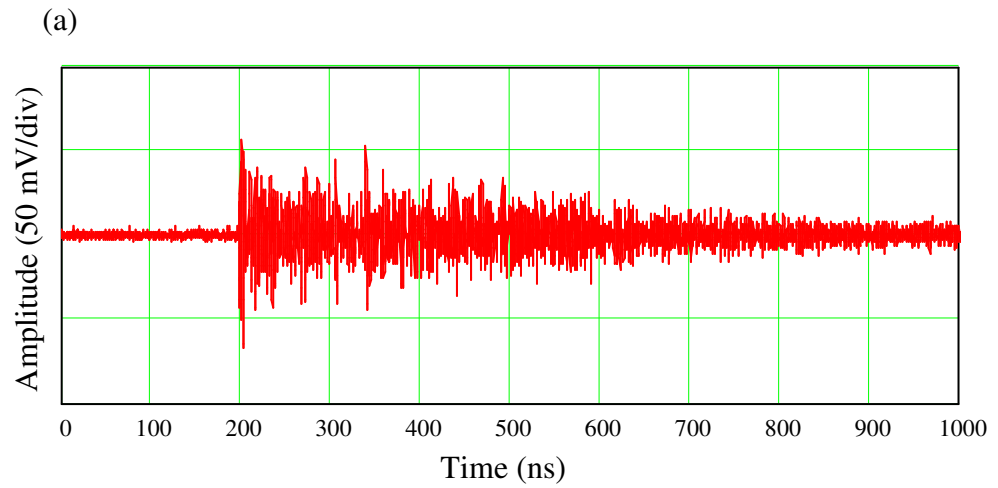


Figure 3.16 The UHF waveform and its R_{iEj} curve: (a) The UHF signal obtained from the laboratory, (b) R_{iEj} curve for this signal.

Considering the R_{iEj} only is not sufficient to identify the arrival time. On closer examination, it was evident that the largest peak did not exactly match the arrival time, which tended to be a bit earlier. However, identifying the time interval containing the arrival time of the UHF signal proves straightforward using R_{iEj} . The arrival time is estimated as corresponding to the first significant peak within R_{iEj} . Furthermore, the largest peak of R_{iEj} sets an upper boundary on the arrival time.

To illustrate the onset of the signal, a combined plot of R_{iEj} and its cumulative energy curve is shown in Figure 3.17. It is clear that the significant peak of R_{iEj} is close to the actual arrival time.

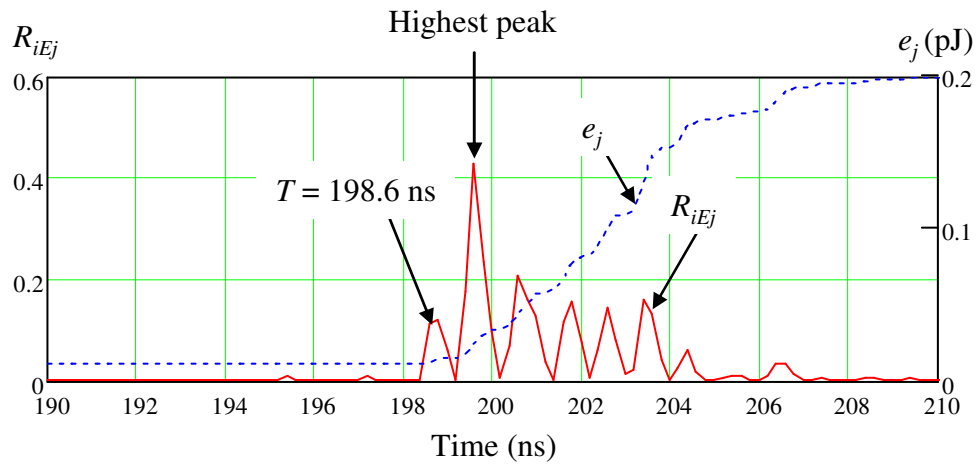


Figure 3.17 Combined plot of R_{iEj} (solid line) and e_i (dotted line) to identify the arrival time.

It is unfortunate that the biggest peak does not exactly coincide with the arrival time; this is why the first significant peak is used. Since choosing the first significant peak is potentially subjective and requires engineering judgement, the method is not immediately suitable for automation. However, a procedure can be formalised by selecting a subset of the data within a specific window prior to and including the highest peak and then applying a threshold crossing method with threshold level being defined as a percentage of the highest peak [100]. From this concept, a flowchart for determining arrival times automatically can be created, as shown in Figure 3.18.

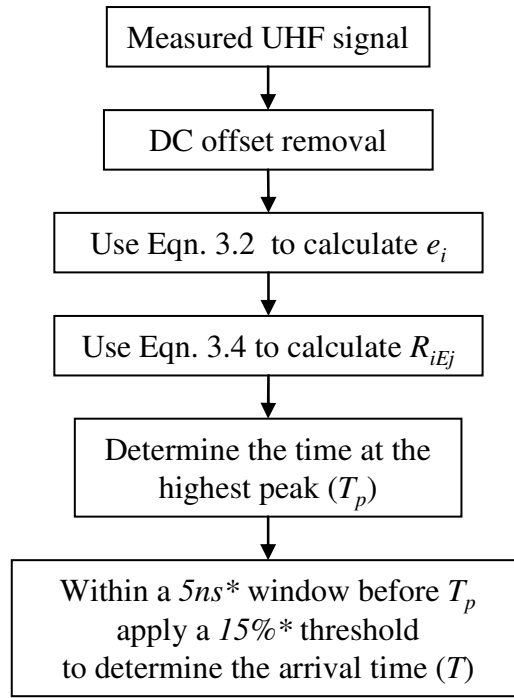


Figure 3.18 Flowchart to determine the arrival time automatically using the relative increase in energy. Note that two parameters indicated by * (the window time and the threshold with respect to the highest peak of R_{iEj}) need to be adjusted to suit PD signals characteristics. The values shown here are only representative for the purpose of understanding the process. Further analysis will be presented in Section 6.3.

3.6 Results and analysis

3.6.1 Pulse injection tests

To evaluate performance of the relative increase in energy method, data from pulse injection tests on a 252 MVA power transformer ($5.9 \times 2.7 \times 4.0$ m), representing single known-position PD sources, were analysed. The pulse injection test arrangement consisted of four UHF sensors (S1, S2, S3 and S4) mounted on the transformer, a commercial pulse generator and a digital oscilloscope with a sampling rate of 5×10^9 samples/sec. A model of the transformer showing positions of the sensors is illustrated in Figure 3.19 (transformer tank is not shown for clarity).

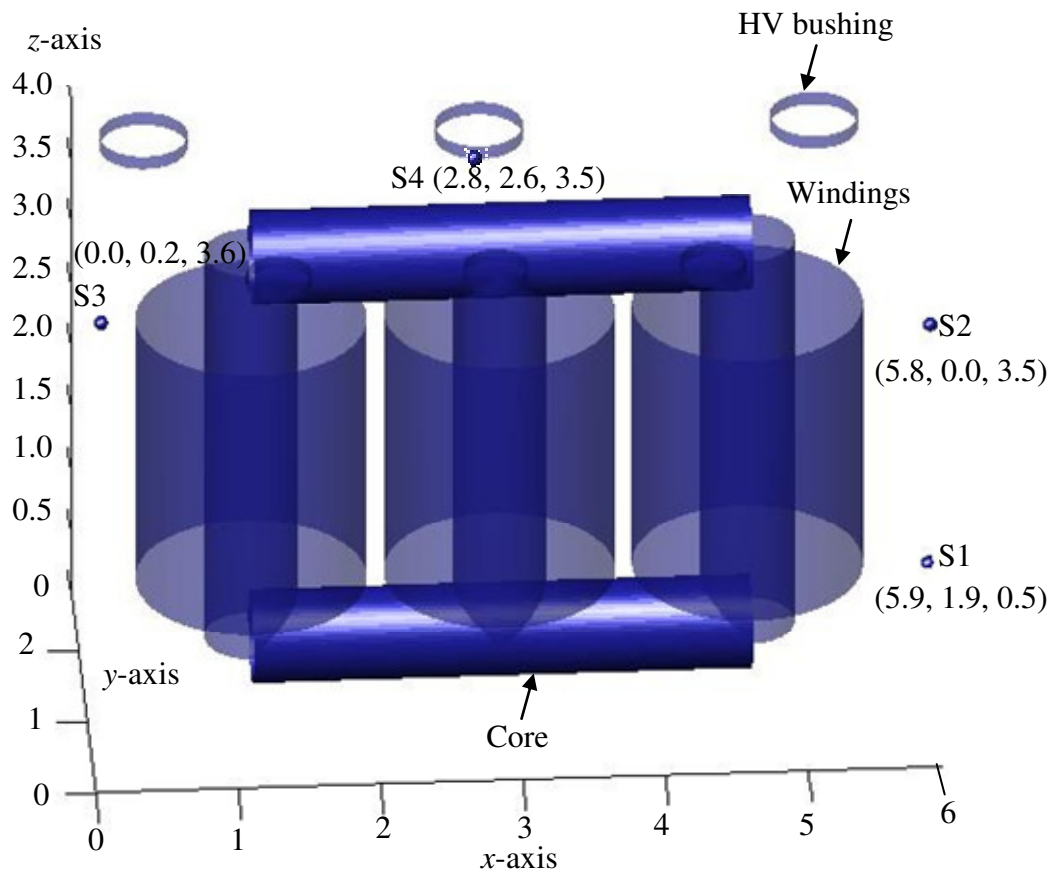


Figure 3.19 Model of the 252 MVA power transformer shows coordinates (x, y, z) of the UHF sensors (S1 – S4) in metres.

During each test, a pulse was injected into one sensor while the other three were used to capture radiated signals. For instance, if the pulse was injected at S4, then S1, S2 and S3 were used to capture the signals. Thus, three arrival times, T_1 , T_2 and T_3 could be obtained for S1, S2 and S3, respectively. In total, four injection positions were investigated, producing 12 UHF signals to analyse. Figure 3.20 illustrates UHF waveforms when a 100 V impulse was injected into S4.

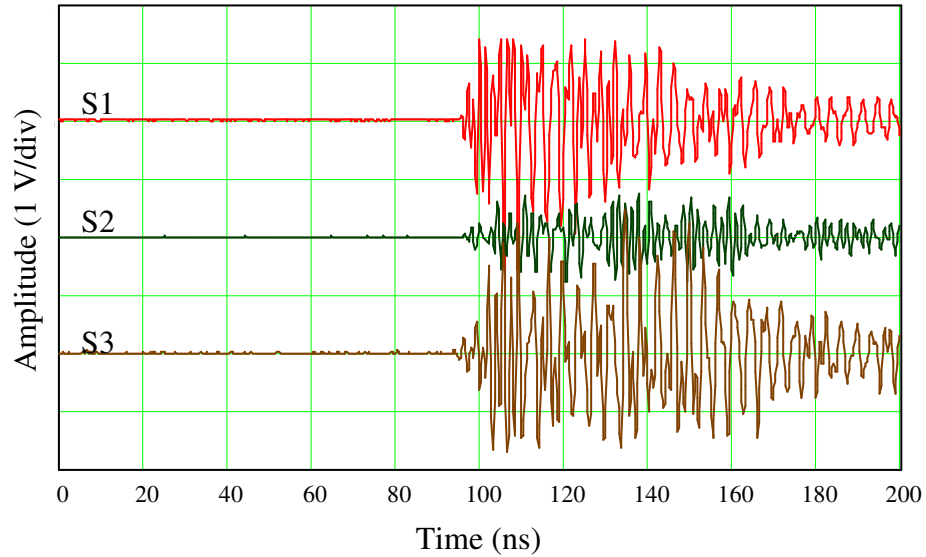


Figure 3.20 UHF signals obtained when a 100 V impulse was injected at S4.

3.6.2 Reference time differences

To establish the expected time differences for this arrangement (to be used as references), they were calculated using the known positions of the sensors and the numerical method described in [49]. This method takes into account the main internal components of the power transformer (e.g. winding, cores, yokes), and material properties to determine the minimum delay path for the signal travelling inside the tank. Using proprietary software that incorporates this model, reference time differences were determined and these are summarised in Table 3.1. An example of three internal propagation paths for pulse injection at S4 can be seen in Figure 3.21.

Table 3.1 Reference time differences when the pulse is injected at each of the four sensors.

Pulse injected at	Reference time differences (ΔT_{ref}) (ns)		
S4	$\Delta T_{12} = 1.5$	$\Delta T_{23} = 1.7$	$\Delta T_{31} = -3.2$
S3	$\Delta T_{12} = 7.3$	$\Delta T_{24} = 10.3$	$\Delta T_{41} = -17.6$
S2	$\Delta T_{13} = -11.3$	$\Delta T_{34} = 8.6$	$\Delta T_{41} = 2.7$
S1	$\Delta T_{23} = -18.6$	$\Delta T_{34} = 14.4$	$\Delta T_{42} = 4.2$

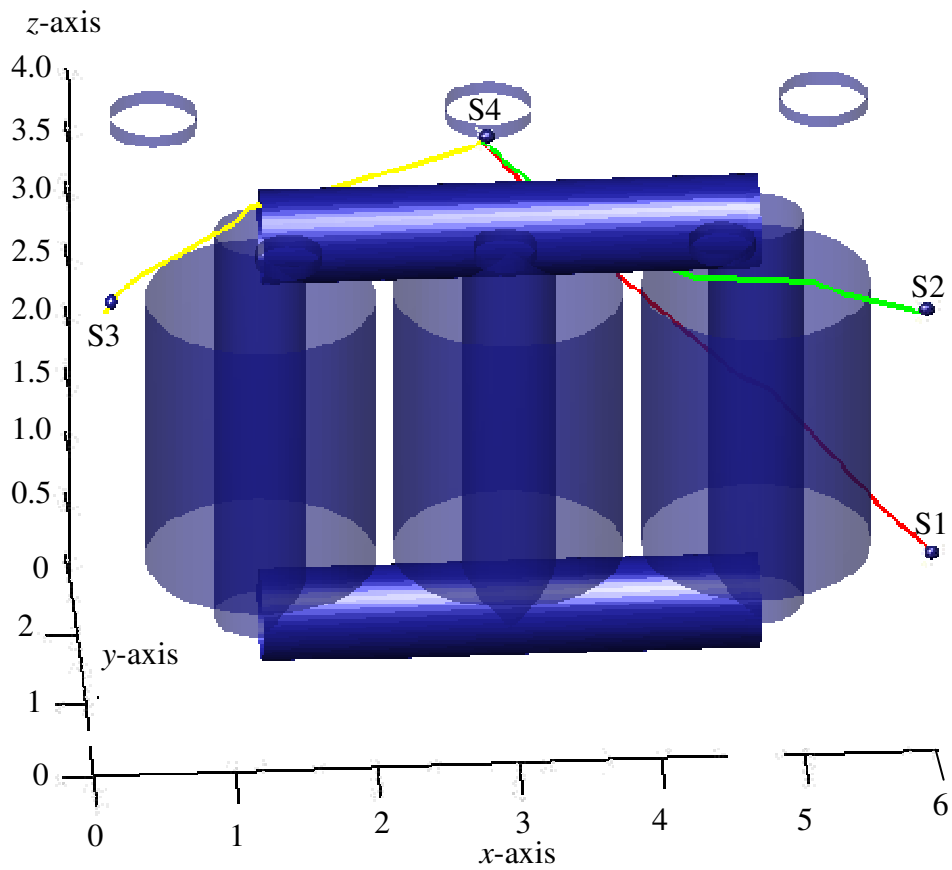


Figure 3.21 Internal propagation paths when the pulse was injected at S4.

3.6.3 Time differences obtained from the 2% threshold

Since arrival times obtained from the 2% threshold crossing (2%TH) of instantaneous squared voltage has been used for practical applications, time differences obtained from 2%TH were compared with the references as well. Table 3.2 summarises time differences obtained from 2%TH.

Table 3.2 Time differences obtained from 2%TH when the pulse is injected at each of the four sensors.

Pulse injected at	Time differences ($\Delta T_{2\%TH}$) (ns)		
S4	$\Delta T_{12} = -1.0$	$\Delta T_{23} = -1.0$	$\Delta T_{31} = 2.0$
S3	$\Delta T_{12} = 16.8$	$\Delta T_{24} = 7.2$	$\Delta T_{41} = -24.0$
S2	$\Delta T_{13} = -11.2$	$\Delta T_{34} = 6.2$	$\Delta T_{41} = 5.0$
S1	$\Delta T_{23} = -27.2$	$\Delta T_{34} = 24.8$	$\Delta T_{42} = 2.4$

3.6.4 Time differences obtained from the relative increase in energy

Firstly, the arrival times were determined from combined plots of R_{iEj} and cumulative energy curves. This is demonstrated using the signals presented in Figure 3.20, whose arrival times are shown in Figure 3.22. On the basis of arrival times, such as ones shown in Figure 3.22, time differences between sensors (ΔT_{12} , ΔT_{23} and ΔT_{31} , for example) can be calculated and are summarised in Table 3.3.

Table 3.3 Time differences obtained from R_{iEj} when the pulse is injected at each of the four sensors.

Pulse injected at	Time differences ΔT_{RiEj} (ns)		
S4	$\Delta T_{12} = 0.4$	$\Delta T_{23} = 1.4$	$\Delta T_{31} = -1.8$
S3	$\Delta T_{12} = 6.2$	$\Delta T_{24} = 10.8$	$\Delta T_{41} = -17.0$
S2	$\Delta T_{13} = -9.2$	$\Delta T_{34} = 7.2$	$\Delta T_{41} = 2.0$
S1	$\Delta T_{23} = -19.6$	$\Delta T_{34} = 14.8$	$\Delta T_{42} = 4.8$

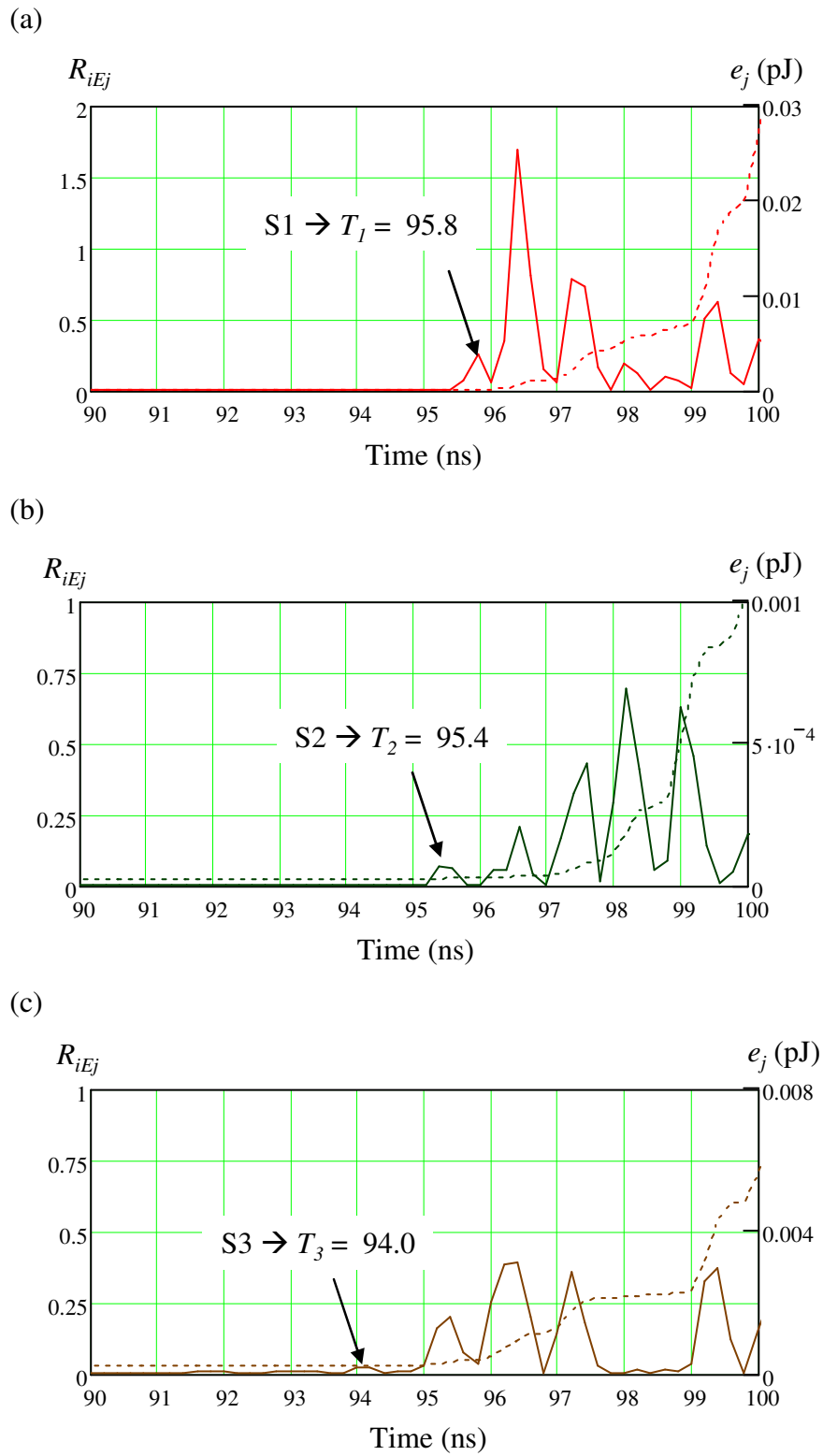


Figure 3.22 Arrival times obtained from R_{iEj} for the UHF signals of Figure 3.20 (solid lines are R_{iEj} and dotted lines are cumulative energy curves): (a) Arrival time of S1, (b) Arrival time of S2, (c) Arrival time of S3.

3.6.5 Evaluation of relative increase in energy

The overall comparison of results is made in Figure 3.23, which shows that almost all values of mean error obtained from the relative increase in energy technique are less than ones obtained from the 2% threshold crossing method [101]. The average value of mean error from the relative increase in energy is significantly less than for the threshold method, being 0.93 ns and 4.58 ns, respectively. Based on a propagation velocity of 2×10^8 m/s for UHF signals in transformer oil, these relate to a mean error of distance for PD location of 0.19 m and 0.92 m, for the relative increase in energy and threshold crossing methods, respectively.

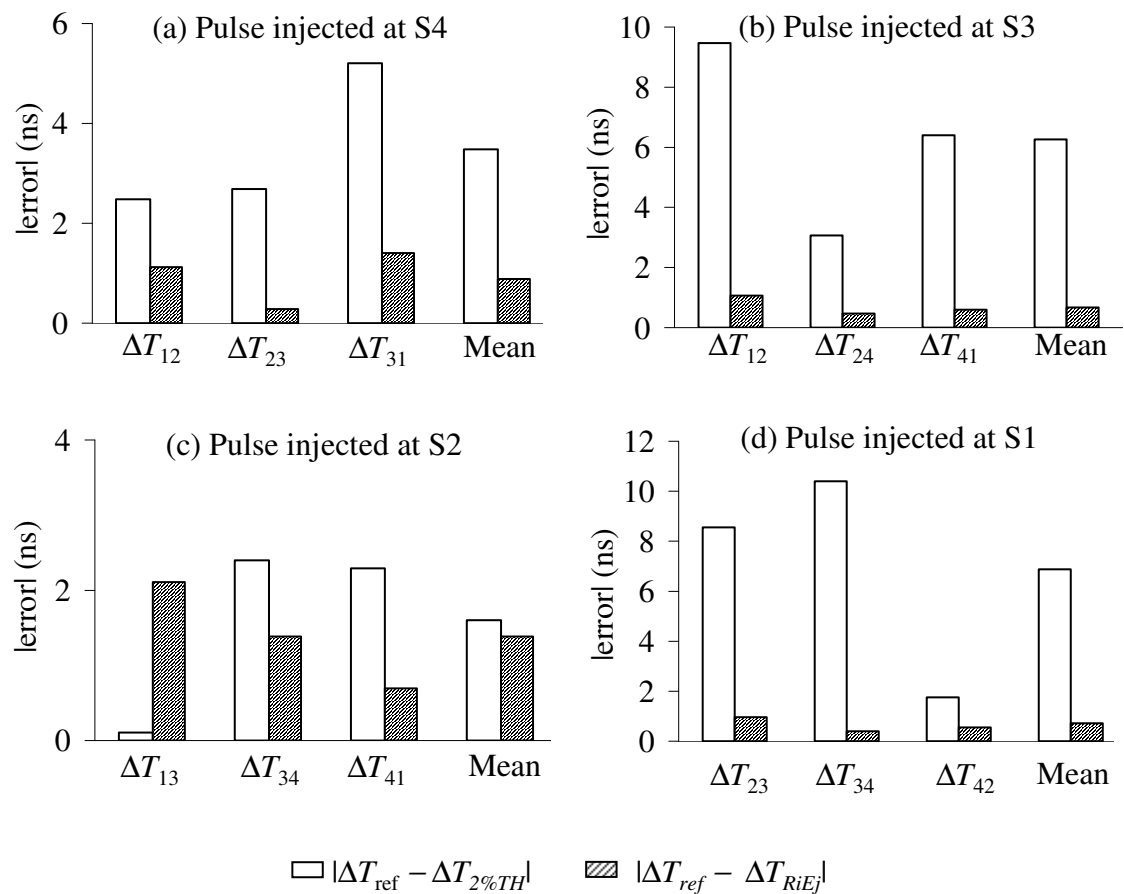


Figure 3.23 Error comparisons between $|\Delta T_{ref} - \Delta T_{2\%TH}|$ and $|\Delta T_{ref} - \Delta T_{RiEj}|$.

3.7 Discussion and conclusions

In this chapter, the importance of arrival times – the key to locate the PD origin – was explained in conjunction with the main factors that affect measured PD waveforms. Four existing techniques for estimating arrival times were introduced, namely (1) expanding time scale and selecting arrival times manually; (2) the threshold crossing of squared voltage; (3) the knee point of cumulative energy curves and (4) the energy criterion. Two of them, the threshold crossing and the energy criterion methods, can be implemented practically by means of automated algorithms. Nevertheless, both techniques require the adjustments of particular constant values, which can introduce some degree of subjectivity to arrival times.

Therefore, the relative increase in energy method has been proposed and its ability for determining arrival times assessed successfully using pulse injection tests on a power transformer. The error comparisons of time differences against expected time differences obtained from proprietary software that takes into account main components of the transformer were calculated. Results show that the error of time differences obtained from the relative increase in energy is 0.93 ns while that of the 2% threshold method (the practical method) is 4.58 ns in this study. This is about five times error reduction compared with the practical method.

Although these promising results for the relative increase in energy were based on a single transformer test, it might be suitable for developing into an alternative option for determining arrival times accurately that can be implemented using an automated system. More practical studies are still required in order to validate this technique against other methods.

Another advantage of the relative increase in energy is that it could be used for time-shifting of signals that have different triggering positions into alignment by aligning the highest peaks of R_{IEj} . Once those signals are aligned, the envelope comparison method can be applied in order to distinguish between different PD sources. Further analysis will be presented in Section 6.3.

4. Investigating the use of Wavelet techniques for improving UHF time of flight measurements

4.1 Introduction

This chapter begins with an overview of wavelet techniques and outlines some of their applications in the field of PD diagnosis. Then, wavelet de-noising, a well-known wavelet technique, will be used to determine arrival times of UHF signals containing various artificial noise levels. This is to investigate the effects of applying wavelet de-noising to the arrival times of UHF signals caused by the modification of de-noised waveforms. The alternative approach of wavelet decomposition will be trialled to determine the arrival times of UHF signals as well. Based on individual signal characteristics of the decomposed signals, more accurate arrival times of UHF signals might be obtained. Both wavelet techniques presented here may offer improvements of UHF time of flight measurements and in turn enhance the accuracy of UHF PD location.

4.2 Overview of wavelet techniques

4.2.1 Introduction

All kinds of signals are normally captured as signal amplitude versus time. In order to analyse these signals, the simplest method is to examine them directly in the time domain, for example, the minimum and maximum amplitudes can be found for the signal itself. However, investigating signals in the amplitude-time domain is not always optimal so many mathematical analysis techniques have been invented in order to facilitate the representation, analysis and interpretation of signals.

Fourier analysis, for example, has long been used for transforming signals from the amplitude-time domain to the amplitude-frequency domain. It can illustrate signals in the amplitude-frequency domain based on a key assumption [102], that the signals are stationary signals, having no change in waveform appearance, such as a constant frequency sinusoidal waveform. This is the critical drawback of Fourier analysis because the majority of signals in real applications involve transient signals, which are non-stationary or time-varying signals. In addition, Fourier analysis lacks a direct link between peaks in the signal spectrum and the times at which they occur.

Therefore, an improved version of Fourier analysis, called the Short-Time Fourier transform, was developed in an effort to address this limitation by using a time windowing technique, in which the signal is mapped to a 2-dimensional function of time and frequency while the signal amplitude is represented in terms of an intensity pattern called a spectrogram [103]. Spectrogram analysis has been used in many applications including electrical problems; for example, multiple PD sources can be distinguished using unique spectrogram patterns of each PD source [82, 104]. To observe this representation, a UHF signal, depicted in Figure 4.1, which was captured during an HVDC reactor PD testing using an oscilloscope with a sampling rate of 5×10^9 samples/sec [73], was used to generate the spectrograms as given by the two examples shown in Figure 4.2.

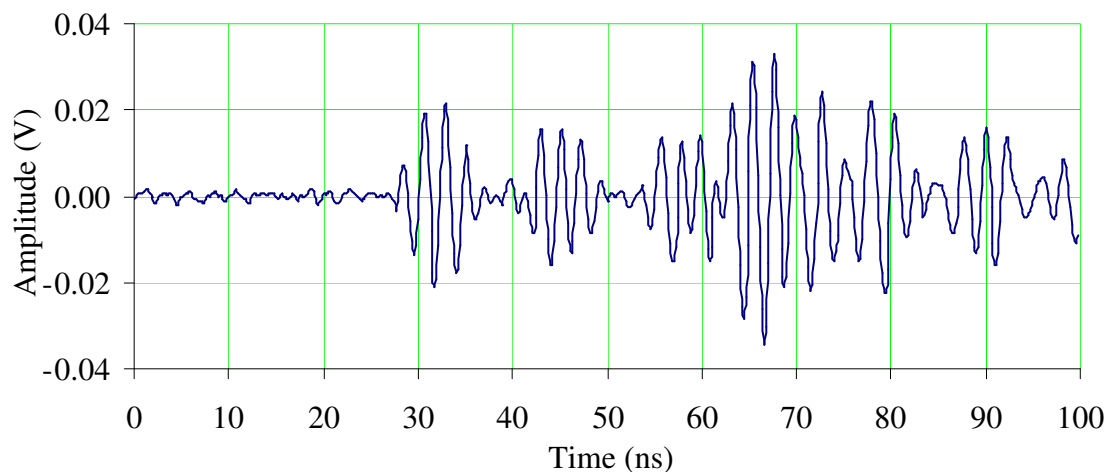


Figure 4.1 The UHF waveform obtained from the HVDC reactor PD testing.

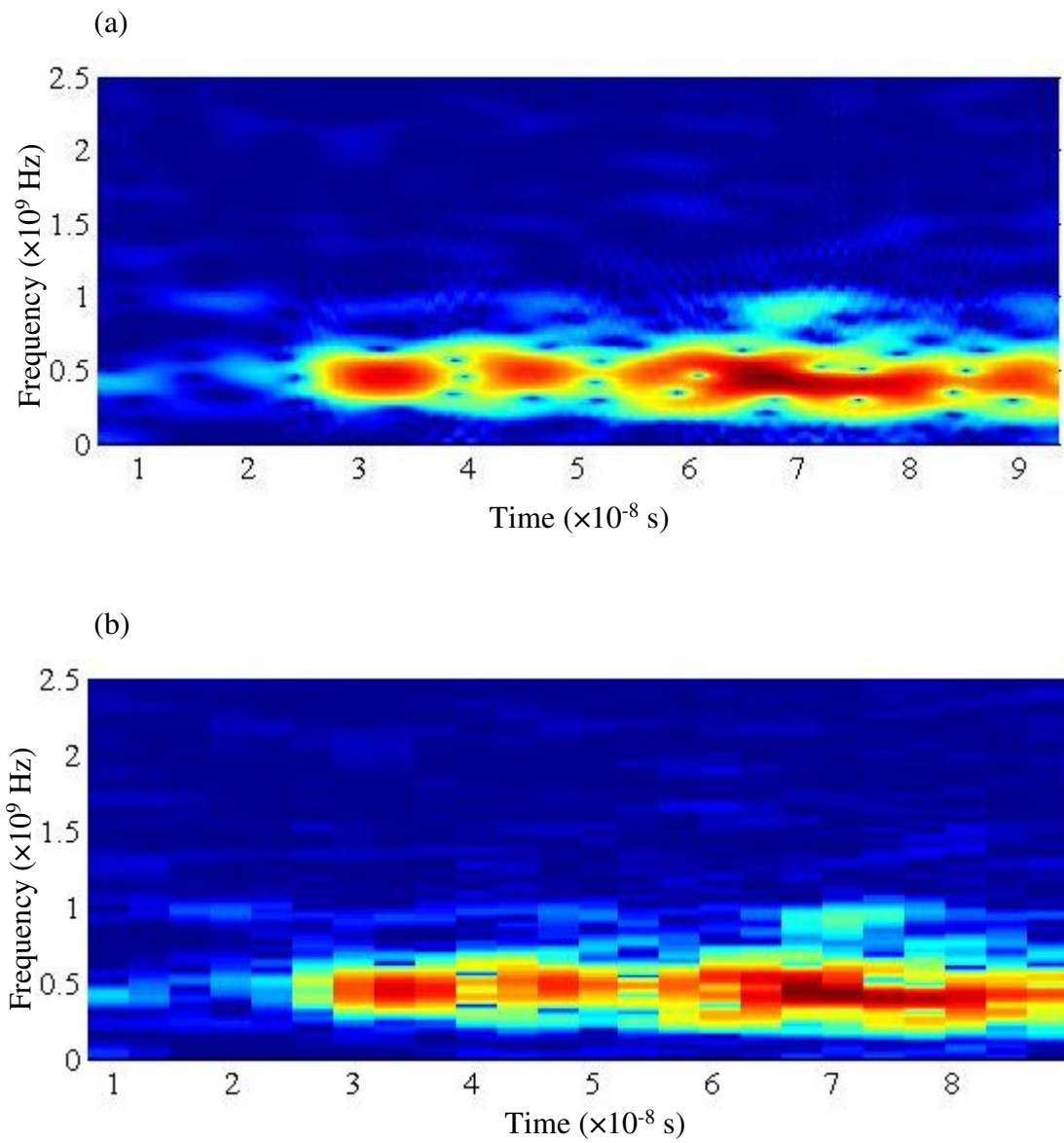


Figure 4.2 Spectrograms generated from the signal depicted in Figure 4.1: (a) With a 64-point time window, (b) With an 80-point time window. This is to illustrate the difference between time and frequency of spectrograms created from different sizes of the time window.

The Short-Time Fourier transform can represent the signal in the time-frequency domain but it still has a disadvantage. As illustrated in Figure 4.2, the two spectrograms are of the same signal (Figure 4.1), but were created using different time window intervals while the other parameters remained the same. This causes different resolutions on both the time and frequency domains, which can be clearly noticed. This is because the Short-Time Fourier transform can only deal with one specific size of time window for the whole signal, whereas many signals require a more flexible approach.

Therefore, the concept of wavelet analysis has been developed [102], aimed at analysing non-stationary signals by means of an algorithm that has a variable time window in order to obtain more accurately either time or frequency information. Wavelet analysis can represent any signal using a time-scale with multi-resolution, in which the scale parameter can be linked to frequency content. Wavelet analysis is recognised as a powerful tool suitable for investigating non-stationary or transient signals as found in many practical applications [102].

4.2.2 Wavelet transform

The concept of Fourier analysis is the breaking down of a signal into various sinusoidal components, where each basis function is extended in time and oscillates for infinity. The concept of wavelet analysis is similar in that it breaks a signal into shifted and scaled versions of a given mother wavelet which has limited duration and zero average value [70, 102]. The continuous wavelet transform of a function $f(t)$ with respect to a given mother wavelet is defined as follows [70]

$$W_{\psi} f(a, b) = \frac{1}{\sqrt{|a|}} \int_{-\infty}^{\infty} f(t) \psi\left(\frac{t-b}{a}\right) dt \quad (4.1)$$

where a = scale parameter that involves stretching or compressing the mother wavelet and relates to frequency content
 b = transition parameter associated with a delay time
 $\psi(t)$ = given mother wavelet function
 $W_{\psi} f(a, b)$ = wavelet coefficients

In Eqn. 4.1, both frequency (a) and time (b) information is computed simultaneously. Moreover, the mother wavelet being applied is also important. There are several families of mother wavelets that have been verified to be useful in electrical applications. For example, the Daubechies wavelet family (dbN , db = Daubechies and N = number of vanishing moments) is suitable for the analysis of PD signals because it can provide almost all the properties required of fast transient and irregular pulses, such as compactness, limited duration, orthogonality and asymmetry [70]. However, using the continuous wavelet transform is computationally intensive and also leads to a redundancy in the wavelet coefficients. Therefore, the discrete wavelet transform was originated based on concepts of ‘powers of two’ and a ‘complementary half-band’ filtering technique [70, 102], resulting in an efficient algorithm and leading to a proliferation of the discrete wavelet transform in practical implementations.

The discrete wavelet transform involves filtering and factor of two down-sampling processes, as summarised in Figure 4.3. A signal is split into two parts (preserving the time duration), resulting in two decomposed signals, which are approximations (cA) obtained from the low-pass filter and details (cD) obtained from the high-pass filter. Both contain the lower half and upper half frequency bands at the Nyquist frequency. For instance, if a signal is captured with a sampling rate of 10×10^9 samples/sec, the Nyquist frequency will be 5×10^9 Hz. As a result, the ideal frequency

band for approximations and details will be $0 \sim 2.5 \times 10^9$ and $2.5 \times 10^9 \sim 5 \times 10^9$ Hz, respectively.

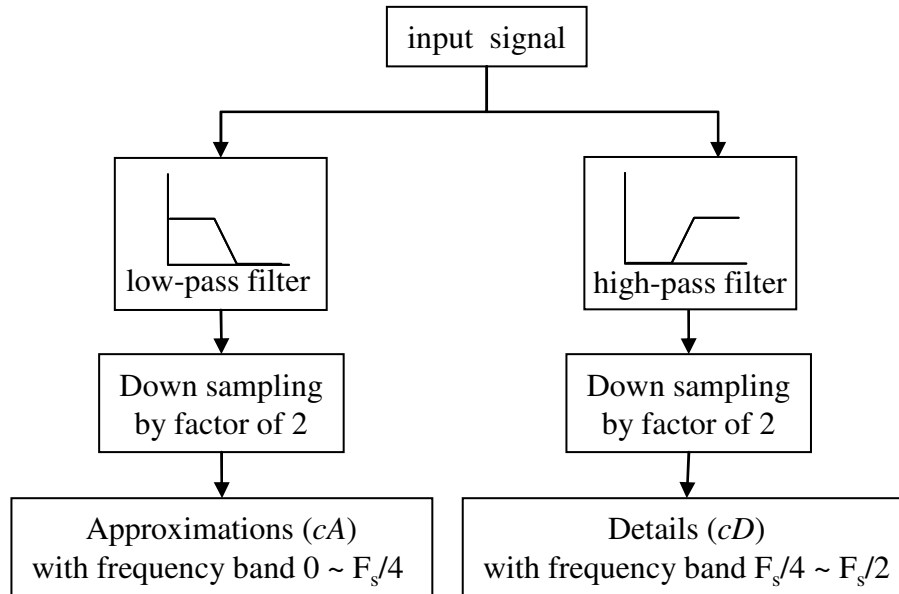


Figure 4.3 Discrete wavelet transform operation consisting of filtering and down sampling processes (F_s = sampling rate).

To illustrate the result created from the discrete wavelet transform, a UHF PD signal as depicted in Figure 4.4(a), captured using a sampling rate of 10×10^9 samples/sec and recorded over 100 ns (1,000 voltage sample points) was used. The signal was fed to the discrete wavelet transform in MATLAB using the ‘*db11*’ mother wavelet. Its approximations and details were computed as shown in Figure 4.4(b) and (c), respectively. In this example, the details consist mostly of noise, while the approximations still closely resemble the original signal.

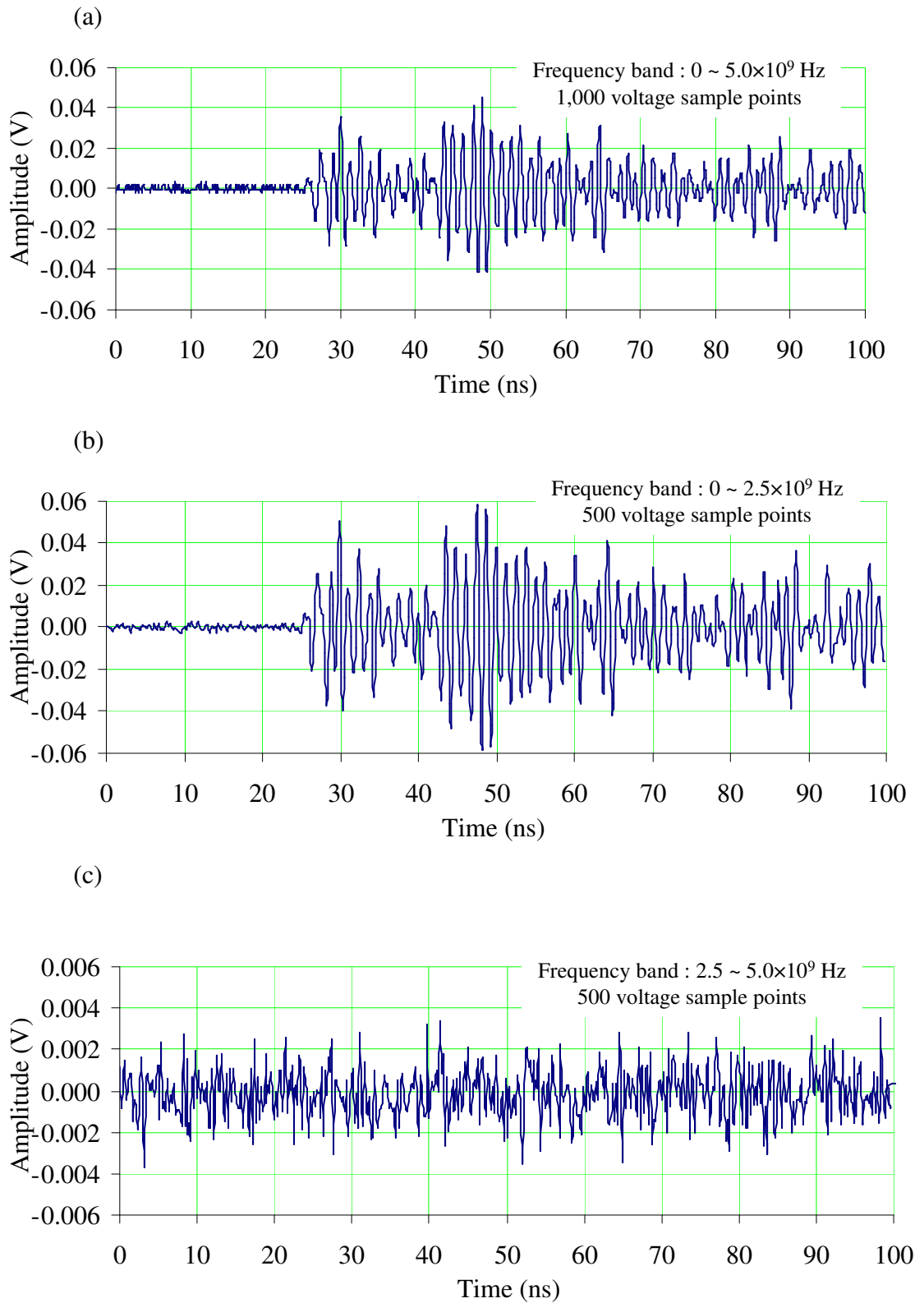


Figure 4.4 The UHF PD signal and its decomposed signals obtained from the discrete wavelet transform: (a) The UHF signal, (b) Approximations, (c) Details.

4.2.3 Wavelet decomposition

Since the discrete wavelet transform breaks a signal into two parts, this process can be iterated as a series of successive approximations. As a result, the signal is broken down into many lower resolution components [102]. This concept is called the wavelet decomposition tree, which is shown in Figure 4.5.

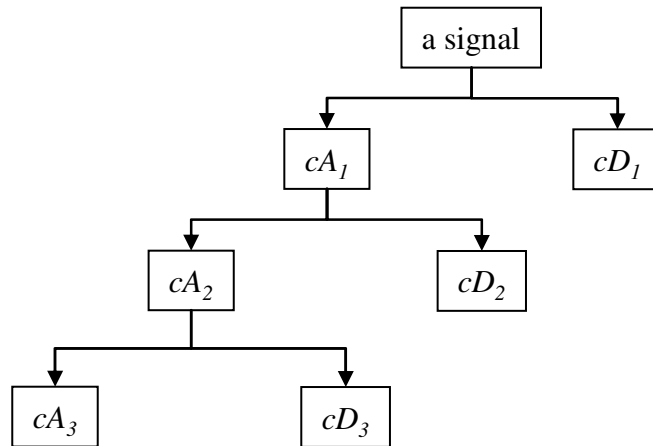


Figure 4.5 Wavelet decomposition tree for three levels.

Figure 4.6 illustrates decomposed signals for the UHF signal depicted in Figure 4.4(a) using wavelet decomposition to three levels with the ‘*db11*’ mother wavelet. Key properties of the decomposed signals at each level are summarised in Table 4.1. The various decomposed signals have potential applications in PD diagnosis, such as PD characterization [105]. In terms of the objectives of this research, the main interest is the possibility of determining signal arrival times more accurately using the decomposed signals.

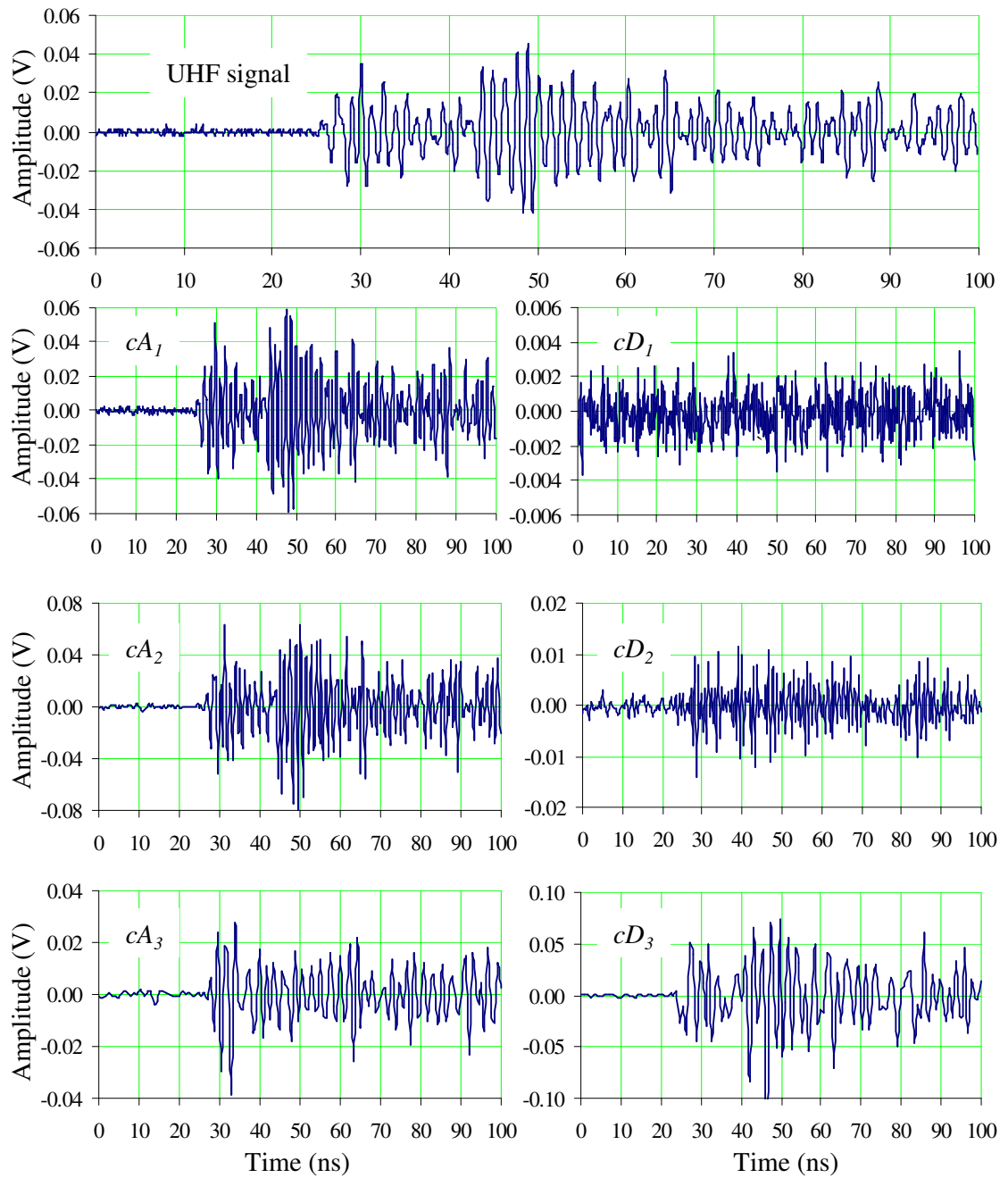


Figure 4.6 A UHF PD signal and its decomposed signals resulting from wavelet decomposition to three levels using db11.

Table 4.1 Properties of the data obtained during wavelet decomposition to 3 levels.

	Signal	cA_1	cD_1	cA_2	cD_2	cA_3	cD_3
Length (points)	1,000	500	500	250	250	125	125
Time (ns) between successive samples	0.1	0.2	0.2	0.4	0.4	0.8	0.8
Frequency band ($\times 10^9$ Hz)	0-5	0-2.5	2.5-5	0-1.25	1.25-2.5	0-0.625	0.625-1.25

The maximum decomposition level to avoid unreasonable processing time can be determined as follows [106]:

$$J_{\max} = \text{fix} \left(\log_2 \left(\frac{N}{N_w} - 1 \right) \right) \quad (4.2)$$

- where N = length of a signal
 N_w = length of filter associated with mother wavelet being used
 fix = rounding toward zero operator
 J_{\max} = maximum decomposition level

From Eqn. 4.2, the relationship between maximum decomposition level and length of signal being analysed for two mother wavelets (db4 and db11) being investigated is shown in Figure 4.7.

The actual length of the decomposed signals is dependent on the mother wavelet being used. For example, using the mother wavelet ‘db N ’, the actual length of cA_1 or cD_1 is $1,000 + (N-1)$ points if the input signal consists of 2,000 sample points. Consequently, the number $N-1$ will be taken into account during the procedure for determining arrival times because the additional $N-1$ points could cause significant error in the determination of PD location, such as a 10-point error for db11 (equivalent to 1 ns or 30 cm propagation path in air using a sampling rate of 10×10^9 samples/sec).

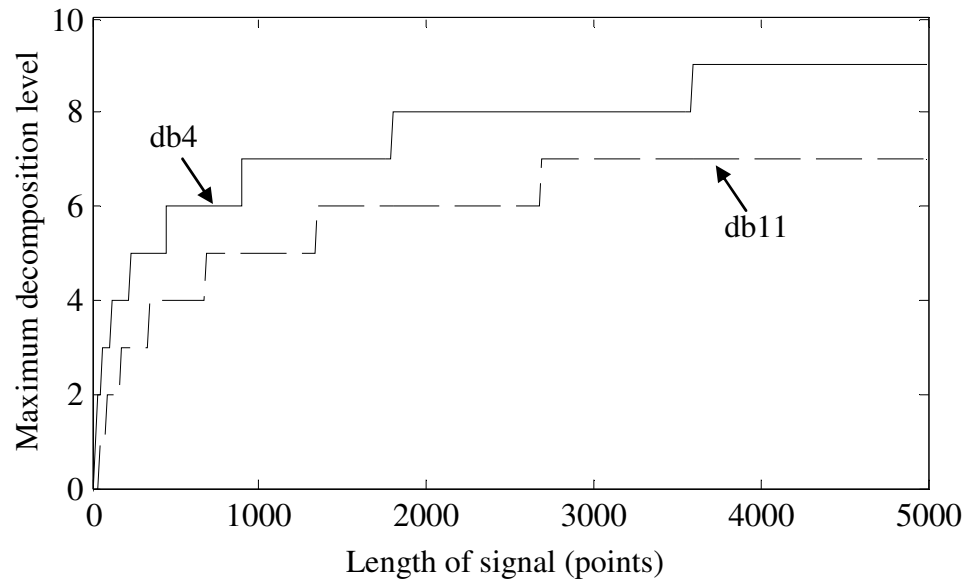


Figure 4.7 Relationship between maximum decomposition level and the length of the signal using db4 and db11.

4.2.4 Wavelet de-noising

One of the main exploitations of wavelets is their use for extracting signals overwhelmed by interference problems where the interference can be contributed by communication systems, operation of switching devices, sinusoidal noise or thermal noise [70, 106, 107]. The use of wavelet techniques in de-noising data containing key features (e.g. PD pulses) has been widely reported and is now implemented in practical systems, such as the application of noise rejection for on-line PD monitoring of HV cables [108], the application of de-noising UHF PD signals in power transformers [109, 110] and the application of suppressing white noise in GIS obtained from UHF PD signals [111].

Wavelet de-noising consists of three main steps as follows:

Step 1) Decomposition

This step involves selecting a specific mother wavelet and level of decomposition. Various wavelet families are available and their selection depends on the particular signals being analysed. Only the Daubechies wavelet (dbN) will be used in this study and the maximum decomposition level defined by Eqn. 4.2 will be used.

Step 2) Threshold application

As a means of recovering or suppressing parts of the signal based on an amplitude criterion, the selection of threshold rules and the application of soft or hard thresholding to the detail coefficients are made in this step. Hard thresholding is the simplest method because it uses a fixed threshold below which the detail is removed (set to zero), as shown in Eqn. 4.3 [103]. Hard thresholding procedure can create discontinuities when signal magnitude is in the region of the threshold, but the soft procedure defined in Eqn. 4.4 [103] does not.

$$y = \begin{cases} x, & |x| \geq \sigma \\ 0, & |x| < \sigma \end{cases} \quad (4.3)$$

$$y = \begin{cases} \text{sign}(x)(|x| - \sigma), & |x| \geq \sigma \\ 0, & |x| < \sigma \end{cases} \quad (4.4)$$

where σ = threshold value

Step 3) Reconstruction

The final step involves recombining (summing) the modified signal components to produce the de-noised signal.

4.2.5 Applications of wavelets in the field of PD diagnosis

Much research has been concerned with wavelet de-noising of PD signals buried with excessive noise levels. After de-noising, the signals can be analysed by a variety of approaches, such as determination of arrival times [112, 113, 114] and diagnosis of phase-resolved patterns [70], etc. This is aimed at better signal interpretation, giving improvements in PD diagnostics.

Another area of application is PD recognition. This application involves the use of wavelet coefficients to recognise multiple PD sources [71, 115]. The coefficients can also be converted into the time-frequency domain to investigate signal characteristics, such as similarity assessment [71] and dynamic spectra [116].

4.3 Effect of wavelet de-noising on arrival times

With the expectation of better signal quality after de-noising process, the arrival times obtained from de-noised signals may offer improvements in UHF PD location using the time of flight method. Although PD signals obtained from UHF monitoring are often quite clear (good SNR), determining the arrival times of these signals can still be challenging due to factors, such as the attenuation of wavefronts that have diffracted around conducting obstacles because there is no ‘line-of-sight’ propagation path. The initial wavefronts can sometimes be comparable with the background noise, making it difficult to accurately determine the onset of PD signals. As a result, wavelet de-noising may be applied in an attempt to improve signal quality. However, a possible concern with the use of wavelet de-noising on UHF signals is that the shapes of de-noised signals may be modified in a way that changes the apparent arrival times, which could degrade the accuracy of PD location

In order to evaluate the effects of wavelet de-noising on UHF PD signals, different wavelet settings were investigated. The signals to be de-noised were obtained from a set of UHF sensors mounted on a power transformer tank. Various types of wavelet

were studied to assess their effect on the accuracy of time of flight measurements for PD location. The results provide useful insight into the selection of wavelet methods for de-noising UHF signals and the range of SNR values for which PD location with acceptable accuracy might be possible.

4.3.1 UHF partial discharge signals to be analysed

In this study, a single set of PD signals recorded during the UHF PD monitoring of an 18 MVA power transformer (single phase 132/25 kV with three UHF sensors installed as shown in Figure 4.8) was used. Further details of the site arrangement can be found in [46].

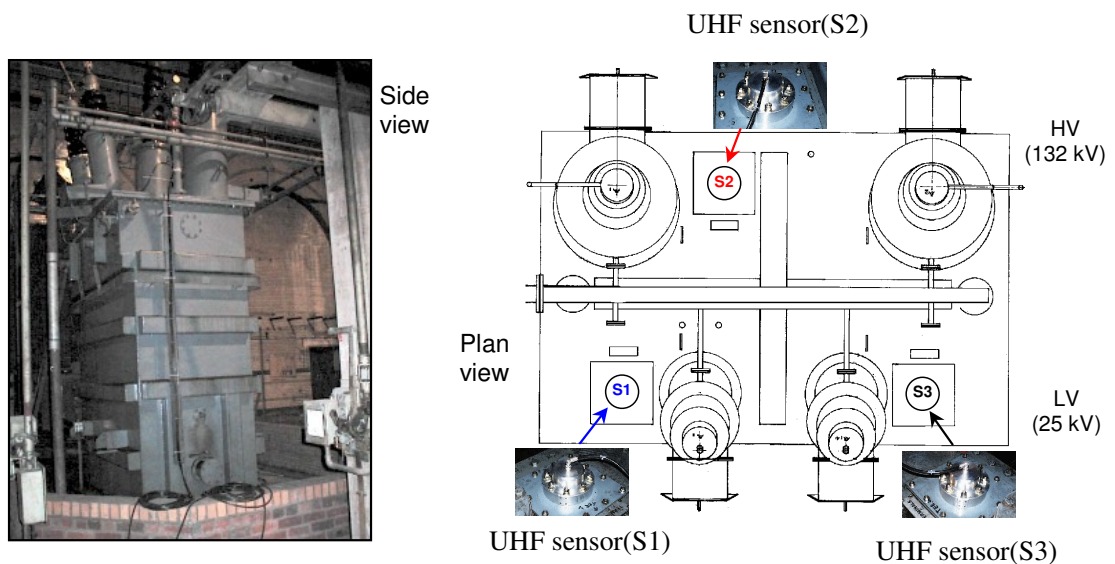


Figure 4.8 Three UHF sensors installed at the top of the 18 MVA single phase power transformer [46].

Outputs from three sensors were fed to an oscilloscope sampling at 10×10^9 samples/sec. Typical UHF waveforms obtained from a single PD source and used in the analysis are illustrated in Figure 4.9. Each set contains three signals and each signal consists of 1,000 voltage sample points recorded over 100 ns. The signals possess good SNR values, and were taken to be representative of ‘clean’ signals.

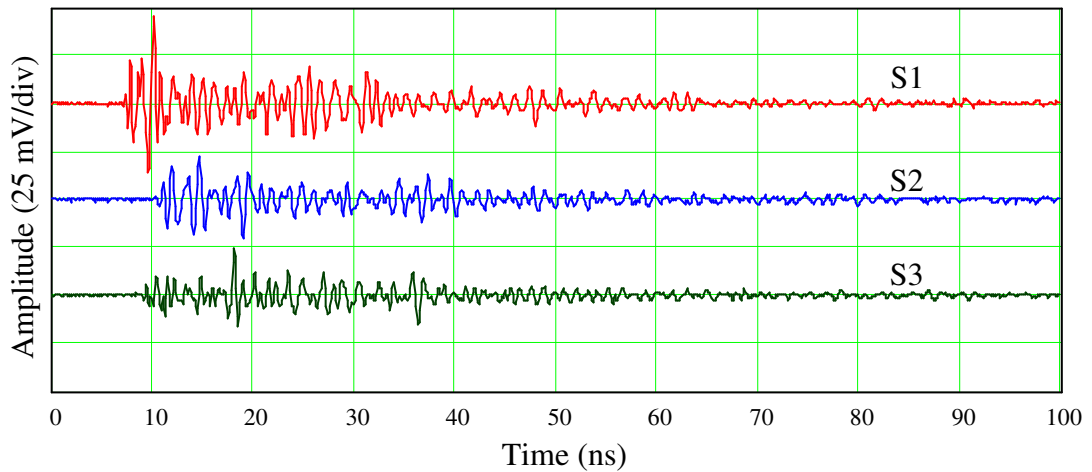


Figure 4.9 Typical UHF PD signals recorded simultaneously at 3 sensors S1-S3.

To locate a PD source using time of flight measurements in power transformers, time differences (ΔT) obtained from pairs of arrival times (T) are the key targets. This is because the absolute arrival times of each sensor in each set may be variable due to different triggering positions during signal acquisition, while the time differences between the three signals should be constant. Once time differences are determined, the PD source position can be located using an algorithm, such as that presented in [49]. In this study, arrival times were investigated and compared with arrival time references obtained from the original PD set (taken to be noise-free). These were calculated using the 2% threshold crossing method of the normalised instantaneous UHF squared voltage. The arrival time references of the three clean signals are shown in Figure 4.10. Reference time differences were then calculated to be -3.1, 1.3 and 1.8 ns for ΔT_{12} , ΔT_{23} , ΔT_{31} , respectively. These references are for the purpose of benchmarking how wavelet de-noising affects the accuracy of UHF PD location.

Although there are many different wavelet settings available for PD de-noising applications [117], in this study, only ‘dbN’ mother wavelets with a range of typical threshold selection methods were used, as summarized in Table 4.2. Figure 4.11 illustrates waveforms of wavelet functions used. The aim was to compare and investigate trends in how these different wavelet settings affect PD location. Only decomposition level 1 was employed for the initial investigation in this study.

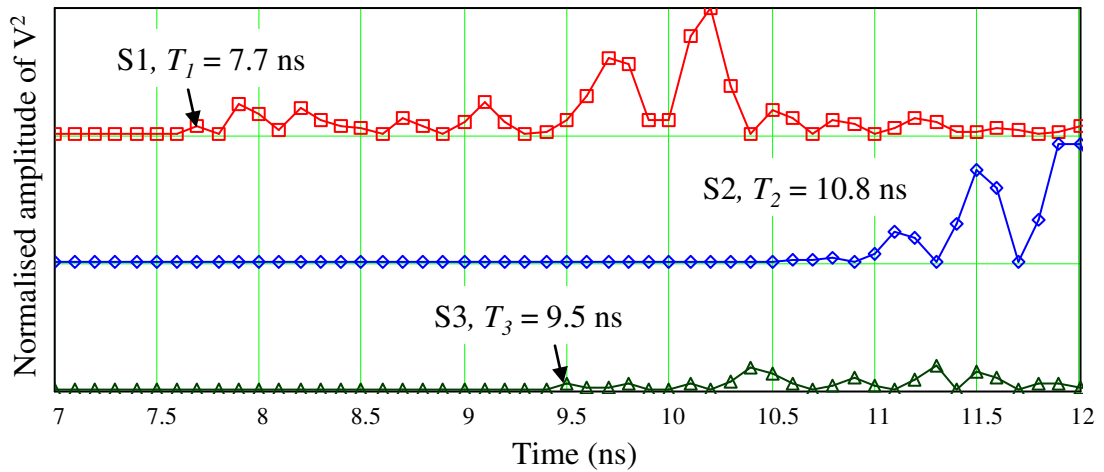


Figure 4.10 Reference arrival times derived from the instantaneous UHF voltages squared of the signal depicted in Figure 4.9. The symbols on each trace correspond to the sample points. Note that the time axis is limited between 7 ns and 12 ns for illustrating the initial wavefronts of signals.

Table 4.2 Mother wavelets and threshold selection methods used in this study.

Mother wavelet	Threshold selection	Label
<i>db4</i>	- Heuristic SURE, soft - Universal, soft	db4-1 db4-2
<i>db7</i>	- Minimax, soft	db7
<i>db10</i>	- Universal, hard	db10
<i>db11</i>	- Heuristic SURE, soft - SURE, soft - Minimax, hard	db11-1 db11-2 db11-3
<i>db12</i>	- Universal, soft	db12

The threshold selections presented in Table 4.2 are outlined as follows [103]:

- ‘SURE’ uses for the soft threshold estimator a rule based on Stein's *Unbiased Risk Estimate* (quadratic loss function). The ‘SURE’ estimator is an estimate of a mean of independent normal random variables using sum of square errors as losses [118]. It is based on the risk of a nearly arbitrary estimate of the mean obtained from an unbiased estimator [118]. The estimate of the risk

for a particular threshold value is determined and the final threshold is determined on the basis of minimizing the risk. The research in [119] presents comprehensively how the ‘SURE’ estimator can be implemented for a threshold selection.

- ‘Universal’ uses a fixed form threshold equal to $\sqrt{2 \times \log(\text{length}(x))}$, where x is signal input;
- ‘Heuristic SURE’ uses a mixture of SURE and Universal; and
- ‘Minimax’ uses a fixed threshold chosen to yield minimax performance for mean square error against an ideal procedure. The ‘minimax’ estimator [103] is an option realising the minimum, over a given set of functions, of the maximum mean square error. The minimax principle is used in statistics to design estimators.

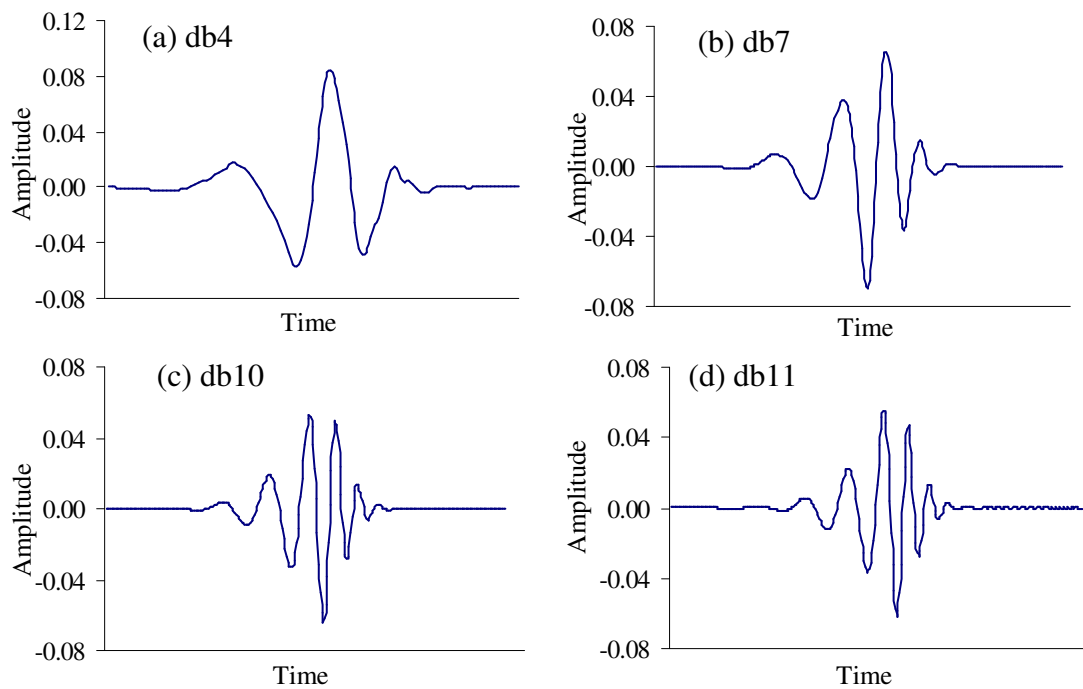


Figure 4.11 Waveforms of wavelet functions: (a) *db4*, (b) *db7*, (c) *db10*, (d) *db11* (*db12* is not shown here because its shape is very similar to *db11*).

Three original UHF signals were mixed with artificial noise, represented as white Gaussian noise for simulation. White Gaussian noise with various SNR values (0, 5, 10, 20 and 50 dB) was generated by MATLAB and added to the original signals. Two examples of the signal mixed with artificial noise for 10 dB and 0 dB, generated from the signal S1 in Figure 4.9, are illustrated in Figure 4.12.

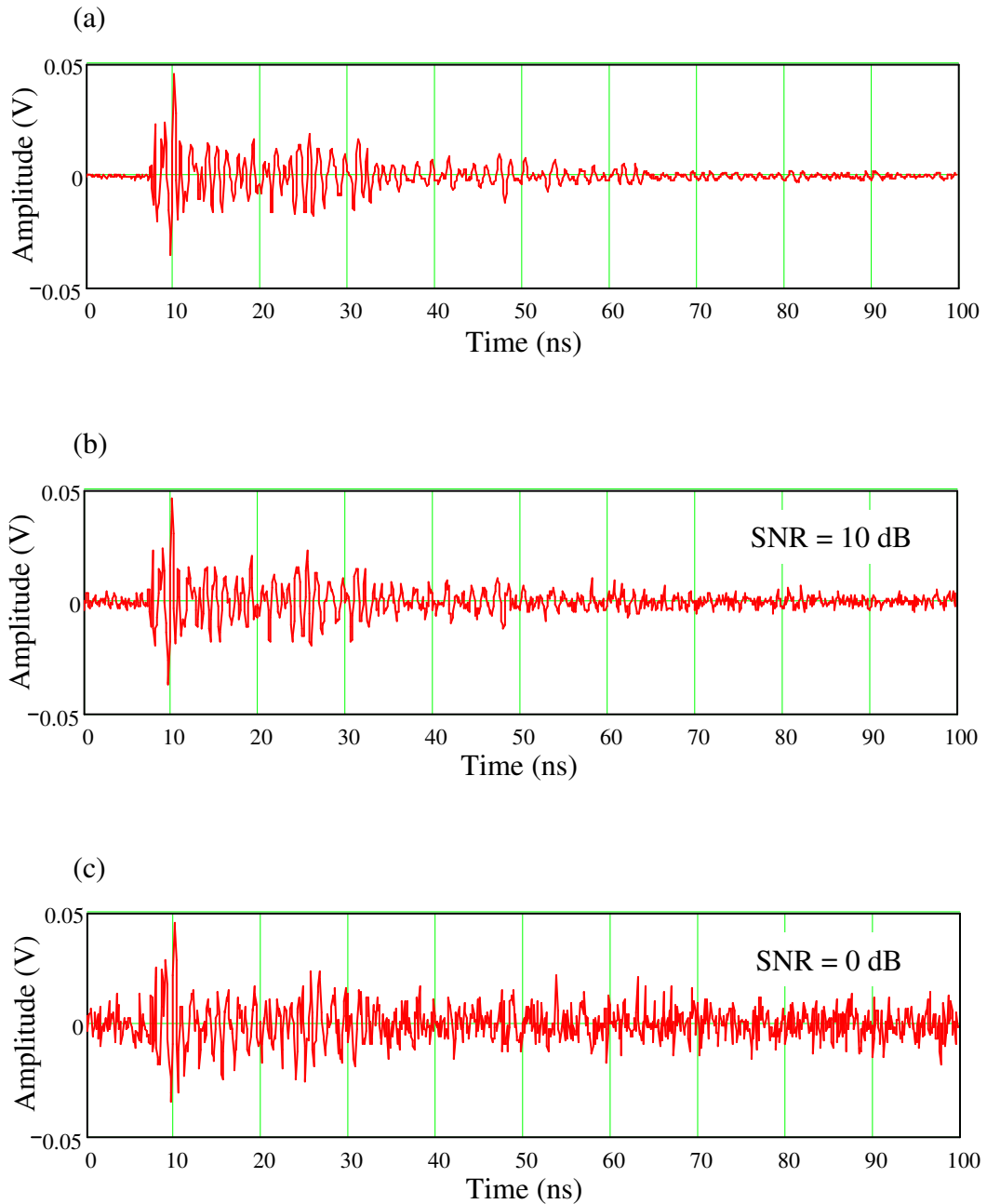


Figure 4.12 UHF signal combined with white Gaussian noise: (a) Original UHF signal – clean signal, (b) With SNR = 10 dB, (c) With SNR = 0 dB.

4.3.2 De-noising partial discharge signals

The wavelet techniques outlined above were used to reconstruct de-noised PD signals. Figure 4.13 illustrates the original signal and its de-noised signals using the db4-1 setting.

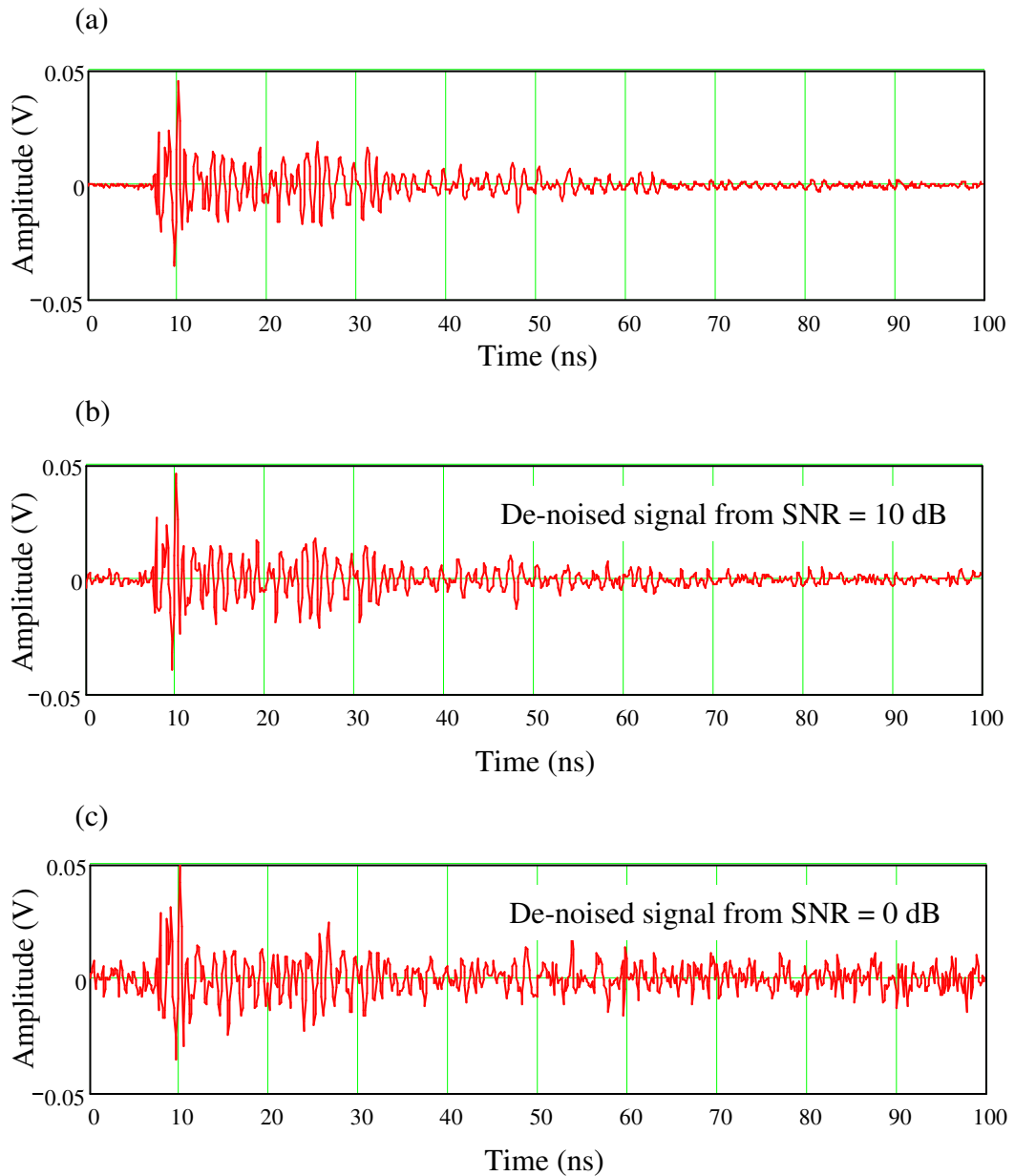


Figure 4.13 Clean signal and de-noised waveforms using db4-1 setting for Figure 4.12: (a) Clean signal (original signal), (b) SNR = 10 dB, (c) SNR = 0 dB.

Considering the de-noised signals, the main concern is that the shapes of the de-noised signals were modified, which could affect the information that needs to be preserved, particularly arrival times. For example, Figure 4.14 shows the clean signal (the signal S1 before noise was artificially added) and its de-noised signal obtained from SNR = 0 dB, in which the arrival time of de-noised signal is changed from 7.7 ns to 7.5 ns. This is based on the db4-1 setting. Note that the de-noised signal appears noisier than the other trace because the clean signal refers to the sensor output S1 before noise was artificially added.

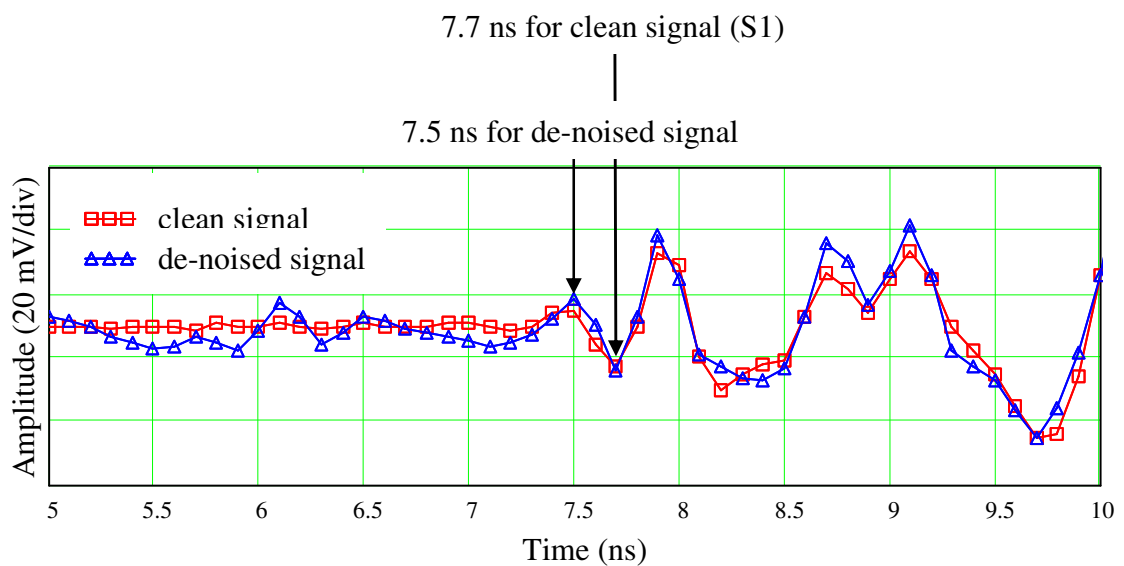


Figure 4.14 Comparison between clean and de-noised PD signals based on SNR = 0 dB (db4-1 setting). This is to illustrate that the shape of de-noised signals is altered in a way that changes its arrival time.

The de-noising analysis applied more generally to UHF signal was carried out according to the following steps:

(i) Adding noise to a clean set of signals from three UHF sensors to produce noisy signals at SNR values varying from 0 dB to 50 dB;

(ii) De-noising in each case using the wavelets and thresholding techniques summarised in Table 4.2;

(iii) Using the 2% threshold crossing method (2% TH) applied to the clean and de-noised signals to identify the arrival times of clean (T_{REF}) and de-noised (T_D) signals. Differential arrival time ($T_{REF} - T_D$) can be then calculated. In this step, the perceived arrival times of all clean and de-noised signals were acquired.

(iv) Calculate time differences of clean signals (ΔT_{REF}) and of de-noised signals (ΔT_D). Finally, differential time of flight errors ($\Delta T_{REF} - \Delta T_D$) were computed.

A comparison was also made between the clean signals and noisy signals (the signals combined with noise without wavelet de-noising) in order to investigate the benefit derived from the wavelet technique. The two block diagrams of Figure 4.15 and Figure 4.16 summarise the whole process.

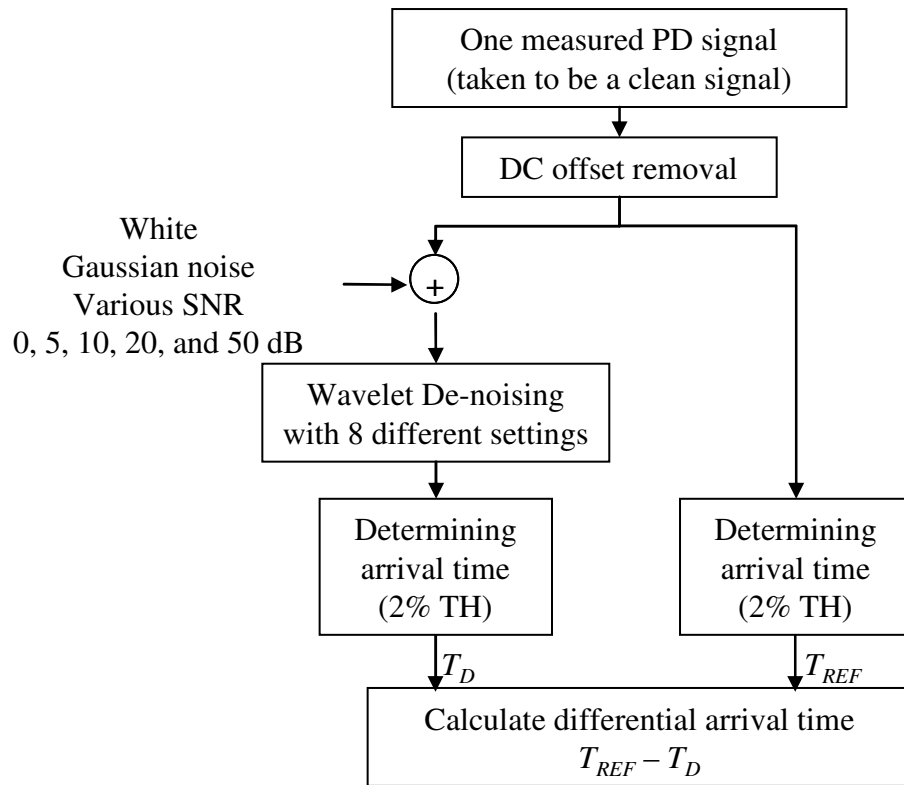


Figure 4.15 'Block 1' outlining the approach for calculating differential arrival time between clean and de-noised signals.

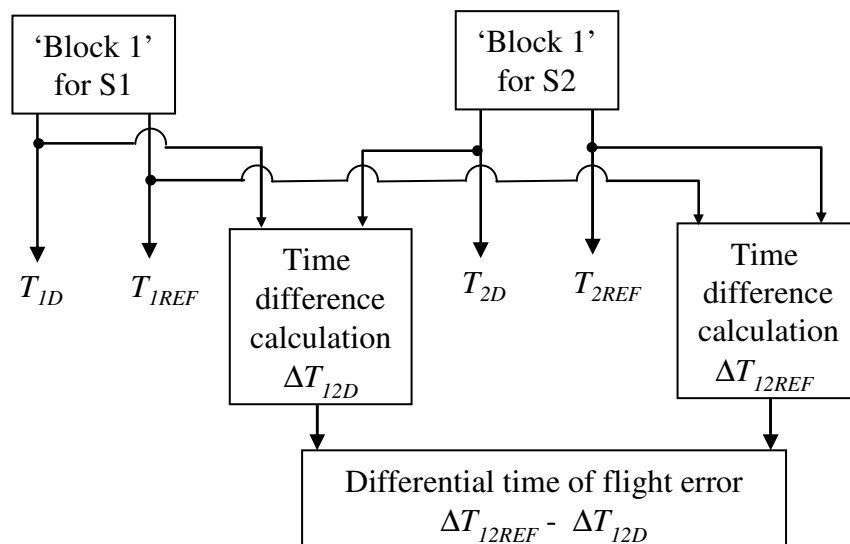


Figure 4.16 'Block 2' outlining the approach for calculating the differential time of flight error.

4.3.3 Results and discussion

(i) Differential arrival times

By following ‘Block 1’ shown in Figure 4.15, differential arrival times were calculated. The results are illustrated in Figure 4.17. The trends in differential arrival times between the clean and de-noised signals generally decrease with increasing of SNR values, as would be expected. It is evident that the majority of differential arrival times are significant when signals are noisy (SNR < 5 dB). Moreover, trends in differential arrival times for each sensor are similar, eventually decreasing to almost zero for high SNR values.

Consider each differential arrival times obtained from each signal. Figure 4.17(a) shows fluctuating differential arrival times at low SNR (< 5 dB). Differential arrival times of S2 in Figure 4.17(b) can be categorised into three groups (A, B, C) corresponding to SNR = 5, 10 and 20 dB, respectively. Similarly, those in Figure 4.17(c) can also be categorised into two groups (A, B) corresponding to SNR = 5 dB and 10 dB, respectively. The groups have been defined in terms of the SNR at which the de-noised signal is good as the original.

Without the application of wavelet de-noising, differential arrival times are always high, especially when the SNR is low (< 5 dB) and apparent arrival times are shifted to earlier times. In terms of UHF signals that have high SNR (> 20 dB), de-noising may not be necessary because the original, de-noised and noisy signals all have similar arrival times. Furthermore, using wavelet de-noising for PD signals that have low SNR (< 5 dB) offers little benefit because differential arrival times remain high.

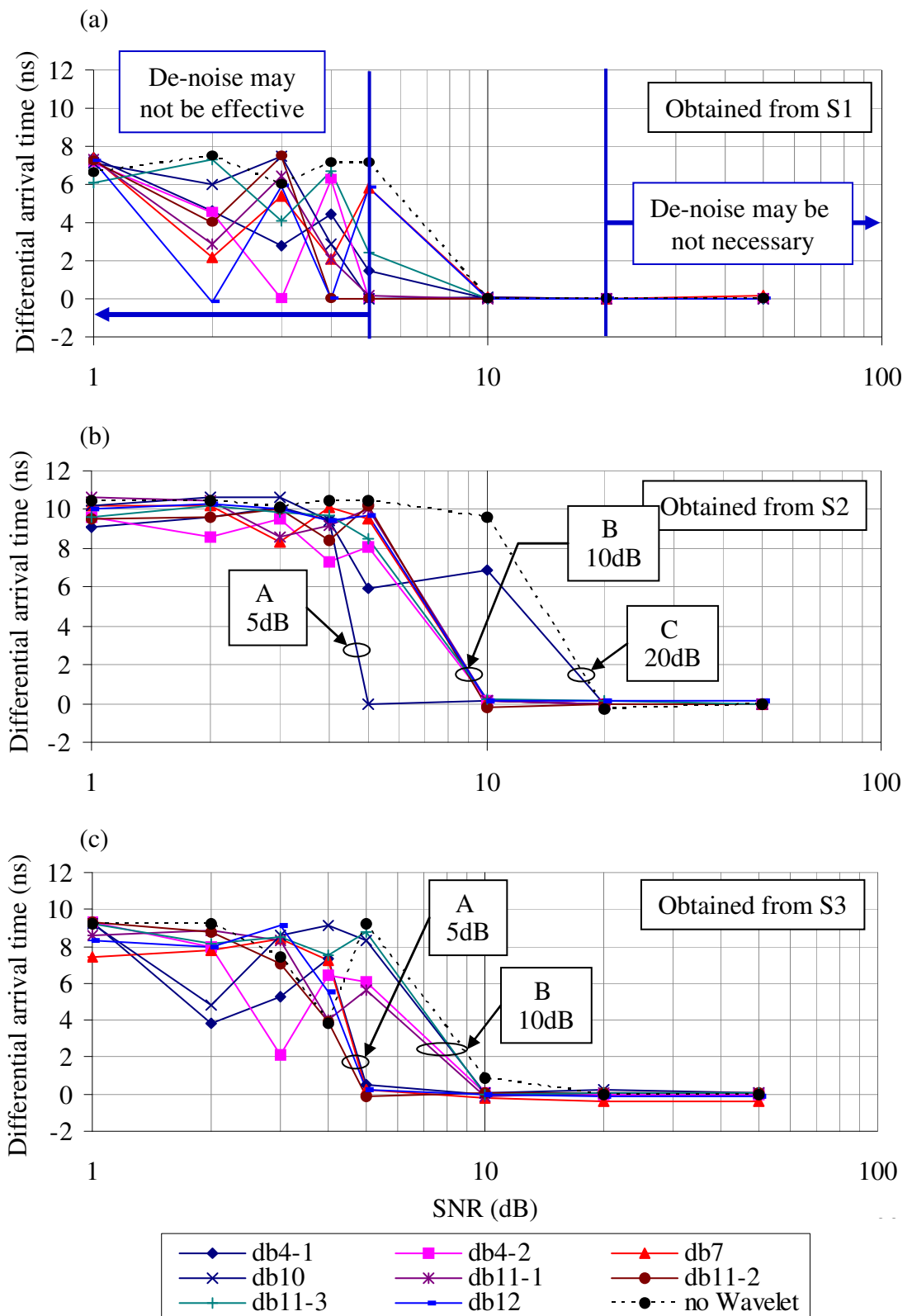


Figure 4.17 Differential arrival times as a function of SNR obtained from: (a) S1, (b) S2, (c) S3.

(ii) Differential time of flight errors

By following 'Block 2' shown in Figure 4.16, differential time of flight errors can be calculated. Typical differential time of flight errors are illustrated in Figure 4.18, obtained from db4-1 and db4-2 settings (differential time of flight errors of other wavelet types showed similar variations).

When the differential time of flight error is zero, there are two possibilities:

- (i) the difference between original and de-noised arrival times of the three signals is zero, or
- (ii) the arrival times of all three signals have been shifted by the same amount and direction during wavelet de-noise processing.

Because there will be no error in locating PD sources if the arrival times of the three sensors are shifted by the same amount and in the same direction, (ii) would be a perfectly acceptable outcome. However, for the wavelets used here, the differential time of flight errors were generally in excess of 1 ns, particularly when the SNR is less than 10 dB.

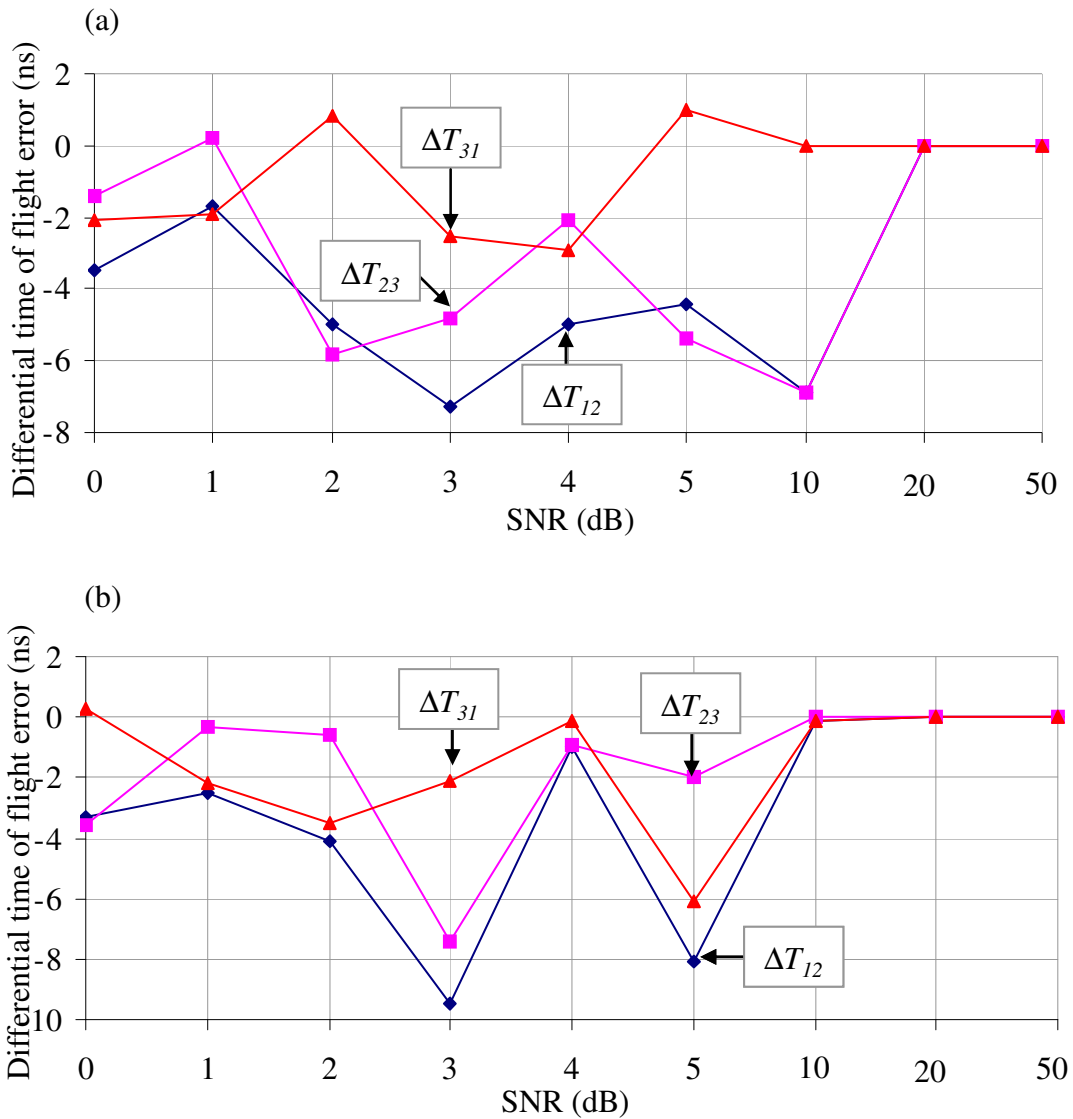


Figure 4.18 Examples of differential time of flight errors: (a) Signals processed by db4-1, (b) Signals processed by db4-2.

Using wavelet techniques to de-noise UHF signals therefore needs to be applied carefully because of its potential effect on the accuracy of PD location [120]. Moreover, de-noising is of little value when the SNR value is better than about 10 dB, since there is little difference in those cases compared with the arrival times based on noisy signals. However, there remains much more scope for varying wavelet parameters in future than it has been possible to explore here, particularly in relation to decomposition level. Nevertheless, the method of analysis that has been proposed will provide a clear framework for future work.

4.4 Wavelet decomposition for determining arrival times

Section 4.3 illustrated that applying wavelet de-noising to UHF signals could affect apparent arrival times due to the modified shape of de-noised signals, which in turn could impact UHF PD location. Another technique, wavelet decomposition, was therefore evaluated as an alternative. In this approach, the signals can be broken down with multiple resolutions using wavelet decomposition and each signal resolution could provide the distinctive characteristics, which may be useful for PD location. In this section, investigations using wavelet decomposition to accurately determine arrival times were carried out in experimental work. Time differences were again used to assess the ability of wavelet decomposition instead of absolute arrival times.

4.4.1 Experimental arrangement

The experiment consisted of a spark unit, two disc-type UHF sensors and two 250 MHz high-pass filters. Tests were carried out in a shielded room ($2.45 \times 2.45 \times 2.45$ m). No additional amplifiers were required in this experiment. A schematic diagram of the test arrangement and coordinates of two sensors (REF and S) are illustrated in Figure 4.19. Note that signals detected by sensor REF were used as trigger signals (fed to channel 1 of an oscilloscope). To clarify abbreviations for these following analyses, two faces of the room, where the sensors REF and S were fixed, are called 'REF' and 'S', and one face at the back of the room is called 'Back'.

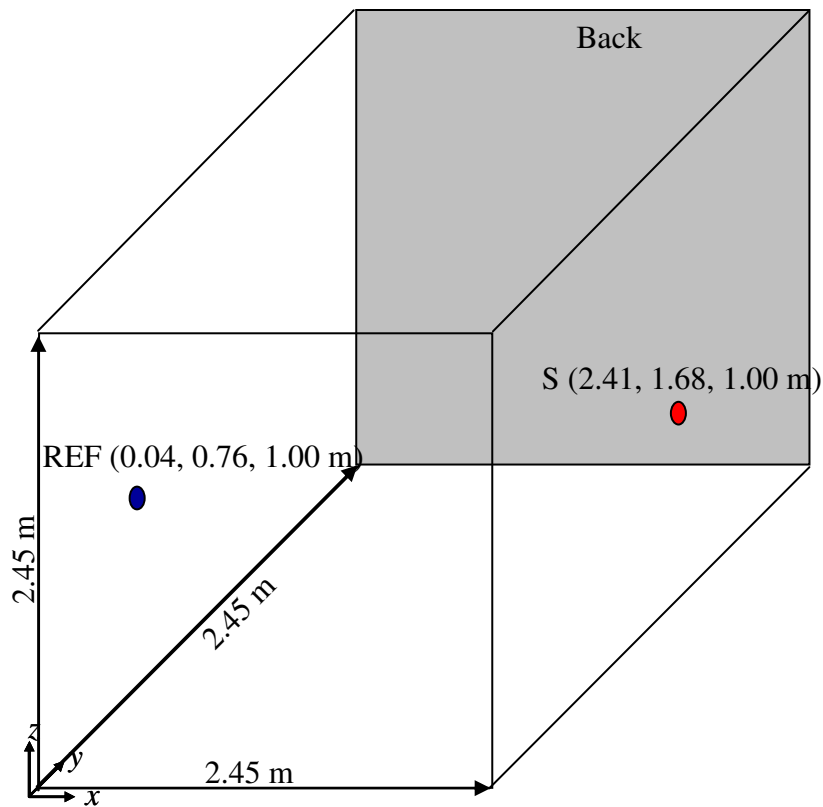


Figure 4.19 Schematic diagram of the test arrangement and coordinates of two sensors (sensor REF and sensor S) in the shielded room.

A spark unit which serves as a PD source has been developed. It generates pluses automatically every 4 seconds using a spark plug, where its spark plug tip is the PD origin, as shown Figure 4.20. The spark unit is a portable device, self-contained in a diecast box with its internal 9 V battery, and can be moved to any position in the shielded room. The circuit diagram of the spark unit is shown in Appendix A.

Note that the radiation pattern of the spark unit was not investigated in this research since the main focus of this research was to use the spark unit as a PD source. However, its free-space radiation pattern would be worth examining in future research.

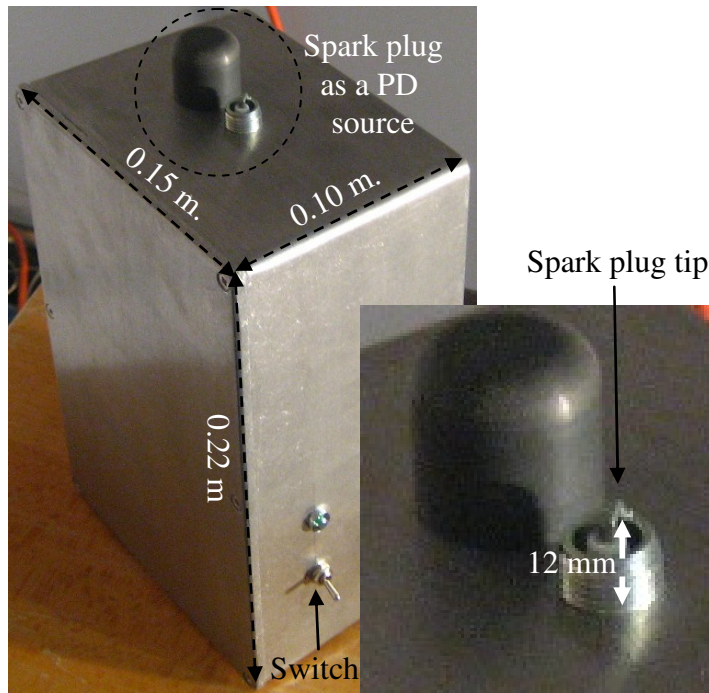


Figure 4.20 Spark unit functioning as a movable PD source.

Two disc-type sensors (one illustrated in Figure 4.21) were installed inside the shielded room at different positions. Outputs of the two sensors were connected to 250 MHz high-pass filters to remove interference below the UHF range. They were then fed to 2 channels (REF – channel 1 and S channel 2) of an oscilloscope with a sampling rate of 10×10^9 samples/sec and bandwidth of 3×10^9 Hz. Output signals were recorded over 100 ns and each contains 1,000 voltage sample points. Figure 4.22 illustrates how UHF signals were captured.

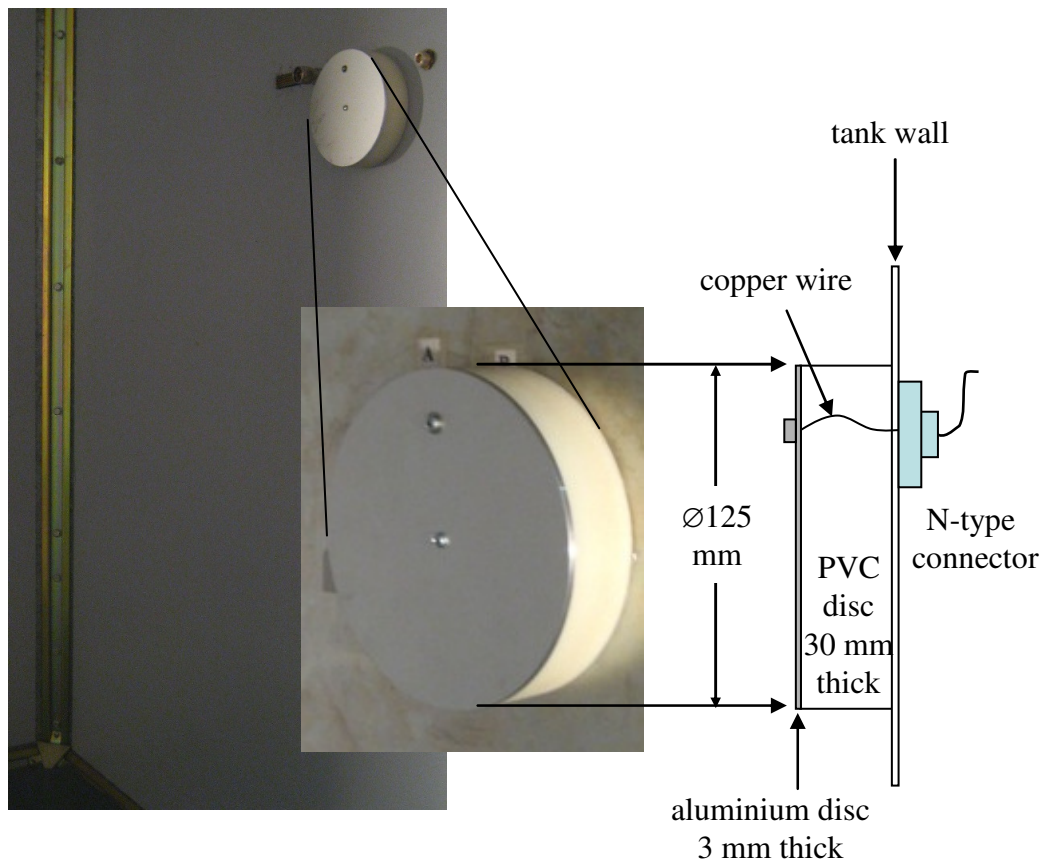


Figure 4.21 Disc-type UHF sensor installed in the shield room.

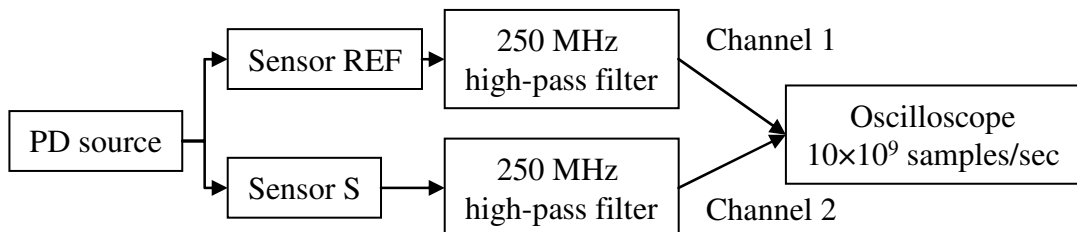


Figure 4.22 Diagram illustrating flow of UHF signals to be analysed.

Before testing, verification of equality of electrical lengths of the measurement cables between each sensor and the oscilloscope was required. By connecting two measurement cables to a single sensor (REF in this observation), this can be validated by observing the similarity of the two sensors outputs that are shown in Figure 4.23.

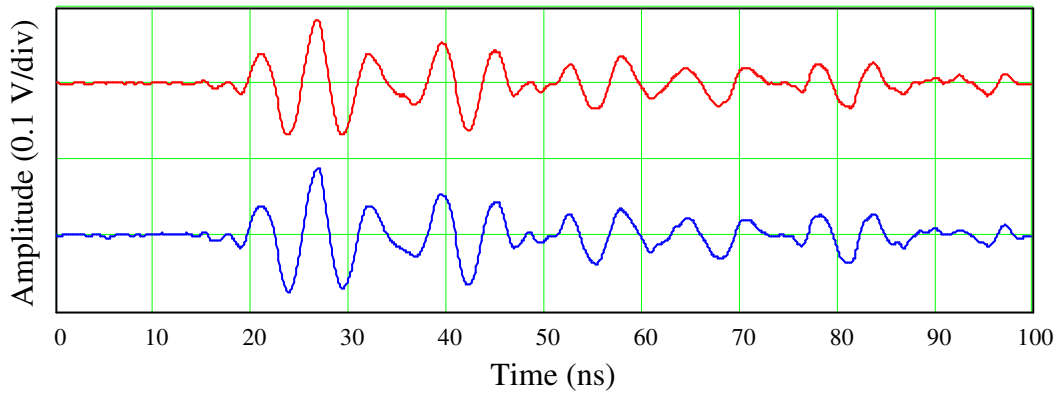


Figure 4.23 Outputs obtained by connecting both measurement cables to REF. This is to validate equality of electrical length of the measurement cables between each sensor and the oscilloscope.

During the test, the spark unit was moved around the shielded room shown in Figure 4.19 to 43 positions in three different layers, with 18 (G1 – G18), 16 (P5 – P20) and 9 (Q1 – Q9) positions in planes at heights $z = 0.23, 0.92,$ and 1.34 m, respectively. The distance error tolerance of ± 1 cm in the position measurements for the PD source are considered negligible because the propagation time of the PD signal for ± 1 cm in air is approximately 33 ps while the time resolution obtained from an oscilloscope is in sub-nanosecond scale, such as 200 ps and 100 ps for sampling rates of 5×10^9 and 10×10^9 samples/sec, respectively. Therefore, any systematic error caused by PD position measurements was insignificant, an assumption that was applied to all subsequent measurements reported in this thesis.

Table 4.3 summarises coordinates of all PD positions for this test. Each data set consisted of 2 measured signals, so 86 signals (43 sets \times 2 signals) were analysed in total. Typical UHF signals can be seen in Figure 4.24, where the spark unit was approximately midway between the two sensors.

Table 4.3 Coordinates of PD positions in the shield rooms.

PD Position	Coordinates in m.			PD Position	Coordinates in m.		
	<i>x</i>	<i>y</i>	<i>z</i>		<i>x</i>	<i>y</i>	<i>z</i>
G1	0.11	0.09	0.23	P5	0.28	0.21	0.92
G2	0.54	0.09	0.23	P6	0.96	0.21	0.92
G3	1.05	0.10	0.23	P7	1.56	0.21	0.92
G4	1.48	0.10	0.23	P8	2.16	0.22	0.92
G5	1.92	0.09	0.23	P9	0.23	1.25	0.92
G6	2.36	0.11	0.23	P10	0.58	1.24	0.92
G7	0.07	1.23	0.23	P11	0.99	1.21	0.92
G8	0.49	1.23	0.23	P12	1.50	1.19	0.92
G9	0.98	1.25	0.23	P13	1.94	1.24	0.92
G10	1.49	1.23	0.23	P14	2.18	1.25	0.92
G11	2.02	1.23	0.23	P15	0.23	2.23	0.92
G12	2.36	1.25	0.23	P16	0.55	2.08	0.92
G13	0.07	2.32	0.23	P17	0.98	2.09	0.92
G14	0.48	2.36	0.23	P18	1.42	2.09	0.92
G15	0.93	2.36	0.23	P19	1.96	2.09	0.92
G16	1.39	2.34	0.23	P20	2.21	2.10	0.92
G17	1.87	2.34	0.23	Q1	0.62	0.25	1.34
G18	2.44	2.34	0.23	Q2	1.19	0.25	1.34
Q3	1.98	0.24	1.34	Q7	0.71	2.12	1.34
Q4	0.66	1.17	1.34	Q8	1.26	2.12	1.34
Q5	1.21	1.25	1.34	Q9	2.01	2.18	1.34
Q6	1.98	1.22	1.34				

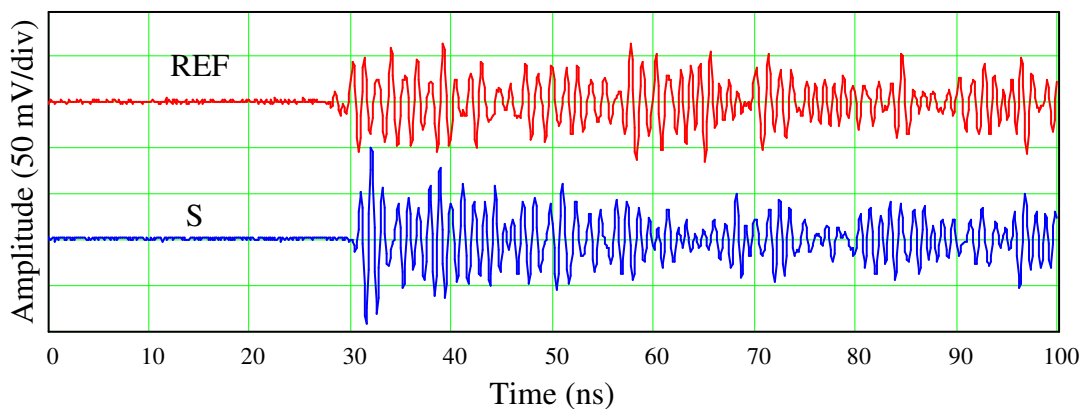


Figure 4.24 Typical UHF signals obtained from two sensors when the spark unit is about halfway between two sensors (P11).

4.4.2 Time differences obtained from geometric calculations

Since the coordinates of all PD positions are accurately known, time differences obtained from geometrical calculations (ΔT_{GEO}) can be used to evaluate the performance of wavelet decomposition for UHF PD location. The time difference between two sensors is a function of the differential distance between each sensor and the spark unit. The speed of electromagnetic waves in air 3×10^8 m/sec, so that:

$$\Delta T_{GEO} = 3.33(\Delta d) \quad (4.5)$$

where Δd = differential distance between each sensors and spark unit (m), defined as $\Delta d = d_{REF} - d_S$, where d_{REF} and d_S are the absolute distances from sensor REF and sensor S to the spark plug tip.

ΔT_{GEO} = expected time differences obtained from geometry (ns)

4.4.3 Results and analysis

Analysis proceeded according to the following steps:

(i) Re-sample all signals from 10×10^9 (actual sampling rate) to 50×10^9 samples/sec using the 'resample' function of MATLAB [103]. This is to ensure that the decomposed signals have a sufficiently high sampling rate for arrival times to be determined accurately.

UHF signals are normally captured with a sampling rate of 5×10^9 or 10×10^9 samples/sec, equivalent to 0.2 or 0.1 ns (6 or 3 cm propagation path in air, respectively). To ensure a sampling interval of no more than about 0.5 ns (15 cm propagation path in air) in the decomposed signals, the original signals were re-sampled to 50×10^9 samples/sec (an increase by a factor of 5). From Figure 4.7, the maximum decomposition level for 5,000 sample points (re-sampled signal) with the specific mother wavelet 'db11' chosen in this study [112, 113] is 7. Thus, the

properties of decomposed signals can be summarised in Table 4.4. From this table, it is apparent that decomposed signals obtained from level 1 to level 5 may be appropriate for accurately determining arrival times.

Table 4.4 Summary of sample points, times between successive samples and equivalent sampling rate of each decomposed level.

Decomposition levels	Approximate sample points	Time between successive samples (ns)	Equivalent sampling rate (samples/sec)
re-sampled signal	5,000	0.02	50×10^9
1	2,500	0.04	25×10^9
2	1,250	0.08	12.5×10^9
3	625	0.16	6.25×10^9
4	313	0.32	3.125×10^9
5	157	0.64	1.56×10^9
6	79	1.28	0.78×10^9
7	40	2.56	0.39×10^9

(ii) The re-sampled signals (now containing 5,000 sample points) were decomposed down to level 5 using the ‘db11’ mother wavelet.

(iii) The approximation waveforms ($cA_1 - cA_5$) were used to determine arrival times, T_{REF} and T_S , where T_{REF} and T_S are arrival times obtained from sensors REF and S, respectively. Before determining arrival times, each approximation waveform was left-shifted by 10 points because its length was extended by 10 points when *db11* was used which was caused by convolving the signal with a particular filter. It is hoped that more accurate measured arrival times could be achievable. Arrival times were again determined using the 2% threshold crossing method (2% TH) of instantaneous cA_1 amplitude squared. The other approximations ($cA_2 - cA_5$) were processed in the same way. From this step, 215 values (43 signals \times 5 decomposition levels) for each sensor of arrival times were acquired. Measured time differences (ΔT_{MEA}), defined as $T_{REF} - T_S$, can be then computed. Figure 4.25 shows the analysis procedures being used. Figure 4.26(a) shows a typical cA_1 waveform (obtained from the re-sampled signal captured at sensor REF for PD position P5, for an example) already left-shifted by 10 sample points. Additionally, Figure 4.26(b) illustrates the

normalised amplitude of cA_I squared and its arrival time is indicated in Figure 4.26(c).

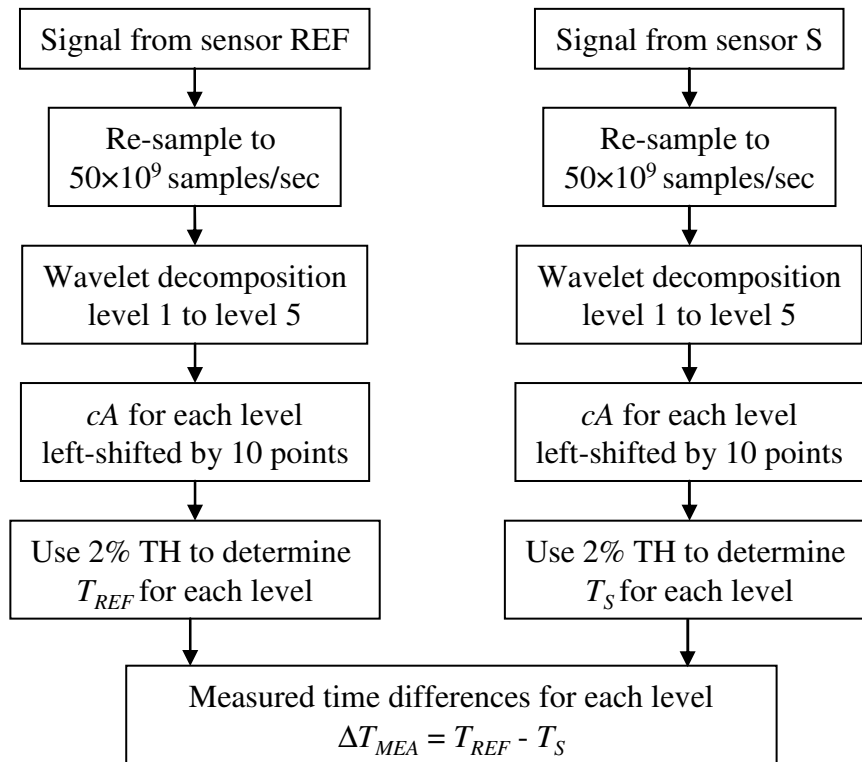


Figure 4.25 Diagram illustrating the analysis procedures.

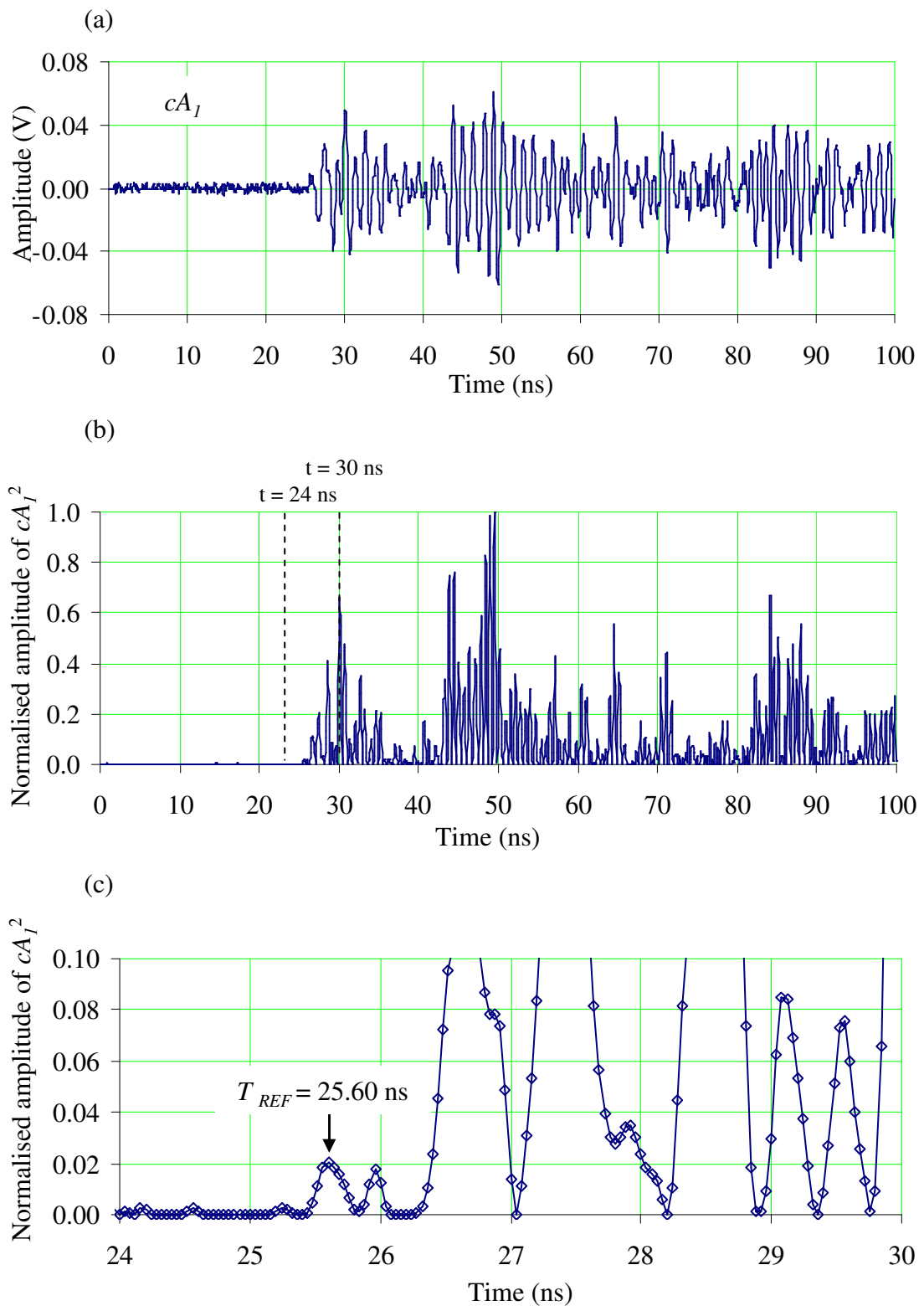


Figure 4.26 Typical approximation waveform for decomposition level 1 (cA_1): (a) cA_1 , (b) Normalised amplitude of cA_1^2 , (c) Expanded view of (b) to determine the arrival time using the 2% threshold crossing method.

To assess results, relationships between differential distances (Δd) and measured time differences (ΔT_{MEA}) of each level were plotted and compared with the theoretical relationship according to Eqn. 4.5. Typical correlations between Δd and ΔT_{MEA} are illustrated in Figure 4.27. The other three levels provide the similar patterns. Results show that the majority of ΔT_{MEA} fall close to the theoretical relationship.

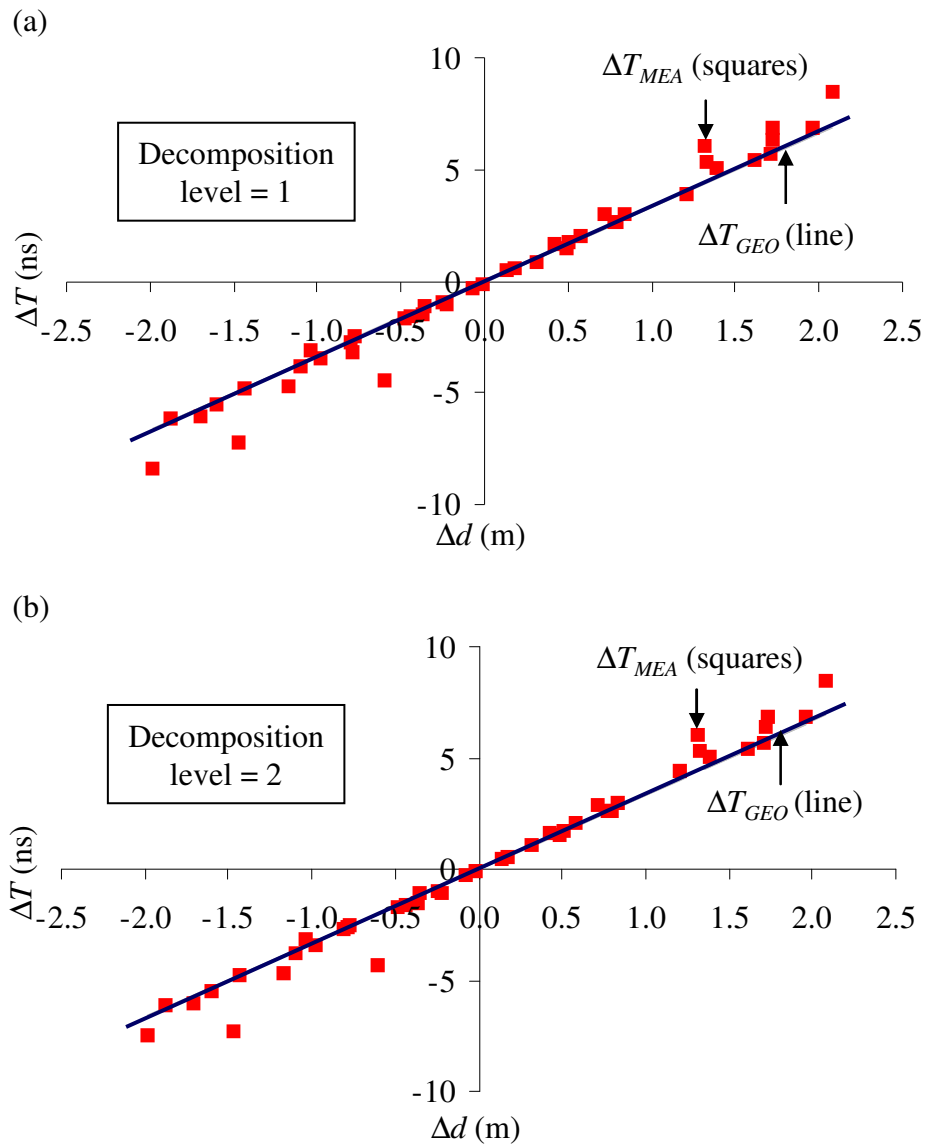


Figure 4.27 Relationship between ΔT_{MEA} and Δd derived from:
 (a) Decomposition level = 1, (b) Decomposition level = 2.

To evaluate the performance of the wavelet decomposition method in determining

arrival times, mean values of absolute errors ($\frac{\sum_{i=1}^{n=43} |\Delta T_{GEO} - \Delta T_{MEA}|_i}{43}$) for each level were computed and these are summarised in Table 4.5. Four of the five values of mean error are below 1 ns, which is equivalent to an absolute error of 0.3 m and 0.2 m propagation distance in air and transformer oil. In addition, the error resulting from cA_2 is minimal.

Table 4.5 Mean values of absolute errors and their propagation distance in air and transformer oil for each decomposition level.

	cA_1	cA_2	cA_3	cA_4	cA_5
Mean (ns)	0.44	0.40	0.68	0.98	1.45
Distance in air (m)	0.13	0.12	0.20	0.29	0.44
Distance in transformer oil (m)	0.09	0.08	0.14	0.20	0.29

For further investigation, consider Figure 4.27: it is indicated that around the halfway point between two sensors ($-1.0 \leq \Delta d \leq 1.0$), ΔT_{MEA} is close to the theoretical relationship while ΔT_{MEA} at longer distances shows increasing magnitudes of Δd in both quadrant one and three. This may be caused by influences of reflections and refractions of propagation paths, which affect initial wavefronts and hence apparent arrival times. Comprehensive investigation will be reported in the next chapter.

4.4.4 Comparison of time differences obtained between wavelet decomposition and original UHF signal

From the investigation above, wavelet decomposition could be suitable for accurately determining arrival times, especially with decompositions at level 1 and 2, because it can provide an error of less than 0.5 ns when the *db11* mother wavelet is used. Therefore, an additional study was conducted to compare time differences resulting from the 2% threshold crossing method and wavelet decomposition. Figure 4.28 illustrates relationship between ΔT_{MEA} obtained from the 2% threshold crossing of UHF voltages squared and Δd .

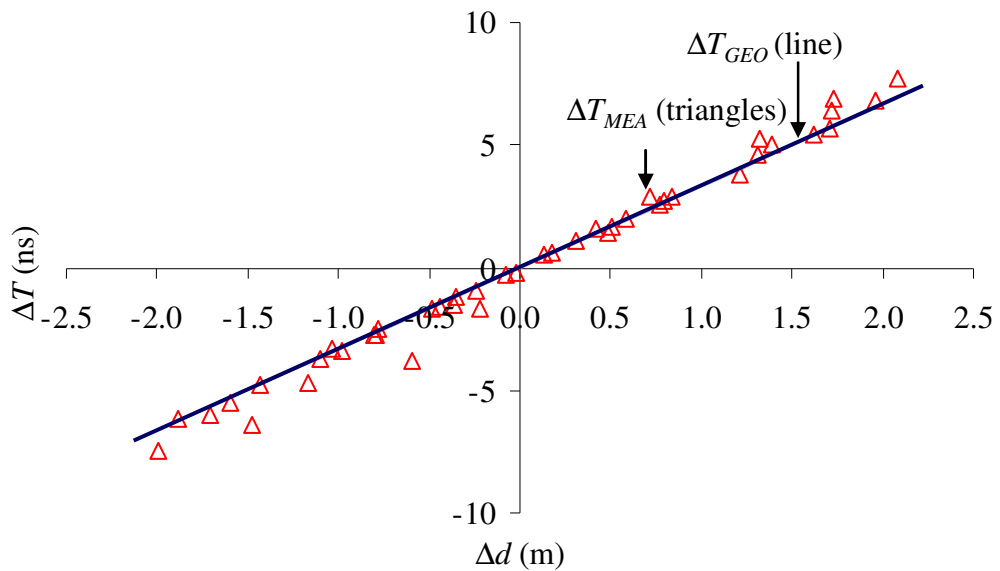


Figure 4.28 Relationship between ΔT_{MEA} and Δd obtained from the 2% threshold crossing method of UHF voltages squared.

To interpret this comparison, mean values of absolute errors obtained from wavelet decomposition in each level and from the UHF voltages squared were compared and results are illustrated in Figure 4.29.

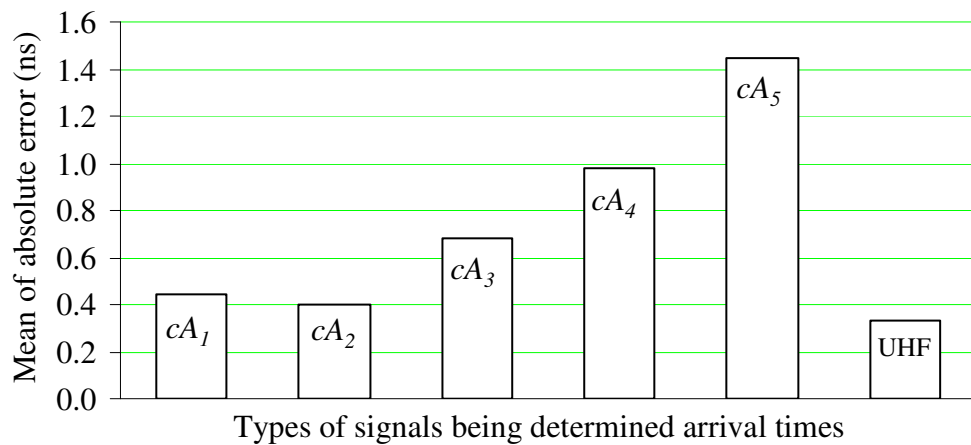


Figure 4.29 Comparison of mean values of absolute errors obtained from wavelet decomposition at 5 levels and from the UHF signal itself.

The means of the absolute errors obtained from wavelet decomposition and from the UHF signal itself are 0.40 (level 2, minimum value) and 0.32 ns, respectively. The wavelet decomposition level = 2 gives slightly higher error but it is still within the required 0.5 ns tolerance. This shows that the 2% threshold crossing of instantaneous UHF voltages squared would still be a more effective approach than the more complicated method used in this study. However, there remains much scope for further work, such as the selection of specific mother wavelets suitable for each group of PD signals.

4.5 Discussion and conclusions

In this chapter, an overview of fundamental knowledge for wavelet analysis was explained, which include wavelet transform, wavelet decomposition, wavelet de-noising as well as applications of wavelets in the field of PD diagnosis. In this research, two wavelet techniques, i.e. wavelet de-noising and wavelet decomposition, were investigated with the aim of improving UHF time of flight measurement for PD location.

Wavelet de-noising with eight different wavelet settings were used to de-noise the UHF signals containing artificial noise levels (0 – 50 dB). This was to investigate the consequences of applying wavelet de-noising to the arrival times of UHF signals in view of the potential modification of de-noised waveforms. Results show that wavelet de-noising alters the UHF waveforms and affects time differences. Especially when SNR is less than 10 dB, differential time of flight error can exceed 1 ns. This could imply that the error values for locating PD after applying wavelet de-noising inside power transformers could be more than 0.2 m based on the velocity of the electromagnetic wave in transformer oil of 0.2 m/ns. Furthermore, using wavelet de-noising for UHF PD signals that have low SNR (< 5 dB) offers little benefit, while for PD signals that have high SNR (> 20 dB) wavelet de-noising techniques may not be necessary. Thus, wavelet de-noising of UHF signals needs to be applied with caution because it can degrade the accuracy of UHF PD location.

Wavelet decomposition could be used for the determination of arrival times with acceptable errors but it cannot provide greater benefit than the 2% threshold crossing method of instantaneous UHF voltages squared. By comparison of mean values of absolute errors obtained from both wavelet decomposition and UHF voltage waveforms, results show that the minimum mean of absolute errors from wavelet decomposition level = 2 is slightly higher than the UHF voltages squared, but it is still within 0.5 ns tolerance. This shows that the 2% threshold crossing method of UHF voltage squared would still be a more effective means than other complicated methods used in this research.

There remains much more scope for both wavelet de-noising and wavelet decomposition in order to improve the accuracy of determining arrival times, such as varying wavelet parameters. Nevertheless, the methodology for analysis presented here will be a clear framework for future study.

5. Experimental investigations into the accuracy of signal arrival time measurements

5.1 Introduction

This chapter describes experimental investigations of signal arrival times carried out in a shielded room that was used to represent a transformer tank. It commences with an experiment for selecting the optimum UHF sensor among disc, monopole and spiral types in UHF PD location applications. After this step, the experimental investigations into the accuracy of absolute arrival times were carried out in the shielded room. To evaluate the accuracy of UHF PD location, those absolute arrival times were used to calculate measured time differences for comparison with ideal geometric time differences. Building on these findings, the possibility of obtaining more accurate absolute arrival times was also investigated and an arrival time consistency index was introduced for evaluating the appropriate threshold percentage that could provide smallest variations in arrival times.

5.2 Selection of UHF sensor for arrival time measurements

5.2.1 Test arrangement and methodology

UHF sensors of different designs will have different response characteristics, which may affect their time-domain response to UHF PD signals, as reported in [47]. Therefore, the transient response characteristics of three typical types of UHF sensors, i.e., disc, monopole and spiral, which are shown in Figure 5.1, were investigated by means of laboratory experiments.

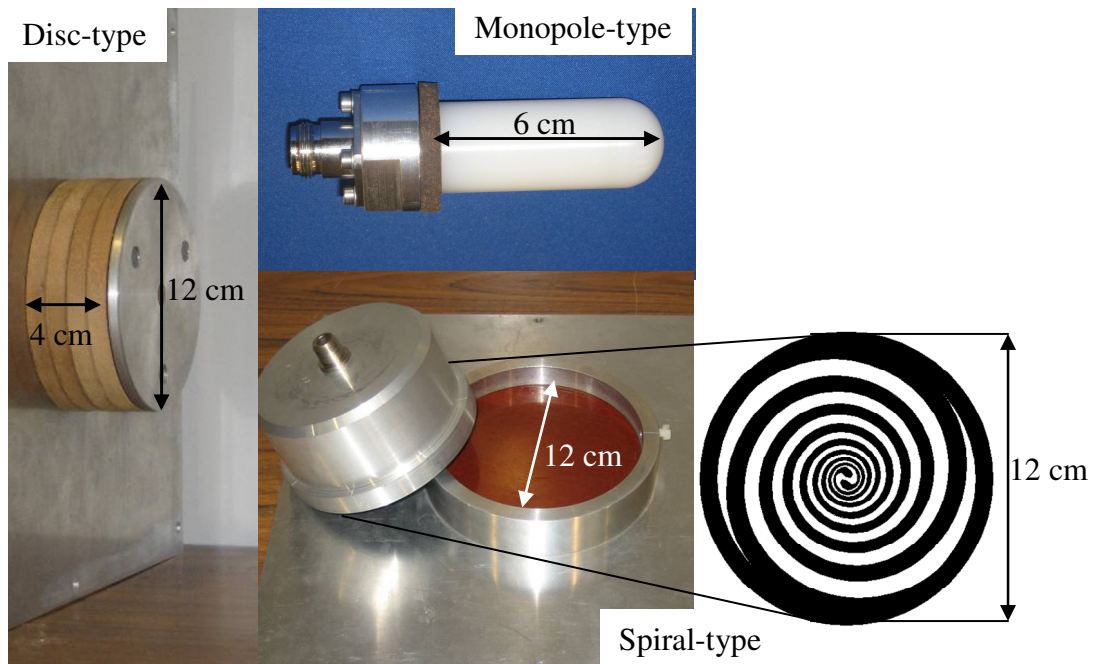


Figure 5.1 Three types of UHF sensors used in the experiments together with a mask showing the shape of the logarithmic spiral antenna.

The experiment made use of an avalanche pulser feeding a 45 mm monopole, which served as a movable PD source. It was carried out in a closed metal tank ($2.51 \times 1.26 \times 1.26$ m) fitted with two UHF sensors. The avalanche pulser shown in Figure 5.2 provided a 10 V, 1 ns pulse to the radiating monopole, which excited repeatable transient UHF signals for comparing the three sensors under test. The two UHF sensors (one as a sensor under test and the other as a timing reference sensor) were used to capture the radiated UHF signals. Outputs of the sensors were fed to an oscilloscope with a sampling rate of 5×10^9 samples/sec, bandwidth of 1×10^9 Hz. The sensor under test will be rotated through disc, monopole and spiral types for each test.

The timing reference sensor used for triggering the oscilloscope was the monopole type (fitted permanently). The test arrangement is shown in Figure 5.3. This experiment was aimed at identifying which UHF sensor type is optimum for giving clear arrival times for UHF PD location.

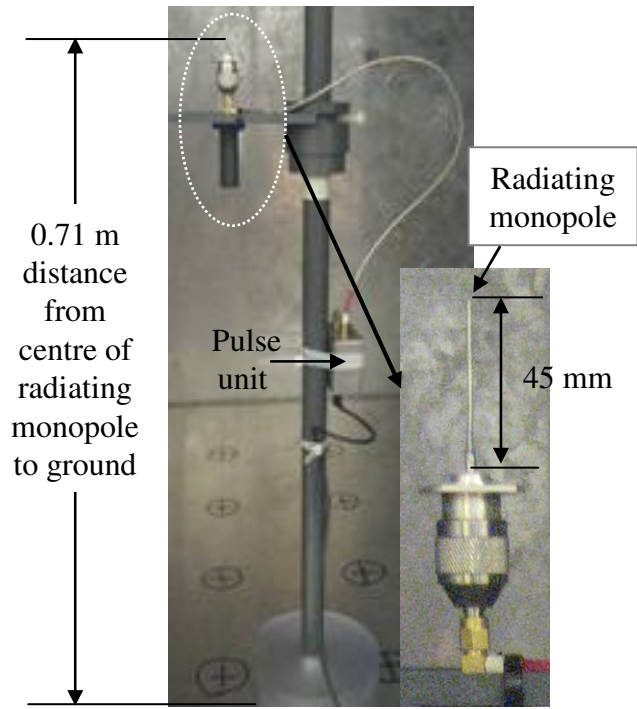


Figure 5.2 The avalanche pulser functioning as a movable PD source inside the tank.

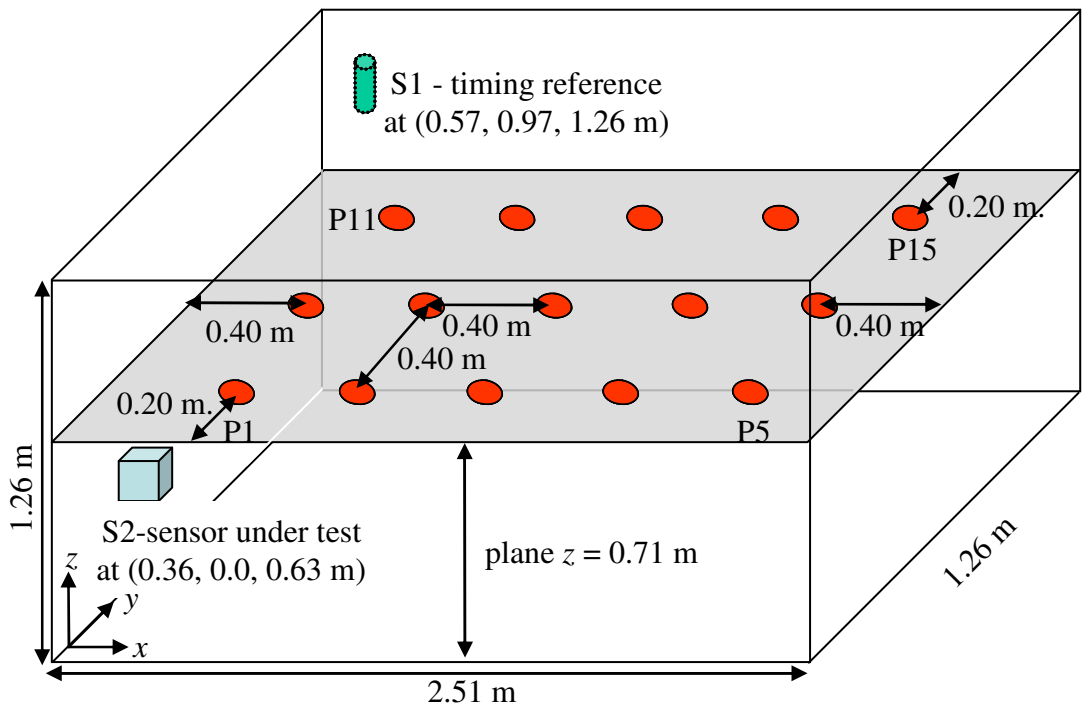


Figure 5.3 The test tank with 2 sensors (S1 and S2) installed showing 15 positions of the PD source (circles) on the plane at $z = 0.71$ m.

To evaluate which UHF sensor type is optimum for this purpose, the absolute errors between measured signals and geometric calculations for each sensor were used according to the test procedures and analysis explained in Sections 5.2.2 and 5.2.3.

5.2.2 Test procedures

The test procedures are outlined below:

- (i) Compensation of the inherent time delays within each sensor.

It is first necessary to measure the different inherent time delays caused by different construction of each type of UHF sensor. This can be achieved by using the gigahertz transverse electromagnetic (GTEM) system [121, 122] shown in Figure 5.4. The GTEM system generates a step electric field with amplitude 34 Vm^{-1} and rise time (10% - 90%) of 0.4 ns [121].

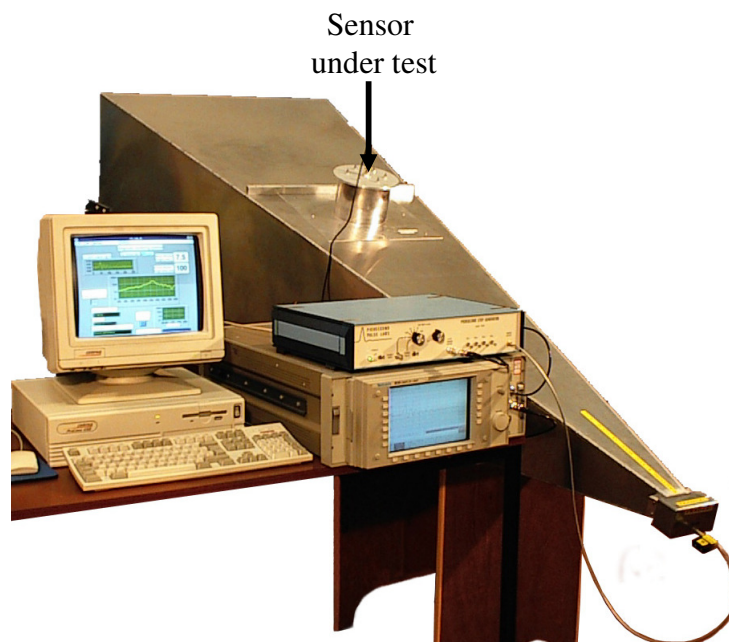


Figure 5.4 GTEM system used to measure the sensor step response.

The internal time delays of each sensor type can be measured with high resolution because the step responses were captured using an oscilloscope with a sampling rate of 10×10^9 samples/sec. It was found that the monopole has the least internal time delay because of its small size and simple structure, followed by the spiral and disc, as illustrated in Figure 5.5.

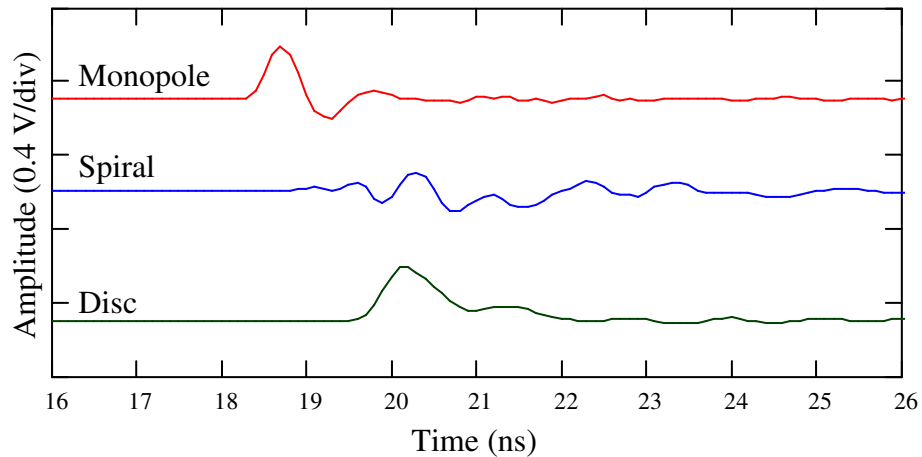


Figure 5.5 Step responses of the sensors measured on the GTEM system.

From Figure 5.1, it is apparent that the conducting spiral arms of the spiral sensor are longer than the radius of an equivalent sized disc sensor. Therefore, currents induced in the spiral arms have to travel significantly further to reach the output terminal and currents induced at simultaneously at different radii will reach the central output connector after different transit times. This tends to ‘smear’ the leading edge of the signal detected by the spiral sensor, making it hard to identify the exact initial wavefront. This is representative of a problem that could exist with other types of broadband antenna that have a complex shape resulting from optimizing the response in the frequency domain rather than the time-domain. However, multiplying the spiral antenna’s step response by a factor of 10, the initial wavefront could be estimated as shown in Figure 5.6, where it seems to arrive between the ones of the monopole and the disc types.

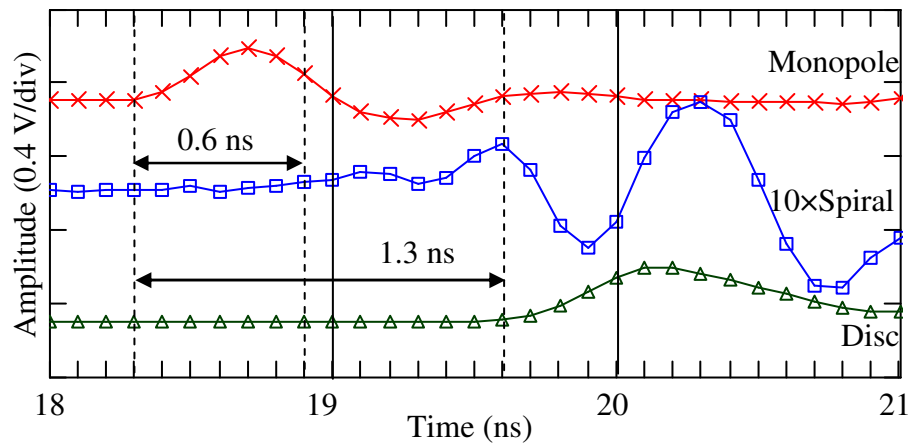


Figure 5.6 Step responses when only the step response of the spiral type was multiplied by a factor of 10 to show initial wavefront more clearly.

(ii) Positions of the two sensors and the movable PD source

With reference to Figure 5.3, the sensor under test was installed at the position marked S2 while the additional timing reference sensor was fitted at the position S1. The PD source was fixed at 0.71 m above ground on an insulating stand and was positioned around the tank at 15 points spaced at 0.4 m intervals.

(iii) Comparisons of PD responses

Starting with the monopole sensor at S2 and the pulse at P1, UHF signals from S1 and S2 were captured over 2,000 ns. Next, S2 was changed to the spiral sensor and both signals were captured again. Finally, S2 was changed to the disc sensor and the procedure was repeated. Only a single pulse per sensor per position was recorded because the avalanche pulser generated repeatable UHF signals for comparing among three sensors. Consequently, there were six signals (3 signals per sensor) for each PD position. The typical UHF signals obtained from the sensors under test are illustrated in Figure 5.7.

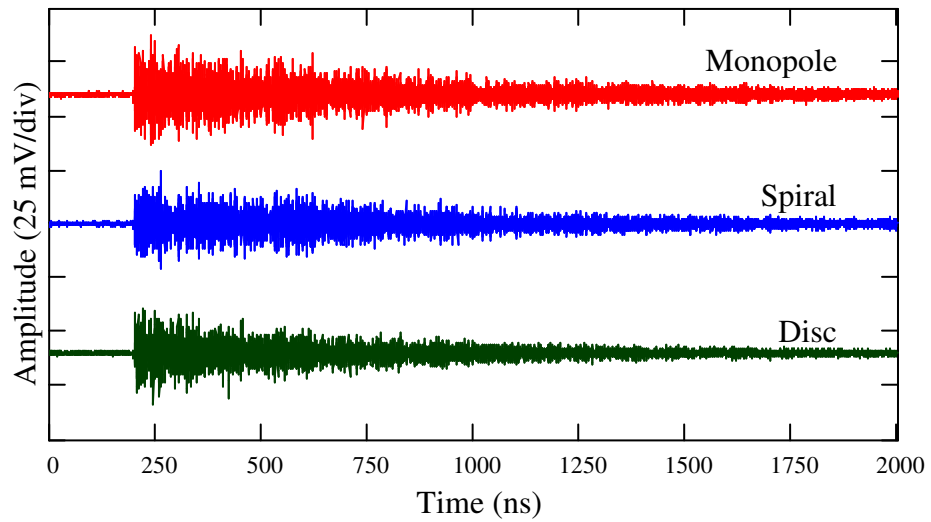


Figure 5.7 Measured UHF waveforms for each type of sensor for the pulser at P15.

(vi) The remaining PD positions were evaluated in the same way. In total, there were 45 signals (15 positions \times 3 different sensors) to be analysed.

5.2.3 Analysis

Evaluation of the three types of UHF sensors was achieved by following steps:

(i) Calculate the straight line distances between the PD source and sensor S2, as shown in Table 5.1.

Table 5.1 Distances (m) between S2 and the PD positions.

Position	Distance	Position	Distance	Position	Distance
P1	0.22	P6	0.61	P11	1.00
P2	0.49	P7	0.75	P12	1.10
P3	0.87	P8	1.04	P13	1.31
P4	1.26	P9	1.38	P14	1.59
P5	1.65	P10	1.75	P15	1.92

(ii) Next, calculate the *differential* distances between each pair of PD positions. For example, the *differential* distance between P1 and P2 = $|0.22 - 0.49| = 0.27$ m, P1 and P3 = $|0.22 - 0.87| = 0.65$ m, etc. In total, there were 105 *differential* distances, as presented in Table 5.2.

Table 5.2 Differential distances (m) for each pair of PD positions.

PD position	P2	P3	P4	P5	P6	P7	P8	P9	P10	P11	P12	P13	P14	P15
P1	0.27	0.65	1.04	1.43	0.39	0.53	0.82	1.16	1.53	0.78	0.88	1.09	1.37	1.70
P2		0.38	0.77	1.16	0.12	0.26	0.55	0.89	1.26	0.51	0.61	0.82	1.10	1.43
P3			0.39	0.78	0.26	0.12	0.17	0.51	0.88	0.13	0.23	0.44	0.72	1.05
P4				0.39	0.65	0.51	0.22	0.12	0.49	0.26	0.16	0.05	0.33	0.66
P5					1.04	0.90	0.61	0.27	0.10	0.65	0.55	0.34	0.06	0.27
P6						0.14	0.43	0.77	1.14	0.39	0.49	0.70	0.98	1.31
P7							0.29	0.63	1.00	0.25	0.35	0.56	0.84	1.17
P8								0.34	0.71	0.04	0.06	0.27	0.55	0.88
P9									0.37	0.38	0.28	0.07	1.38	0.54
P10										0.75	0.65	0.44	0.16	0.17
P11											0.10	0.31	0.59	0.92
P12												0.21	0.49	0.82
P13													0.28	0.61
P14														0.33

(iii) Compute theoretical propagating times for the differential distances obtained at step (ii) based on the propagation velocity of electromagnetic wave in air of 3×10^8 m/sec. For instance, the time difference between P1 and P2 should be $(0.27/3 \times 10^8) = 0.9$ ns. From this step, the theoretical propagating times of Table 5.3 were obtained.

(iv) Determine arrival times for each sensor type (S2 position) using the 2% threshold crossing of instantaneous UHF voltages squared, as shown in Table 5.4. Only the signals obtained from S2 were used because of the requirement for measuring observed propagating times when the signal propagated from one position to another position.

Table 5.3 Theoretical propagating times (ns) corresponding to Table 5.2.

	P2	P3	P4	P5	P6	P7	P8	P9	P10	P11	P12	P13	P14	P15
P1	0.9	2.2	3.5	4.8	1.3	1.8	2.7	3.9	5.1	2.6	2.9	3.6	4.6	5.7
P2		1.3	2.6	3.9	0.4	0.9	1.8	3.0	4.2	1.7	2.0	2.7	3.7	4.8
P3			1.3	2.6	0.9	0.4	0.6	1.7	2.9	0.4	0.8	1.5	2.4	3.5
P4				1.3	2.2	1.7	0.7	0.4	1.6	0.9	0.5	0.2	1.1	2.2
P5					3.5	3.0	2.0	0.9	0.3	2.2	1.8	1.1	0.2	0.9
P6						0.5	1.4	2.6	3.8	1.3	1.6	2.3	3.3	4.4
P7							1.0	2.1	3.3	0.8	1.2	1.9	2.8	3.9
P8								1.1	2.4	0.1	0.2	0.9	1.8	2.9
P9									1.2	1.3	0.9	0.2	4.6	1.8
P10										2.5	2.2	1.5	0.5	0.6
P11											0.3	1.0	2.0	3.1
P12												0.7	1.6	2.7
P13													0.9	2.0
P14														1.1

Table 5.4 Arrival times (ns) of measured signals.

Position	Monopole	Spiral	Disc
P1	196.4	198.0	197.6
P2	197.5	198.8	198.5
P3	197.9	199.7	199.3
P4	199.7	200.9	199.7
P5	200.6	201.5	200.9
P6	199.1	198.0	198.1
P7	200.2	199.5	200.1
P8	200.6	207.4	200.4
P9	201.4	201.3	201.5
P10	200.9	201.7	201.8
P11	202.3	200.5	201.7
P12	201.9	202.9	202.0
P13	201.9	202.4	202.3
P14	201.6	202.3	202.1
P15	202.2	203.8	202.9

(v) Calculate observed propagating times between all pairs of PD positions for each sensor type from these arrival times shown in Table 5.4. For instance, the observed propagating time between P1 and P2 for the disc sensor will be $|197.6 - 198.5| = 0.9$ ns. From this step, all observed propagating time between pairs of PD positions for each sensor type were acquired. For example, results for the disc type are summarized in Table 5.5.

Table 5.5 Observed propagating times (ns) between pairs of PD positions obtained from the disc type sensor.

PD position	P2	P3	P4	P5	P6	P7	P8	P9	P10	P11	P12	P13	P14	P15
P1	0.9	1.7	2.1	3.2	0.5	2.5	2.7	3.9	4.2	4.0	4.4	4.7	4.4	5.3
P2		0.8	1.2	2.3	0.4	1.6	1.8	3.0	3.3	3.1	3.5	3.8	3.5	4.4
P3			0.4	1.5	1.2	0.8	1.0	2.2	2.5	2.4	2.7	3.0	2.8	3.6
P4				1.2	1.6	0.5	0.7	1.8	2.1	2.0	2.3	2.6	2.4	3.2
P5					2.7	0.7	0.5	0.6	1.0	0.8	1.2	1.5	1.2	2.0
P6						2.0	2.2	3.4	3.7	3.5	3.9	4.2	3.9	4.8
P7							0.2	1.4	1.7	1.5	1.9	2.2	1.9	2.8
P8								1.1	1.5	1.3	1.7	2.0	1.7	2.6
P9									0.3	0.2	0.5	0.8	0.6	1.4
P10										0.2	0.2	0.5	0.2	1.1
P11											0.4	0.7	0.4	1.2
P12												0.3	0.0	0.9
P13													0.2	0.6
P14														0.8

(vi) Compare observed propagating time obtained at step (v) with those expected based purely on the theoretical calculations obtained at step (iii) to evaluate the absolute errors.

5.2.4 Results

Following the procedure outlined in Section 5.2.3, the absolute errors between observed propagating times and theoretical calculations can be obtained to identify the optimum sensor for the UHF PD location applications. An example of the absolute errors calculated for the disc sensor is shown in Table 5.6. To assess among three types of UHF sensor (disc, monopole, and spiral), absolute errors are plotted together in Figure 5.8.

Table 5.6 Absolute errors (ns) for the disc type sensor.

PD positions	P2	P3	P4	P5	P6	P7	P8	P9	P10	P11	P12	P13	P14	P15
P1	0.01	0.49	1.41	1.54	0.79	0.75	0.01	0.00	0.90	1.43	1.47	1.05	0.13	0.40
P2		0.50	1.42	1.55	0.00	0.74	0.02	0.01	0.91	1.42	1.46	1.04	0.14	0.41
P3			0.92	1.05	0.31	0.43	0.47	0.49	0.41	1.92	1.95	1.54	0.36	0.09
P4				0.13	0.61	1.25	0.07	1.41	0.51	1.11	1.80	2.46	1.28	1.01
P5					0.75	2.29	1.53	0.26	0.64	1.36	0.66	0.33	1.01	1.14
P6						1.54	0.78	0.79	0.10	2.23	2.26	1.85	0.66	0.40
P7							0.76	0.75	1.64	0.69	0.72	0.31	0.88	1.14
P8								0.02	0.88	1.18	1.48	1.07	0.12	0.38
P9									0.90	1.10	0.40	0.59	4.03	0.40
P10										2.33	1.97	0.98	0.30	0.50
P11											0.03	0.38	1.56	1.83
P12												0.41	1.59	1.86
P13													0.68	1.45
P14														0.27

The values in each cell in Table 5.6 represent the error in observed time between pairs of PD locations compared with the theoretical time based on geometrical path length.

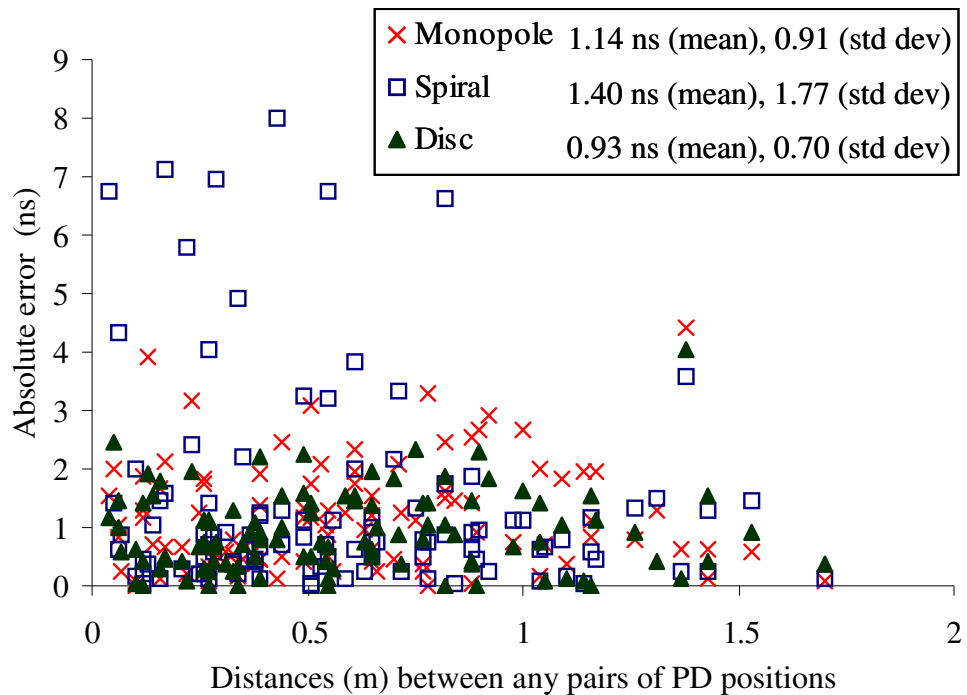


Figure 5.8 Relationship between absolute errors of 3 types of UHF sensors plotted against distances.

Most of the errors for the disc are in a limited band with a mean of 0.93 ns and standard deviation of 0.70 ns. For the monopole and spiral, there is more scatter with means of 1.14 ns and 1.40 ns, and standard deviations of 0.91 and 1.77 ns, respectively. Therefore, among the monopole, disc and spiral UHF sensors tested, the disc could provide the highest accuracy for PD location applications when it is used for capturing measured UHF PD signals [123]. Consequently, the disc-type UHF sensor was used in subsequent studies concerned with determining absolute arrival times.

5.3 Experimental arrangement

The experimental arrangement employed here is similar to that described in section 4.4.1. However, the objective of the laboratory experiments was to investigate the accuracy of measured arrival times with the following three sets of conditions that may arise during PD monitoring.

5.3.1 Study 1: The PD moved around the shielded room (Figure 4.19)

The aim of this study was to investigate the accuracy of UHF PD location in the shielded room when only the PD direct propagation paths were considered. In these tests, the spark plug tip (Figure 4.20) was maintained in the upright direction. It was moved around the room in a total of 43 positions at three different heights, which were on the planes $z = 0.23$ m (G1 – G18), 0.92 m (P5 - P20) and 1.34 m (Q1 - Q9). The coordinates are given in Table 5.7.

Table 5.7 Coordinates of PD positions for study 1.

PD Position	Coordinates in m.			PD Position	Coordinates in m.		
	<i>x</i>	<i>y</i>	<i>z</i>		<i>x</i>	<i>y</i>	<i>z</i>
G1	0.11	0.09	0.23	P5	0.28	0.21	0.92
G2	0.54	0.09	0.23	P6	0.96	0.21	0.92
G3	1.05	0.10	0.23	P7	1.56	0.21	0.92
G4	1.48	0.10	0.23	P8	2.16	0.22	0.92
G5	1.92	0.09	0.23	P9	0.23	1.25	0.92
G6	2.36	0.11	0.23	P10	0.58	1.24	0.92
G7	0.07	1.23	0.23	P11	0.99	1.21	0.92
G8	0.49	1.23	0.23	P12	1.50	1.19	0.92
G9	0.98	1.25	0.23	P13	1.94	1.24	0.92
G10	1.49	1.23	0.23	P14	2.18	1.25	0.92
G11	2.02	1.23	0.23	P15	0.23	2.23	0.92
G12	2.36	1.25	0.23	P16	0.55	2.08	0.92
G13	0.07	2.32	0.23	P17	0.98	2.09	0.92
G14	0.48	2.36	0.23	P18	1.42	2.09	0.92
G15	0.93	2.36	0.23	P19	1.96	2.09	0.92
G16	1.39	2.34	0.23	P20	2.21	2.10	0.92
G17	1.87	2.34	0.23	Q1	0.62	0.25	1.34
G18	2.44	2.34	0.23	Q2	1.19	0.25	1.34
Q3	1.98	0.24	1.34	Q7	0.71	2.12	1.34
Q4	0.66	1.17	1.34	Q8	1.26	2.12	1.34
Q5	1.21	1.25	1.34	Q9	2.01	2.18	1.34
Q6	1.98	1.22	1.34				

5.3.2 Study 2: Variation of spark plug tip orientation

Different directions of PD current pulse flow will radiate electric fields with different orientations, so the UHF sensors may respond differently, as reported in [124]. Moreover, the study in [87] has shown that the UHF signals at the UHF sensor are governed by the radial electric field incident on the UHF sensor. Hence, it is possible that different orientations of the PD source could affect the initial wavefronts of UHF signals. Consequently, changing the spark plug direction was investigated in terms of its effect on the accuracy on UHF PD location.

The PD source was placed approximately in the centre line of the shielded room (Figure 4.19) with plane $z = 0.92$ m for five positions (D1 – D5), as shown in Figure 5.9, while the spark plug tip was altered in four directions for each PD position, which were upright, pointing to REF, pointing to S, and pointing to Back. Table 5.8 lists the coordinates of the PD positions.

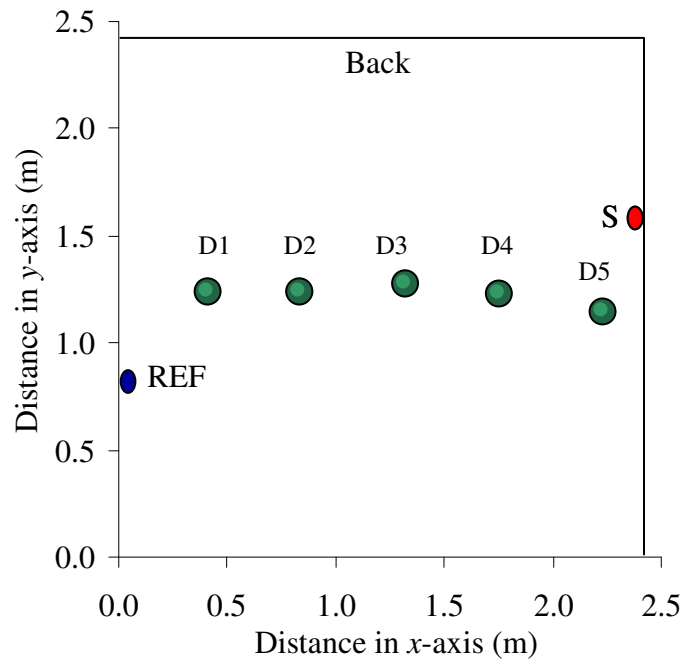


Figure 5.9 Top view of the shielded room showing the five PD positions (D1–D5).

Table 5.8 Coordinates of PD positions for study 2.

PD position	Coordinates (m)		
	<i>x</i>	<i>y</i>	<i>z</i>
D1	0.40	1.25	0.92
D2	0.83	1.25	0.92
D3	1.31	1.28	0.92
D4	1.75	1.24	0.92
D5	2.22	1.14	0.92

5.3.3 Study 3: Increasing the sensitivity of the measurement

One factor that could affect the accuracy of arrival time measurement is an effect of the sensitivity of an oscilloscope being recorded. For the same signal, different ranges will give different noise levels, as demonstrated in Figure 5.10. Compared between 10 mV/div and 50 mV/div settings, it is clearly seen that the UHF signal acquired at 10 mV/div contains less background noise than the other. The high background noise level produced by 50 mV/div sensitivity comes from the analogue to digital conversion process of the oscilloscope itself, not from the sensors.

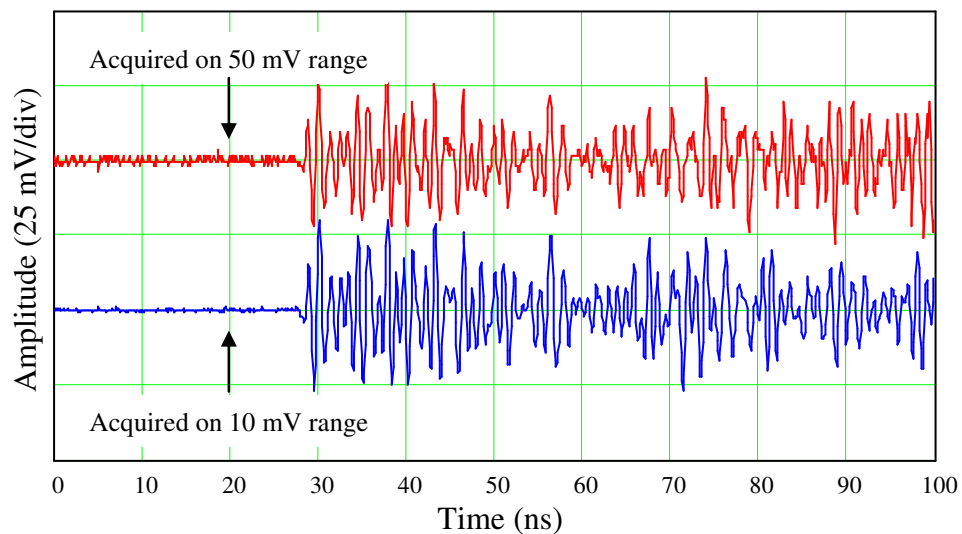


Figure 5.10 UHF signals at position D1 of study 2. This is to indicate the different noise levels may arise when different sensitivity settings are used.

Thus, the effect of the sensitivity of the oscilloscope on PD location accuracy was investigated in this study. The spark plug tip was fixed in the upright direction and was kept at height $z = 0.92$ m. The PD source was placed in nine positions (R1 – R9) around a quarter of the shielded room (Figure 4.19), as shown in Figure 5.11. The PD position coordinates are given in Table 5.9. Since the means of absolute errors discovered during study 1 in this quarter (see Section 5.5.1) were higher than

elsewhere in the shielded room, it was selected as the focus for this experiment in order to observe whether errors can be reduced.

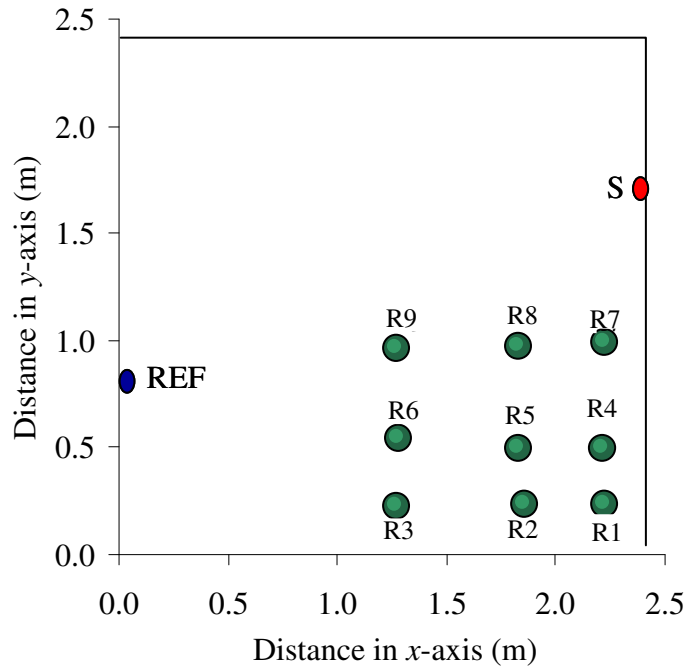


Figure 5.11 Top view of the shielded room to illustrate PD positions (R1 – R9).

Table 5.9 Coordinates of PD positions for study 3.

PD position	Coordinates (m)		
	x	y	z
R1	2.22	0.24	0.92
R2	2.21	0.50	0.92
R3	2.22	1.08	0.92
R4	1.90	0.24	0.92
R5	1.82	0.50	0.92
R6	1.82	0.98	0.92
R7	1.26	0.23	0.92
R8	1.27	0.55	0.92
R9	1.26	0.97	0.92

The oscilloscope used in studies 1 and 2 was the model TDS694C, which has a maximum sensitivity of 10 mV/div, vertical resolution of 8 bits, a sampling rate of

10×10^9 samples/sec and a bandwidth of 3×10^9 Hz. The 50 mV/div setting was used to allow capture of the signals without any clipping.

For study 3, where clipping was permitted to allow sensitive measurements of the leading edge, a LeCroy WaveRunner 104Xi with 2 mV/div sensitivity and vertical resolution of 8 bits was used. It captured the UHF signals with a sampling rate of 5×10^9 samples/sec and bandwidth of 1×10^9 Hz.

5.4 Methodology

The methodology explained here will be employed for all three studies. To determine absolute arrival times obtained from the sensors, the 2 % threshold crossing (2% TH) of instantaneous UHF voltage squared was used. However, absolute arrival times themselves cannot be evaluated directly in these studies because they depend on the variable triggering position. Hence, measured time *differences* (ΔT_{MEA}) computed between sensor REF and sensor S were used. These were compared with geometric time differences (ΔT_{GEO}) in order to evaluate the accuracy of PD location. An evaluation method for the accuracy of UHF PD location can be represented conceptually by using a diagram illustrated in Figure 5.12.

In the diagram shown in Figure 5.12, the right hand side generates the expected linear relationship between the geometric time differences (ΔT_{GEO}) and differential distances (Δd) based on geometric calculation. d_{REF} and d_S were measured as distances from the spark plug tip to the centres of sensors REF and S, respectively. Values of Δd for each PD position were acquired by subtraction between d_{REF} and d_S . The left hand side of the diagram is concerned with generating measured time differences (ΔT_{MEA}) obtained from the laboratory experiments.

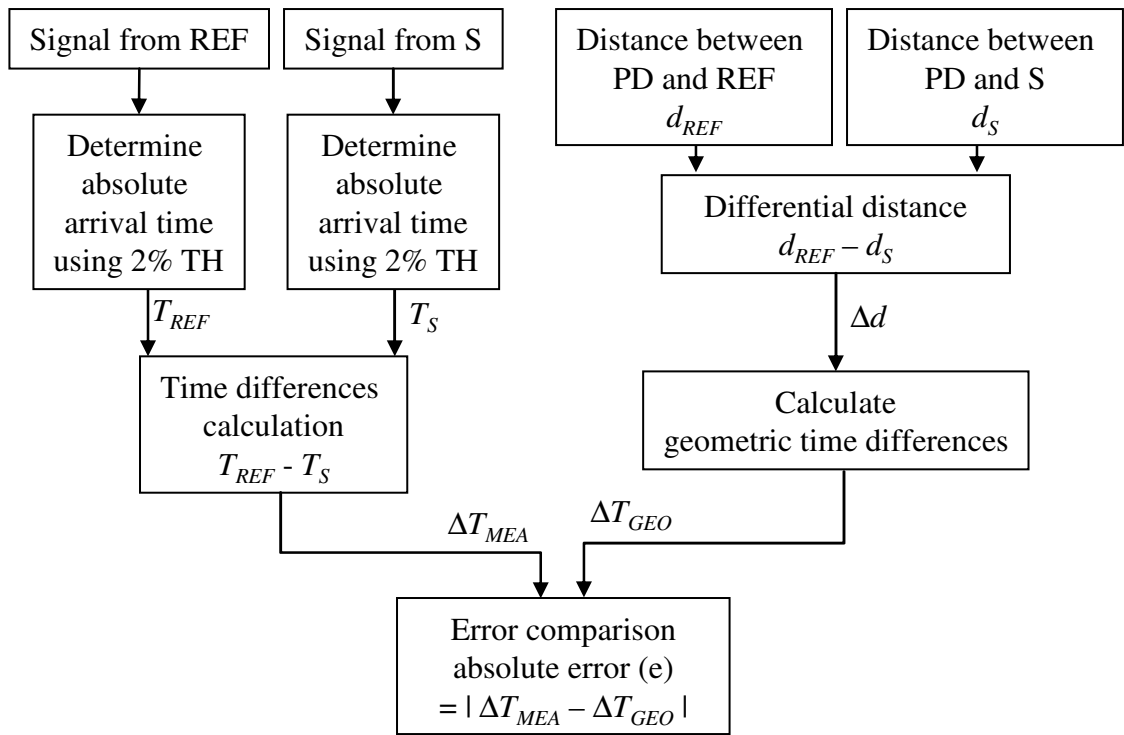


Figure 5.12 Diagram to illustrate the process for evaluating the accuracy of the UHF PD location.

Ten pairs of the UHF signals were captured for each PD position during the laboratory experiments, so that 10 ΔT_{MEA} values were obtained. Accordingly, the average values from those 10 ΔT_{MEA} values were used to be representative of ΔT_{MEA} for each PD position and were used for error comparisons. The accuracy of UHF PD location was assessed by error comparisons, computed between $|\Delta T_{MEA} - \Delta T_{GEO}|$ for each PD position and the velocity of PD propagation in insulating materials (e.g. propagation in air = 0.30 m/ns, in transformer oil = 0.20 m/ns).

The error comparison analysis was divided into two approaches. The first way was to consider the mean of the errors for the whole shielded room and the second was to assess the absolute errors relative to Δd . The entire procedure is summarised in Figure 5.13.

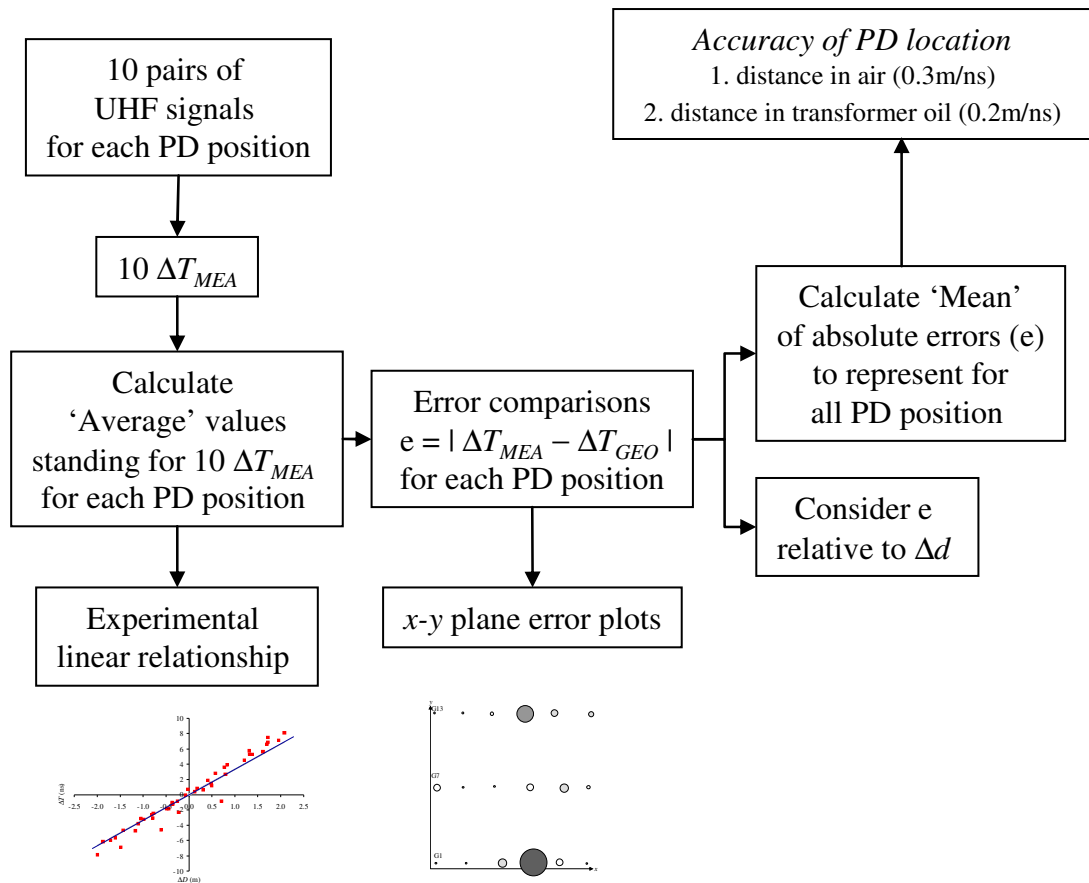


Figure 5.13 Diagram to illustrate the entire procedure used in the analysis.

5.5 Results and analysis

5.5.1 Study 1: The PD moved around the shielded room (Figure 4.19)

Following the methodology explained in Section 5.4, all ΔT_{GEO} , $\Delta T_{ME A}$, and Δd values were computed. Δd and $\Delta T_{ME A}$ values obtained from the laboratory experiments are plotted in Figure 5.14 along with the expected linear relationship between Δd and ΔT_{GEO} . It can be seen that the majority of the measured time differences align well with the expected linear relationship.

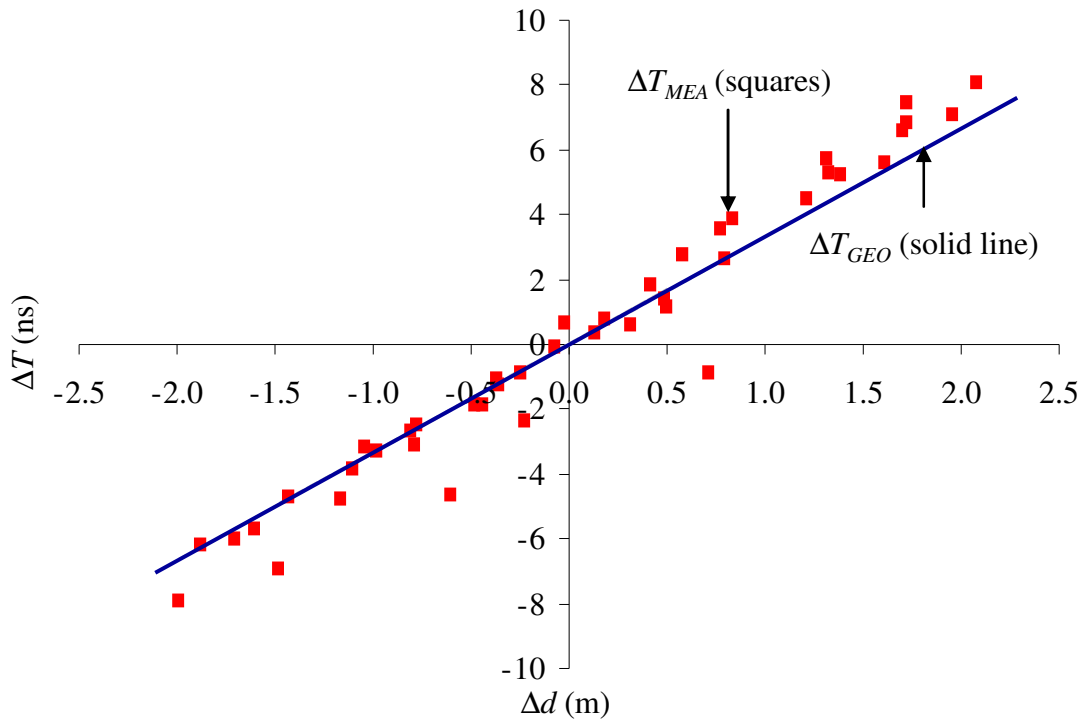


Figure 5.14 Relationship between ΔT and Δd for ΔT_{MEA} and ΔT_{GEO} , tested in the shielded room.

In terms of the accuracy of PD location, x - y plane plots illustrating the mean of absolute errors (e) for each PD position in the shielded room are shown in Figure 5.15. The circles in these plots have a radius proportional to the error e .

In Figure 5.15, there are 24 out of 43 positions (56%) providing an error e within the acceptable 0.5 ns tolerance and 3 positions (7%) giving the error e in excess of 2.0 ns. Considered in relation to PD position, the error values around the centre of the shielded room are relatively low (< 1 ns), while those values for positions near to the x -axis are comparatively high (> 2.0 ns). For the other positions, the error values disperse. Consequently, there is no clear pattern of error e as a function of PD position.

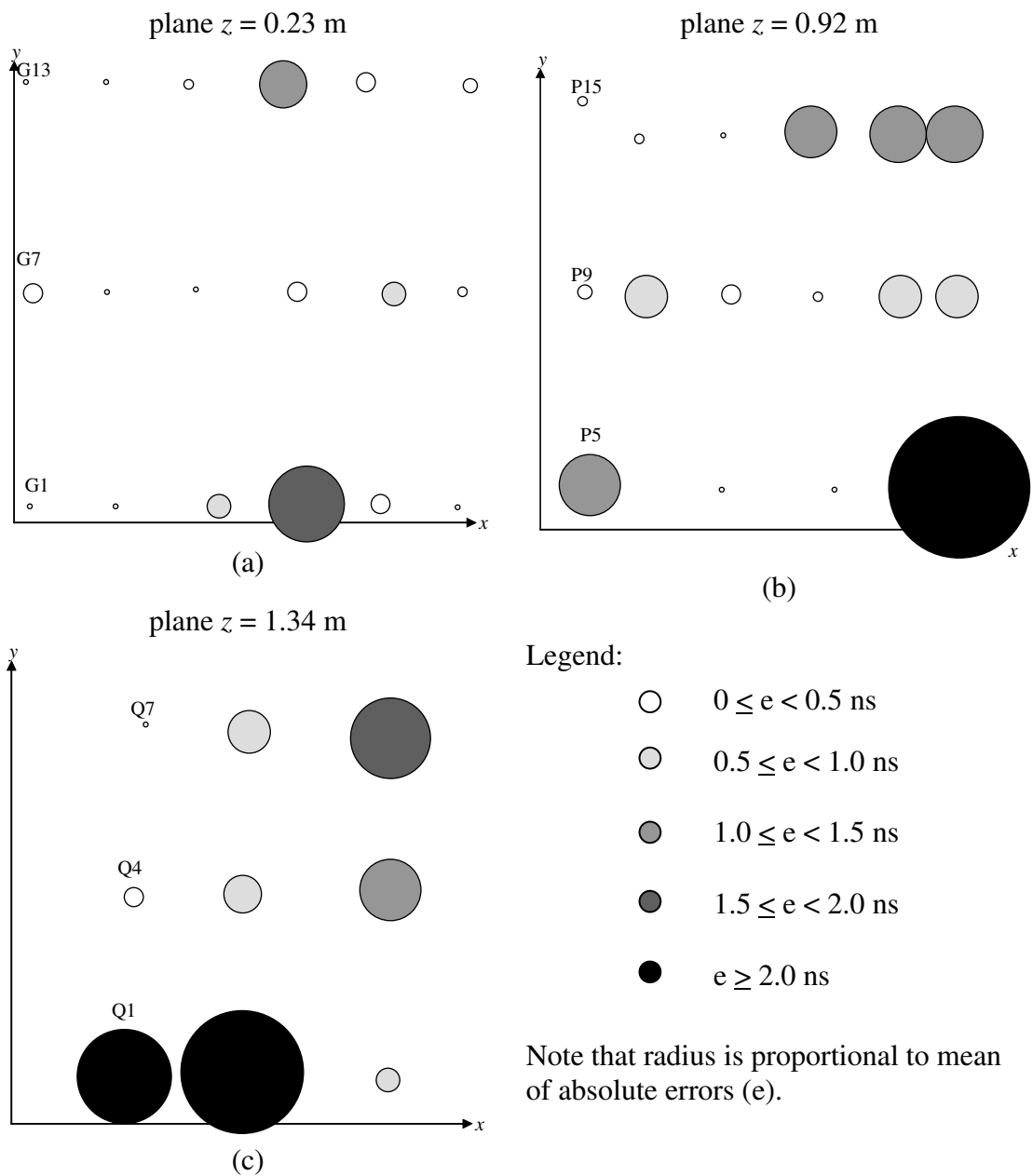


Figure 5.15 x - y plane plots for each z -plane to illustrate the means of absolute errors (e) of each PD position, tested in the shielded room: (a) At plane $z = 0.23$ m, (b) At plane $z = 0.92$ m, (c) At plane $z = 1.34$ m.

5.5.2 Study 2: Variation of spark plug tip orientation

The results according to the process described in Section 5.4 are illustrated in Figure 5.16. This is to show how the measured time differences deviate from the expected linear relationship while the influence of spark plug tip orientation is visible simultaneously. Figure 5.16 reveals that the trends of measured time differences obtained from different spark plug tip orientations follow the linear relationship reasonably well, except at the longer differential distances.

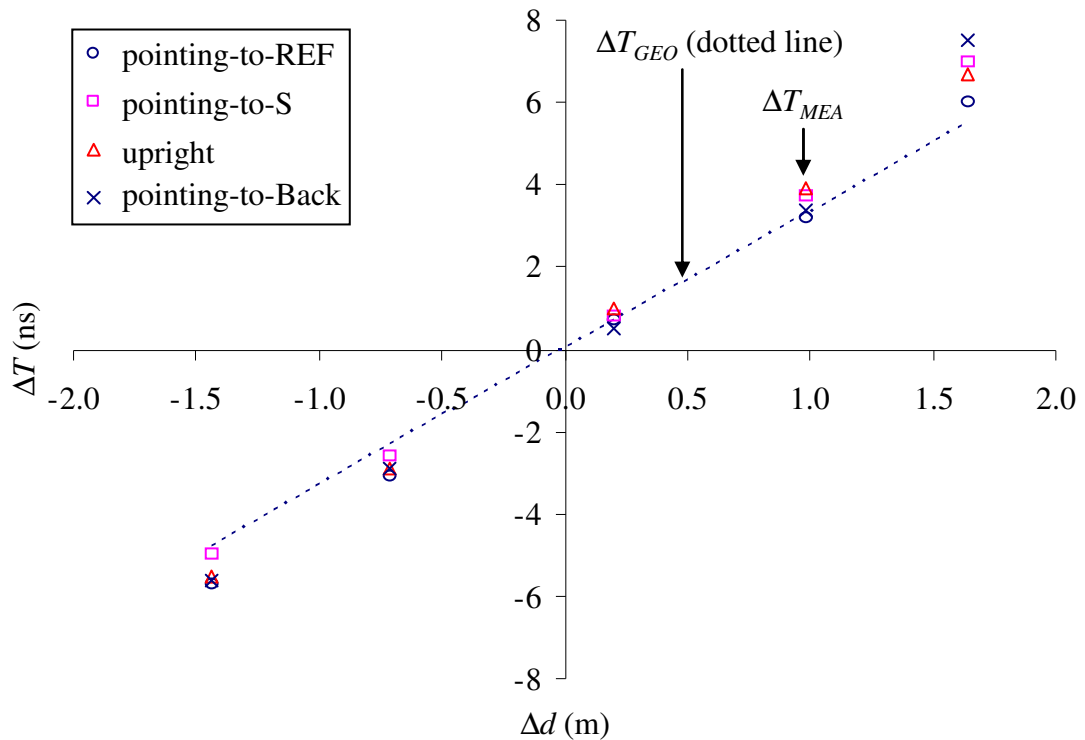
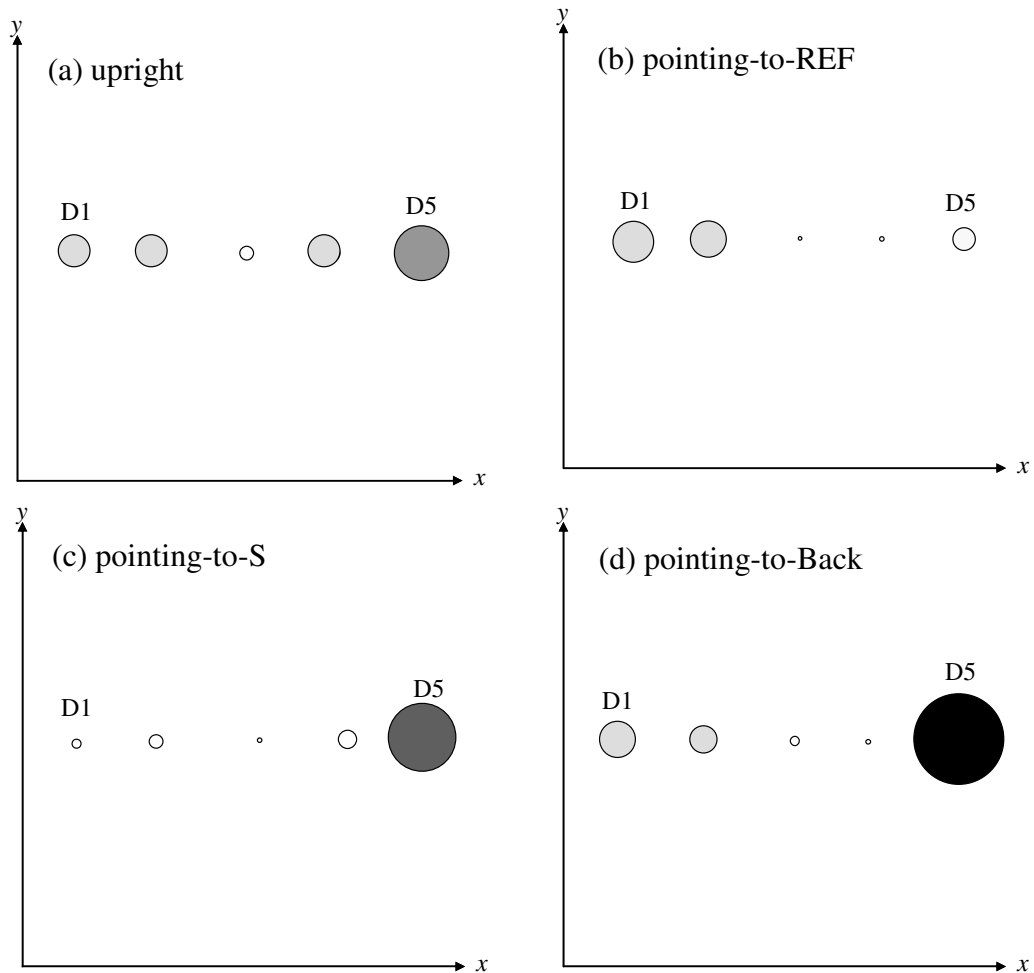


Figure 5.16 Relationship between ΔT and Δd for ΔT_{MEA} and ΔT_{GEO} when variation of the spark plug tip orientation was investigated.

In Figure 5.17, x - y plane plots illustrating the mean of absolute errors (e) for each PD position are depicted. This shows that the variation of the PD source orientation can affect the initial wavefronts of the UHF signals, especially when the PD takes place further away from the sensors.



Legend:

- $0 \leq e < 0.5$ ns
- $0.5 \leq e < 1.0$ ns
- $1.0 \leq e < 1.5$ ns
- $1.5 \leq e < 2.0$ ns
- $e \geq 2.0$ ns

Note that radius is proportional to mean of absolute errors (e).

Figure 5.17 x-y plane plots for each variation of the spark plug tip orientation to illustrate the means of absolute errors (e) for each PD position in the shielded room: (a) Upright, (b) Pointing-to-REF, (c) Pointing-to-S, (d) Pointing-to-Back.

5.5.3 Study 3: Increasing the sensitivity of the measurement

The UHF signals used in this study were acquired using the 2 mV range in order to investigate improvement of arrival time measurements using higher sensitivity settings. Note that all the UHF signals used in studies 1 and 2 were acquired using the 50 mV range.

Applying the procedures presented in Section 5.4, the results shown in Figure 5.18 are obtained. Figure 5.19 shows x - y plane plots illustrating the mean of absolute errors (ϵ) for each PD position in the shielded room. The results show that increasing the sensitivity of the measurement could offer better resolution of the initial wavefronts of the UHF signals, causing improvement of the accuracy of the measured time differences.

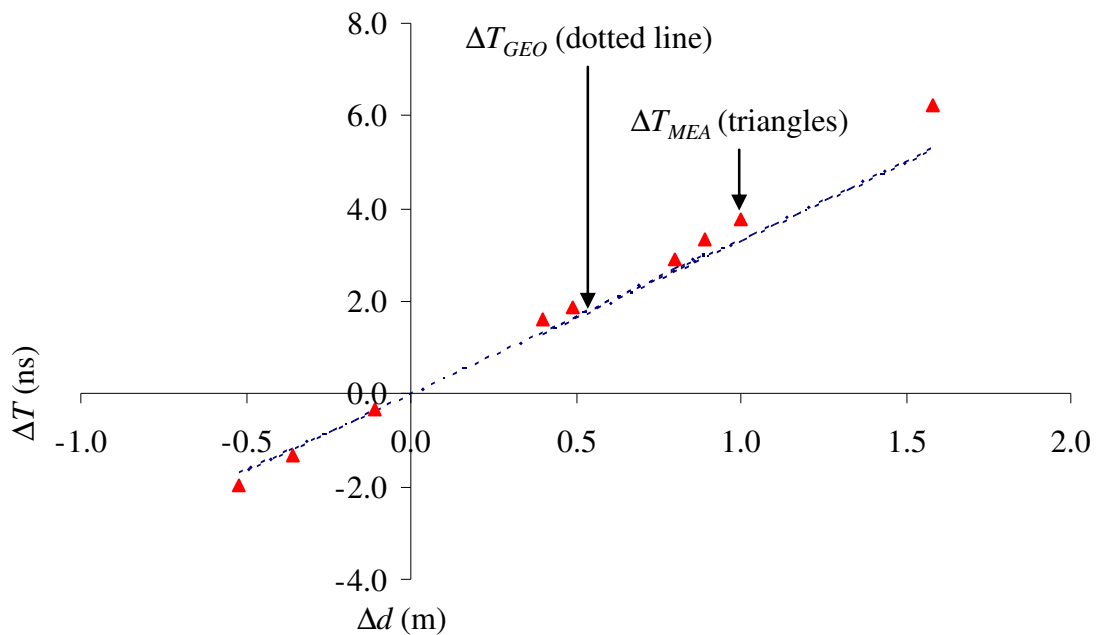


Figure 5.18 Relationship between ΔT and Δd for ΔT_{MEA} and ΔT_{GEO} when the sensitivity of 2 mV/div was utilised.

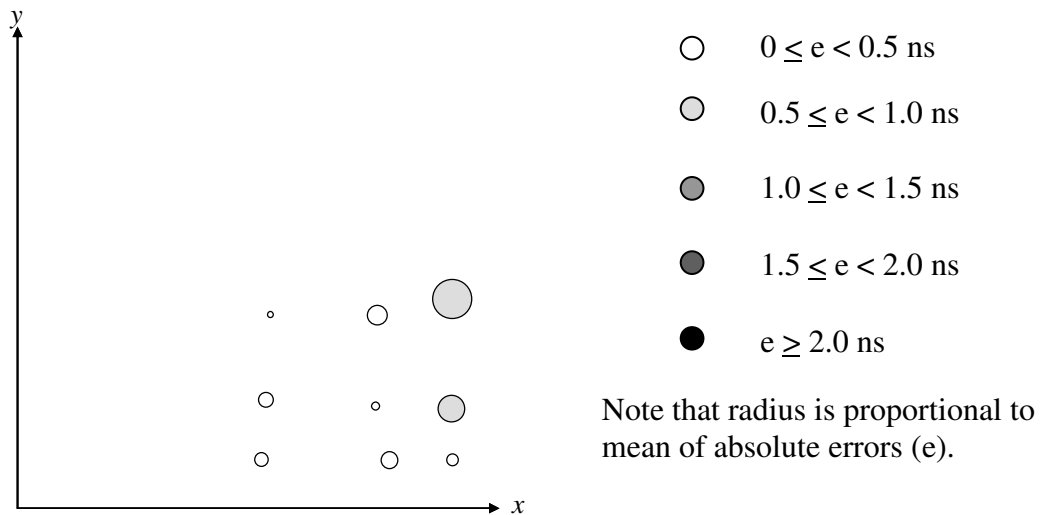


Figure 5.19 x-y plane plots to illustrate the means of absolute errors (e) for each PD position of the shielded room when the sensitivity of 2mV/div was utilised.

5.5.4 Evaluation of results

(i) Test arrangement summary

Table 5.10 summarises the three test arrangements investigated in studies 1, 2 and 3 including the measurement configurations and total number of PD positions tested.

(ii) Comparisons of accuracy for PD location

Using the procedure outlined in Figure 5.13, mean values of absolute errors and the accuracy of PD location for all three studies are summarised in Table 5.11. These are 0.68 ns, 0.60 ns and 0.32 ns for studies 1, 2 and 3, respectively. These errors correspond to 0.20 m, 0.18 m, and 0.10 m propagation distances in air and 0.14 m, 0.12 m and 0.06 m in transformer oil. Studies 1 and 2 both provided higher mean values of absolute errors than study 3, in which the sensitivity of the measurement was increased. This suggests that using a very high sensitivity acquisition setting can reduce absolute errors, improving the accuracy of PD location. In terms of the

influence of spark plug orientation, there is no strong effect on the accuracy of PD location within the scope of the test carried out in study 2.

Table 5.10 Summary of test arrangements.

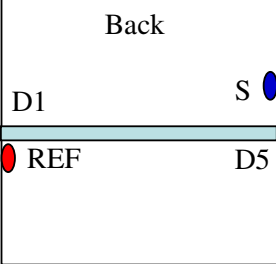
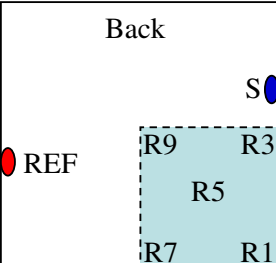
Test in Section	Sensitivity	Spark plug tip direction	Spark unit locations at plane z =	No. of PD Positions
5.3.1	50mV/div	upright	0.23 m 0.92 m 1.34 m	18 (G1 – G18) 16 (P5 – P20) 9 (Q1 – Q9) <i>total = 43</i>
5.3.2	50mV/div	upright pointing-to-REF pointing-to-S pointing-to-Back	0.92 m 	5 (D1 – D5) with 4 tip directions <i>total = 20</i>
5.3.3	2mV/div	upright	0.92 m 	R1 – R9 <i>total = 9</i>

Table 5.11 Results obtained from test arrangements shown in Table 5.10.

Test in Section	Spark plug tip direction	Mean values of absolute errors (ns)	Accuracy of PD location Distance (m.)	
			in air	in oil
5.5.1	upright	0.68	0.20	0.14
5.5.2	upright	0.68	0.20	0.14
	direct-to-REF	0.46	0.14	0.09
	direct-to-S	0.50	0.15	0.10
	direct-to-Back	0.74	0.22	0.15
	<i>average all orientations</i>	<i>0.60</i>	<i>0.18</i>	<i>0.12</i>
5.5.3	upright	0.32	0.10	0.06

(iii) Evaluating errors (e) relative to differential distances (Δd) between the two sensors and the PD sources

Only data from study 1 was considered because the 43 PD positions were well dispersed around the shielded room (shown in Figure 4.19) and should reflect the characteristics of measured time differences for the whole tank. Figure 5.20 shows the experimental data and its best straight line fit, together with the expected theoretical linear relationship.

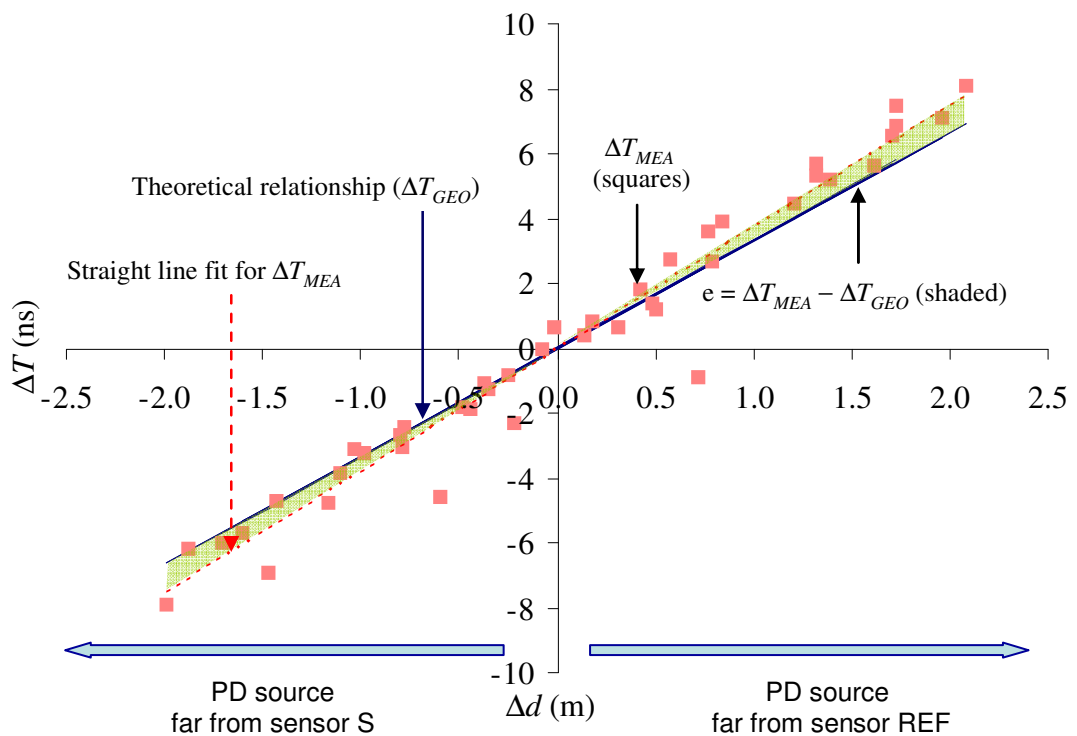


Figure 5.20 Experimental (ΔT_{MEA}) and theoretical (ΔT_{GEO}) relationships for study 1 showing the error e relative to differential propagation distances (Δd).

The best straight line fit to the experimental data (ΔT_{MEA}) shown in Figure 5.20 was calculated using the least squares fit, which is $\Delta T_{MEA} = 3.77(\Delta d)$ with a correlation coefficient R^2 of 0.96. Based on the theoretical relationship (ΔT_{GEO}) in Eqn. 4.5 $\{\Delta T_{GEO} = 3.33(\Delta d)\}$, the error e relative to the differential propagation distances can be computed as follows:

$$e = \Delta T_{MEA} - \Delta T_{GEO} = 0.44(\Delta d) \quad (5.1)$$

The shaded area between the lines in Figure 5.20 indicates the variation of error e with differential propagation distance Δd obtained using Eqn. 5.1. Since it is impossible for the signal to arrive earlier than expected, it must be that the signal at the more distant sensor appears to arrive later than expected. For example, consider the right hand side of the graph in Figure 5.20. The distance from the PD source to sensor REF is further than to sensor S, and the measured arrival time from sensor REF appears later than expected.

From the comparisons between experimental results and geometric calculations, when Δd values increase, the error $\Delta T_{MEA} - \Delta T_{GEO}$ increases at a rate of 0.44 ns/m. This effect may be due to dispersion of the wavefront that has travelled further, which means it satisfies the onset criteria later.

5.6 Arrival time consistency index for evaluating the signal onset

5.6.1 Concept

Determining accurate UHF signal arrival times is a challenging task to automate and various approaches have been proposed, among which the 2% threshold crossing of instantaneous UHF voltage squared is efficient and simple for practical implementation. However, the use of a specific percentage needs to be justified. Ideally, each UHF signal from the sensor would provide a consistent arrival time if the signal possesses a high rate of change of voltage with time, like the extreme example of an impulse shown in Figure 5.21. The arrival time of the impulse is constant at 50 ns whether the threshold is 2%, 20%, 50% or 99%.

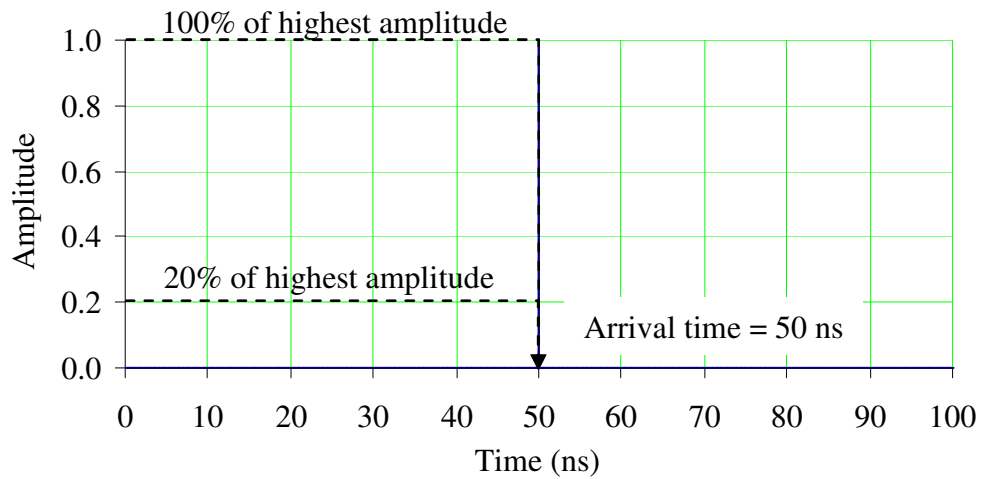


Figure 5.21 An impulse to show the ideal scenario for determining the signal arrival time.

Practical UHF signals captured in real applications have continuously variable rates of changes of voltage with time. Prior to the arrival of the UHF signal, there will always be a certain level of noise. The best choice of threshold is a compromise between not triggering too early (on noise) or too late (because the signal is small). The quality of a particular threshold might be judged by assessing the sensitivity of arrival time to small changes in the threshold value. To demonstrate the potential variability of arrival times of UHF signals, two UHF signals from study 3 were used. The signal shown in Figure 5.22 gives a constant arrival times for threshold from 1% to 5%, while the signal illustrated in Figure 5.23 exhibits quite variable arrival times. Considering the slopes of the initial wavefronts, the signal in Figure 5.22(b) rises much more steeply than the one in Figure 5.23(b).

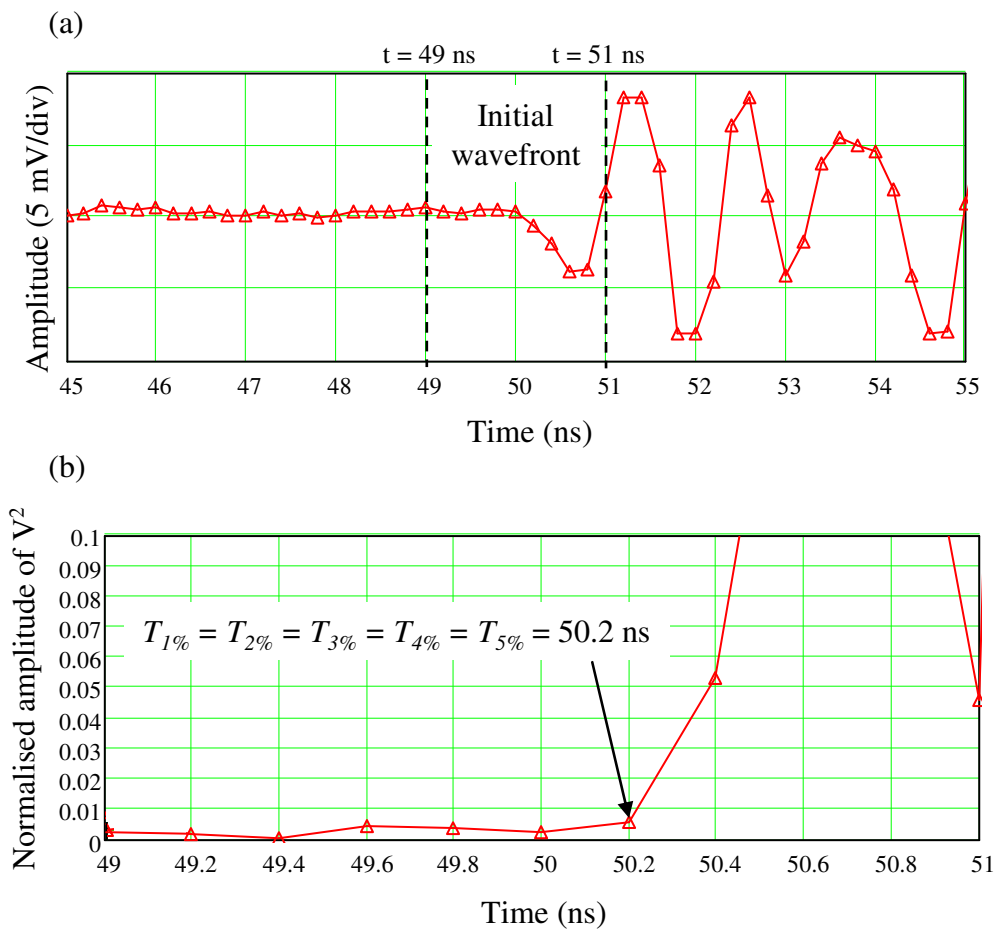


Figure 5.22 UHF signal obtained from sensor S at $R3$: (a) Initial wavefront, (b) Its constant arrival times resulted from 1% to 5% threshold crossing. This is to demonstrate consistent arrival times.

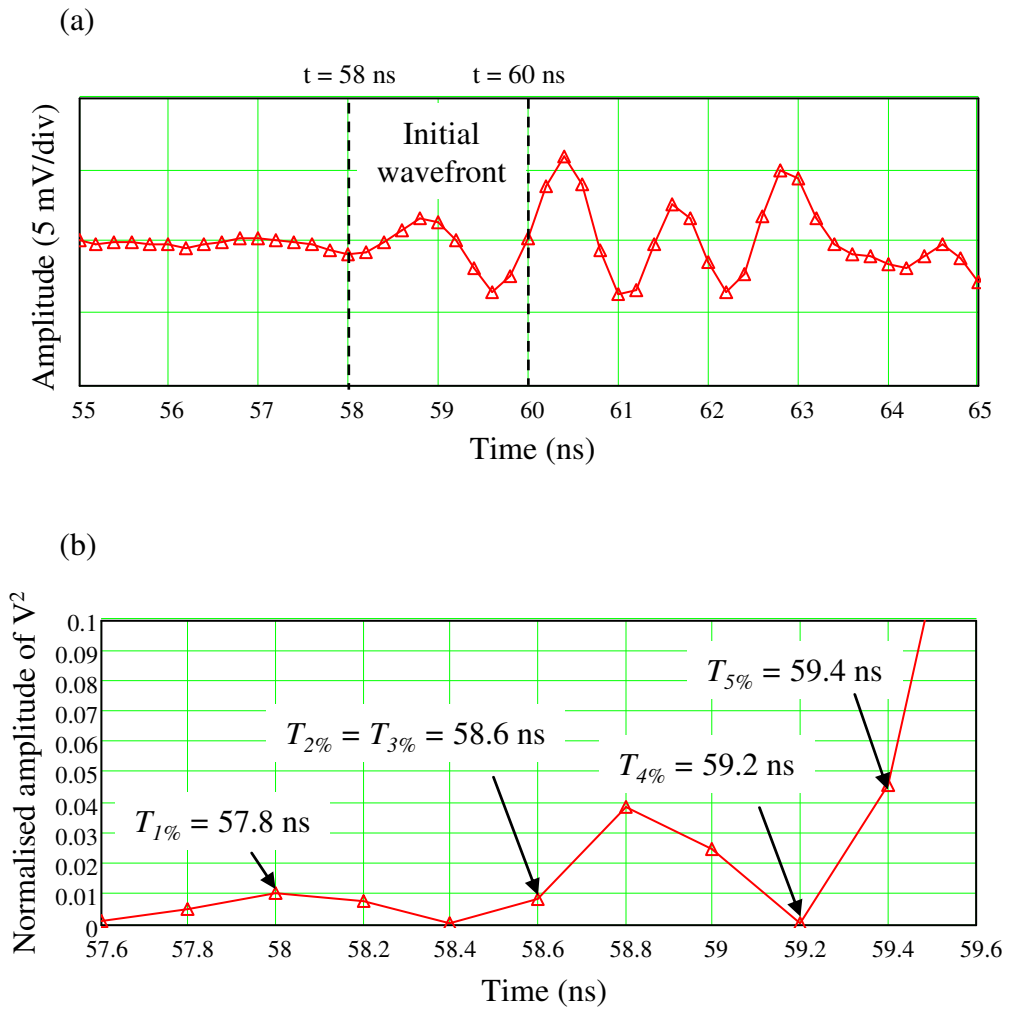


Figure 5.23 UHF signal obtained from sensor REF at R2: (a) Initial wavefront, (b) Its variable arrival times resulted from 1% to 5% threshold crossing. This is to illustrate the challenge of selecting a specific threshold that gives a consistent arrival time when there is high sensitivity of arrival times to small changes of threshold value.

Hence, a new index, namely an arrival time *consistency index* (CI), is proposed (based on the concept of standard deviation) in order to assess the sensitivity of arrival time to small changes in the threshold value within a particular threshold interval. To define the arrival time consistency index clearly, Eqn. 5.2 [125] was employed.

$$\sigma = \sqrt{\frac{\sum (x - \bar{x})^2}{n}} \quad (5.2)$$

where σ = standard deviation
 x = values of each sample
 \bar{x} = mean value of all samples
 n = size of samples

To understand clearly how the *CI* is adapted from Eqn. 5.2, it is beneficial to decide a threshold being assessed (e.g. 2% threshold) and a threshold interval of interest (e.g. 1% to 5%). Therefore, σ becomes *CI* and \bar{x} becomes the arrival time obtained from 2% (the threshold being assessed). The x values have been replaced with arrival times obtained from 1% to 5%, excluding 2%. Finally, n is set to 4 because there are four values of arrival times obtained from 1% to 5% being assessed against 2% threshold.

To demonstrate how the calculation might be applied for the 2% threshold, the UHF signals shown in Figure 5.22 and Figure 5.23 were again used. For the signal shown in Figure 5.22, the arrival times obtained from 1% to 5% are 50.2 ns for all threshold values and a low score for *CI* would also be expected. To compute *CI* at 2%, substitute the five arrival times into Eqn. 5.2, which are $T_{2\%} = 50.2$ ns, $T_{1\%} = T_{3\%} = T_{4\%} = T_{5\%} = 50.2$ ns, $n = 4$. *CI* at 2% can be calculated as follows:

$$CI_{2\%} = \sqrt{\frac{(50.2 - 50.2)^2 + (50.2 - 50.2)^2 + (50.2 - 50.2)^2 + (50.2 - 50.2)^2}{4}} = 0$$

For the signal illustrated in Figure 5.23, the arrival times are variable and a higher score for *CI* would be expected. To assess *CI* at 2%, replace the variables of the signal into Eqn. 5.2, which are $T_{2\%} = 58.6$ ns, $T_{1\%} = 57.8$ ns, $T_{3\%} = 58.6$ ns, $T_{4\%} = 59.2$ ns, $T_{5\%} = 59.4$ ns, and $n = 4$. *CI* at 2% can be computed as follows:

$$CI_{2\%} = \sqrt{\frac{(57.8 - 58.6)^2 + (58.6 - 58.6)^2 + (59.2 - 58.6)^2 + (59.4 - 58.6)^2}{4}} = 0.64$$

It would be preferable if CI was large if the threshold gives consistent arrival times, but low where the threshold yields arrival times. Therefore, it is preferable that the CI values above be modified to $1/CI$. Consequently, $1/CI$ values at 2% for the signals shown in Figure 5.22 and Figure 5.23 will be ∞ and 1.56, respectively, meaning that the arrival time of the signal shown in Figure 5.22 is more consistent based on the 2% threshold being evaluated within a range of threshold interval between 1% and 5%.

5.6.2 Results and analysis

Signals to be analysed were obtained from study 3 (described in Section 5.3.3). There were 180 UHF signals {9 PD positions (R1 – R9) \times 10 signals recorded \times 2 sensors}. Ten signals recorded for PD position R1 obtained from sensor REF are used to demonstrate the following steps as an example:

Step 1) Determine arrival times in the threshold interval of interest (i.e. 1% to 5%) by the threshold crossing and these arrival times are summarised in Table 5.12.

Table 5.12 Arrival times obtained from PD at R1 measured using sensor REF.

PD set no.	Arrival time (ns) obtained from threshold				
	1%	2%	3%	4%	5%
1	56.8	57.4	57.6	57.6	58.0
2	58.5	58.6	58.6	58.6	58.6
3	57.4	58.0	58.0	58.0	58.2
4	58.2	58.2	58.8	58.8	58.8
5	44.0	58.4	58.6	58.6	58.6
6	58.2	58.6	58.6	58.6	58.8
7	17.0	58.2	58.8	58.8	58.8
8	58.0	58.8	58.8	58.8	58.8
9	58.6	58.6	58.6	58.8	58.8
10	23.0	58.6	58.6	58.8	58.8

From this table, it is evident that the arrival times obtained from 1% threshold sometimes show dramatic variations, such as those of set 7 and set 10. As a result, the range of threshold interval being evaluated in this study was kept between 2% and 5%.

Step 2) Select the specific threshold being assessed ($x\%$) and calculate all squared terms in the numerator of Eqn. 5.2. Table 5.13 summarises the squared terms for 2% threshold being evaluated.

Table 5.13 Values of squared terms for evaluating using 2% threshold.

PD set no.	Squared terms between the two threshold values		
	3% – 2%	4% – 2%	5% – 2%
1	0.04	0.04	0.36
2	0.00	0.00	0.00
3	0.00	0.00	0.04
4	0.36	0.36	0.36
5	0.04	0.04	0.04
6	0.00	0.00	0.04
7	0.36	0.36	0.36
8	0.00	0.00	0.00
9	0.00	0.04	0.04
10	0.00	0.04	0.04
summation for each column			
	3% – 2%	4% – 2%	5% – 2%
	0.80	0.88	1.28

Step 3) Calculate CI and $1/CI$ for ten PD signal sets.

$$CI_{2\%} = \sqrt{\frac{0.80 + 0.88 + 1.28}{30}} = 0.314$$

$$1/CI_{2\%} = 3.18$$

These ten signals at PD position R1 yield $1/CI_{2\%}$ equal to 3.18 in the range of threshold interval between 2% and 5%.

For the remaining PD positions (R2 – R9), the analysis procedures were repeated (*step 1 to step 3*) and the full set of results are summarised in Table 5.14.

Table 5.14 Values of $1/CI_{x\%}$ for all PD positions.

PD position	$1/CI_{x\%}$ for signals captured at sensor REF				$1/CI_{x\%}$ for signals captured at sensor S			
	2%	3%	4%	5%	2%	3%	4%	5%
R1	3.18	5.00	5.00	4.04	3.37	5.00	5.00	3.87
R2	2.74	3.14	3.18	2.40	2.73	4.08	3.76	3.69
R3	2.69	3.54	3.54	2.69	13.69	19.36	19.36	13.69
R4	2.36	3.16	3.16	2.67	2.17	2.77	2.66	2.42
R5	1.90	2.69	2.54	1.90	3.04	4.63	4.39	4.39
R6	2.99	3.37	3.37	2.69	7.60	9.13	9.13	8.26
R7	2.70	3.16	3.25	2.73	4.13	4.56	4.56	3.66
R8	2.36	3.04	2.97	2.97	4.63	6.64	5.98	5.98
R9	4.92	5.27	5.71	3.76	5.00	5.00	5.00	4.70

Each value in Table 5.14 represents ten arrival times calculated for each PD position for each threshold being assessed. These values can be compared to evaluate the consistency (the sensitivity) of arrival times for each PD position to small changes in threshold value. For instance, the arrival times obtained from position R3 captured using sensor S being assessed using the threshold values of 3% and 4% have the highest consistency (lowest sensitivity to changes of threshold) because the values for $1/CI$ of these threshold values are maximum.

To determine the optimum threshold value in the range of threshold interval between 2% and 5% for all PD positions, all values in Table 5.14 are plotted and illustrated in Figure 5.24. Results show that the optimum thresholds for all PD positions are around the 3% and 4% values. This interval provides lower sensitivity of arrival times to small changes in threshold values than other thresholds.

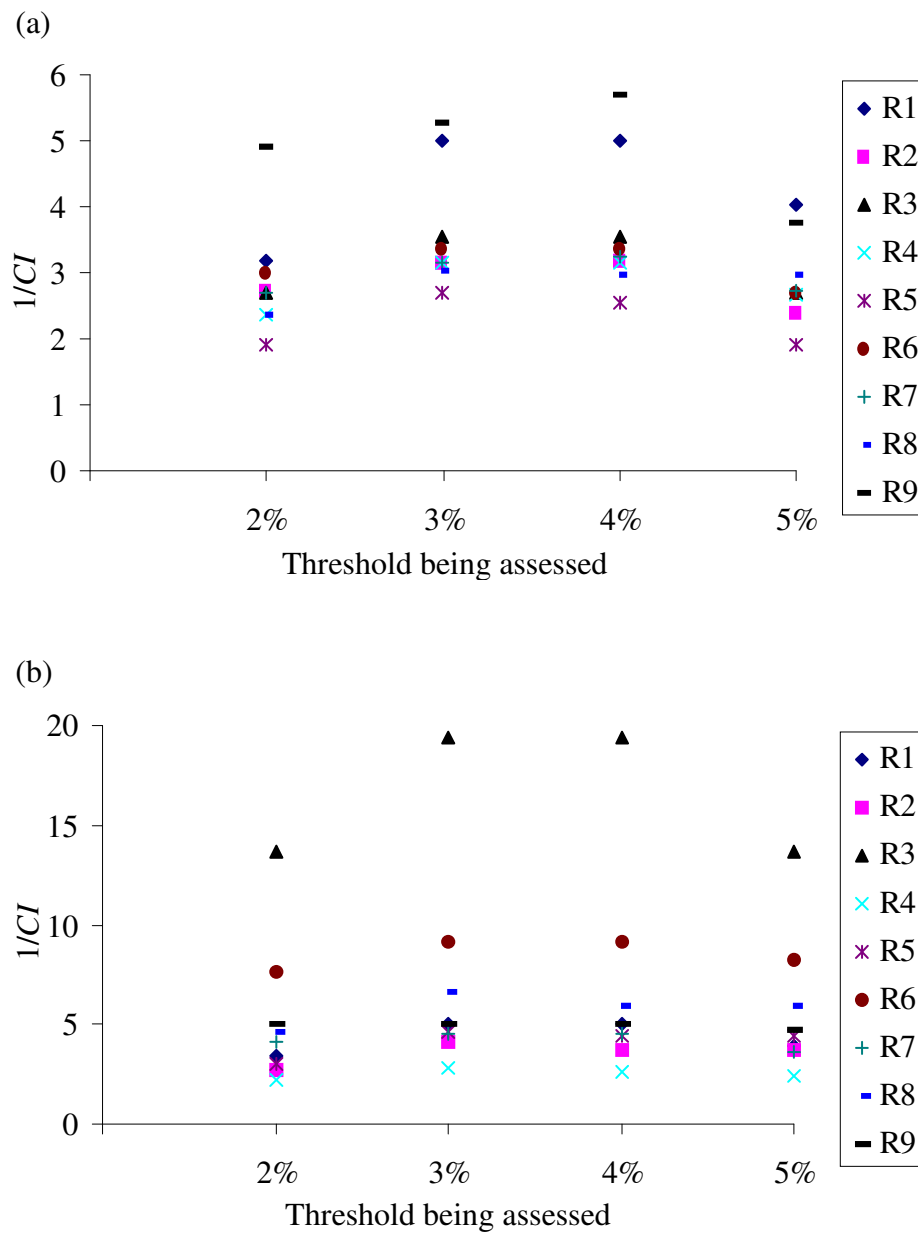


Figure 5.24 $1/CI$ evaluated in the range of threshold values between 2% and 5% for each PD positions (R1 – R9) producing from the signals captured at: (a) Sensor REF, (b) Sensor S.

5.7 Discussion and conclusions

In this chapter, the accuracy of measuring UHF signal arrival times has been assessed experimentally in three approaches.

The first approach dealt with the selection of types of UHF sensor among three typical types (monopole, disc and spiral) to assess which sensor type could be the optimum sensor in the applications of UHF PD location. The results show that most errors for the disc sensor are in a limited band with a mean of 0.93 ns and standard deviation of 0.70 ns. For the monopole and spiral sensors, there is more scatter with means of 1.14 ns and 1.40 ns, and standard deviations of 0.91 ns and 1.77 ns, respectively. These results show that the disc-type sensor could provide the highest accuracy for PD location applications.

The second approach involved laboratory experiments into some factors that affect measured arrival times. The results indicate that the accuracy of measured arrival times could be improved by a factor of 2 through increasing the sensitivity of the measurement at the cost of accepting signal clipping within the oscilloscope. This decreased the absolute errors from 0.68 ns (study 1) to 0.32 ns (study 3), corresponding to distance error reductions from 0.20 m to 0.10 m in air or 0.14 m to 0.06 m in transformer oil. Moreover, results from study 1 to assess the characteristics of measured time differences for the whole tank show that the error $\Delta T_{MEA} - \Delta T_{GEO}$ relative to differential propagation distance (Δd) increased at a rate of 0.44 ns/m. This confirms that the accuracy of measured arrival times at more distance sensors could be degraded since their initial wavefronts are more difficult to identify. In terms of variation of PD pulse orientation (study 2), no strong effect on the accuracy of PD location was observed in this study.

Determining arrival times using threshold crossing is effective and suitable for automation, but defining the particular threshold presents a challenge. Therefore, a new index, called the arrival time *consistency index* (*CI*), to evaluate the reliability of particular threshold values (in contrast, to assess the sensitivity of arrival times to small changes of thresholds) has been adapted based on the standard deviation calculation. The experiments carried out suggest that a threshold value of 3% or 4% is the most reliable for application to instantaneous UHF voltage squared, within the threshold interval of 2% and 5%.

6. Practical implementations

6.1 Introduction

The previous chapters were dedicated to concepts, numerical processes and experimental investigations concerned with techniques for distinguishing between different PD sources and for determining arrival times of UHF signals. The results, together with the formal methodology adopted, have demonstrated how those techniques can be applied effectively in distinguishing between different PD sources in UHF PD location. This chapter is concerned with utilising those techniques in practical applications to PD monitoring based on the UHF detection technique, including applications to other monitoring systems that detect unknown transient signals.

The first will be a practical implementation of an electronic circuit concept for capturing UHF signal envelopes, which will be used for the envelope comparison method. The second will be an application of the relative increase in energy for aligning UHF signals that have different triggering positions but may possibly be generated by the same PD sources. Finally, possible applications to other types of monitoring system will be presented.

6.2 Practical implementation of the envelope comparison method

6.2.1 Hardware concept of the envelope detector circuit

The study reported in [126] has shown that envelopes of UHF signals in GIS can be detected by means of an electronic circuit, as illustrated by the UHF signal and its envelope shown in Figure 6.1. Similarly, the numerical process of smoothing UHF signals by means of the Gaussian kernel (presented in Chapter 2) is also capable of

implementation in practical hardware using standard electronic components, as shown in Figure 6.2.

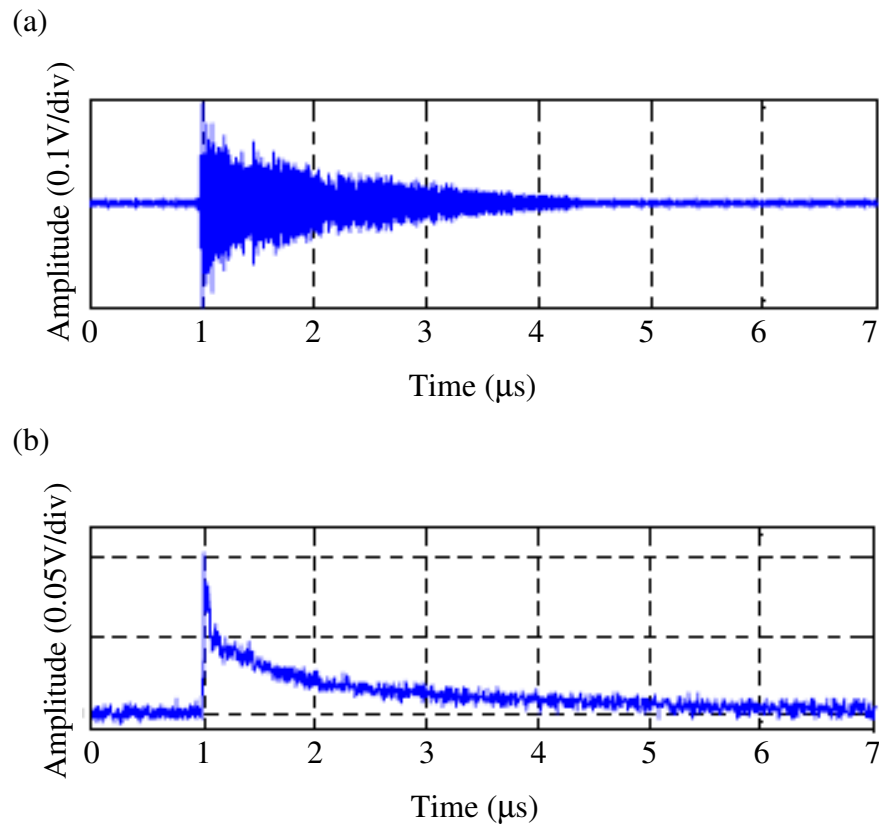


Figure 6.1 Comparison of UHF signal and its envelope obtained from one type of defect [126]: (a) UHF signal, (b) Envelope.

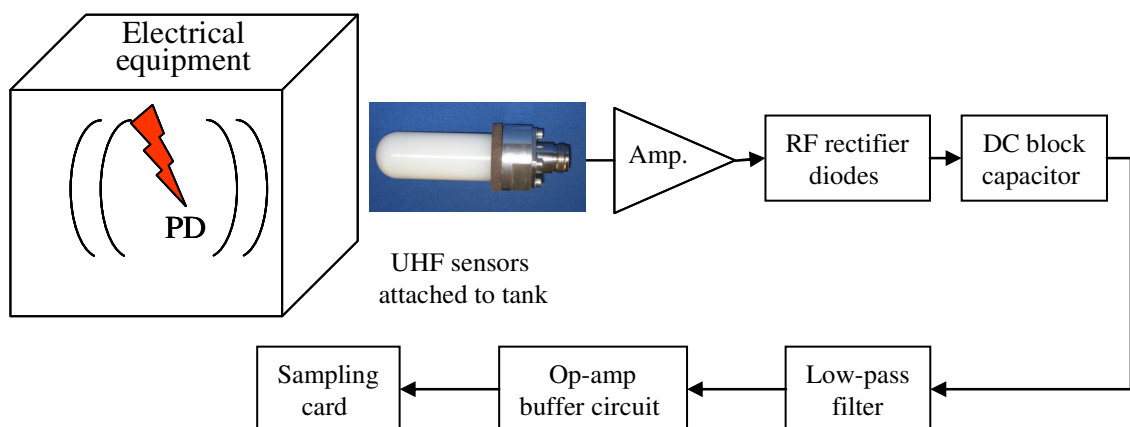


Figure 6.2 Hardware diagram for capturing the envelope of UHF signals.

When a PD occurs in electrical equipment, its radiated UHF signals are captured by UHF sensors, such as the monopole-type sensor shown in Figure 6.2. Typically, the incoming signals would first be amplified. A process similar to squaring UHF signals to make them unipolar could be achieved using RF rectifier diodes. Any DC offset would then be removed with a blocking capacitor and the envelopes of those UHF signals smoothed using a low-pass filter. This would be followed by an op-amp buffer circuit and a sampling card, which might operate in the region 50×10^6 – 100×10^6 samples/sec. This would be much more economical than one operating in the region of 5×10^9 samples/sec. After this step, efficient envelopes representing radiated UHF signals can be stored for subsequent analysis (such as distinguishing between PD sources).

The key objective in using an envelope detector circuit is to reduce the sampling rate used for capturing the radiated UHF signals by at least a factor of 100, such as from 5×10^9 to 50×10^6 samples/sec. This could lead to a reduction in the capital expense for the measurement system and data storage device, as well as a large reduction in the power requirement, which might in future allow processing to be carried out at the sensor node.

6.2.2 Investigating use of reduced sampling rate envelopes for distinguishing between different PD sources using computer modelling

Before building electronic hardware for an envelope detector, the principle was verified through computer modelling using UHF signals obtained from the laboratory experiments presented in Section 2.4. These UHF signals were created from a contact discharge test cell and experiments were carried out in the metal tank ($2.51 \times 1.26 \times 1.26$ m), fitted with three UHF sensors. The PD source was placed in five different locations 0.40 m and 0.60 m apart in x - and y -axes and the UHF signals were captured using an oscilloscope with a sampling rate of 5×10^9 samples/sec.

Envelopes were created in two different ways.

(i) The first approach involved 4-ns Gaussian kernel smoothing (*ksmooth* function of Mathcad) of the UHF voltage squared signal at the original sampling rate (5×10^9 samples/sec). The procedure for creating envelopes is shown in Figure 6.3. To demonstrate this process, the UHF signal shown in Figure 6.4 will be used. Transformation from the UHF voltage squared to its envelope is illustrated in Figure 6.5 and Figure 6.6.

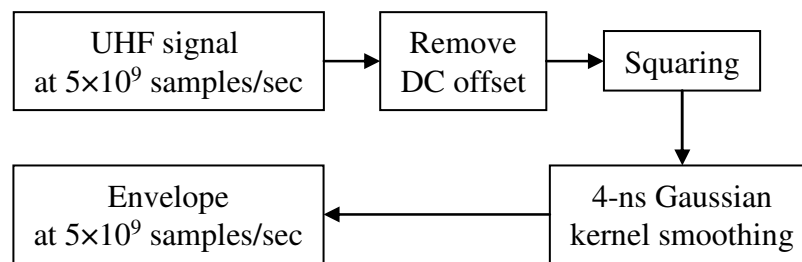


Figure 6.3 Diagram to illustrate procedures for obtaining envelopes at original sampling rate.

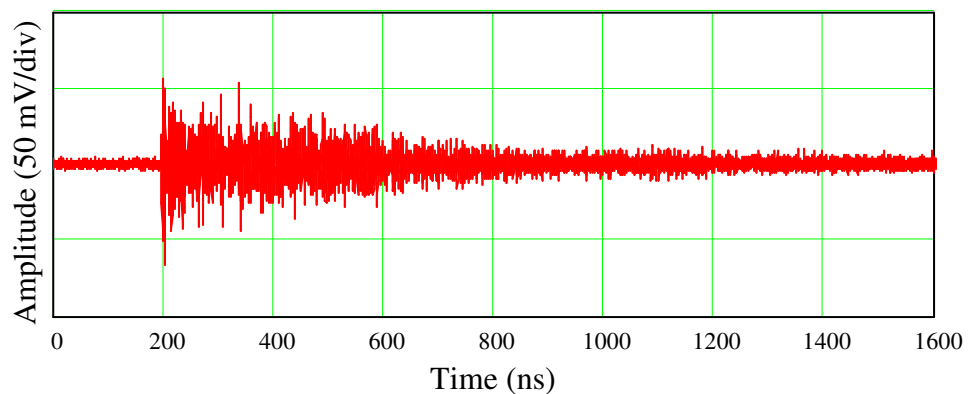


Figure 6.4 Typical UHF signal obtained from the experiment in Section 2.4.

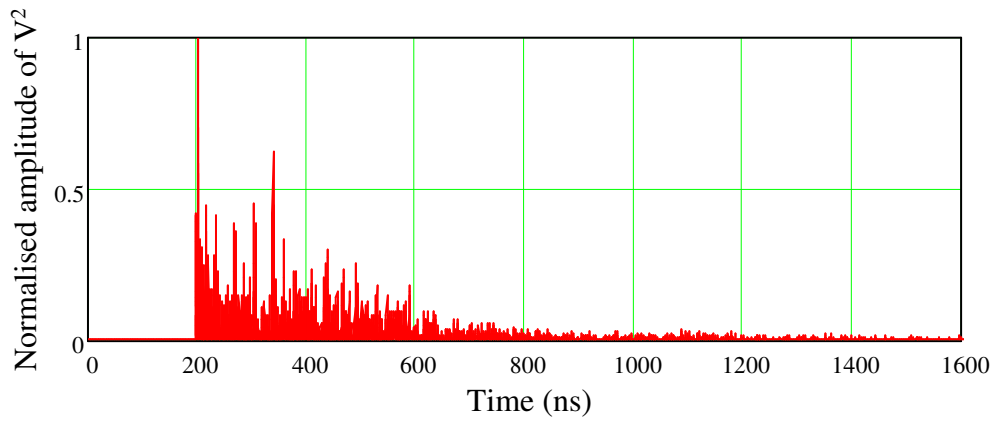


Figure 6.5 Normalised UHF voltage squared of the signal shown in Figure 6.4.

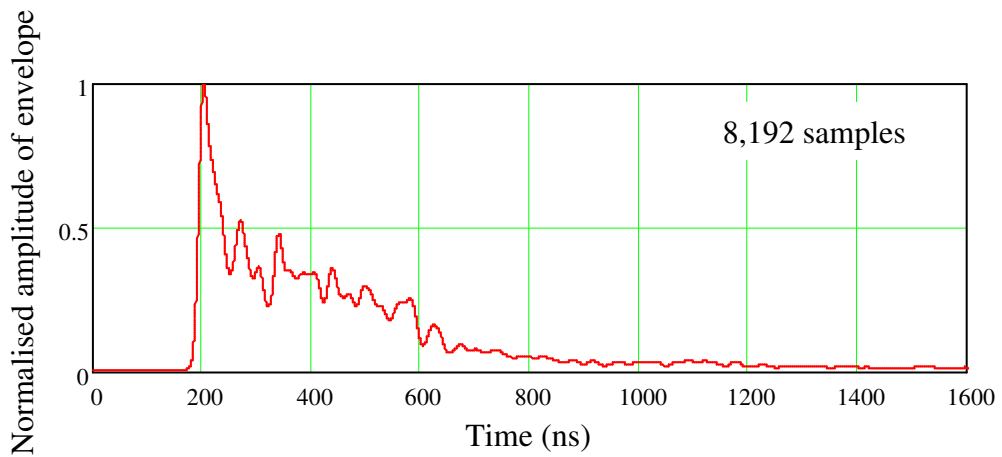


Figure 6.6 The envelope of the signal shown Figure 6.4 generated using 4-ns Gaussian kernel smoothing. This envelope still comprises 8,192 samples over 1,600 ns.

(ii) The second approach was to pass the envelopes through a low-pass filter, for which a simple low-pass Butterworth response in MATLAB was selected. The Butterworth filter in this study was defined as third-order with 10 MHz cut-off frequency. Before feeding UHF signals to the filter, it was necessary to make them half-wave rectified signals according to the conceptual circuit of Figure 6.2. Outputs from the filter were then re-sampled at a lower sampling rate. Figure 6.7 summarises

the process for creating reduced signal sampling rate envelopes. Figure 6.8 shows the ideal half-wave rectified version of the UHF signal from Figure 6.4. Figure 6.9 illustrates the reduced sampling rate envelope created from the Butterworth filter output sampled at 50×10^6 samples/sec.

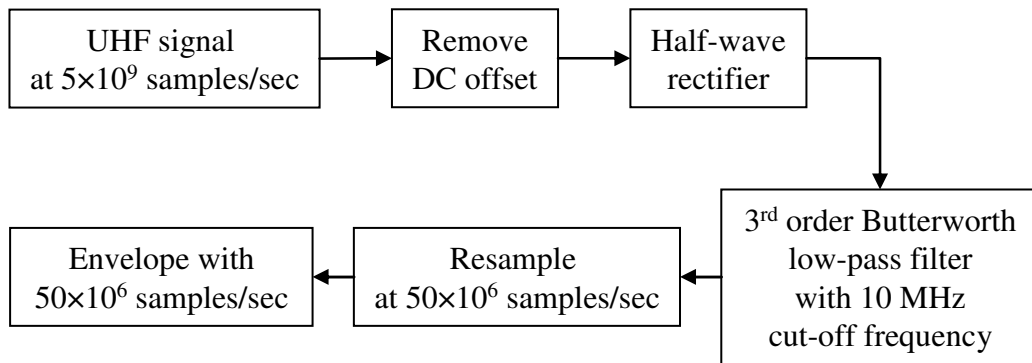


Figure 6.7 Diagram to illustrate procedures for obtaining reduced signal sampling rate envelopes.

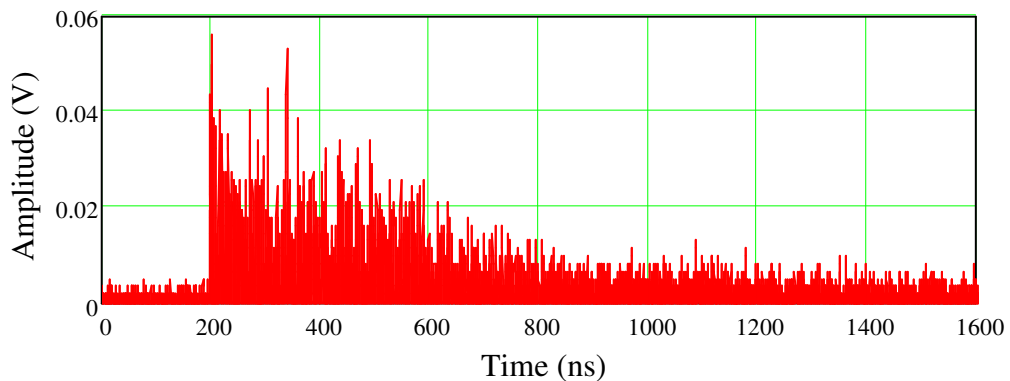


Figure 6.8 Half-wave rectified version of the signal shown in Figure 6.4.

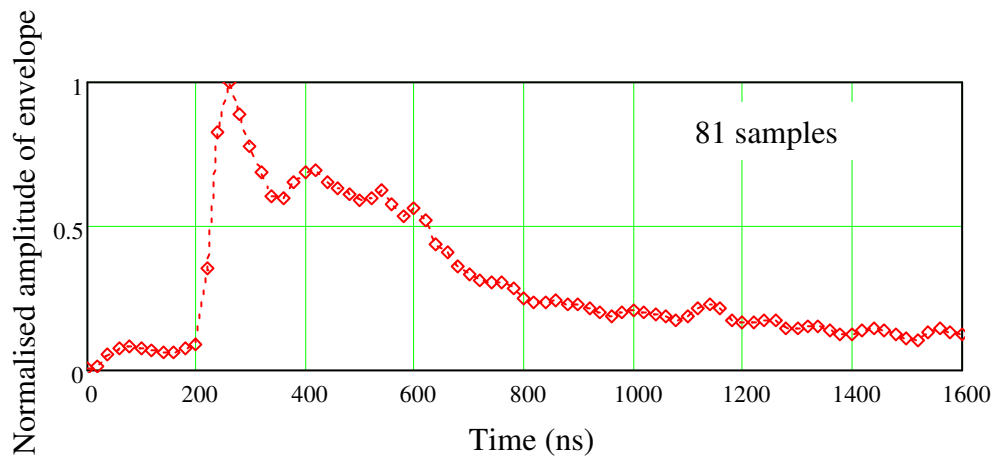


Figure 6.9 Reduced sampling rate envelope created from the third-order Butterworth 10 MHz low-pass filter. This envelope consists of 81 samples over 1,600 ns.

Having generated the envelopes, the comparison method for distinguishing between different PD sources was applied to both groups of envelopes. This is to verify that reduced sampling rate envelopes can be used to distinguish between different PD sources in the same manner as original sampling rate envelopes. Results are shown in Figure 6.10 and Figure 6.11.

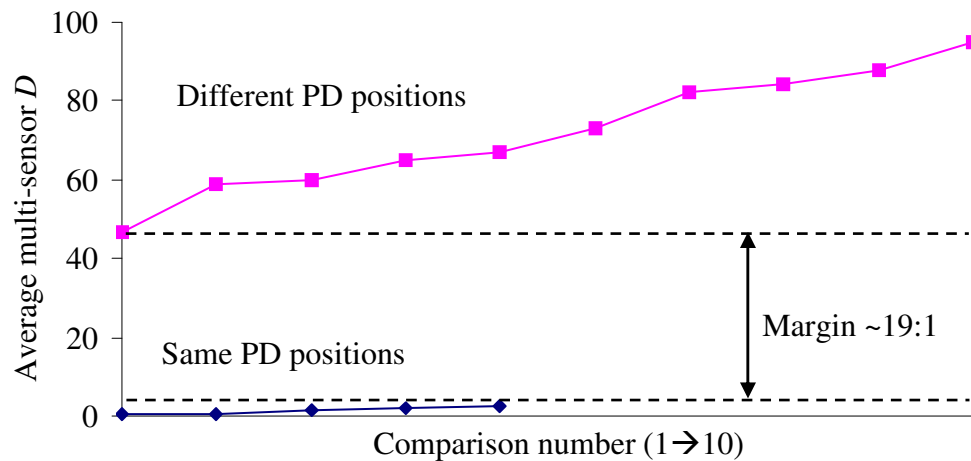


Figure 6.10 Margin between the same and different PD positions derived from the envelopes sampled with the sampling rate of 5×10^9 samples/sec.

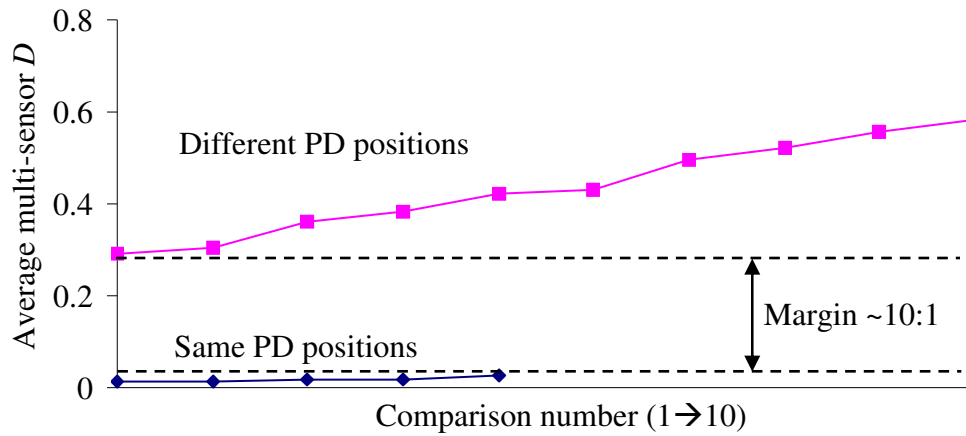


Figure 6.11 Margin between the same and different PD positions derived from the envelopes sampled with the sampling rate of 50×10^6 samples/sec, a sampling rate reduction by a factor of 100.

Figure 6.10 shows that the margin between the same and different PD positions obtained from the *original* sampling rate envelope is 19:1 while Figure 6.11 shows a good margin for the *reduced* sampling rate envelopes of 10:1. The reduction in number of samples has reduced the margin somewhat, but this analysis suggests that the envelopes captured with a reduced sampling rate could still be used for differentiating successfully between different PD sources [127].

6.2.3 The envelope detector circuit

Based on a PD detector circuit outlined in [128], a simple UHF envelope detector was constructed to the circuit diagram shown in Figure 6.12. Inputs to the circuit are UHF signals from the sensors while outputs are signal envelopes intended for capture using an oscilloscope with a sampling rate of 50×10^6 samples/sec. The RF diodes used in the circuit were HSMS 2820 Schottky barrier diodes (see the datasheet in Appendix B). This process is illustrated in Figure 6.13. In this study, two identical envelope detector circuits were constructed, as shown in Figure 6.14.

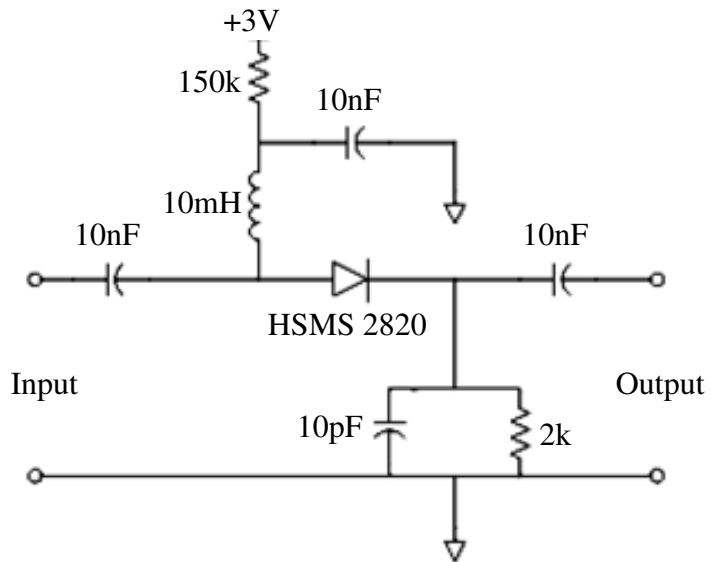


Figure 6.12 Simple circuit diagram of the envelope detector.

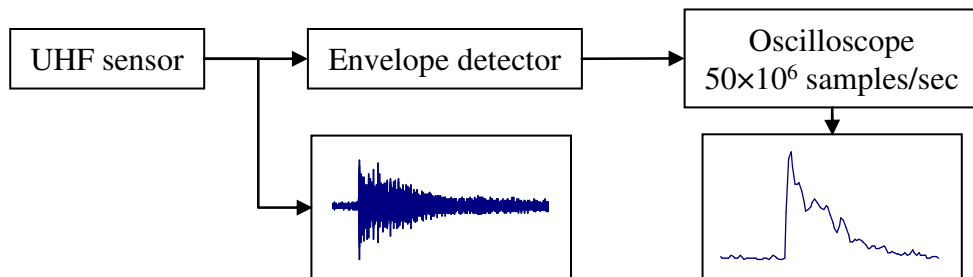


Figure 6.13 Diagram to illustrate the input and output of the envelope detector circuit.

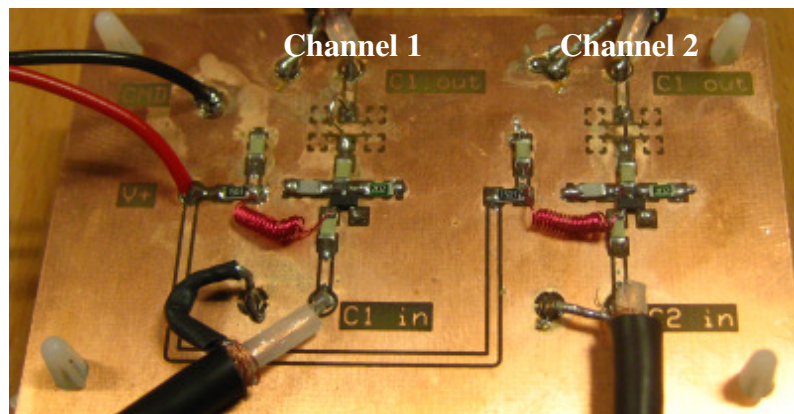


Figure 6.14 Pair of identical envelope detector circuits used in the experiments.

Consider the circuit diagram in Figure 6.12: no additional low-pass filter is used, so that it is expected that some high frequency content will still be present at the output. Figure 6.15 illustrates the envelope and its spectral density plot in which some frequencies above 10 MHz can be seen. However, it is possible to further reduce high frequency content using built-in filtering available in the oscilloscope.

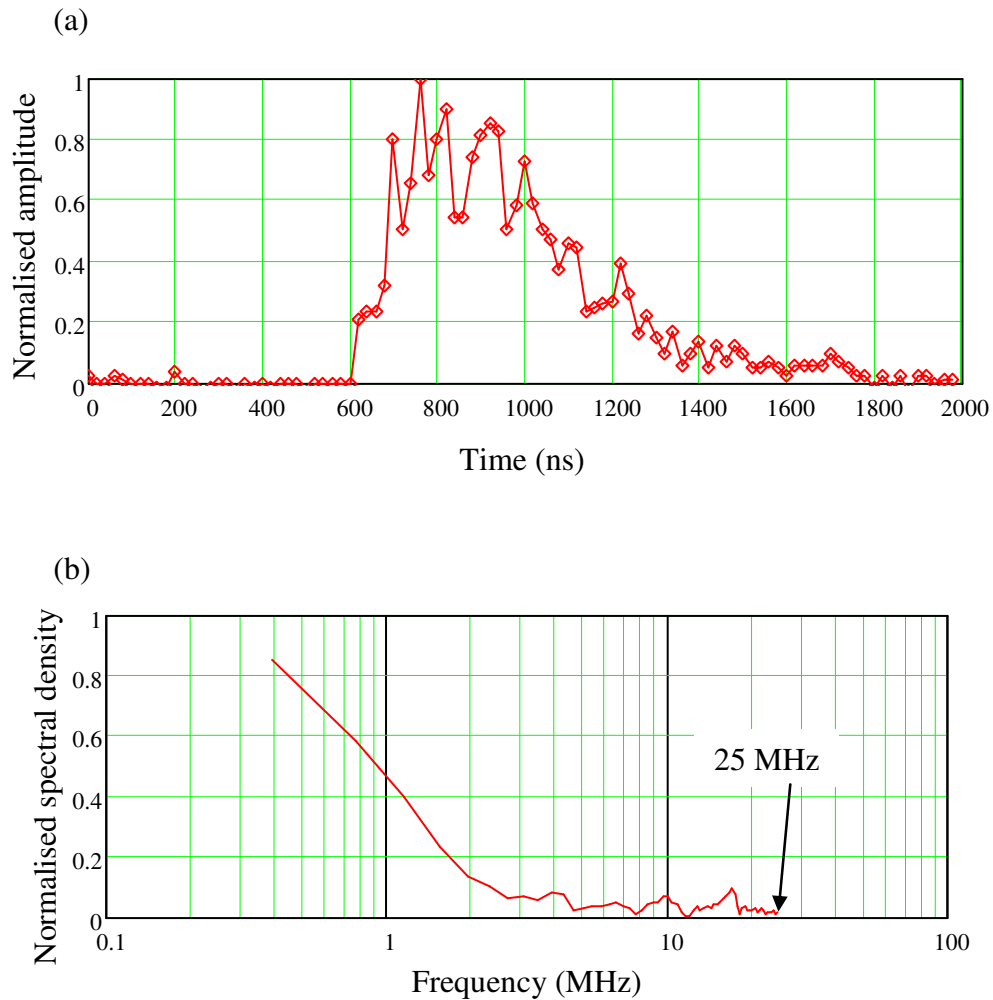


Figure 6.15 Output of the envelope detector circuit obtained from the contact discharge test cell: (a) Normalised voltage envelope, (b) Its frequency spectrum.

6.2.4 Laboratory experiments

6.2.4.1 Investigation in a shielded room

The aim of this laboratory experiment is to investigate the ability to distinguish between different PD sources using the envelope comparison method obtained from reduced sampling rate envelopes. Experiments employed two disc-type UHF sensors (REF and S) fitted to the shielded room, as shown in Figure 6.16. Two different types of PD sources (contact discharge test cell and the spark unit) were used, placed in two different locations in the shielded room, as indicated in Table 6.1. This is to simulate a situation of multiple PD sources occurring in the system (different PD types at different locations).

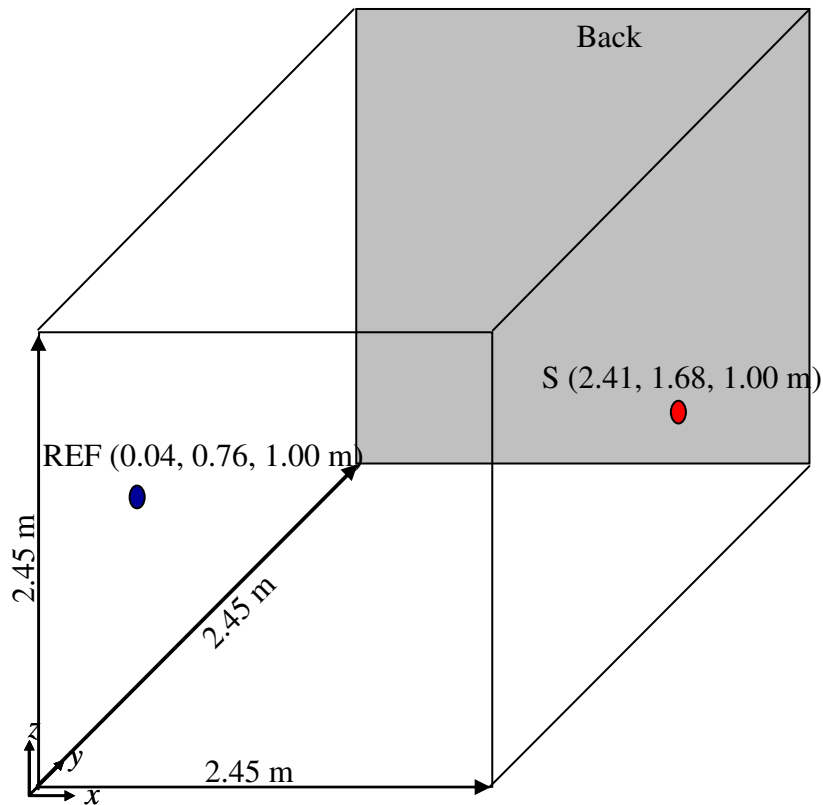


Figure 6.16 Test arrangement, REF and S are disc-type UHF sensors.

Table 6.1 Coordinates of two different PD sources.

Types of PD sources	Coordinates (m)		
	<i>x</i>	<i>y</i>	<i>z</i>
Spark unit	1.73	1.20	0.95
Contact discharge test cell	0.17	0.08	0.09

The oscilloscope (LeCroy WaveRunner 104Xi) sampling rate was set at 50×10^6 samples/sec. Envelopes were recorded over 2,000 ns and each therefore contained 100 voltage sample points. They were captured 11 times (set 1 – set 11) for each PD source. Care was taken to ensure that no clipping took place and the triggering position was consistent because of the simple shape of the waveform in this investigation. The envelopes to be analysed were passed through an additional ‘eres’ built-in filter of the oscilloscope as in Figure 6.17. The ‘eres’ built-in filter [129] is the Enhanced Resolution Function that applies a Finite Impulse Response (FIR) filter. This filter is similar to smoothing the signal with a simple moving average filter. In this experiment, the resolution was set with enhancement = 2 bits, which applies a low-pass -3dB bandwidth at $0.5 \times \text{Nyquist}$ frequency. Consequently, the *filtered envelopes* being analysed have an upper frequency limit of $0.5 \times 25 \times 10^6 = 12.5 \times 10^6$ Hz. These envelopes recorded for analysis will be called ‘*filtered envelopes*’. Figure 6.18 compares the original and filtered outputs from the envelope detector in the time-domain and the frequency-domain.

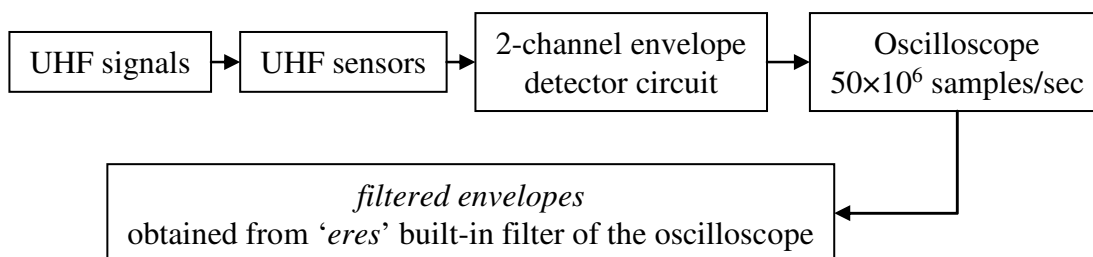


Figure 6.17 Diagram to illustrate how the envelopes to be analysed were acquired.

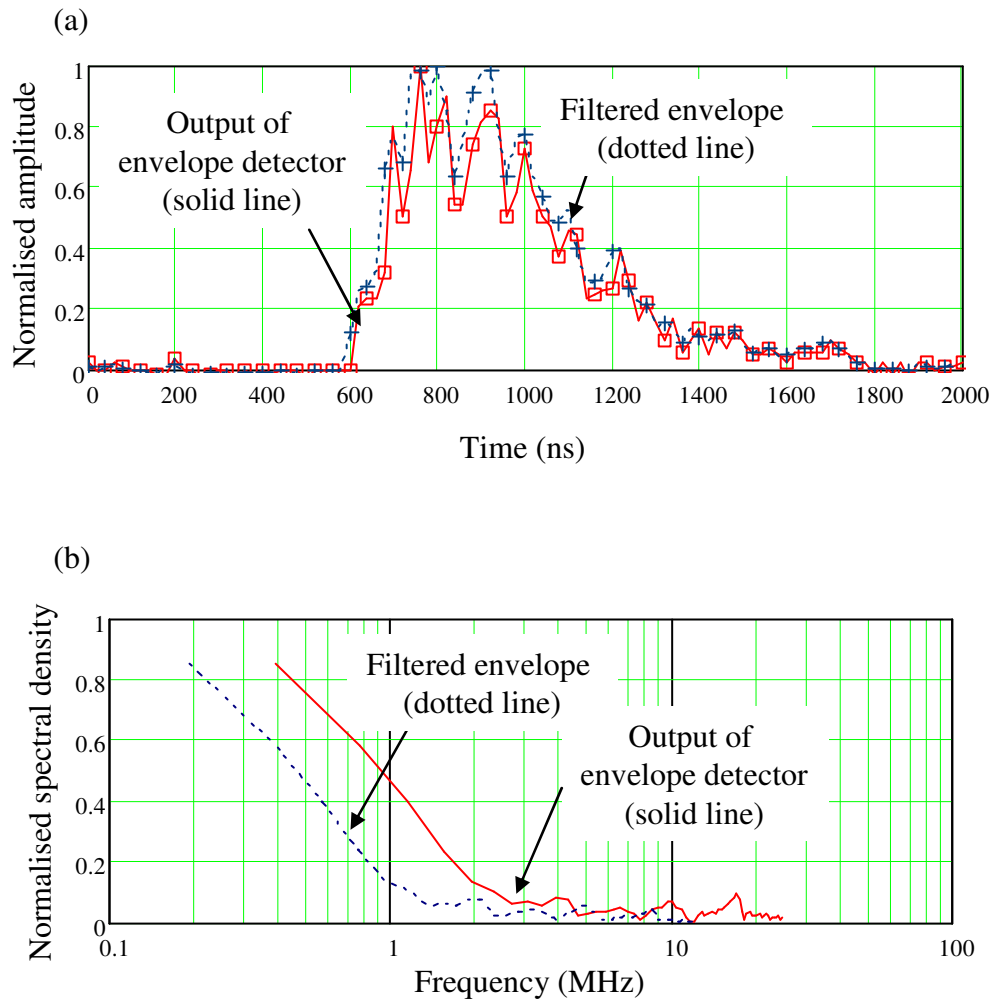


Figure 6.18 Comparison between the output of the envelope detector and its 'eres' filtered envelope created from UHF signals excited by the contact discharge test cell: (a) Normalised voltage envelopes, (b) Frequency spectra.

6.2.4.2 Results and analysis for the shielded room experiments

Results in Figure 6.19 and in Figure 6.20 indicate that the envelopes produced by the spark unit and the contact discharge test cell are significantly different.

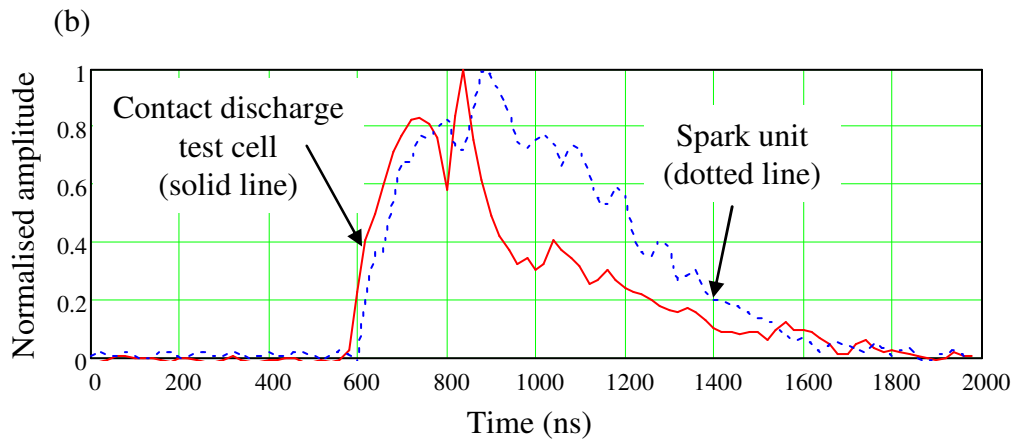
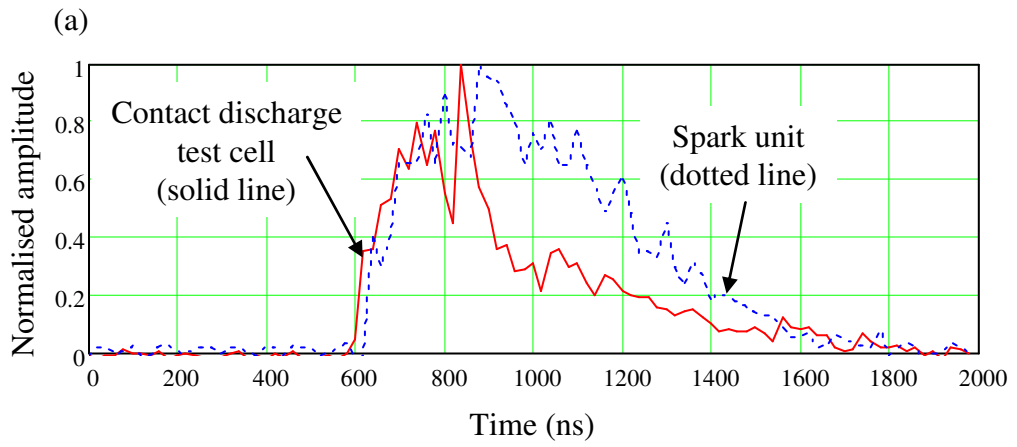


Figure 6.19 Comparison between the envelopes generated from two different types of PD sources recorded at sensor S: (a) Their direct sampled envelopes from the envelope detector, (b) Their filtered envelopes to be analysed.

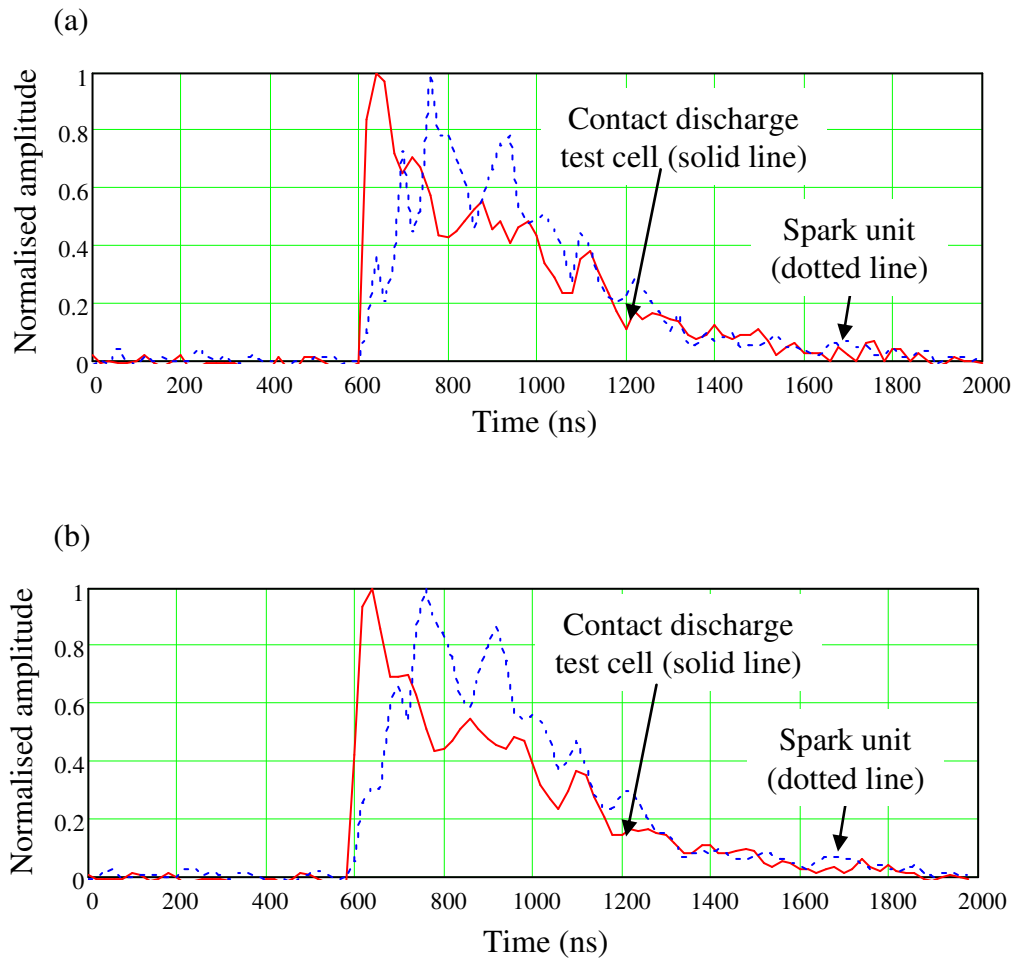


Figure 6.20 Comparison between the envelopes generated from two different types of PD sources recorded at sensor REF: (a) Output envelopes from the envelope detector, (b) Their filtered envelopes to be analysed.

To determine the margin between the same and different PD sources, values of D and average multi-sensor D between pairs of filtered envelopes generated from the same PD sources were first computed, which are summarised in Table 6.2 for the spark unit and Table 6.3 for the contact discharge test cell. These values of D were expected to be relatively low. Next, the calculations were applied to pairs of filtered envelopes between the different PD sources. The values of D and average multi-sensor D , which are expected to be comparatively high, are summarised in Table 6.4. To assess the results, a plot of average multi-sensor D values between the same and different PD sources was prepared, which is shown in Figure 6.21.

Table 6.2 Values of difference coefficient (D) and average multi-sensor D calculated from the *spark unit*.

PD sets being compared	Values of D		Values of average multi-sensor D
	REF	S	
1-2	0.292	0.440	0.366
1-3	0.082	0.163	0.123
1-4	0.441	0.139	0.290
1-5	0.134	0.245	0.190
1-6	0.096	0.157	0.127
1-7	0.173	0.169	0.171
1-8	0.109	0.120	0.115
1-9	0.092	0.259	0.176
1-10	0.442	0.229	0.336
1-11	0.099	0.158	0.129
<i>Average for all</i>			0.202

Table 6.3 Values of difference coefficient (D) and average multi-sensor D calculated from the *contact discharge test cell*.

PD sets being compared	Values of D		Values of average multi-sensor D
	REF	S	
1-2	0.905	0.282	0.594
1-3	0.398	0.387	0.393
1-4	0.569	0.115	0.342
1-5	0.557	0.289	0.423
1-6	0.515	0.291	0.403
1-7	0.525	0.302	0.414
1-8	0.293	0.261	0.277
1-9	0.364	0.313	0.339
1-10	0.395	0.178	0.287
1-11	0.435	0.241	0.338
<i>Average for all</i>			0.416

Table 6.4 Values of difference coefficient (D) and average multi-sensor D compared between the spark unit (set 1) and contact discharge test cell (set 1 – set 11).

PD sets being compared	Values of D		Values of average multi-sensor D
	REF	S	
1-1	4.023	2.718	3.371
1-2	2.290	3.166	2.728
1-3	3.037	2.107	2.572
1-4	2.933	3.011	2.972
1-5	2.785	2.645	2.715
1-6	2.988	2.806	2.897
1-7	2.858	2.953	2.906
1-8	3.429	2.205	2.817
1-9	3.395	2.023	2.709
1-10	3.329	2.651	2.990
1-11	2.796	3.317	3.057
<i>Average for all</i>			2.885

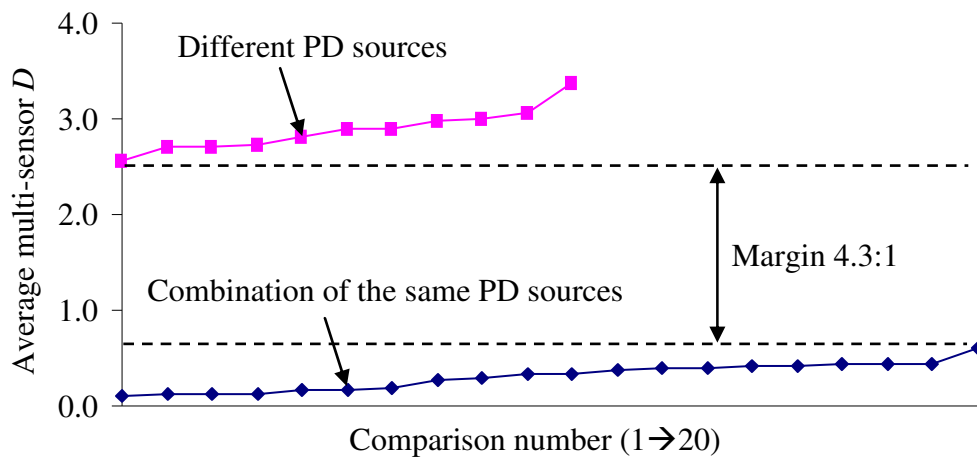
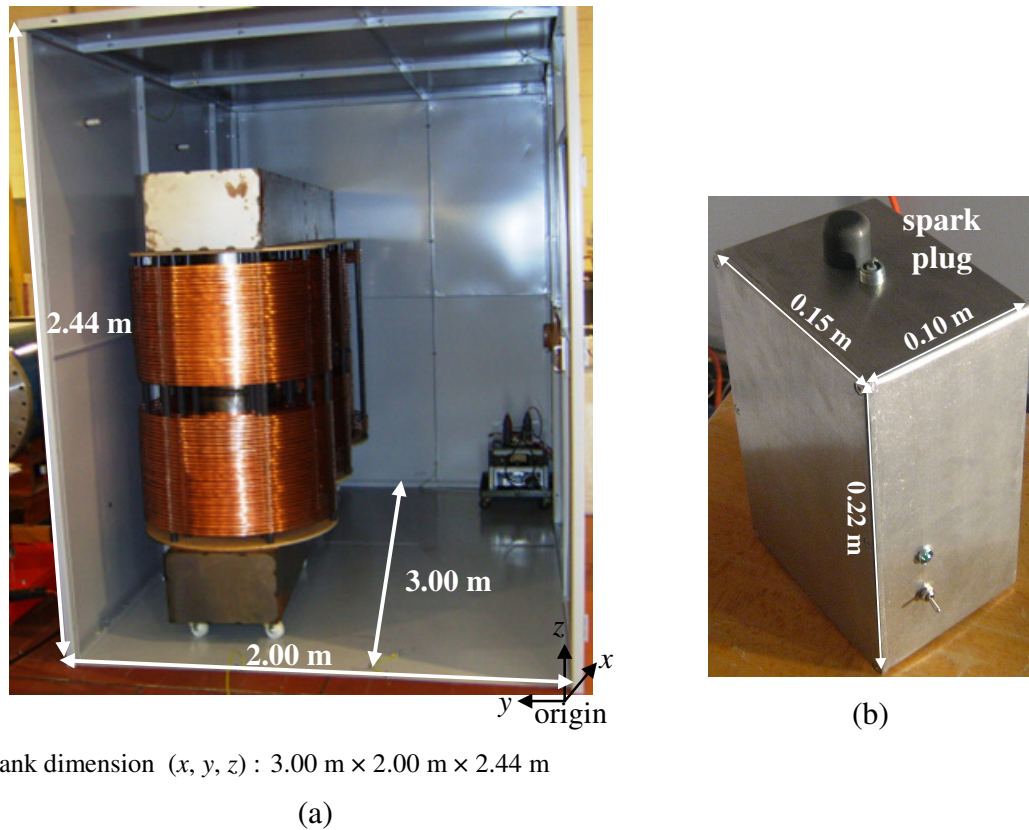


Figure 6.21 Margin between the same and different PD positions.

These results from the shielded room confirm that reduced sampling rate envelopes could be used for distinguishing between different PD sources successfully. The next investigation was a test in a simplified transformer consisting of a set of windings and cores in a tank with two proprietary UHF transformer sensors installed.

6.2.4.3 Investigation in a model transformer tank

To better simulate reality, experiments were carried out in a transformer model that consists of a steel core structure, three windings and two proprietary UHF sensors installed. PD pulses were generated using the spark unit. The test set is shown in Figure 6.22. The sensor and the spark unit positions are defined in Table 6.5. For each PD position, five pulses were recorded.



Tank dimension (x, y, z) : 3.00 m x 2.00 m x 2.44 m

(a)

(b)

Figure 6.22 Test arrangement: (a) Transformer model consisting of a steel core structure and three windings in a steel tank. Note that the winding assembly was moved to the centre of the transformer tank and the end panel was replaced during the experiments (b) The spark unit used as a movable PD source.

Table 6.5 Coordinates of UHF sensors and PD sources.

		Coordinate (m)		
		<i>x</i>	<i>y</i>	<i>z</i>
UHF sensors	S1	1.30	0.00	0.40
	S2	2.70	2.00	0.40
PD positions	SPK1	1.46	0.74	0.23
	SPK2	2.57	1.28	0.23
	SPK3	1.53	1.15	1.72

As with the test in Section 6.2.4.2, envelopes to be analysed were outputs from the 2-channel envelope detector passed through the eres filter and captured with a sampling rate of 50×10^6 samples/sec. Each reduced sampling rate envelope consists of 100 sample points over 2,000 ns. Reduced sampling rate envelopes for each PD position obtained from each sensor are illustrated in Figure 6.23. By observation, it can be said that these envelopes appear similar for the same PD positions captured with the same sensor while they look dissimilar for the different PD positions captured. Before calculating values of average multi-sensor D , time offset compensation was made manually to optimise alignment of these envelopes.

After analysing the time shifted versions of reduced sampling rate envelopes, values of average multi-sensor D between each pair of PD location comparisons were plotted as shown in Figure 6.24. The margins for each comparison are 5.0:1, 1.7:1 and 3.6:1 for comparisons SPK1-SPK2, SPK1-SPK3 and SPK2-SPK3, respectively. Results confirm that reduced sampling rate envelopes can be used to distinguish between different PD sources. Note that, because of the reduced sampling rate, there may be a systematic error due to variability of the sample times in relation to the underlying ideal envelope shape (for example, there is no guarantee that one of the samples will coincide with the peak value of the envelope). However, no strong effect of this error was observed in the work reported here.

The studies presented in Section 6.2 suggest that reduced sampling rate envelopes (factor of 100 sampling rate reduction) can be used to differentiate between different PD sources successfully. This could lead to a lower cost for the measurement system, reduced data storage requirements, as well as a large reduction in the power

consumption, which might in future allow processing to be carried out at the sensor node.

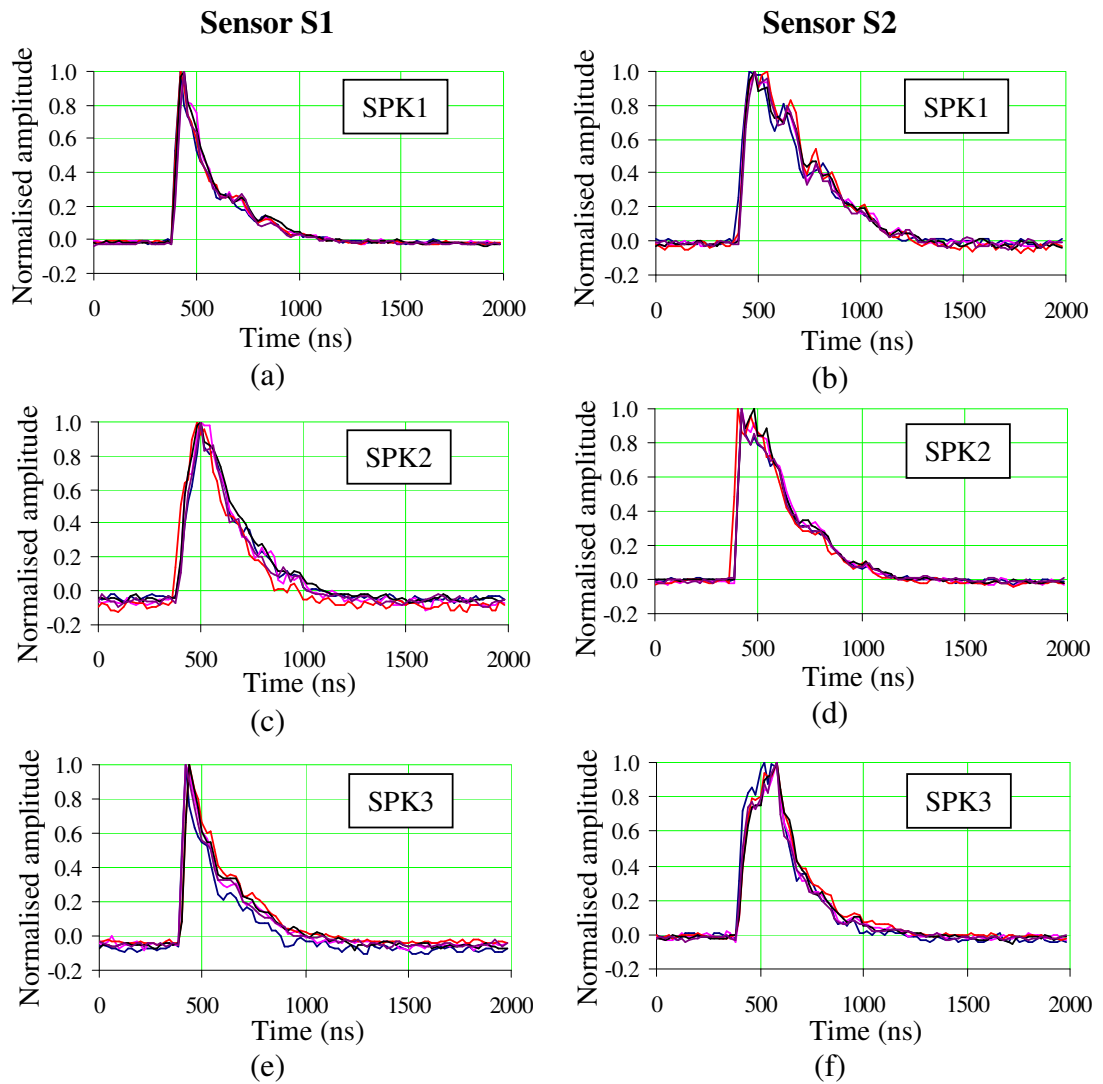


Figure 6.23 Reduced sampling rate envelopes (five envelopes per sub-figure) obtained from: (a) S1 at SPK1, (b) S2 at SPK1, (c) S1 at SPK2, (d) S2 at SPK2, (e) S1 at SPK3, (f) S2 at SPK3.

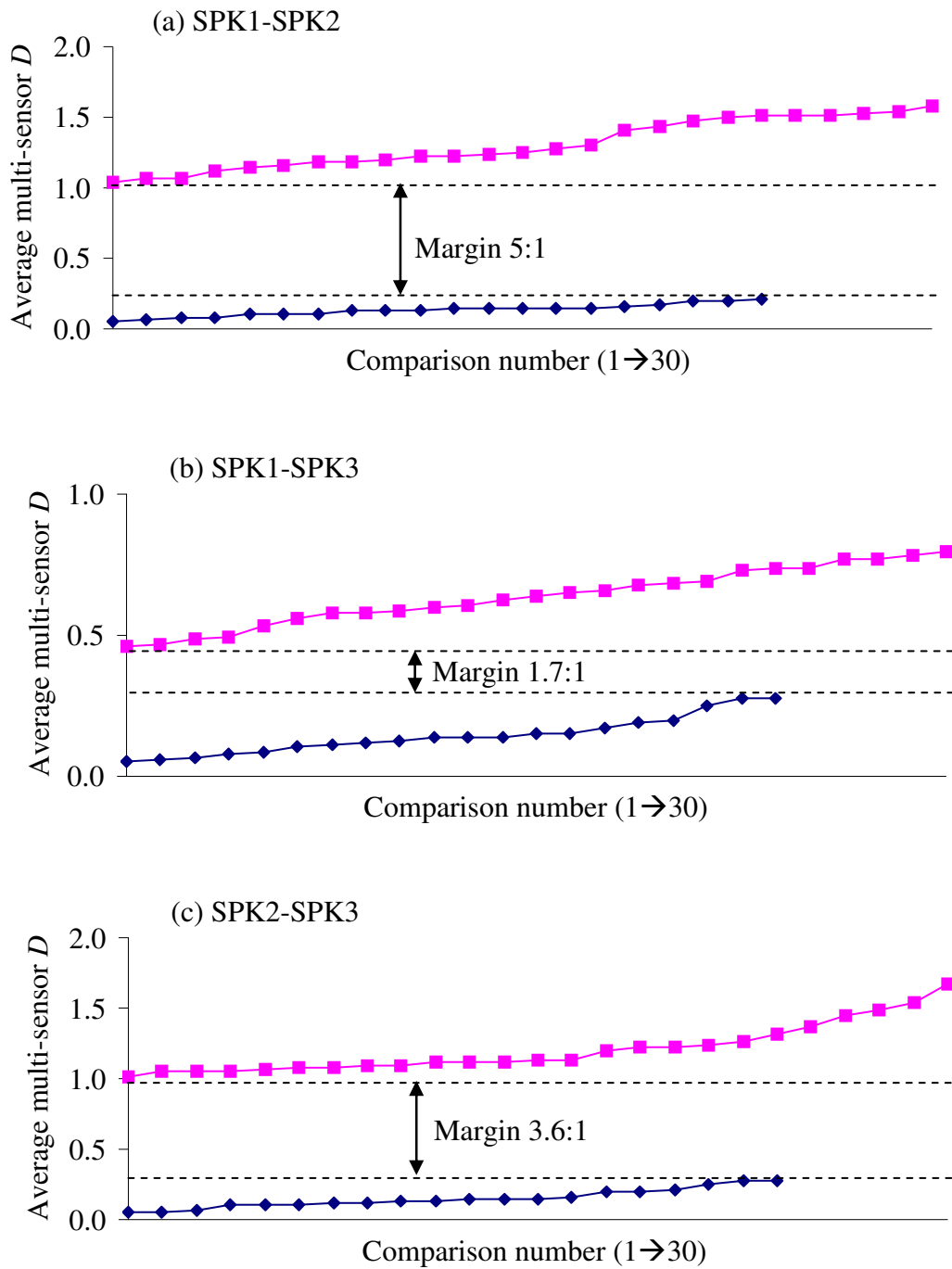


Figure 6.24 Values of average multi-sensor D calculated from three comparisons of SPK1, SPK2 and SPK3, sorted into ascending order: (a) SPK1 and SPK2, (b) SPK1 and SPK3, (c) SPK2 and SPK3. Note that upper bands are for different PD position comparisons and lower bands are for same PD position comparisons.

6.3 Applications of the relative increase in energy

6.3.1 Determining arrival times by an automated process

By applying the relative increase in energy (R_{iEj}) presented in Chapter 3 to a PD signal, combined with its cumulative energy plot, the expected arrival time can be identified manually based on engineering judgement [100, 101]. However, as discussed previously a basic method to identify absolute arrival times (i.e., selecting them manually) is not appropriate for practical implementation. Thus, an automated solution for identifying absolute arrival times is preferable. Once absolute arrival times are obtained, time differences between them can be calculated easily.

Using R_{iEj} for a UHF signal, the time of occurrence of the highest peak (T_p) of R_{iEj} waveform can be obtained. The absolute arrival time must be somewhat earlier. This is illustrated using the UHF signal sampled at 5×10^9 samples/sec over 100 ns from PD testing of an HVDC reactor [73], shown in Figure 6.25. Its normalised R_{iEj} waveform showing T_p is illustrated in Figure 6.26. From this data, T_p can be determined and set as the upper limit for absolute arrival time of this UHF signal.

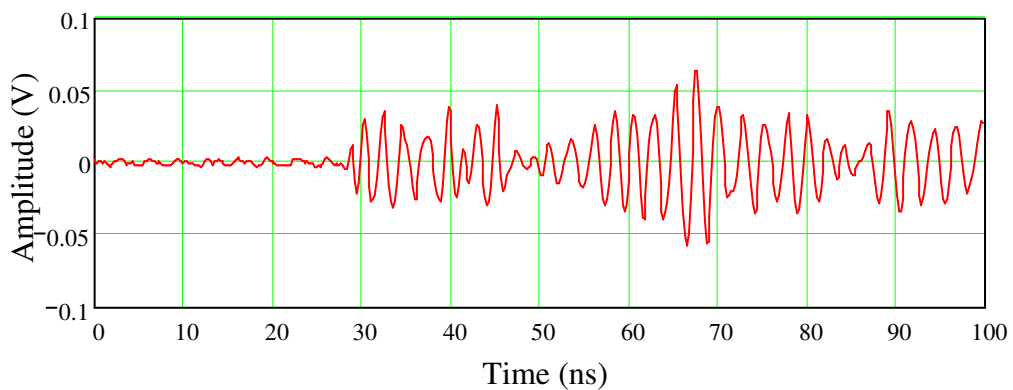


Figure 6.25 UHF signal obtained from UHF PD monitoring of an HVDC reactor.

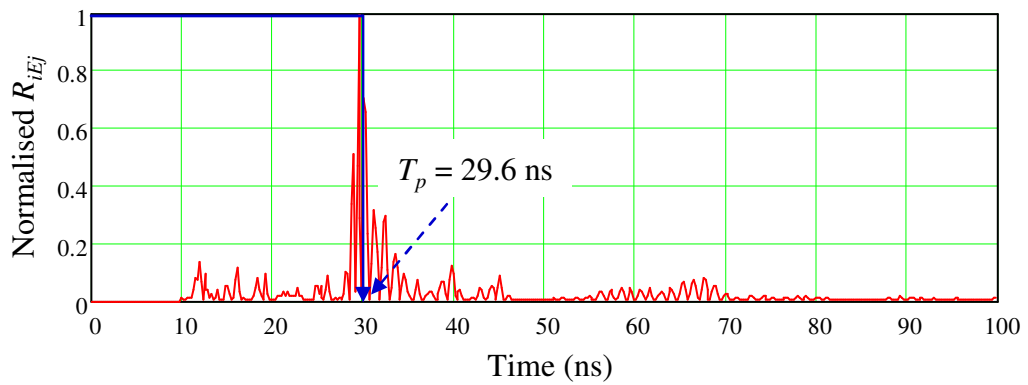


Figure 6.26 Normalised R_{iEj} waveform of the signal shown in Figure 6.25. This is to show that T_p can be identified immediately.

Within a particular window length prior to T_p (e.g. a 5-ns window), it is possible to determine absolute arrival times using the threshold crossing method with respect to the highest value of R_{iEj} , as shown in Figure 6.27. In this case, the absolute arrival time is found within R_{iEj} data between 24.6 ns and 29.6 ns. Following the concept described previously, the automated process for determining expected arrival times could be implemented using the flowchart given in Figure 3.18.

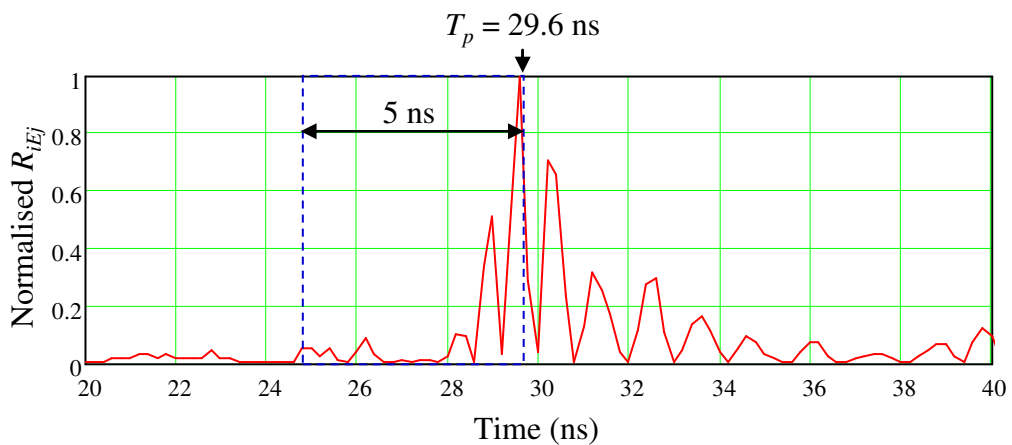


Figure 6.27 Expanded view of Figure 6.26 to illustrate the boundaries and search region for the expected arrival time.

To evaluate the performance of R_{iEj} , five UHF data sets (set 1 – set 5) obtained during HV testing of an HVDC reactor were used, where the test arrangement can be found in [73]. Each set contains four signals (S1 – S4) received from four UHF sensors. Typical UHF waveforms are illustrated in Figure 6.28. There were 20 signals in total for analysis, all from the same PD source.

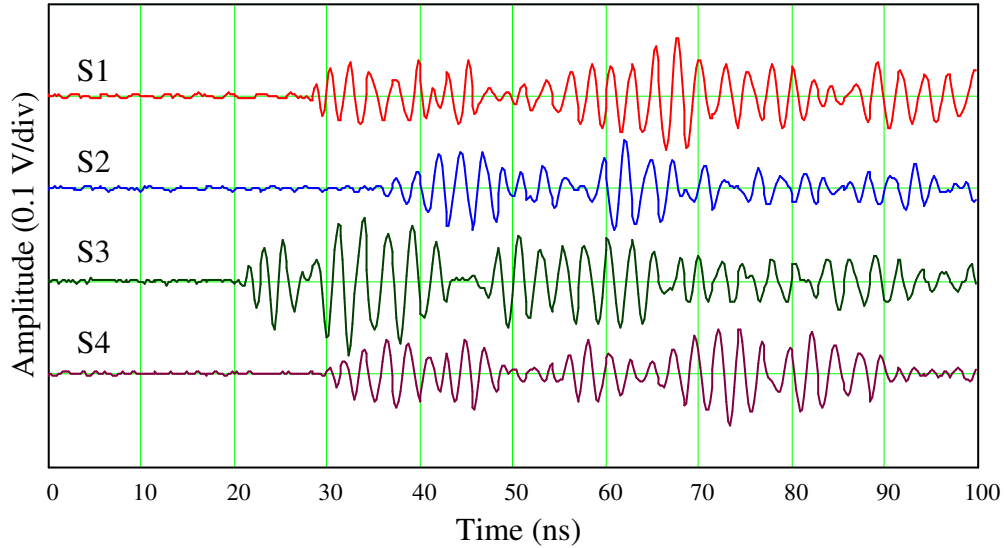


Figure 6.28 UHF signals obtained from four sensors, recorded simultaneously.

Following the process shown in Figure 3.18, the first step is to identify T_p for each signal. These are summarised in Table 6.6. The second is to apply the threshold with respect to the highest peak of R_{iEj} , which is varied between 5% and 20% to determine absolute arrival times for set 2 to set 5 within a 5-ns window length (for these sets of data only) prior to T_p . The absolute arrival times for each threshold level are thus established and Table 6.7 shows an example of the absolute arrival times obtained from various threshold levels using PD set 2. The measured time *differences* for each set are calculated afterwards, and some examples are shown in Table 6.8.

Table 6.6 Time of highest peak, T_p (ns).

PD set	S1	S2	S3	S4
1	29.6	38.6	22.4	31.0
2	38.0	54.6	30.2	39.2
3	34.6	44.4	28.2	36.8
4	45.6	54.6	38.4	49.0
5	48.0	54.4	40.0	50.0

Table 6.7 Examples of arrival times (ns) obtained from PD set 2.

PD set 2	Threshold being determined arrival times			
	5%	10%	15%	20%
S1	37.0	37.0	37.2	37.2
S2	49.6	49.6	49.6	49.8
S3	28.6	28.6	29.2	29.4
S4	38.4	38.4	38.6	38.6

Table 6.8 Time differences (ns) calculated from Table 6.7.

PD set 2	Threshold being determined arrival times			
	5%	10%	15%	20%
ΔT_{12}	-12.6	-12.6	-12.4	-12.6
ΔT_{23}	21.0	21.0	20.4	20.4
ΔT_{34}	-9.8	-9.8	-9.4	-9.2
ΔT_{41}	1.4	1.4	1.4	1.4

To evaluate the performance of R_{iEj} , PD set 1 was used to calculate reference time differences. By using combined plots of R_{iEj} waveforms and cumulative energy curves, absolute arrival times were identifying manually. These were 28.8 ns, 35.6 ns, 21.0 ns, and 30.4 ns for S1, S2, S3 and S4, respectively. This approach is considered the most effective means to get accurate times. Reference time differences were then computed as -6.8, 14.6, -9.4 and 1.6 ns for ΔT_{12} , ΔT_{23} , ΔT_{34} and ΔT_{41} , respectively. After analysing expected time differences when varying thresholds between 5% and 20% for PD set 2 to 4, absolute errors between expected and reference time differences and their average values were then calculated. Results are summarised in Table 6.9, for instance. By plotting the average values of absolute error against threshold level, it was found that a 15% threshold level is the most effective choice in this study [100], as shown in Figure 6.29. Three of four error

values are less than 0.5 ns (equivalent to 0.15 m propagation path in air) with this choice of threshold.

Table 6.9 Absolute errors (ns) and their average values for each threshold level calculated from Table 6.8.

Absolute errors for	Threshold			
	5%	10%	15%	20%
ΔT_{12}	5.8	5.8	5.6	5.8
ΔT_{23}	6.4	6.4	5.8	5.8
ΔT_{34}	0.4	0.4	0	0.2
ΔT_{41}	0.2	0.2	0.2	0.2
Average	3.2	3.2	2.9	3.0

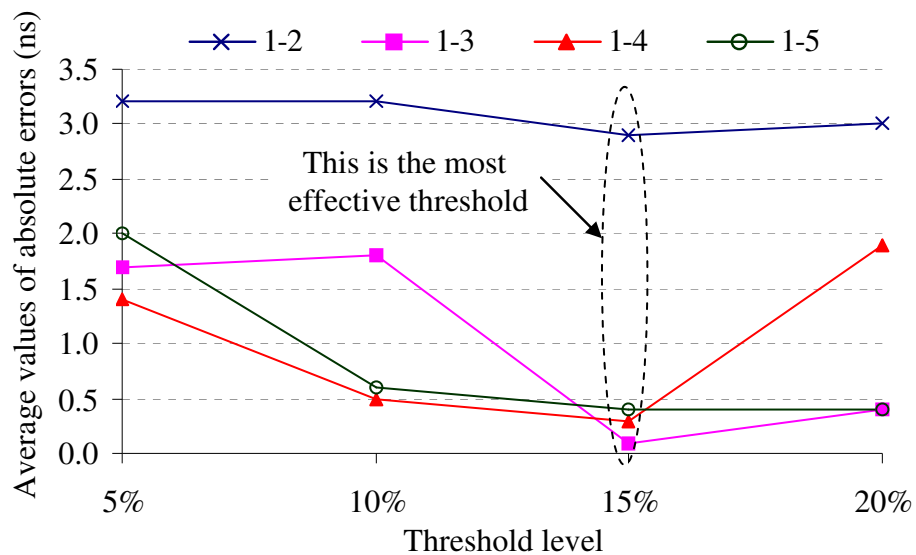


Figure 6.29 Average values of absolute errors for 4 sensors plotted against threshold levels. This is to illustrate that the 15% threshold level is the most effective option in this study.

6.3.2 Contribution to time offset compensation

The main intention of using R_{iEj} is to identify absolute arrival times of UHF signals. However, an additional application for the R_{iEj} method could be in aligning PD signals generated from same PD source but presenting different triggering positions by means of the highest peaks of R_{iEj} waveforms. During signal acquisition, it is common that UHF PD waveforms caused by the same PD source can have different triggering positions as a consequence of stochastic signal amplitude variations. These different alignments can make their envelopes appear dissimilar when the difference coefficient is calculated. The highest peak within R_{iEj} could provide a marker to indicate how much time compensation should be applied. This approach can align the same PD waveforms that have different triggering positions automatically, which may be useful for the envelope comparison method.

An example of this functionality will be presented using the same data sets used in Section 6.3.1. Those signals were created from the same PD source. From Table 6.6, time shifts and their average values of each set can be calculated, which are summarised in Table 6.10. Figure 6.30 illustrates typical UHF waveforms captured by sensor 1 while Figure 6.31 shows these waveforms after time offset compensation where they have been shifted by the average time shifts from Table 6.10. From this figure, it is indicated that using highest peaks of R_{iEj} can align UHF signals successfully to within a few ns [100], which is satisfactory for subsequent envelope comparison.

Table 6.10 Time shifts and their averages.

PD set	Time shift (ns) of each channel				Average time shift	
	S1	S2	S3	S4	ns	points
1	-	-	-	-	<i>reference</i>	-
2	8.4	16.0	7.8	8.2	10.1	51
3	5.0	5.8	5.8	5.8	5.6	28
4	16.0	16.0	16.0	18.0	16.5	83
5	18.4	15.8	17.6	19.0	17.7	86

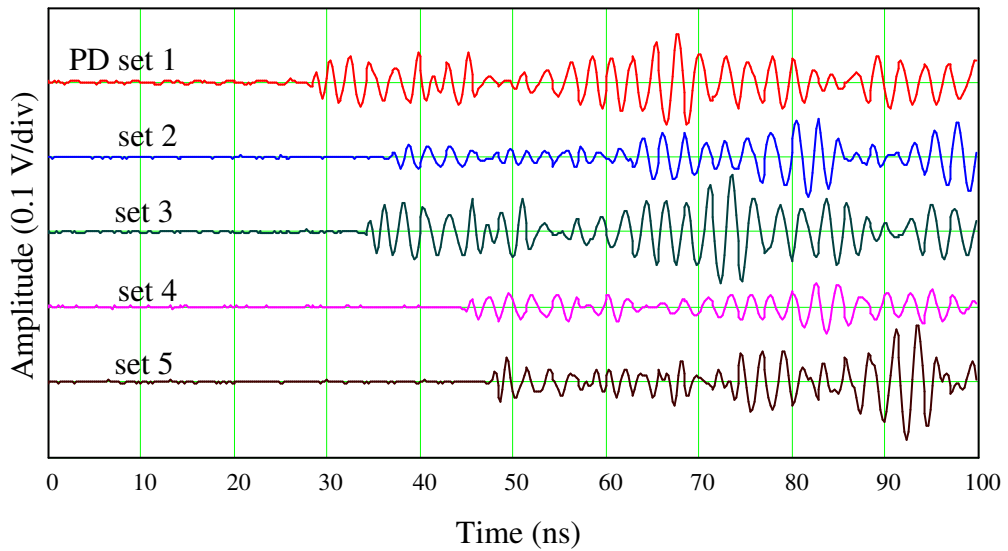


Figure 6.30 Original UHF signals captured by sensor 1.

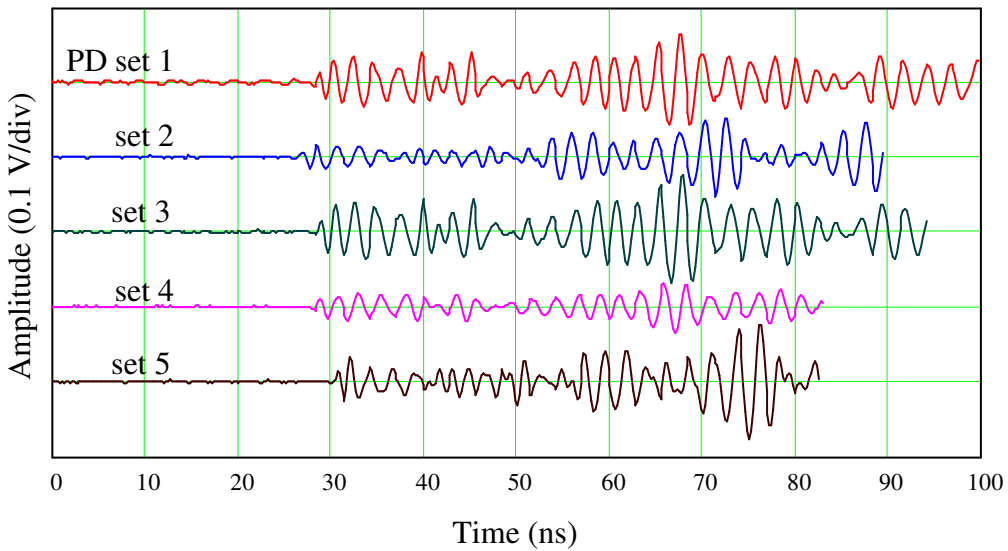


Figure 6.31 Waveforms after time offset compensation, which is done by aligning peaks of R_{iEj} .

Once the UHF signals are aligned, the envelope comparison method presented in Chapter 2 can be applied for distinguishing between different PD sources. To roughly evaluate the similarity of the waveforms shown in Figure 6.31, consideration of envelopes may be used. Envelopes of original and shifted version were created

using the 4-ns Gaussian kernel smoothing. Their envelopes are depicted in Figure 6.32(a) and (b) for original envelopes and shifted versions, respectively. Figure 6.32(b) shows that three envelopes possess very comparable shapes whereas the other two are dissimilar. This indicates that at least two categories of the signal envelopes can be distinguished successfully. This process could be beneficial when massive sets of UHF data need to be analysed.

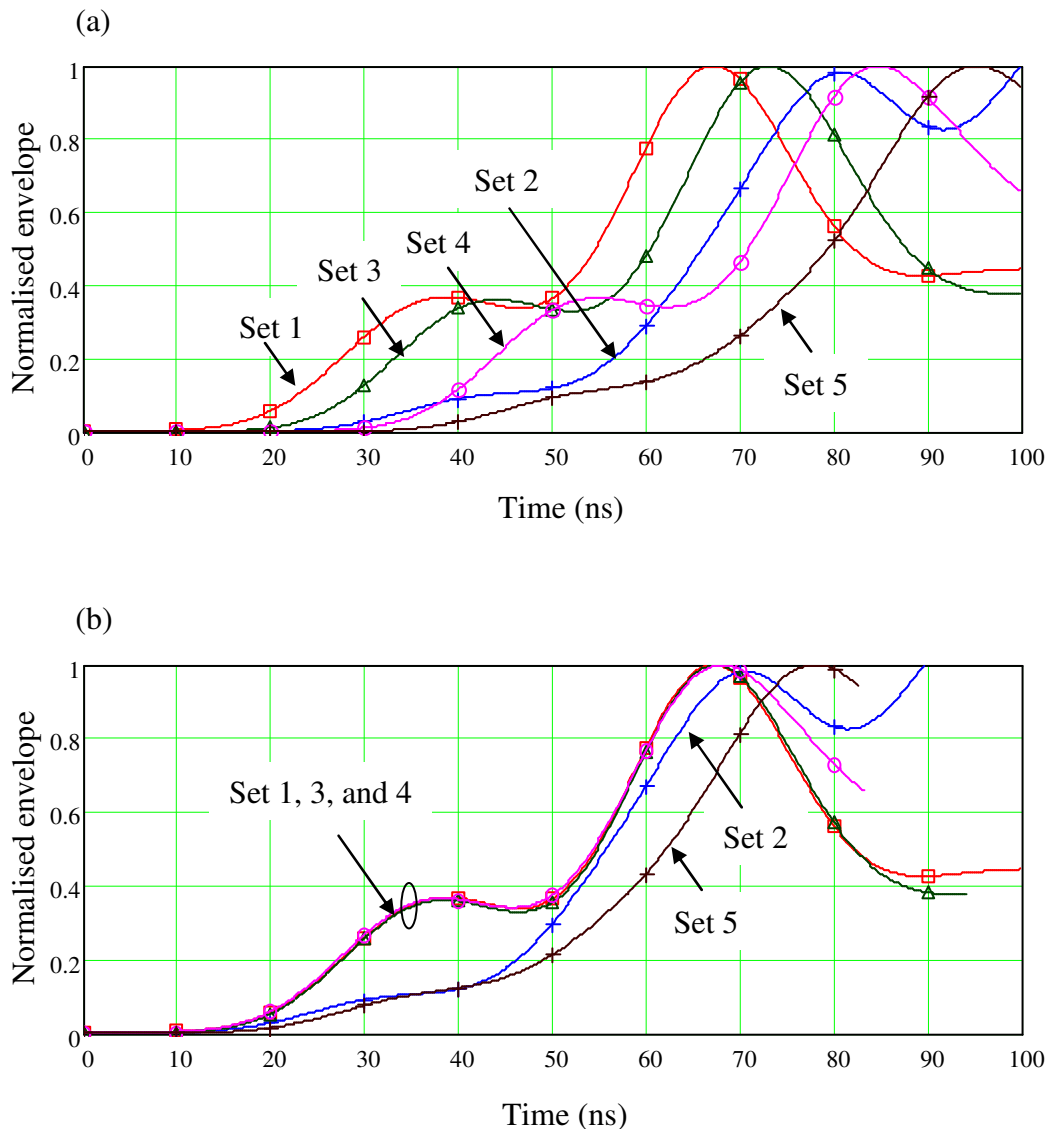


Figure 6.32 Normalised envelopes of: (a) Original UHF signals shown Figure 6.30, to show that original envelopes appear dissimilar when considering in the same period of time, (b) Shifted version.

6.4 Applications to other types of monitoring system

In the previous chapters, the focus has been on the techniques for analysis and interpretation of UHF PD signals. These include the envelope comparison method for distinguishing between different PD sources, studies of various techniques for accurately determining arrival times and implementing those techniques in PD practical applications. Moreover, a new technique, called *relative increase in energy*, for determining arrival times and the new *arrival time consistency index* for evaluating reliability of choices for particular threshold percentages, have been presented.

All methods mentioned here are capable of being applied in other monitoring systems that detect unknown transient signals. For example, an acoustic detection system for PD signals in power transformers provides transient signals captured at acoustic sensors, such as the acoustic signal shown in Figure 6.33 and its envelope shown in Figure 6.34 [95]. It would be possible to apply relative increase in energy or wavelet decomposition methods to the transient signal illustrated in Figure 6.33 to acquire its arrival time, for example. Additionally, the envelope comparison method might also be applied to the envelope shown in Figure 6.34 for distinguishing between different PD sources.

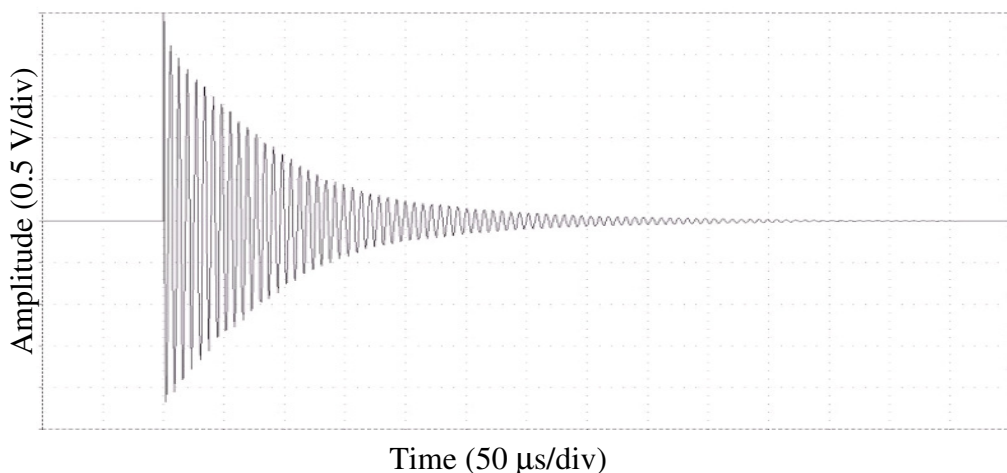


Figure 6.33 Acoustic signal created from the PD source in power transformer [95].

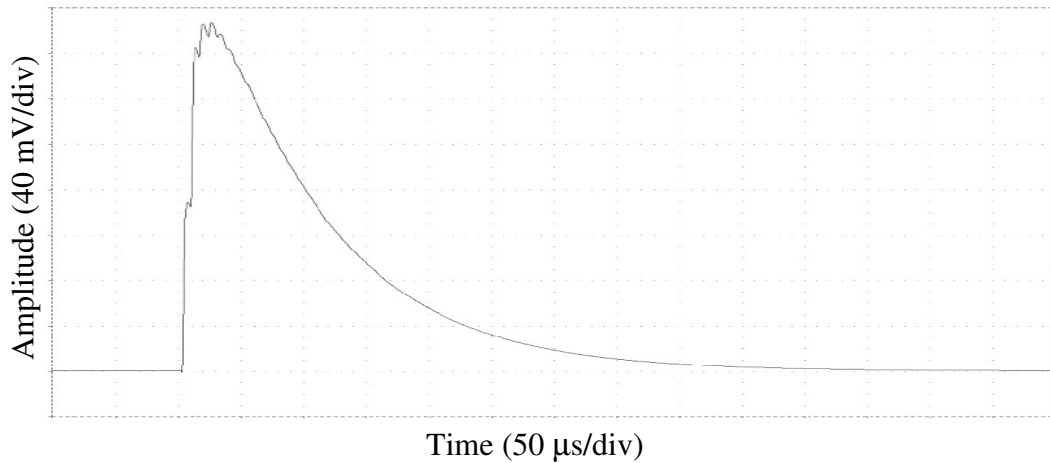


Figure 6.34 Envelope signal taken from the signal shown in Figure 6.33 [95].

Another instance would be to determine arcing times in HVAC circuit breakers based on the radio frequency technique presented in [130]. To identify arcing time ($\Delta t_{arc} = t_1 - t_0$) of an HVAC circuit breaker, the rising (t_0) and falling (t_1) edges can be observed, which is $\Delta t_{arc} = 6.8 - 3.4 = 3.4$ ms, illustrated in Figure 6.35. Both rising and falling times can be manually selected in this application but they are potentially subjective dependent on an operator's skill. By using relative increase in energy, both edges could be automatically determined using the procedure depicted in Figure 3.18.

In addition, for some specific circumstances (e.g. where only one monitoring sensor can be installed because of limited accessibility) the envelope comparison method can be used to distinguish between different signal sources. This is because it considers comparisons between successive envelopes for each calculation, as defined conceptually in Figure 2.4.

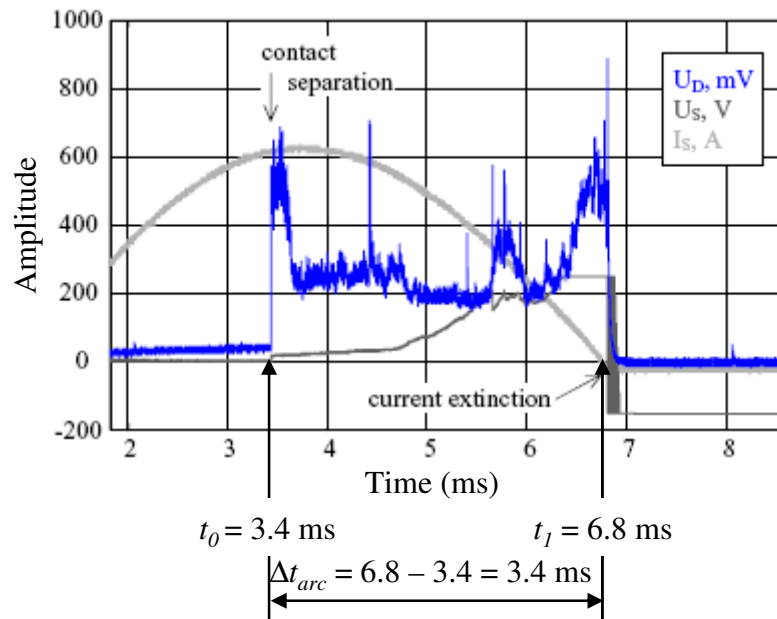


Figure 6.35 Demodulated output of the sensor, switch voltage (U_s) and current (I_s). Contact separation is seen at $t_0 = 3.4$ ms and the arc is extinguished at $t_1 = 6.8$ ms, so that its arcing time is 3.4 ms [130].

6.5 Discussion and conclusions

In this chapter, practical applications for the concepts presented in Chapter 2 and Chapter 3 have been explained.

In Chapter 2, it was shown that different PD sources can be distinguished by means of envelope comparison. Hence, envelopes of UHF signals were created using Gaussian kernel smoothing and average multi-sensor difference coefficient values were calculated using Eqn. 2.5 (similarity assessment equation) between pairs of envelopes. Following this step, difference coefficient values obtained from the same and different PD locations were divided into two different bands with clear margins of 19:1 for $W = 4$ ns and of 23:1 for $W = 20$ ns. No reduction in data sample points took place during the creation of envelopes using Gaussian kernel smoothing in this analysis. Since Gaussian kernel smoothing acts like a low-pass filter, offering

potential benefits of sampling rate reduction, envelopes captured using a lower sampling rate may also be suitable for distinguishing between different PD sources.

To verify the principle using computer modelling, a 3rd order low-pass Butterworth filter with 10 MHz cut-off frequency was used to generate envelopes and these envelopes were then re-sampled with a lower sampling rate (reduced from 5×10^9 to 50×10^6 samples/sec). The envelope comparison method was applied to those reduced sampling rate envelopes and a margin of 10:1 was obtained for PD in different locations.

Thereafter, a two-channel envelope detector was constructed and its outputs were captured with a sampling rate of 50×10^6 samples/sec and passed through to the built-in 'eres' function of the oscilloscope which applied further smoothing. Two laboratory experiments showed that reduced signal sampling rate envelopes can be used for differentiating between different PD sources successfully.

The concept of relative increase in energy has been introduced in Section 3.5. Its first application is in automatically determining arrival times. After applying the relative increase in energy equation to UHF signals, the upper limits of the arrival times can be identified by means of times at highest peaks of each relative increase in energy waveform. Within a specific time window (e.g. 5 ns) prior to and including time at highest peak, accurate absolute arrival times can be determined automatically by means of a threshold crossing method applied to the normalised relative increase in energy waveforms. Results indicate that absolute arrival times obtained from this method are within ± 0.5 ns tolerance. Another application of relative increase in energy is concerned with time offset compensation. Time offset between PD pulses generated from same PD sources are one of concern in practical PD analysis since the triggering position on UHF PD signals is variable. Results verify that re-aligning signals in the time-domain can be achieved by means of highest peaks in the relative increase in energy waveforms. Once PD pulses are shifted into alignment, other analysis methods can be applied with greater confidence.

The concepts presented in Chapter 2 and Chapter 3 can potentially find use in any monitoring systems that detect unknown transient signals. Acoustic signals produced by PD sources, for example, could employ relative increase in energy or wavelet decomposition for determining absolute arrival times, as well as the envelope comparison method for distinguishing between different signal sources. The relative increase in energy could be used to determine arcing time of circuit breakers. In circumstances where only one sensor is available, the envelope comparison method can perform a valuable function to distinguish between different sources of signals.

7. Conclusions and Future Work

This chapter will summarise the main conclusions drawn from the research activity including additional opportunities for research which may be pursued as a result of the findings reported in this thesis.

7.1 Envelope comparison

The envelope comparison method is a valuable technique for distinguishing between different PD sources that may be caused by either different PD types or different locations, based on their distinctive envelopes. The envelope comparison method is concerned with representing original transient signals as their envelopes by applying a smoothing kernel. These envelopes still retain sufficient signal variation details for assessing the similarity by comparisons between pairs of envelopes.

Evaluated using UHF PD signals from both laboratory experiments and HV industrial tests, results confirm that envelope comparison can be used to distinguish between different PD sources successfully based on average multi-sensor difference coefficient values when the smoothing kernel parameters are selected appropriately. For example, 4-ns and 20-ns Gaussian kernel smoothing windows provided margins of 19:1 and 23:1 respectively for experiments and the 4-ns Gaussian kernel smoothing window provided margins of 30:1 and 9:1 respectively for the switched HVDC reactor and the 252 MVA power transformer (actual HV industrial tests). These are based on original signal sampling rate of 5×10^9 samples/sec.

Gaussian kernel smoothing is effectively a low-pass filter, so sampling rate reduction for recording UHF envelopes is possible. By investigating the bandwidth of filtering by Gaussian kernel smoothing as a function of window width, it was found that the sampling rate can be reduced by a factor of 100 with the 4-ns smoothing window. To investigate further, computer modelling was used to assess this principle. Using a 3rd order Butterworth low-pass filter with 10 MHz cut-off frequency to create UHF

envelopes, which were re-sampled at 50×10^6 samples/sec, computer modelling confirmed that it is possible to distinguish between different PD sources using a reduced sampling rate envelope, giving a margin of 10:1 (reduced by 47% from the original sampling rate result).

Therefore, a simple 2-channel UHF envelope detector was constructed and its outputs captured using a sampling rate of 50×10^6 samples/sec. Evaluation was conducted by means of experiments in a shielded room and in a model transformer. Results in both cases showed that reduced sampling rate envelopes of UHF signals can be used to distinguish between different PD sources with margins of 4.3:1 for a shielded room and between 5.0:1 and 1.7:1 in a model transformer. Although margins reduced significantly, they were effective for separation.

Successful envelope comparison using reduced sampling rates will reduce the cost of the measurement system and minimise data storage requirements. The potential reduction in power consumption might in future allow processing to be carried out at the sensor node. The envelope comparison method could be applied to other monitoring systems that detect unknown transients (e.g. acoustic signals). Even when only one sensor is available, it is still possible to use the envelope comparison method to distinguish between different signal sources.

7.2 Relative increase in energy

Arrival times of UHF signals are important because locating PD sources by means of time of flight measurement requires accurate time differences. Determining arrival times accurately is challenging because it is dependent on signal characteristics and the measurement system. In this thesis, four existing methods for determining arrival times have been considered, namely, expanding time scale, threshold crossing of squared voltage, knee point of cumulative energy and the energy criterion. These methods each possess some limitations, such as certain degrees of bias caused by the operator's experience. However, the threshold crossing of squared voltage and knee

point of the cumulative energy curve have been prove to be effective for practical applications. Thus, the relative increase in energy (R_{iEj}) method has been introduced building on these two methods for determining arrival times of UHF signals. Arrival times can be indentified manually using a combined plot of R_{iEj} and cumulative energy, where the arrival time is the time of the first significant peak of R_{iEj} .

Evaluating this method by pulse injection tests on a 252 MVA power transformer showed that mean errors of time differences obtained from the relative increase in energy curve is 0.93 ns while that of the 2% threshold crossing of voltage squared method is 4.58 ns. This confirmed that arrival times resulting from the combined plot of R_{iEj} and cumulative energy curves perform effectively. However, this approach to identifying arrival times is potentially subjective and requires engineering judgements.

Hence, a more robust algorithm was proposed, which can be automated. This algorithm involves selecting a subset of the data within a pre-defined window prior to and including the highest peak of R_{iEj} and then applying a threshold crossing method with threshold level being defined as a percentage of the highest peak. Applying this automated process to PD data sets obtained from the switched HVDC reactor, results show that arrival times obtained from this method are within ± 0.5 ns tolerance based on an optimum 15% threshold of the peak value of R_{iEj} .

Additionally, relative increase in energy is beneficial for time offset compensation. Using PD pulses with varying trigger positions yet produced from the same PD source, results verify that aligning them can be facilitated by means of highest peaks in the R_{iEj} waveforms. Once PD pulses are shifted into alignment, other analysis methods can be applied. Using R_{iEj} is not limited only the signals produced from PD sources, it might be applied to other signals that need time duration to be identified automatically, such as the arc timing of HV breakers.

7.3 The use of wavelet analysis

A concern about using wavelet de-noising of UHF PD signals is that the shape of de-noised signals may be modified in a way that alters their apparent arrival times. This could degrade the accuracy of UHF PD location using the time of flight technique. Investigating this concern using PD signals obtained from an 18 MVA power transformer test showed that wavelet de-noising may be not necessary for signals with an SNR of more than 20 dB and it may offer little benefit for signals with SNR less than 5 dB when arrival times are the main factor of interest. Moreover, wavelet de-noising can cause errors of time differences in excess of 1 ns (corresponding to 0.2 m propagation path error in transformer oil), especially for signals with SNR less than 10 dB. Therefore, using wavelet de-noising on UHF signals needs to be applied with caution.

An alternative aspect of wavelet analysis potentially useful to determine arrival times is the use of wavelet decomposition. It was found necessary to artificially increase the sampling rate of the original signal in order to retain sufficient time resolution after the signal was decomposed through many levels. This was investigated and results indicate that 2-level decomposition gave the minimum mean value of absolute errors of 0.40 ns. Compared with the 2% threshold crossing of original UHF voltage squared (mean value of absolute error 0.32 ns), wavelet decomposition at level 2 showed slightly higher error. Although wavelet decomposition did not improve on the 2% threshold crossing method of voltage squared, there remains much scope for further work.

The methodologies for analysis presented in this thesis will provide a clear framework for future study. There remains much more scope for both wavelet de-noising and wavelet decomposition in order to improve the accuracy of determining arrival times, such as the selection of alternative mother wavelets suitable for UHF PD signals.

7.4 Experimental investigation into the accuracy of signal arrival time measurements

Accuracy of arrival time measurements depends on a variety of factors. In this thesis, comprehensive investigations were carried out experimentally. Building on the findings, a number of approaches for obtaining more accurate arrival times have been outlined.

The first approach to improve the accuracy of arrival time measurement is the selection of UHF sensors among common types of sensor construction (disc, monopole and spiral). Measurements indicated that most of errors of the disc sensor were in a limited band with mean value of 0.93 ns and standard deviation of 0.70 ns. Corresponding values for the monopole and spiral had more scatter with their mean errors of 1.14 and 1.40 ns and standard deviations of 0.91 and 1.77 ns, respectively. Thus, among the monopole, disc and spiral UHF sensors tested, the disc type should provide the better accuracy for PD location applications.

A second investigation studied the effect of variations in PD current direction and concluded that there is no strong effect on the accuracy of UHF PD location based on arrival times. Results also showed that errors in arrival times can be improved by a factor of 2 by increasing the sensitivity of the measurement, at the expense of signal clipping on the oscilloscope. This test emphasises the influence of different oscilloscope acquisition settings, which can be selected so as to improve accuracy and allow for better interpretation of the measured signal data. Results also reveal that the accuracy of arrival times at the more distant sensor may be degraded since their initial wavefronts become more difficult to identify, causing errors during the calculation.

A third approach was to introduce an arrival time consistency index to assess the reliability of choices for particular threshold percentages between 2% and 5% for determining arrival times. Experimental results indicate that a threshold of 3% or 4% is most effective when applied to the instantaneous UHF voltage squared.

7.5 Future work

Specific work that should be carried out to build upon and enhance this research will be summarised here.

In relation to techniques used for measuring the similarity of two signals by means of envelope comparison, the similarity assessment proposed in terms of the difference coefficient needs to be rigorously compared with conventional correlation techniques. This will provide benchmarking across these two techniques. Moreover, to implement the envelope comparison method using reduced sampling rate envelopes, the relationship between sampling rate reduction and the reduced margin of difference coefficient values should be investigated in detail. This investigation should assess the ability of UHF monitoring systems using reduced sampling rate envelopes to perform effectively despite the reduced margins.

Since the relative increase in energy method provided good estimates of arrival times (as presented in Chapter 3), an arrival time comparison between this method and the wavelet analysis reported in Chapter 4 should be investigated. This comparison should consider the possibility of combining these two techniques in order to improve the determination of UHF signal arrival times. In addition, the relationship between a biggest peak amplitude and time of the biggest peak for time-shifting UHF signals (to correct for variable triggering positions) should be investigated as it may provide remarkable features for distinguishing between different PD sources. However, the relative increase in energy still requires more experimental and practical tests to validate its capability for indentifying arrival times of UHF PD signals.

The relationship between arrival time consistency indexes and differential distances between sensors and PD positions should be investigated as it may provide useful guidelines for improving PD location accuracy. The radiation pattern of the spark unit should also be characterized to establish clearly whether or not its radiation

pattern is significantly directional, as this aspect may play an important role in the interpretation of results derived from its use.

8. References

- [1] IEC International Standard 60270. *High-voltage test techniques - Partial discharge measurements*. International Electrotechnical Commission (IEC), 2000.
- [2] F. H. Kreuger. *Partial discharge detection in high-voltage equipment*, Butterworth & Co., 1989.
- [3] E. Lemke. Guide for partial discharge measurements in compliance to IEC60270, available from http://www.doble-lemke.eu/en/Media/Technical_Papers/Teilentladung_Veroeffentlichung.html
- [4] Y. Takahashi. Two hundred years of Lichtenberg figures, *Journal of Electrostatics*, Vol. 6, Issue. 1, pp. 1 – 13, 1979.
- [5] L. Niemeyer. A generalized approach to partial discharge modeling, *IEEE Transactions on Dielectrics and Electrical Insulation*, Vol. 2, No. 4, pp. 510 – 528, 1995.
- [6] A. A. Hossam-Eldin. Analysis of discharge damage and breakdown in gaseous cavities in insulating materials, *Journal of Physics D: Applied Physics*, Vol. 17, pp. 412 – 428, 1984.
- [7] T. Tanaka. Internal partial discharge and material degradation, *IEEE Transactions on Electrical Insulation*, Vol. 21, No. 6, pp. 899 – 905, 1986.
- [8] P. H. F. Morshuis. Degradation of solid dielectrics due to internal partial discharge: Some thoughts on progress made and where to go now, *IEEE Transactions on Dielectrics and Electrical Insulation*, Vol. 12, No. 5, pp. 905 – 913, 2005.
- [9] E. Gulski. Computer-aided measurement of partial discharges in HV equipment, *IEEE Transactions on Electrical Insulation*, Vol. 28, No. 6, pp. 969 – 983, 1993.
- [10] A. Krivda. Automated recognition of partial discharges, *IEEE Transactions on Dielectrics and Electrical Insulation*, Vol. 2, No. 5, pp. 796 – 821, 1995.

- [11] A. Cavallini, G. C. Montanari, F. Puletti, and A. Contin. A new methodology for the identification of PD in electrical apparatus: Properties and applications, *IEEE Transactions on Dielectrics and Electrical Insulation*, Vol. 12, No. 2, pp. 203 – 215, 2005.
- [12] B. H. Ward. A survey of new techniques in insulation monitoring of power transformers, *IEEE Electrical Insulation Magazine*, Vol. 17, No. 3, pp. 16 – 23, 2001.
- [13] M. D. Judd, S. D. J. McArthur, J. R. McDonald, and O. Farish. Intelligent condition monitoring and asset management partial discharge monitoring of power transformers, *Power Engineering Journal*, Vol. 16, No. 6, pp. 297 – 304, 2002.
- [14] J. P. van Bolhuis, E. Gulski, and J. J. Smit. Monitoring and diagnostic of transformer solid insulation, *IEEE Transactions on Power Delivery*, Vol. 17, No. 2, pp. 528 – 536, 2002.
- [15] Y. Han and Y. H. Song. Condition monitoring techniques for electrical equipment – a literature survey, *IEEE Transactions on Power Delivery*, Vol. 18, No. 1, pp. 4 – 13, 2003.
- [16] E. Kuffel. W. S. Zaengl. and J. Kuffel. *High voltage engineering: Fundamentals*, Butterworth-Heinemann, 2nd edn, 2000.
- [17] A. Pedersen. Criteria for spark breakdown in sulphur hexafluoride, *IEEE Transactions on Power Apparatus and Systems*, Vol. 89, No. 8, pp. 2043 – 2048, 1970.
- [18] M. M. Morcos, and K. D. Srivastava. On the statistical testing of solid insulation systems, *IEEE Power Engineering Review*, Vol. 20, No. 6, pp. 55 – 57, 2000.
- [19] J. J. O'Dwyer. Breakdown in solid dielectrics, *IEEE Transactions on Electrical Insulation*, Vol. EI-17, No. 6, pp. 484 – 487, 1982.
- [20] O. Lesaint. “Streamers” in liquids: relation with practical high voltage insulation and testing of liquids, In Proceedings of *IEEE International Conference on Dielectric Liquids*, pp. 1 – 6, Futuroscope-Chasseneuil, 2008.

- [21] S. A. Boggs. Partial discharge – part III: Cavity-induced PD in solid dielectrics, *IEEE Electrical Insulation Magazine*, Vol. 6, No. 6, pp. 11 – 20, 1990.
- [22] T. Kalicki and J. R. Densley. Partial discharge characteristics of voids in extruded insulations – theoretical studies, In *Proceedings of 11th International High Voltage Engineering Symposium*, Vol. 4, pp. 200 – 203, London, 1999.
- [23] Y. Murooka, T. Takada, and K. Hidaka. Nanosecond surface discharge and charge density evaluation part I: Review and experiments, *IEEE Electrical Insulation Magazine*, Vol. 17, No. 2, pp. 6 – 16, 2001.
- [24] J. Wang, Y. X. Zhou, P. Yan, W. L. Huang, G. J. Li, S. C. Zhang, and G. S. Sun. Study on dielectric surface discharge in transformer oil under high voltage nanosecond pulse, *Journal of Electrostatics*, Vol. 63, pp. 665 – 671, 2005.
- [25] R. Patsch. Electrical and water treeing: a chairman’s view, *IEEE Transactions on Electrical Insulation*, Vol. 27, No. 3, pp. 532 – 542, 1992.
- [26] S. A. Boggs. Partial discharge: Overview and signal generation, *IEEE Electrical Insulation Magazine*, Vol. 6, No. 4, pp. 33 – 39, 1990.
- [27] K. Wu, Y. Suzuoki, T. Mizutani, and H. Xie. Model for partial discharges associated with treeing breakdown: II. tree growth affected by PDs, *Journal of Physics. D: Applied Physics*, Vol. 33, pp. 1202 – 1208, 2000.
- [28] *IEEE guide for the interpretation of gases generated in oil-immersed Transformers*, IEEE standard C57.104, 2008.
- [29] M. Duval and A. dePablo. Interpretation of gas-in-oil analysis using new IEC publication 60599 and IEC TC10 databases, *IEEE Electrical Insulation Magazine*, Vol. 17, No. 2, pp. 31 – 41, 2001.
- [30] M. Duval. A review of faults detectable by gas-in-oil analysis in transformers, *IEEE Electrical Insulation Magazine*, Vol. 18, No. 3, pp. 8 – 17, 2002.
- [31] J. M. Braun and F. Y. Chu. Novel low-cost SF₆ arcing byproduct detectors for field use in gas-insulated switchgear. *IEEE Transactions on Power Systems*, Vol. 1, No. 2, pp. 81 – 86, 1986.

- [32] H. Yang and C. Liao. Adaptive fuzzy diagnosis system for dissolved gas analysis of power transformers, *IEEE Transactions on Power Delivery*, Vol. 14, No. 4, pp. 1342 – 1350, 1999.
- [33] L. E. Lundgaard. Partial discharge – Part XIII: Acoustic partial discharge detection – Fundamental considerations, *IEEE Electrical Insulation Magazine*, Vol. 8, No. 4, pp. 25 – 31, 1992.
- [34] *IEEE guide for the detection and location of acoustic emissions from partial discharges in oil-immersed power transformers and reactors*, IEEE standard C57.127, 2007.
- [35] L. E. Lundgaard. Partial discharge – Part XIV: Acoustic partial discharge detection – Practical application, *IEEE Electrical Insulation Magazine*, Vol. 8, No. 5, pp. 34 – 43, 1992.
- [36] S. Markalous, S. Tenbohlen, and K. Feser. Detection and location of partial discharges in power transformers using acoustic and electromagnetic signals, *IEEE Transactions on Dielectrics and Electrical Insulation*, Vol. 15, No. 6, pp. 1576 – 1583, 2008.
- [37] Y. Lu, X. Tan, and X. Hu. PD detection and localisation by acoustic measurements in an oil-filled transformer, *IEE Proceedings Science, Measurement and Technology*, Vol. 147, No. 2, pp. 81 – 85, 2000.
- [38] M. E. Haque, A. B. Darus, M. M. Yaacob, and F. Ahmed. Diagnosis of GIS based on acoustic sensing technique, In *Proceedings of 4th International Conference on Advances in Power System Control, Operation and Management*, Vol. 2, pp. 556 – 558, Hong Kong, 1997.
- [39] N. Kock, B. Coric, and R. Pietsch. UHF PD detection in gas-insulated switchgear – Suitability and sensitivity of the UHF method in comparison with the IEC 270 method, *IEEE Electrical Insulation Magazine*, Vol. 12, No. 6, pp. 20 – 26, 1996.
- [40] I. A. Metwally. Status review on partial discharge measurement techniques in gas-insulated switchgear/lines, *Electrical Power Systems Research*, Vol. 69, No. 1, pp. 25 – 36, 2004.

- [41] J. S. Pearson, O. Farish, B. F. Hampton, M. D. Judd, D. Templeton, B. W. Pryor, and I. M. Welch. Partial discharge diagnostics for gas insulated substations, *IEEE transactions on Dielectrics and Electrical Insulation*, Vol. 2, No. 5, pp. 893 – 905, 1995.
- [42] M. D. Judd. Radiometric partial discharge detection, In *Proceedings of International Conference on Condition Monitoring and Diagnosis*, pp. 1025 – 1030, Beijing, 2008.
- [43] B. F. Hampton, and R. J. Meats, Diagnostic measurements at UHF in gas insulated substations. *IEE Proceedings Generation, Transmission and Distribution*, Vol. 135, No. 2, pp. 137 – 145, 1988.
- [44] T. Huecker, and J. Gorablenkow. UHF partial discharge monitoring and expert system diagnosis, *IEEE Transactions on Power Delivery*, Vol. 13, No. 4, pp. 1162 – 1167, 1998.
- [45] J. Pearson, B. F. Hampton, M. D. Judd, B. Pryor, and P. F. Coventry. Experience with advanced in-service condition monitoring techniques for GIS and transformers, In *Proceedings of IEE Colloquium on HV Measurements, Condition Monitoring and Associated Database Handling Strategies*, pp. 8/1 – 8/10, London, June, 1998.
- [46] M. D. Judd, L. Yang, and I. B. B. Hunter. Partial discharge monitoring for power transformers using UHF sensors part 2: Field experience, *IEEE Electrical Insulation Magazine*, Vol. 21, No.3, pp. 5 – 13, 2005.
- [47] J. Lopez-Roldan, T. Tang, and M. Gaskin. Optimisation of a sensor for onsite detection of partial discharges in power transformers by the UHF method, *IEEE Transactions on Dielectrics and Electrical Insulation*, Vol. 15, No. 6, pp. 1634 – 1639, 2008.
- [48] B. Xu, J. Li, W. Si, and Y. Li. Simulating propagation characteristic of UHF signal for PD monitoring in transformers by FDTD technique, In *Proceedings of Asia-Pacific Power and Energy Engineering Conference*, pp. 1 – 4, Wuhan, 2009.

- [49] M. D. Judd, L. Yang, and I. B. B. Hunter. Partial discharge monitoring for power transformers using UHF sensors part 1: Sensors and signal interpretation, *IEEE Electrical Insulation Magazine*, Vol. 21, No.2, pp. 5 – 14, 2005.
- [50] J. Yang, D. Li, J. Li, P. Yuan, and Y. Li. Study of time delay of UHF signal arrival in location partial discharge, In *Proceedings of International Conference on Condition Monitoring and Diagnosis*, pp. 1088 - 1092, Beijing, 2008.
- [51] P. Kakeeto, M. D. Judd, J. Pearson, D. Templeton. Experimental investigation of positional accuracy for UHF partial discharge location, In *Proceedings of International Conference on Condition Monitoring and Diagnosis*, pp. 1070 - 1073, Beijing, 2008.
- [52] A. Reid. *A new approach to partial discharge measurement for testing electrical insulation systems*, PhD thesis, University of Strathclyde, 2007.
- [53] T. Hoshino, H. Koyama, S. Maruyama, and M. Hanai. Comparison of sensitivity between UHF method and IEC 60270 for onsite calibration in various GIS, *IEEE Transactions on Power Delivery*, Vol. 21, No. 4, pp.1948 – 1953, 2006.
- [54] G. C. Stone. Partial discharge diagnostics and electrical equipment insulation condition assessment, *IEEE Transactions on Dielectrics and Electrical Insulation*, Vol. 12, No. 5, pp. 891 – 904, 2005.
- [55] *IEC International Standard 60076-1. Power transformers part 1 general*. International Electrotechnical Commission (IEC), 2000.
- [56] K. Newman. Quality assurance and in-house testing, In proceedings of *IEE Colloquium on Transformer Life Management*, pp. 3/1 – 3/5, London, 1998.
- [57] J. P. van Bolhuis, E. Gulski, and J. J. Smit. On-line PD detection, requirements for practical use, In proceeding of *IEEE International Symposium on Electrical Insulation*, pp. 158 – 161, Boston, 2002.
- [58] J. N. Jagers, J. Khosa, P. J. De Klerk, and C. T. Gaunt. Transformer reliability and condition assessment in a South Africa Utility, In proceedings of *XVth International Symposium on High Voltage Engineering*, pp. 1 – 6, Ljubljana, 2007.

- [59] A. Sabot, A. Petit, and J. P. Taillebois. GIS insulation co-ordination: on-site tests and dielectric diagnostic techniques, a utility point of view, *IEEE Transactions on Power Delivery*, Vol. 11, No. 3, pp. 1309 – 1316, 1996.
- [60] M. Wang, A. J. Vandermaar, and K. D. Srivastava. Review of condition assessment of power transformers in service, *IEEE Electrical Insulation Magazine*, Vol. 18, No. 6, pp. 12 – 25, 2002.
- [61] B. D. Sparling, and J. Aubin. Power transformer life extension through better monitoring, available from http://www.gepower.com/prod_serv/plants_td/en/thought_leadership.htm.
- [62] R. Bartnikas. Partial discharges Their Mechanism, Detection and Measurement, *IEEE Transactions on Dielectrics and Electrical Insulation*, Vol. 9, No. 5, pp. 763 – 808, 2002.
- [63] M. G. Danikas, N. Gao, and M. Aro. Partial discharge recognition using neural networks: a review”, *Journal of Electrical Engineering* (Springer Berlin/ Heidelberg), Vol. 85, No. 2, pp. 87 – 93, 2003.
- [64] E. Gulski, and A. Krivda. Neural networks as a tool for recognition of partial discharges, *IEEE Transactions on Electrical Insulation*, Vol. 28, No. 6, pp. 984 – 1001, 1993.
- [65] M. M. A. Salama, and R. Bartnikas. Fuzzy logic applied to PD pattern classification, *IEEE Transactions on Dielectrics and Electrical Insulation*, Vol. 7, No. 1, pp. 118 – 123, 2000.
- [66] A. Cavallini, M. Conti, A. Contin, and G. C. Montanari. Advance PD Interference in On-field Measurements Part 2: Identification of Defects in Solid Insulation Systems, *IEEE Transactions on Dielectrics and Electrical Insulation*, Vol. 10, No. 3, pp. 528 – 538, 2003.
- [67] B. T. Phung, T. R. Blackburn, and R. E. James. Recognition of partial discharge using fuzzy logic, In *Proceedings of International Symposium on Electrical Insulating Materials*, pp. 657 – 660, Toyohashi, 1998.
- [68] A. Cavallini, G. C. Montanari, A. Contin, and F. Puletti. A new approach to the diagnosis of solid insulation systems based on PD signal interference, *IEEE Electrical Insulation Magazine*, Vol. 19, No. 2, pp. 23 – 30, 2003.

- [69] L. Hao, and P. L. Lewin. Partial discharge source discrimination using a support vector machine, *IEEE Transactions on Dielectrics and Electrical Insulation*, Vol. 17, No. 1, pp. 189 – 197, 2010.
- [70] X. Ma, C. Zhou, and I. J. Kemp. Interpretation of wavelet analysis and its application in partial discharge detection, *IEEE Transactions on Dielectrics and Electrical Insulation*, Vol. 9, No. 3, pp. 446 – 457, 2002.
- [71] L. Yang, and M. D. Judd. Recognising multiple partial sources in power transformers by wavelet analysis of UHF signals, *IEE Proceedings Science, Measurement and Technology*, Vol. 150, No. 3, pp. 119 – 127, 2003.
- [72] Y. Tian, P. L. Lewin, A. E. Davies, S. J. Sutton, and S. G. Swingler. Application of acoustic emission techniques and artificial neural networks to partial discharge classification, In *Proceedings of IEEE International Symposium on Electrical Insulation*, pp. 119 – 123, Boston, 2002.
- [73] M. D. Judd, S. D. J. McArthur, A. J. Reid, V. M. Catterson, L. Yang, B. Jacobson, K. O. Svensson, and M. Gunnarsson. Investigation of radiometric partial discharge detection for use in switched HVDC testing, In *Proceedings of Power Engineering Society General Meeting Conference*, pp. 1 – 7, Montreal, 2006.
- [74] P. Jarman et. al. Recommendations for condition monitoring and condition assessment facilities for transformers, CIGRE (Paris), Tech. Rep. Brochure 343, April 2008.
- [75] R. Sutton, and A. Barto. *Reinforcement Learning: An Introduction*, MIT Press, 1998.
- [76] I. Watson. *Applying Case Based Reasoning: Techniques for Enterprise Systems*, Morgan Kaufman Publishers, 1997.
- [77] T. Pinpart, G. West, S. Galloway, and M. D. Judd. A method for distinguishing between complex transient signals in condition monitoring applications”, In *Proceedings of International Conference on 5th Condition Monitoring and Machinery Failure Prevention Technologies*, pp. 1163 – 1171, Edinburgh, 2008.
- [78] *Mathcad PLUS 6.0 User’s Guide*, MathSoft Inc., Cambridge, Massachusetts, USA, 1995.

- [79] M. D. Judd, P. F. Coventry, and J. Blackett. Contact discharge test cell: A means of generating signals for sensitivity verification of UHF PD detection in GIS, In *Proceedings of IEEE International Symposium on Electrical Insulation*, pp. 407 – 410, Boston, 2002.
- [80] M. D. Judd. Contact discharges as a source of sub-nanosecond high voltage pulses, *Journal of physics D: Applied physics*, Vol. 34, No. 18, pp. 2883 – 2893, 2001.
- [81] F. G. Stremmer. *Introduction to Communication Systems*, Prentice Hall, 3rd edn., 1990.
- [82] T. Pinpart, J. E. Fletcher, and M. D. Judd. Methods for distinguishing between partial discharges based on the UHF detection technique, In *Proceedings of International Conference on Condition Monitoring and Diagnosis*, pp. 1060 – 1064, Beijing, 2008.
- [83] S. Tenbohlen, D. Denissov, S. Hoek, and S. M. Markalous. Partial discharge measurement in the ultra high frequency (UHF) range, *IEEE Transactions on Dielectrics and Electrical Insulation*, Vol. 15, No. 6, pp. 1544 – 1552, 2008.
- [84] M. D. Judd. *Lecture Materials, EE902 Instrumentation and Condition Monitoring*, University of Strathclyde, 2007.
- [85] R. Bartnikas. A comment concerning the rise times of partial discharge pulses, *IEEE Transactions on Dielectrics and Electrical Insulation*, Vol. 12, No. 2, pp. 196 – 202, 2005.
- [86] H. Okubo, N. Hayakawa, and A. Matsushita. The relationship between partial discharge current pulse waveforms and physical mechanisms, *IEEE Electrical Insulation Magazine*, Vol. 18, No.3, pp. 38 – 45, 2002.
- [87] M. D. Judd, O. Farish, and B. F. Hampton. The excitation of UHF signals by partial discharges in GIS, *IEEE Transactions on Dielectrics and Electrical Insulation*, Vol. 3, No. 2, pp. 213 – 228, 1996.
- [88] L. Yang, M. D. Judd, and C. J. Bennoch. Time delay estimation for UHF signals in PD location of transformers, In *Proceedings of Annual Report Conference on Electrical Insulation and Dielectric Phenomena*, pp 414 – 416, Colorado, 2004.

- [89] M. D. Judd, O. Farish, J. S. Pearson, and B. F. Hampton. Dielectric windows for UHF partial discharge detection, *IEEE Transactions on Dielectrics and Electrical Insulation*, Vol. 8, No. 6, pp 953 – 958, 2001.
- [90] P. J. Orr, A. J. Reid, and M. D. Judd. Sensor response characteristics for UHF location of PD sources, In *Proceedings of International Conference on Condition Monitoring and Diagnosis*, pp. 1119-1122, Beijing, 2008.
- [91] S. Meijer, P. D. Agoris, J. J. Smit, M. D. Judd, and L. Yang. Application of UHF diagnostics to detect PD during power transformer acceptance tests, In *Proceedings of IEEE International Symposium on Electrical Insulation*, pp. 416 – 419, Toronto, 2006.
- [92] Z. Tang, C. Li, X. Huang, Z. Li, and S. Fu. The feasibility of locating PD source in transformers using the UHF technology, In *Proceedings of Annual report conference on Electrical Insulation and Dielectric Phenomena*, pp. 477 – 480, Colorado, 2004.
- [93] E. Howells, and E. T. Norton. Location of partial discharge sites in on-line transformers, *IEEE Transactions on Power Apparatus and Systems*, Vol. PAS-100, No. 1, pp. 158 – 161, 1981.
- [94] P. J. Moore, I. E. Portugues, and I. A. Glover. Radiometric location of partial discharge sources on energized high-voltage plant, *IEEE Transactions on Power Delivery*, Vol. 20, No. 3, pp. 2264 – 2272, 2005
- [95] J. Ramírez-Niño, and A. Pascacio. Acoustic measuring of partial discharge in power transformers, *IEE Proceedings Science, Measurement and Technology*, Vol. 20, No. 11, pp. 1 – 9, 2009.
- [96] P. Wagenaars, P. A. A. F. Wouters, P. C. J. M. van der Wielen, and E. F. Steennis. Accurate estimation of the time-of-arrival of partial discharge pulses in cable systems in service, *IEEE Transactions on Dielectrics and Electrical Insulation*, Vol. 15, No. 4, pp 1190 – 1199, 2008.
- [97] P. Kundu, N. K. Kishore, and A. K. Sinha. A non-iterative partial discharge source location method for transformers employing acoustic emission techniques, *Applied Acoustics*, Vol. 70, No. 11-12, pp. 1378-1383, 2009.

- [98] J. H. Kurz, C. U. Grosse and H. Reinhardt. Strategies for reliable automatic onset time picking of acoustic emissions and of ultrasound signals in concrete, *Ultrasonics*, Vol. 43, No. 7, pp. 538 – 546, 2005.
- [99] C. Herold, T. Leibfried, S. Markalous, and I. Quint. Algorithms for automated arrival time estimation of partial discharge signals in power cables, In *Proceedings of XVth International Symposium on High Voltage Engineering*, pp. 1 – 5, Ljubljana, 2007.
- [100] T. Pinpart, and M. D. Judd. Improving UHF partial discharge location in high voltage equipment, In *Proceedings of the 44th International Universities' Power Engineering Conference*, Glasgow, 2009.
- [101] T. Pinpart, and M. D. Judd. Improved technique for locating insulation defects in high voltage equipment, In *Proceeding of 2nd UHVnet Colloquium*, pp. 69 – 72, Glasgow, 2009.
- [102] M. Misiti, Y. Misiti, G. Oppenheim, and J. Poggi. *Wavelet toolbox user's guide version 3*, The MathWorks, Inc, 2004.
- [103] *MATLAB*[®], version 7.7.0471(R2008b), 17th September, 2008.
- [104] M. L. Chai, Y. H. M. Thayoob, P. S. Ghosh, A. Z. Sha'ameri, and M. A. Talib. Identification of different types of PD sources from AE signals in the time-frequency representation, In *Proceedings of IEEE International Power and Energy Conference*, pp. 580 – 585, Patrajaya, 2006.
- [105] Y. Tian, P. L. Lewin, S. J. Sutton, and S. G. Swingler. PD characterization using wavelet decomposition of acoustic emission signals, In *Proceedings of International Conference on Solid Dielectrics*, Vol. 2, pp. 699 – 702 Toulouse, 2004.
- [106] X. Zhou, C. Zhou, and I. J. Kemp. An improved methodology for application of wavelet transform to partial discharge measurement denoising, *IEEE Transactions on Dielectrics and Electrical Insulation*, Vol. 12, No. 3, pp. 586 – 594, 2005.
- [107] L. Satish, and B. Nazneen. Wavelet-based de-noising of partial discharge signals buried in excessive noise and interference, *IEEE Transactions on Dielectrics and Electrical Insulation*, Vol. 10, No. 2, pp. 354 – 367, 2003.

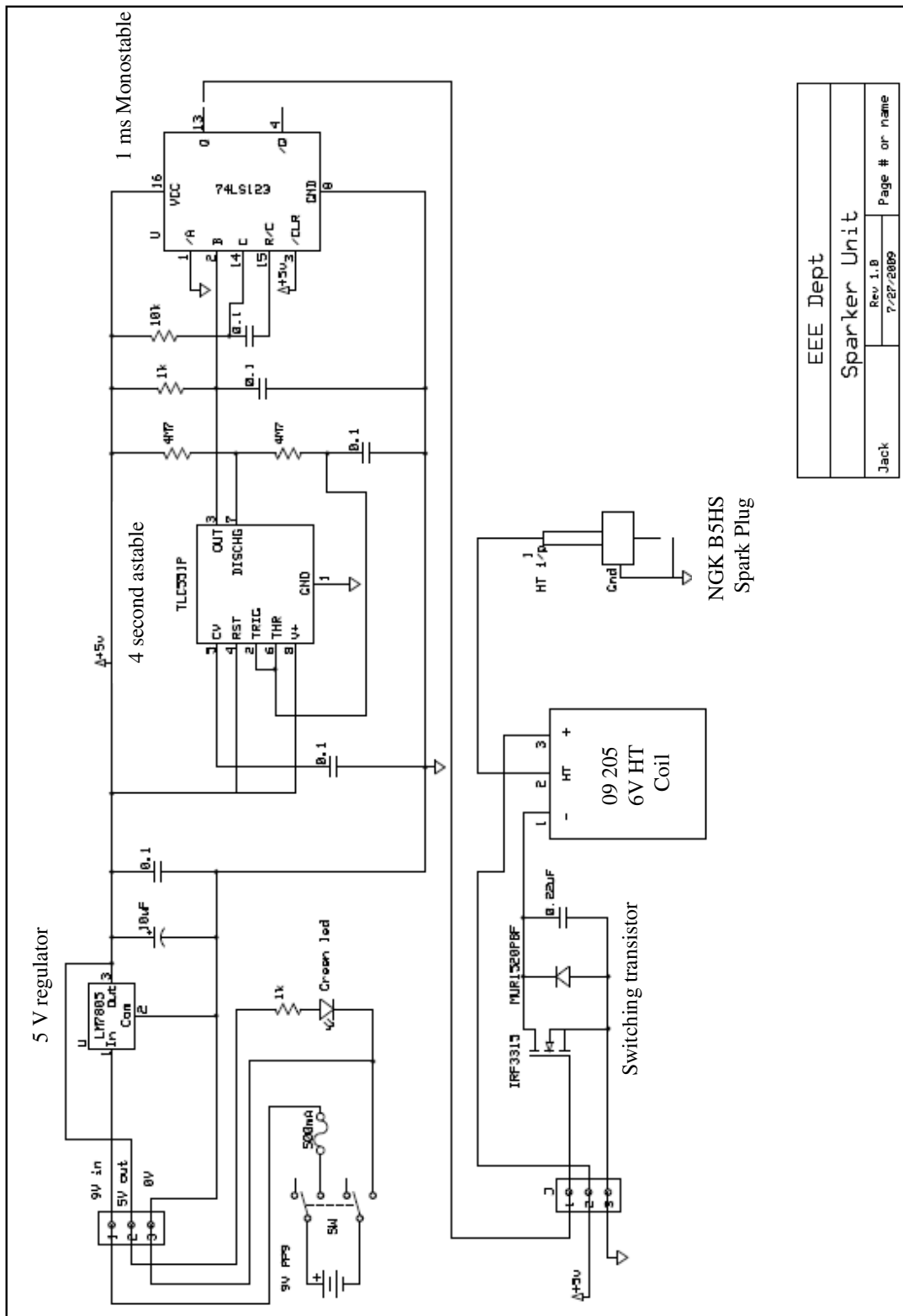
- [108] H. Zhang, T. R. Blackburn, B. T. Phung, and D. Sen. A novel wavelet transform technique for on-line partial discharge measurements part 1: WT de-noising algorithm, *IEEE Transactions on Dielectrics and Electrical Insulation*, Vol. 14, No. 1 pp. 3 – 14, 2007.
- [109] L. Yang, M. D. Judd, and C. J. Bennoch. Denoising UHF signal for PD detection in transformers based on wavelet technique, In *Proceedings of Report conference on Electrical Insulation and Dielectric Phenomena*, pp. 166 – 169, Colorado, 2004.
- [110] P. D. Agoris, S. Meijer, E. Gulski, and J. J. Smit. Threshold selection for wavelet de-noising of partial discharge data, In *Proceedings of Conference record of IEEE International Symposium on Electrical Insulation on Electrical Insulation*, Indianapolis, pp. 62 – 65, Indianapolis, 2004.
- [111] Z. Xu, J. Tu, and C. Sun. Application of complex wavelet transform to suppress white noise in GIS UHF PD signals, *IEEE Transactions on Power Delivery*, Vol. 22, No. 3, pp. 1498 – 1504, 2007.
- [112] X. Song, M. Judd, and C. Zhou. An optimal algorithm for applying wavelet transform in identifying the arrival time of PD pulse in a UHF detection system, In *Proceedings of 42nd International Universities Power Engineering Conference*, pp. 495 – 498, Brighton, 2007.
- [113] X. Song, C. Zhou, and D. M. Hepburn. An algorithm for identifying the arrival times of PD pulses for PD source location, In *Proceedings of Annual Report Conference on Electrical Insulation and Dielectric Phenomena*, pp. 379 – 382, Québec, 2008.
- [114] S. Markalous, T. Strehl, C. Herold, and T. Leibfried. Enhanced signal processing for conventional and unconventional PD measurement methods: Wavelet de-noising, automatic detection algorithms and averaging for arrival time-based PD location in transformers and power cables, In *Proceedings of International Conference on Condition Monitoring and Diagnosis*, pp. 1115 – 1118, Beijing, 2008.
- [115] E. M. Lalitha, and L. Satish. Wavelet analysis for classification of multi-source PD patterns, *IEEE Transactions on Dielectrics and Electrical Insulation*, Vol. 7, No. 1, pp. 40 – 47, 2000.

- [116] M. Kawada, A. Tungkanawanich, Z. Kawasaki, and K. Matsu-Ura. Detection of wide-band E-M signals emitted from partial discharge occurring in GIS using wavelet transform, *IEEE Transactions on Power Delivery*, Vol. 15, No. 2, pp. 467 – 471, 2000.
- [117] C. S. Chang, J. Jin, S. Kumar, Q. Su, T. Hoshino, M. Hanai, and N. Kobayashi. Denoising of Partial Discharge Signals in Wavelet Packets Domain, *IEE Proceedings Science, Measurement and Technology*, Vol. 152, No. 3, pp. 129 – 140, 2005.
- [118] C. M. Stein. Estimation of the mean of a multivariate normal distribution, *The Annals of Statistics*, Vol. 9, No. 6, pp. 1135 – 1151, 1981.
- [119] D. L. Donoho, and I. M. Johnstone. Adapting to Unknown Smoothness via Wavelet Shrinkage, *Journal of the American Statistical Association*, Vol. 90, No. 432, pp. 1200 – 1224, 1995.
- [120] T. Pinpart, A. M. bin Ishak, and M. D. Judd. Effect of wavelet de-noising on signal timing accuracy for UHF partial discharge location, In *Proceedings of 11th International Electrical Insulation Conference*, pp 128 – 133, Birmingham, 2009.
- [121] M. D. Judd, and O. Farish. A pulsed GTEM system for UHF sensor calibration, *IEEE Transactions on Instrumentation and Measurement*, Vol. 47, No. 4, pp 875 – 880, 1998.
- [122] M. D. Judd. Transient calibration of electric field sensors, *IEE Proceedings Science, Measurement and Technology*, Vol. 146, No. 3, pp. 113 – 116, 1999.
- [123] T. Pinpart, and M. D. Judd. Experimental comparison of UHF sensor types for PD location applications, In *Proceedings of IEEE Electrical Insulation Conference*, pp 26 – 30, Montreal, 2009.
- [124] S. Coenen, S. Tenbohlen, T. Streh, and S. Markalous. Fundamental characteristics of UHF PD probes and the radiation behaviour of PD sources in power transformers, In *Proceedings of 16th International Symposium on High Voltage Engineering*, Cape Town, 2009.
- [125] *Microsoft Excel 2003 (11.8316.8221) SP3*, 1995 – 2003 Microsoft Corporation.

- [126] L Li, C. Huang, Y. Zeng, X. Jiang. Partial discharge diagnosis on GIS based on envelope detection, *World Scientific and Engineering Academy and Society Transactions on Systems*, Vol. 7, No. 11, pp. 1238 – 1247, 2008.
- [127] T. Pinpart, and M. D. Judd. Differentiating between partial discharges by comparing UHF signal envelopes with reduced signal sampling rate, *In Proceeding of 3rd UHVnet Colloquium*, Manchester, 2010.
- [128] P. C. Baker, B. Stephen, M. D. Judd, and S. D. J. McArthur. Development of an integrated low-power RF partial discharge detector, *In Proceedings of IEEE Electrical Insulation Conference*, Montreal, pp. 273 - 277, 2009.
- [129] Application note AN006A Enhance Resolution, available from http://www.lecroy.com/tm/library/AppNotes/EnhancedRes/AN_006a.pdf
- [130] M. Chapman. Radio-frequency-based determination of arcing duration in HVAC breakers, *In Proceedings of 18th International Conference on Electricity Distribution*, Turin, 2005.

Appendix A

Schematic diagram of the spark unit



EEE Dept	
Sparker Unit	
Jack	Page # or name
Rev 1.0	7/27/2009

Appendix B

Datasheet of HSMS 2820 Schottky diode

Surface Mount RF Schottky Barrier Diodes

Technical Data

HSMS-282x Series

Features

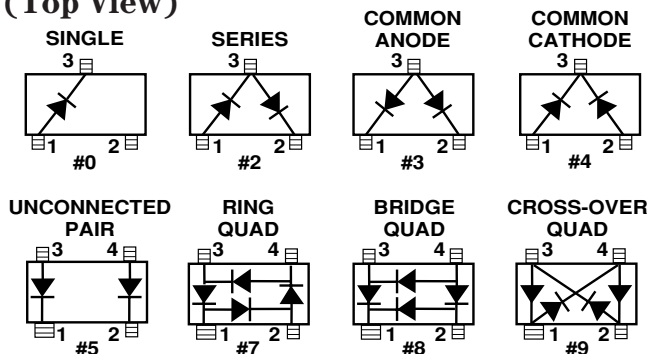
- **Low Turn-On Voltage**
(As Low as 0.34 V at 1 mA)
- **Low FIT (Failure in Time) Rate***
- **Six-sigma Quality Level**
- **Single, Dual and Quad Versions**
- **Unique Configurations in Surface Mount SOT-363 Package**
 - increase flexibility
 - save board space
 - reduce cost
- **HSMS-282K Grounded Center Leads Provide up to 10 dB Higher Isolation**
- **Matched Diodes for Consistent Performance**
- **Better Thermal Conductivity for Higher Power Dissipation**
- **Lead-free Option Available**

* For more information see the Surface Mount Schottky Reliability Data Sheet.

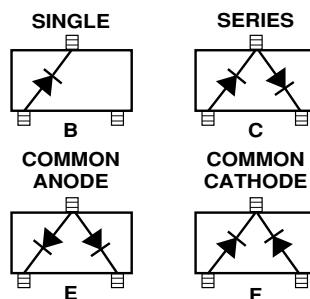
Description/Applications

These Schottky diodes are specifically designed for both analog and digital applications. This series offers a wide range of specifications and package configurations to give the designer wide flexibility. Typical applications of these Schottky diodes are mixing, detecting, switching, sampling, clamping,

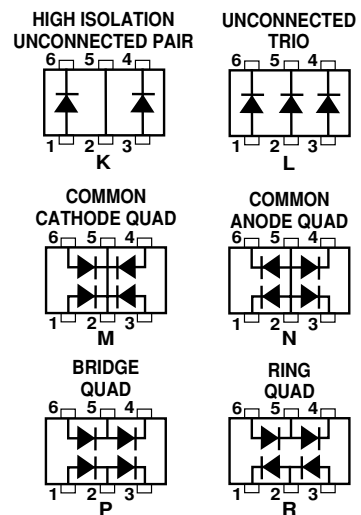
Package Lead Code Identification, SOT-23/SOT-143 (Top View)



Package Lead Code Identification, SOT-323 (Top View)



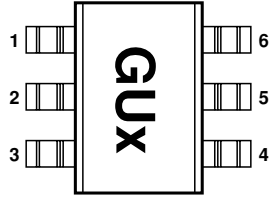
Package Lead Code Identification, SOT-363 (Top View)



and wave shaping. The HSMS-282x series of diodes is the best all-around choice for most applications, featuring low series resistance, low forward voltage at all current levels and good RF characteristics.

Note that Agilent's manufacturing techniques assure that dice found in pairs and quads are taken from adjacent sites on the wafer, assuring the highest degree of match.

Pin Connections and Package Marking



Notes:

1. Package marking provides orientation and identification.
2. See “Electrical Specifications” for appropriate package marking.

Absolute Maximum Ratings^[1] $T_C = 25^\circ\text{C}$

Symbol	Parameter	Unit	SOT-23/SOT-143	SOT-323/SOT-363
I_F	Forward Current (1 μs Pulse)	Amp	1	1
P_{IV}	Peak Inverse Voltage	V	15	15
T_j	Junction Temperature	$^\circ\text{C}$	150	150
T_{stg}	Storage Temperature	$^\circ\text{C}$	-65 to 150	-65 to 150
θ_{jc}	Thermal Resistance ^[2]	$^\circ\text{C}/\text{W}$	500	150

Notes:

1. Operation in excess of any one of these conditions may result in permanent damage to the device.
2. $T_C = +25^\circ\text{C}$, where T_C is defined to be the temperature at the package pins where contact is made to the circuit board.

Electrical Specifications $T_C = 25^\circ\text{C}$, Single Diode^[4]

Part Number HSMS ^[5]	Package Marking Code	Lead Code	Configuration	Minimum Breakdown Voltage V_{BR} (V)	Maximum Forward Voltage V_F (mV)	Maximum Forward Voltage V_F (V) @ I_F (mA)	Maximum Reverse Leakage I_R (nA) @ V_R (V)	Maximum Capacitance C_T (pF)	Typical Dynamic Resistance R_D (Ω) ^[6]						
2820	C0 ^[3]	0	Single	15	340	0.5 10	100 1	1.0	12						
2822	C2 ^[3]	2	Series												
2823	C3 ^[3]	3	Common Anode												
2824	C4 ^[3]	4	Common Cathode												
2825	C5 ^[3]	5	Unconnected Pair												
2827	C7 ^[3]	7	Ring Quad ^[5]												
2828	C8 ^[3]	8	Bridge Quad ^[5]												
2829	C9 ^[3]	9	Cross-over Quad												
282B	C0 ^[7]	B	Single												
282C	C2 ^[7]	C	Series												
282E	C3 ^[7]	E	Common Anode												
282F	C4 ^[7]	F	Common Cathode												
282K	CK ^[7]	K	High Isolation Unconnected Pair												
282L	CL ^[7]	L	Unconnected Trio												
282M	HH ^[7]	M	Common Cathode Quad												
282N	NN ^[7]	N	Common Anode Quad												
282P	CP ^[7]	P	Bridge Quad												
282R	OO ^[7]	R	Ring Quad												
Test Conditions										$I_R = 100 \mu\text{A}$	$I_F = 1 \text{ mA}^{[1]}$			$V_F = 0 \text{ V}$ $f = 1 \text{ MHz}^{[2]}$	$I_F = 5 \text{ mA}$

Notes:

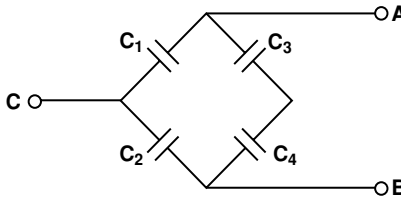
1. ΔV_F for diodes in pairs and quads in 15 mV maximum at 1 mA.
2. ΔC_{TO} for diodes in pairs and quads is 0.2 pF maximum.
3. Package marking code is in white.
4. Effective Carrier Lifetime (τ) for all these diodes is 100 ps maximum measured with Krakauer method at 5 mA.
5. See section titled “Quad Capacitance.”
6. $R_D = R_S + 5.2 \Omega$ at 25°C and $I_F = 5 \text{ mA}$.
7. Package marking code is laser marked.

Quad Capacitance

Capacitance of Schottky diode quads is measured using an HP4271 LCR meter. This instrument effectively isolates individual diode branches from the others, allowing accurate capacitance measurement of each branch or each diode. The conditions are: 20 mV R.M.S. voltage at 1 MHz. Agilent defines this measurement as “CM”, and it is equivalent to the capacitance of the diode by itself. The equivalent diagonal and adjacent capacitances can then be calculated by the formulas given below.

In a quad, the diagonal capacitance is the capacitance between points A and B as shown in the figure below. The diagonal capacitance is calculated using the following formula

$$C_{\text{DIAGONAL}} = \frac{C_1 \times C_2}{C_1 + C_2} + \frac{C_3 \times C_4}{C_3 + C_4}$$

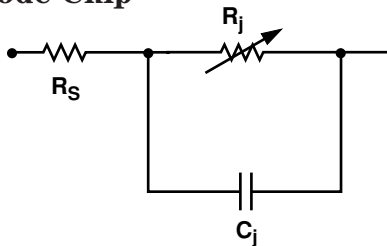


The equivalent adjacent capacitance is the capacitance between points A and C in the figure below. This capacitance is calculated using the following formula

$$C_{\text{ADJACENT}} = C_1 + \frac{1}{\frac{1}{C_2} + \frac{1}{C_3} + \frac{1}{C_4}}$$

This information does not apply to cross-over quad diodes.

Linear Equivalent Circuit Model Diode Chip



R_s = series resistance (see Table of SPICE parameters)

C_j = junction capacitance (see Table of SPICE parameters)

$$R_j = \frac{8.33 \times 10^{-5} \text{ nT}}{I_b + I_s}$$

where

I_b = externally applied bias current in amps

I_s = saturation current (see table of SPICE parameters)

T = temperature, °K

n = ideality factor (see table of SPICE parameters)

Note:

To effectively model the packaged HSMS-282x product, please refer to Application Note AN1124.

ESD WARNING:

Handling Precautions Should Be Taken To Avoid Static Discharge.

SPICE Parameters

Parameter	Units	HSMS-282x
B_V	V	15
C_{J0}	pF	0.7
E_G	eV	0.69
I_{BV}	A	1E-4
I_S	A	2.2E-8
N		1.08
R_S	Ω	6.0
P_B	V	0.65
P_T		2
M		0.5

Typical Performance, $T_C = 25^\circ\text{C}$ (unless otherwise noted), Single Diode

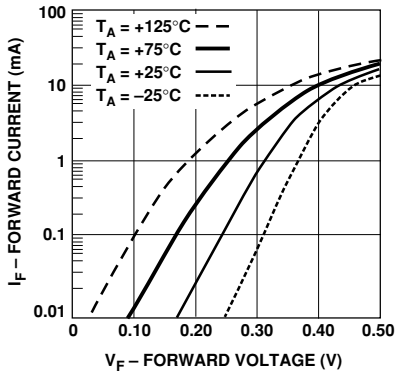


Figure 1. Forward Current vs. Forward Voltage at Temperatures.

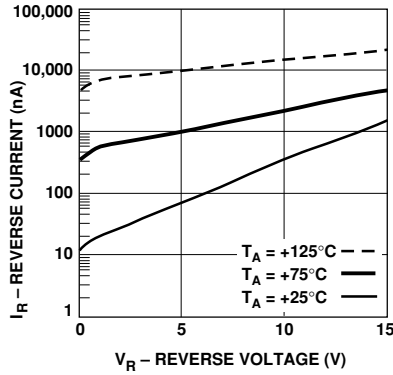


Figure 2. Reverse Current vs. Reverse Voltage at Temperatures.

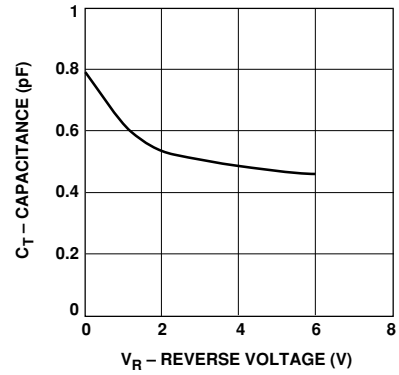


Figure 3. Total Capacitance vs. Reverse Voltage.

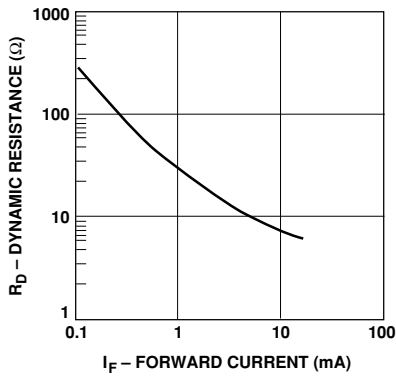


Figure 4. Dynamic Resistance vs. Forward Current.

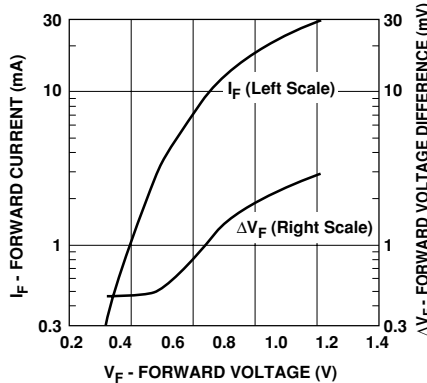


Figure 5. Typical V_f Match, Series Pairs and Quads at Mixer Bias Levels.

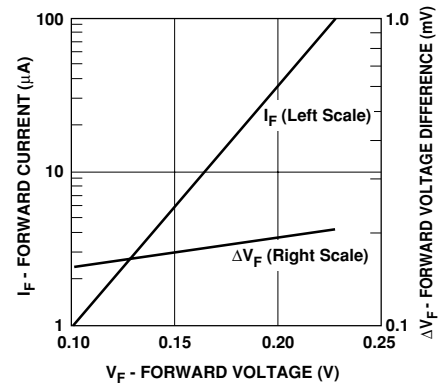


Figure 6. Typical V_f Match, Series Pairs and Quads at Detector Bias Levels.

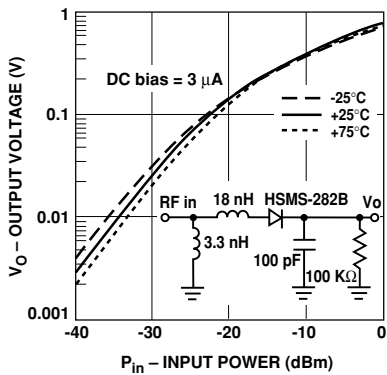


Figure 7. Typical Output Voltage vs. Input Power, Small Signal Detector Operating at 850 MHz.

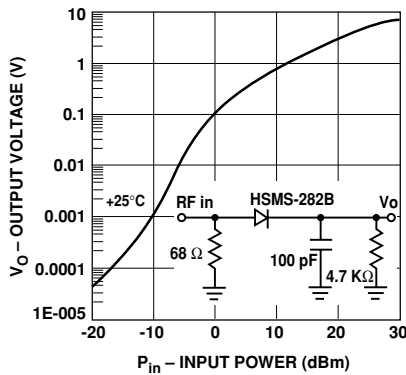


Figure 8. Typical Output Voltage vs. Input Power, Large Signal Detector Operating at 915 MHz.

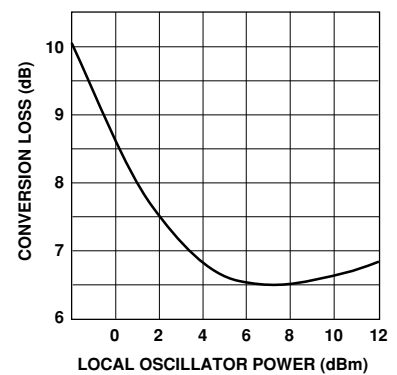


Figure 9. Typical Conversion Loss vs. L.O. Drive, 2.0 GHz (Ref AN997).